OUKA
The University of Osaka
Institutional Knowledge Archive

Title	High-sensitivity Raman scattering microscopy for imaging molecules in living cells
Author(s)	小池, 康太
Citation	大阪大学, 2022, 博士論文
Version Type	VoR
URL	https://doi.org/10.18910/88028
rights	
Note	

The University of Osaka Institutional Knowledge Archive : OUKA

https://ir.library.osaka-u.ac.jp/

The University of Osaka

High-sensitivity Raman scattering microscopy for imaging molecules in living cells

by
Kota KOIKE

A dissertation submitted in partial fulfillment
of the requirement for the degree of
Doctor of Philosophy in Engineering

Graduate School of Engineering
Osaka University

January 2022

Copyright © 2022 by Kota Koike
ORCID: 0000-0002-5631-5138



All Rights Reserved.

Acknowledgements

I would like to thank my supervisor, Prof. Katsumasa Fujita, for his support and encouragement during my Ph.D. study. I always enjoyed spending time with him teaching me how to write and present scientific papers. I was lucky to have him as my professor as I enjoyed discussing with him and learning the fun of science through his optimistic approach to every problem and discovery. He provided me with many opportunities to present my work at international conferences and symposia during my study. He also encouraged me to study at Wei Min's lab at Columbia University. I have learned and experienced many things here that I would never have been able to do elsewhere.

I want to thank Assoc. Prof. Nicholas Smith for supporting me in all my projects through his helpful advice. By working with him, I learned how to write better research papers. I was also able to do a short research project in his lab for 4 months, and it was a great time for me.

I thank Assist. Prof. Yasuaki Kumamoto, Assoc. Prof. Masahito Yamanaka, Prof. Yasushi Inoue, Prof. Verma Prabhat, Dr. Ryosuke Oketani, Dr. Yasunori Nawa, Dr. Menglu Li, Dr. Kentaro Nishida, Dr. Toshiki Kubo, and Tai Fanfang for their helpful advice and discussions during my Ph.D. study.

I thank Assist. Prof. Kazuki Bando for the SERS research. He helped me to build the optical setup and visualize the SERS data. The experiments and discussions with Prof. Bando were always enjoyable.

I also want to thank Dr. Hiroyuki Kawagoe for the SRS research. His contribution to the data acquisition system made the SRS research possible.

I thank Dr. Giulia Zanini for doing the initial SRS research together and teaching me the fundamental of pump-probe microscopy and how to build the optical setup. Working together for 4-5 months was a great time for me. I also enjoyed Thanksgiving vacation with her in Washington D.C. during my research at Columbia University. I wish her all the best in the U.S.

Thank you, Lecturer Takayuki Umakoshi, for inviting me to participate in his AFM-SRS research project. It was a good experience for me to optimize the system and finally find the signal.

This thesis would not have been possible without all the input from my collaborators, Dr. Jun Ando, Dr. Mikiko Sodeoka, and other researchers in the RIKEN Sodeoka Group.

I am grateful to Vaibhav Bansode for the many times we have talked about things other than research and supported each other through difficult times as friends. I have always been impressed with his ideas on making research work forward. I hope we can have a tea time again at another place soon.

I also would like to thank my lab members, Kenta Temma, Atsushi Nakayama, Hao-Xiang Liao, and others who had helped me in the experiments and interesting discussions over the years.

Last but not least, I would like to thank my wife, Kanako Koike, and my family for their support and encouragement during my Ph.D. studies.

Abstract

Raman scattering microscopy has emerged as a label-free imaging tool, making it possible to observe the distribution of substances in a sample by detecting molecular vibration. Due to its non-invasiveness and chemical specificity, Raman scattering microscopy is particularly useful in bioimaging applications such as analyzing various tissue/cell types and visualizing small molecules. The rise of Raman scattering microscopy came together with surface-enhanced Raman scattering (SERS) and newly emerged stimulated Raman scattering (SRS) techniques. SERS enhances the detection sensitivity by 10^4 to 10^{14} through plasmon resonance of metallic nanoparticles. SRS offers high-speed and quantitative label-free imaging by coherent Raman scattering process. In my Ph.D. thesis, I explore SERS and SRS to develop new vibrational microscopy methods with higher sensitivity and higher temporal/spatial resolution to visualize biomolecules and small molecules in living cells.

Chapter 1 introduces the basics of spontaneous Raman scattering, SERS, and SRS and their applications to imaging and sensing of biological and small molecules in living cells.

Chapter 2 proposes using SERS to visualize the drug entry into live cells in 3D. Alkyne-tagged small molecules are used to detect within a complex intracellular environment. Gold nanoparticles introduced into the cell act as a reporter to indicate the arrival of small-molecule drugs. Digital SERS counting enables quantitative analysis of uptake speed under different chemical and physical conditions.

Chapter 3 presents the application of spectral focusing to picosecond pulsed SRS microscopy. The chirped 14 ps laser pulses achieve a spectral resolution of 2 cm^{-1} and a 2-fold improvement in a signal-to-background ratio compared to the 2 ps laser pulses. Furthermore, time-lapse SRS imaging for 100 frames with higher SNR is realized by reducing nonlinear photodamage.

Chapter 4 explores the saturation effect of SRS to address the relatively low spatial resolution of SRS microscopy. The idea of differential saturated excitation (dSAX) microscopy is adopted to extract the saturated SRS signal. The resolution enhancement is evaluated theoretically and experimentally using diamond crystals and PMMA beads.

Chapter 5 discusses the theoretical improvement of spatial resolution down to about 100 nm by combining visible wavelength (VW) and dSAX techniques. The first attempt (but failure) of super-resolution VW-SRS of HeLa cells labeled with the Carbow probe is presented. Discussion toward successful super-resolution VW-SRS imaging is also provided.

Chapter 6 performs high-speed multiplex SRS spectroscopy of pre-resonance Raman probes. A hyperspectral SRS microscope with spectral focusing of femtosecond laser pulses is developed. High-speed 2-, 4- and 8-color multiplex SRS spectroscopy of MARS is demonstrated, which will lead to high-speed SRS imaging of multiple organelles in living cells with high sensitivity.

List of Publications and Scholarships

Original articles

1. K. Koike, K. Bando, J. Ando, H. Yamakoshi, N. Terayama, K. Dodo, N. I. Smith, M. Sodeoka, K. Fujita, "Quantitative Drug Dynamics Visualized by Alkyne-Tagged Plasmonic-Enhanced Raman Microscopy", *ACS Nano*, 14 (11), 15032-15041 (2020)
(日本光学会「日本の光学研究 2020」に選出。光学 50 (6), 32)
2. K. Koike, N. I. Smith, K. Fujita, "Spectral focusing in picosecond pulsed stimulated Raman scattering microscopy", *Biomedical Optics Express*, 13 (2), 995-1004 (2022).
3. K. Koike, N. I. Smith, K. Fujita, "Visible-wavelength Stimulated Raman Scattering Microscopy with Saturated Excitation toward Super-resolution Vibrational Imaging", in preparation.

Review article

1. J. Ando, K. Bando, K. Koike, K. Fujita, "Applications of Metallic Nanoparticles in Bio-imaging and Molecular Spectroscopy", *Material Matters*, 16 (2), 18-22 (2021)

Other original article

1. F. Tai, K. Koike, H. Kawagoe, J. Ando, Y. Kumamoto, N. I. Smith, M. Sodeoka, K. Fujita, "Detecting nitrile-containing small molecules by infrared photothermal microscopy", *Analyst*, 146, 2307-2312 (2021)

Conference proceedings

1. K. Koike, K. Bando, J. Ando, N. I. Smith, K. Dodo, S. Kawata, M. Sodeoka, K. Fujita,"Dynamic 3D SERS imaging of small molecules in live cells", Proc. SPIE 11140, Biomedical Imaging and Sensing Conference, pp.1114001-54-55 (2019) doi: 10.1117/12.2535451
2. K. Koike, K. Bando, J. Ando, N. I. Smith, K. Dodo, S. Kawata, M. Sodeoka, K. Fujita,"Alkyne-tag SERS imaging for visualizing small molecule drugs in live cells", Proc. SPIE 11219, Visualizing and Quantifying Drug Distribution in Tissue IV, pp.112190D-1-4 (2020) doi: 10.1117/12.2545872
3. K. Koike, N. I. Smith, K. Fujita, "Stimulated Raman scattering microscopy with spectral focusing of 2-ps laser pulses for higher spectral resolution and signal-to-background ratio", Proc.

SPIE, accepted, Advanced Chemical Microscopy for Life Science and Translational Medicine (2022)

International Conference

1. K. Koike, G. Zanini, H. Kawagoe, R. Oketani, N. I. Smith, K. Fujita,"Spatial Resolution Improvement of Vibrational Imaging with Saturated-Stimulated Raman Scattering Microscopy", The Global Nanophotonics 2017, P-27, Puerto Princesa, Philippines, Dec. 2017 (Poster, No peer-reviewed)
2. K. Koike, J. Ando, K. Bando, N. I. Smith, and K. Fujita, "Time-lapse 3D SERS imaging of alkyne-tagged drug molecules in live cells", The International Symposium for Materials Scientists Ⅲ, P-57, Osaka Pref., December 2018 (Poster, Peer-reviewed)
3. K. Koike, K. Bando, J. Ando, N. I. Smith, K. Dodo, S. Kawata, M. Sodeoka, K. Fujita,"Dynamic 3D SERS imaging of small molecules in live cells", Optics&Photonics International Congress 2019, BISC-3-03, Kanagawa Pref., April 2019 (Oral, Peer-reviewed)
4. K. Koike, K. Bando, J. Ando, N. I. Smith, K. Dodo, S. Kawata, M. Sodeoka, K. Fujita,"4D SERS Imaging of Alkyne-tagged small molecules in living cells", Focus on Microscopy 2019, TU-AF1-PAR-B, London, United Kingdom, April 2019 (Oral, Peer-reviewed)
5. K. Koike, K. Bando, J. Ando, N. I. Smith, K. Dodo, S. Kawata, M. Sodeoka, K. Fujita,"Dynamic 3D surface-enhanced Raman imaging of small molecules in live cells", CLIRSPEC Summer School in ASIA, Kobe, Hyogo Pref., August 2019 (Poster, No peer-reviewed)
6. K. Koike, K. Bando, J. Ando, N. I. Smith, K. Dodo, S. Kawata, M. Sodeoka, K. Fujita, "Alkyne-tag SERS imaging for visualizing small molecule drugs in live cells", SPIE Photonics West 2020, Visualizing and Quantifying Drug Distribution in Tissue IV, 112190D, San Francisco, USA, February 2020 (Oral, Peer-reviewed)
7. K. Koike, N. I. Smith, K. Fujita, "Stimulated Raman scattering microscopy with spectral focusing of 2-ps laser pulses for higher spectral resolution and signal-to-background ratio", SPIE Photonics West 2022, Advanced Chemical Microscopy for Life Science and Translational Medicine, 11973-41, San Francisco, USA, January 2022 (Oral, Peer-reviewed)

Domestic Conference

1. G. Zanini, K. Koike, H. Kawagoe, R. Oketani, N. I. Smith, K. Fujita,"Spatial Resolution Improvement of Vibrational Imaging with Saturated-Stimulated Raman Scattering Microscopy", 「第 43 回レーザ顕微鏡研究会 & シンポジウム」, P-5, 大阪府吹田市, 2018 年 1 月 (ポスター, 査読無)

2. 小池 康太, Giulia Zanini, 川越 寛之, 桶谷 亮介, Nicholas. I. Smith, 藤田 克昌, ”誘導ラマン散乱の飽和信号を用いた超解像イメージング”, 「第 65 回応用物理学会春季学術講演会」19p-A302-2, 東京都, 2018 年 3 月 (口頭, 査読無)
3. 小池 康太, 安藤 潤, 畔堂 一樹, スミス ニコラス, 藤田 克昌, ”アルキンで標識した薬剤分子の細胞内 3D 表面増強ラマンイメージング”, 「第 16 回医用分光学研究会」, P-6, 北海道札幌市, 2018 年 11 月 (ポスター、査読無)
4. 小池 康太, 畔堂 一樹, 安藤 潤, スミス ニコラス, どど 孝介, 河田 聡, 袖岡 幹子, 藤田 克昌, ”細胞内における低分子化合物の 3 次元表面増強ラマンイメージング”, 「第 18 回産総研 LS-BT 合同研究発表会」, 茨城県つくば市, 2019 年 5 月 (ポスター、査読無)
5. 小池 康太, 畔堂 一樹, 安藤 潤, 山越 博幸, スミス ニコラス, どど 孝介, 袖岡 幹子, 藤田 克昌, ”表面増強ラマン散乱による細胞中の低分子薬剤の可視化”, 「第 19 回産総研 LS-BT 合同研究発表会」, P-40, オンライン, 2021 年 5 月 (ポスター、査読無)

Invited Talks

1. K. Fujita, K. Koike, ”Slit-scanning Raman microscopy using Bessel beam illumination”, SPIE Photonics West 2022, Advanced Chemical Microscopy for Life Science and Translational Medicine, 11973-17, San Francisco, USA, 23 January 2022
2. K. Fujita, K. Koike, ”Enhancing Raman microscopy by structured light”, SPIE Photonics West 2022, Biomedical Vibrational Spectroscopy 2022: Advances in Research and Industry, 11957-8, San Francisco, USA, 22 January 2022
3. K. Koike, ”Highly-sensitive Raman imaging of molecules in living cells”, Seminar: Coherent Raman microscopy and other nonlinear imaging techniques-development and applications, Jagiellonian University Raman Imaging Group, online, 22 February 2022

Scholarships and grants

1. Research Fellowship for Young Researchers (DC2) 2021-2022, Japan Society for the Promotion of Science (日本学術振興会 特別研究員 DC2, 21J11008)
2. Technical Exchange Grant Program 2019, Nakatani Foundation for advancement of measuring technologies in biomedical engineering (中谷医工計測技術振興財団 2019 年度技術交流助成交流プログラム海外派遣)
3. Research Assistant 2018-2022, Photo-Bio OIL, AIST-Osaka University (大阪大学-産総研 先端フォトニクス・バイオセンシングオープンイノベーションラボラトリ リサーチアシスタント)

List of Figures

1.1 Schematic of energy diagram of processes of Rayleigh scattering, Stokes Raman scattering, and anti-Stokes Raman scattering 4
1.2 Schematic of SRS microscope setup 15
1.3 Various types of SRS signal detection schemes 17
2.1 Optical setup of slit scanning SERS microscopy for 2D and 3D imaging 28
2.2 Step voltage sent from function generator to galvanometer-mirror and piezoelectric stage for the 3D imaging 28
2.3 Raman spectroscopy of alkyne-tagged acyloxymethyl ketone type inhibitor (Alt-AOMK) 30
2.4 Detection limit of spontaneous Raman peak of alkynes in Alt-AOMK 30
2.5 Raman imaging of living macrophages with and without gold nanoparticles 32
2.6 Bright field observation of macrophages with hemocytometers for cell viability assay using trypan blue solution 33
2.7 Time-lapse 2D SERS imaging of living cells at a concentration of 10 μM of Alt-AOMK. 34
2.8 Time-lapse 2D SERS imaging of a single living cell at a concentration of 10 μM of Alt-AOMK 35
2.9 Three-dimensional SERS imaging of living cells with Alt-AOMK 35
2.10 Time-lapse 3D SERS imaging to monitor the uptake of Alt-AOMK into living cells . 37
2.11 Bright field observation of living macrophages before and after the time-lapse 3D SERS measurement incubated with Alt-AOMK at different concentrations 38
2.12 Bright field observation of living macrophages after the time-lapse 3D SERS measurement incubated with Alt-AOMK with/without laser irradiation 39
2.13 Scheme for digital SERS counting to obtain the number of SERS spots of alkynes in each cell 40
2.14 Processing flow for the alkyne peak detection 41
2.15 Cell-shape detection of the cells bright field image and 3D SERS image 41
2.16 Temporal behaviors of the number of SERS spots in each cell 42
2.17 Digital SERS counting of alkynes at different administration concentrations 42
2.18 Three-dimensional SERS imaging of living macrophages with gold nanoparticles incubated at 37 ℃ and 4 ℃ 44
2.19 Temporal behaviors of the number of SERS spots of living macrophages incubated at 37 (red plot) and 4 ℃ (blue plot) 45

2.20 Extinction spectrum of gold nanoparticles with 50 nm diameter 47
2.21 SERS spectroscopy of Alt-AOMK 48
2.22 Possible binding motifs of alkyne-Au 49
2.23 Time-lapse 2D SERS imaging of living cells without Alt-AOMK 50
2.24 Analysis procedure of SERS signal blinking by autocorrelation 51
2.25 Autocorrelation analysis of SERS spectra of alkyne blinking with different excitation intensities 52
2.26 Dark-field observation of macrophage cells 53
2.27 Molecular structures of (a) L-Propargylglycine and (b) alkyne-tagged Tat peptide. (c) Representative SERS spectra of Alt-Tat from gold nanoparticle SERS substrate . . . 54
3.1 Time-Frequency profile of pulsed beam before and after chirp 62
3.2 Single-grating chirp setup 63
3.3 Optical setup for SRS microscopy with picosecond pulse chirpers 65
3.4 Autocorrelation measurement of pump and Stokes laser pulses 66
3.5 Block diagram of noise measurement 67
3.6 Relation between noise (standard deviation of output signal (V)) and pump power on PD (mW) 69
3.7 SRS imaging of PMMA beads without and with pre-amplifier 70
3.8 SRS imaging of PMMA beads with 300 nm diameter 70
3.9 Calibration of delay line position and wavenumber 72
3.10 SRS imaging of diamond crystals with different pulse widths 73
3.11 SRS imaging of PS beads 4.5 μm with different pulse widths 75
3.12 Pulse width dependence on the signal intensity, SBR, and SNR 76
3.13 Mathematical SBR simulation based on SRS spectrum with different Raman peak widths and pulse widths 78
3.14 Simulation of saturation response of SRS with different pulse width 79
3.15 Pre-resonance SRS spectroscopy of Rhodamine 800 81
3.16 SRS imaging of EdU in HeLa cells with 2 ps and 14 ps laser pulses. 82
3.17 Time-lapse SRS imaging with 2, 7, and 14 ps laser pulses at low average powers . . . 84
3.18 Time-lapse SRS imaging with 2, 7, and 14 ps laser pulses at high average powers . . 85
3.19 Grating-based chirper 87
3.20 Beam profiles of pump and Stokes beams at 2 ps (a), 7 ps (b), and 14 ps modes (c). . 90
3.21 Characterization of photodamage rate in time-lapse live-cell imaging 91
3.22 Block diagram of SRS measurements in lock-in detection and boxcar averaging with UHFLI 93
3.23 Waveform of the voltage signal from the detector 94

3.24 SRS imaging of PMMA beads with lock-in detection and boxcar averaging and calculation of SNR . . . 95
3.25 SRS imaging of PMMA beads with lock-in detection and boxcar averaging and calculation of SNR . . . 95
4.1 Calculated SRS signal intensity as a function with product excitation intensity of pump and Stokes beam . . . 103
4.2 Imaging of light by a lens with (a) $\lambda/d' > NA$ and (b) $\lambda/d = NA$ . . . 104
4.3 Idea of differential saturated-excitation microscopy . . . 105
4.4 Relationship of excitation intensity and SRS signal intensity with saturation response, and how to extract the saturation signal . . . 106
4.5 PSF calculations of pump, Stokes, and SRS signals . . . 107
4.6 Calculation of PSFs of SRS signals with dSAX technique . . . 108
4.7 Optical setup of SRS microscopy . . . 109
4.8 Schematic of SRS imaging procedure . . . 110
4.9 SRS imaging of diamond crystals with different excitation intensities . . . 111
4.10 Applying dSAX for saturated SRS images obtained with different excitation intensities 112
4.11 Line profiles of the 2nd-order SRS signals . . . 113
4.12 SRS imaging of PMMA beads with different excitation intensities . . . 114
5.1 Electric distribution of pump and Stokes beams and the distribution of SRS signal under NIR-SRS and VW-SRS excitations . . . 123
5.2 Spatial distributions of SRS signal under VW-SRS excitation with dSAX technique . 124
5.3 Optical setup for visible-wavelength SRS microscopy . . . 125
5.4 Phase matching of type-I SHG in a uniaxial crystal . . . 127
5.5 Characterization of laser pulses after SHG crystals such as beam profile and pulse width 129
5.6 VW-SRS imaging of PS beads 147 nm . . . 129
5.7 VW-SRS imaging of fixed HeLa cells . . . 130
5.8 VW-SRS measurement of Carbow2086 Lyso . . . 132
5.9 VW-SRS imaging of living HeLa cells labeled with Carbow2086 Lyso . . . 133
6.1 Optical setup of a hyperspectral SRS microscope with femtosecond laser pulses . . . 140
6.2 SRS spectroscopy of Carbow probes 10 mM . . . 141
6.3 Hyperspectral SRS imaging of polystyrene (PS) beads labeled with three Carbow probes . . . 143
6.4 SRS imaging of tubulin of fixed HeLa cells labeled with Carbow 2-yne . . . 143
6.5 SRS spectroscopy of Rh800 and MARS probes . . . 145
6.6 4-color and 8-color SRS spectroscopy of Rh800 and MARS probes . . . 146

List of Tables

2.1 Summary of cell viability assay of gold nanoparticles (GNP) and Alt-AOMK 32
3.1 Spectral resolution 74
3.2 Comparison of SNR between lock-in detection and boxcar averaging with 555 ps of gate width in SRS imaging 95
3.3 Comparison of SNR between lock-in detection and boxcar averaging with 18.9 ns of gate width in SRS imaging 96
5.1 Conversion efficiency measurement of SHG crystals 128
6.1 SNR comparison between InSight and APE SRS systems based on Carbow 2-yne measurement 142

Table of Contents

Acknowledgements **i**

Abstract **ii**

List of Publications, Scholarships, and Grants **iii**

List of Figures **viii**

List of Tables **ix**

Table of Contents **xi**

1 Raman imaging of biological samples **1**

Introduction 2
1.1 Spontaneous Raman scattering 3
1.2 Surface-enhanced Raman scattering (SERS) microscopy 7
1.3 Stimulated Raman scattering (SRS) microscopy 12
Conclusion 20
Reference 21

2 Visualizing drug dynamics in living cells by alkyne-tag SERS microscopy **25**

Introduction 26
2.1 Raman and SERS spectroscopy of small-molecule drug 27
2.2 Time-lapse SERS imaging of small-molecule drug in living cells . . . 33
2.3 Digital SERS counting for quantitative analysis of drug dynamics . . 37
Discussion and Conclusion 44
Appendix 47
Reference 54

3 Stimulated Raman scattering microscopy with spectral focusing of picosecond laser pulses **58**

Introduction 59
3.1 Application of spectral focusing for SRS microscopy 60
3.2 Development of SRS microscopy with single grating chirpers 64
3.3 Spectral resolution improvement by spectral focusing 72

3.4 Quantitative analysis of imaging sensitivity with different pulse width 74
3.5 SRS imaging of small molecule and biological molecules 81
Discussion and Conclusion 84
Appendix 87
Reference 97

4 SRS microscopy with saturated excitation for higher spatial resolution 100
Introduction 100
4.1 Theoretical description of saturation effects in SRS 101
4.2 Spatial resolution of SRS microscopy 102
4.3 Experimental evaluation of spatial resolution improvement 108
Discussion and Conclusion 113
Appendix 115
Reference 119

5 Visible-wavelength SRS microscopy toward super-resolution and high-sensitivity vibrational imaging 121
Introduction 122
5.1 Super-resolution visible-wavelength SRS microscopy 122
5.2 Development of visible-wavelength SRS microscopy 125
5.3 Toward super-resolution VW-SRS with dSAX technique 131
Discussion and Conclusion 132
Appendix 134
Reference 137

6 Hyperspectral multiplex SRS spectroscopy of preresonance Raman probes 138
Introduction 138
6.1 Hyperspectral SRS microscopy 139
6.2 Multiplex pre-resonance SRS spectroscopy 143
Discussion and Conclusion 146
Reference 147

Chapter 1
Raman imaging of biological samples

A part of the contents of this chapter have been published in:
J. Ando, K. Bando, K. Koike, K. Fujita, "Applications of Metallic Nanoparticles in Bio-imaging and Molecular Spectroscopy", *Material Matters*, 16 (2), 18-22 (2021)

Introduction

This chapter begins with the principles of spontaneous Raman scattering and its application for spectroscopy and microscopy. Each molecule has unique functional groups consisting of several atoms. Each functional group shows a different Raman peak corresponding to its molecular vibration frequency. Therefore, Raman spectroscopy and microscopy can be used to directly measure and visualize chemical compounds of samples. In recent years, Raman microscopy has been recognized as a strong tool for label-free live-cell observation because it does not require labeling that may harm cells. It can also be performed under aqueous conditions because water absorption is weak at visible wavelengths. Although it takes a long time to acquire Raman spectra of cells with high SNR due to low Raman scattering efficiency, parallel detection of spectra, such as multifocal and line-illumination techniques, enables Raman imaging of biological functions of living cells within a reasonable time. I will also present recent advances in alkyne-tagged Raman imaging, which takes advantage of the unique Raman spectral properties of alkynes, nitriles, and carbon-deuterium to visualize the distribution of small-molecule compounds in living cells.

The imaging time and detection sensitivity can be further enhanced using plasmon resonance of metallic nanoparticles, called surface-enhanced Raman scattering (SERS). The enhancement factor can range from 10^4 to 10^{14} due to the electromagnetic and chemical enhancement. SERS spectroscopy is highly sensitive to the spatial information on molecular species near metal surfaces, enabling the analysis of biological functions, such as organelle transportations, drug uptake, and cell cycle. I briefly review the recent progress and application of SERS for imaging and molecular spectroscopy within biological systems.

The newly emerged coherent Raman scattering (CRS) microscopy utilizing coherent anti-Stokes Raman scattering (CARS) and stimulated Raman scattering (SRS) is another way to boost Raman scattering signals several orders of magnitude higher than that of spontaneous Raman scattering. The nonlinear coherent Raman process occurs when the frequency difference of the two pulsed lasers coincides with the vibration frequency of molecules. CARS and SRS microscopy are superior to spontaneous Raman scattering in signal acquisition time. However, each modality has its disadvantages, such as setup complexity, limited spectral regions that can be acquired at once, and nonlinear background signals due to ultrashort laser pulses and intensity modulation. In the second half of this chapter, I mainly focus on recent progress of SRS microscopy to overcome these issues, such as hyperspectral SRS, background-free detection methods, super-multiplexing of Raman probes, and pre-resonance and photoswitchable Raman probes for highly sensitive and specific imaging of molecules.

1.1 Spontaneous Raman scattering

Classical theory of Raman scattering

When light interacts with matter, a part of photons is scattered in a different direction. Most scattered photons have the same frequency as the incident light. This elastic scattering phenomenon is known as Rayleigh scattering. In 1928, C.V. Raman and K. S. Krishnan observed for the first time that some scattering photons had a frequency that was different from the original incident light. This inelastic scattering phenomenon is now called Raman scattering, named after C. V. Raman. Raman scattering occurs when the molecular polarizability periodically oscillates due to the irradiation of the electromagnetic field. Until now, many kinds of Raman scattering have been discovered and reported, such as surface-enhanced Raman scattering,[1] coherent Raman scattering including coherent anti-Stokes Raman scattering (CARS)[2] and stimulated Raman scattering (SRS).[3] First, I describe the principle of Raman scattering based on classical theory.

Here, we assume a diatomic molecule as a sample interacting with light. The polarizability of the molecule depends on the interatomic distance of the molecule, $x(t)$. The distance varies due to the intrinsic molecular bond frequency Ω_R, and it can be expressed as

$$x(t) = x_0 \cos(\Omega_R t + \phi) \tag{1.1}$$

where x_0 is the amplitude of the displacement and ϕ is the phase of the vibration. When the displacement $x(t)$ is small, the polarizability $\alpha(t)$ is expressed using a Taylor expansion as

$$\alpha(t) = \alpha_0 + \left(\frac{\partial \alpha}{\partial x}\right)_0 x(t) \tag{1.2}$$

Assuming the electric field given by the following equation irradiates the molecule.

$$E(t) = E_0 \cos(\omega_E t) \tag{1.3}$$

This electric field induces the dipole moment $\vec{p}$ inside the molecule.

$$\vec{p}(t) = \varepsilon_0 \alpha(t) \vec{E}(t) \tag{1.4}$$

where ε_0 is permittivity of the material. Inserting Eq.1.2 into Eq.1.4 gives us

$$\begin{aligned} p(t) &= \varepsilon_0 \Big[\alpha_0 + \left(\frac{\partial \alpha}{\partial x}\right)_0 x_0 \cos(\Omega_R t + \phi)\Big] E_0 \cos(\omega_E t) \\ &= \varepsilon_0 \alpha_0 E_0 \cos(\omega_E t) \\ &+ \frac{1}{2}\varepsilon_0 \left(\frac{\partial \alpha}{\partial x}\right)_0 E_0 x_0 \cos[(\omega_E - \Omega_R)t + \phi] \\ &+ \frac{1}{2}\varepsilon_0 \left(\frac{\partial \alpha}{\partial x}\right)_0 E_0 x_0 \cos[(\omega_E + \Omega_R)t + \phi] \end{aligned} \tag{1.5}$$

The induced dipole moment given by Eq.1.5 contains three components oscillating at three different frequencies. The oscillating induced dipole moments emit electromagnetic waves oscillating simultaneously with the components. Thus, the emitted electromagnetic waves have three different frequency components ω_E, $(\omega_E - \Omega_R)$, and $(\omega_E + \Omega_R)$. The electromagnetic wave with frequency ω_E is called Rayleigh scattering. The other two waves with frequencies $(\omega_E - \Omega_R)$, and $(\omega_E + \Omega_R)$ are called Stokes Raman scattering and anti-Stokes Raman scattering.

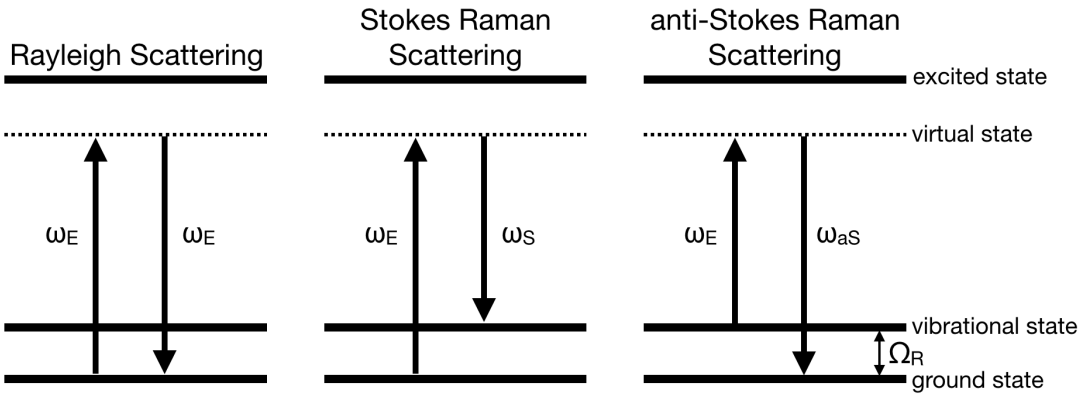

Figure 1.1. Schematic of energy diagram of processes of Rayleigh scattering, Stokes Raman scattering, and anti-Stokes Raman scattering.

Rayleigh scattering

Rayleigh scattering has the same frequency ω_E as the incident electromagnetic field. Fig.1.1 introduces an energy diagram of Raman scattering processes based on a quantum theory of Raman scattering. During the process of Rayleigh scattering, photons experience no energy loss, and this process is also called elastic scattering. Most of the radiation from the induced dipole moment consists of Rayleigh scattering.

Stokes Raman scattering

The radiation from the second term $\cos[(\omega_E - \Omega_R)t - \phi]$ is Stokes Raman scattering. The frequency of Stokes Raman scattering is down-shifted by Ω_R. Thus, in this process, the energy of scattering photons has lost by the energy of the molecular vibration. This energy difference is used by the molecule to excite the vibrational mode at Ω_R. The frequency term also has a phase component ϕ. Originally, since every molecule oscillates at their phases with each other, the phase of Stokes Raman scattering from molecules is also different from molecule to molecule. Thus, Stokes Raman scattering is incoherent light scattering, and it also called spontaneous Raman scattering.

Anti-Stokes Raman scattering

Anti-Stokes Raman scattering arises from the third term $\cos[(\omega_E - \Omega_R)t + \phi]$ of Eq.1.5. This process begins at the excited vibrational state and finishes in the ground state. The energy of scattering photons can gain the energy of Ω_R. Anti-Stokes Raman scattering is also an incoherent process like Stokes Raman scattering.

Raman shift

I consider only Stokes Raman scattering from here, and simply refer to it as Raman scattering or spontaneous Raman scattering. The photon energy of Raman scattering $\hbar\omega_S$is shifted by $\hbar\Omega_R$ from the excitation light.

$$\hbar\omega_S = \hbar\omega_E - \hbar\Omega_R \tag{1.6}$$

Since angular frequency ω equals to $2\pi\nu$, Eq.1.6 can be written as

$$\nu_S = \nu_E - \nu_R \tag{1.7}$$

$$\therefore \nu_R = \nu_E - \nu_S \tag{1.8}$$

The frequency ν_R is called the Raman shift. This value is different from molecule to molecule. Here is one example of how to calculate the Raman shift. If a 660 nm laser is used to excite Ethanol solution, this will give strong Raman scattering at 700.8 nm from C-C stretching mode.[4] We can calculate the Raman shift (wavenumber) of the peak as below.

$$\begin{aligned}\nu_R &= \nu_E - \nu_S \\ &= \Big(\frac{1}{\lambda_E} - \frac{1}{\lambda_S}\Big)\times 10^7 \\ &= \Big(\frac{1}{660} - \frac{1}{700.8}\Big)\times 10^7 \\ &= 883 \ \text{cm}^{-1}\end{aligned} \tag{1.9}$$

A Raman spectrum shows the relative intensity of scattered light of molecular vibrations as a function of the Raman shift (wavenumber). This information makes it possible to determine what molecules and molecular structures are contained within a focal volume. Optical systems and methods that can detect Raman spectra in this way are called Raman spectroscopy. It is also possible to visualize the distribution of molecules in a sample by scanning the laser beam in two dimensions and collecting Raman spectra from each focal point, which is called Raman scattering microscopy.

Raman scattering microscopy

Raman scattering microscopy is a label-free laser scanning optical microscopy that detects molecular vibrations as Raman spectra from a sample. It consists of illumination and detection optical paths. A visible CW laser (532-785 nm) is installed in the illumination path as the excitation source. The

laser is focused onto a sample through an illumination objective lens. As for the detection path, the same objective lens is used to collect scattering lights (Rayleigh scattering, Raman scattering) from the sample. Then, only the Raman scattered light passes through the long-pass filter and is focused on the spectrometer. A slit in front of the polychromator eliminates the light from outside the focus. The Raman scattering is spatially dispersed by diffraction gratings of the polychromator. The dispersed lights are focused onto a multi-channel CCD (charge-coupled device). The detected Raman scattering is displayed as a Raman spectrum. Using a galvanometer mirror placed in the illumination path and a movable sample stage, the laser focusing position can be scanned to obtain the Raman spectrum at each sample position. In this way, a two-dimensional Raman map of the molecular distribution for a particular Raman vibration mode can be obtained.

The study of biological samples such as living cells by confocal Raman spectroscopy has been conducted since the 1990s.[5] Pupples et al. acquired a non-resonant Raman spectrum of DNA by a 660 nm laser from a single living cell. Since the beginning of the 2000s, Raman spectroscopy has been applied to microscope imaging systems, allowing us to measure the Raman spectrum of each pixel by single-point scanning and observe the two-dimensional molecular distribution.[6, 7] One of the major challenges of Raman scattering microscopy is the low Raman scattering efficiency. In order to obtain high-contrast Raman images, long imaging times of tens of minutes to several hours are required. However, when the sample is a living cell or spheroid, such a long measurement time is not possible because the spatial localization of molecules changes, and the sample is degraded or damaged. To address this issue, Hamada et al. developed a slit-scan (line-illumination) Raman microscope that provides a line-shaped focus on the sample and detects hundreds of Raman spectra simultaneously.[8] A single living cell was measured within 6 min 30 s with 78x281 pixels. Line-illumination Raman microscopy is becoming a powerful imaging and analysis tool to understand the various types of biological phenomena with label-free, such as releasing of cytochrome c during apoptosis[9] and initiation of calcification by the presence of beta-carotene.[10]

From small-molecule imaging to cellular diagnosis and high-throughput analysis

Raman scattering microscopy can also be used to observe the accumulation of small molecule drugs and compounds introduced from outside the cell into specific organelles. Yamakoshi and his colleagues used alkynes (carbon-carbon triple bond) as small Raman vibrational tags.[11] The Raman peak of alkynes exists in 2080-2260 cm^{-1}, depending on the surrounded molecular structure of alkyne. This region corresponds to the silent region 1800-2800 cm^{-1}, where no other biological Raman peaks are present. Hence, the alkyne signal can be selectively detected within complex intracellular environments. The molecular weight of alkyne is only 24. Thus, labeling by alkynes has a minimal impact on the native functions of the labeled molecules. As the first demonstration of alkyne-tag Raman imaging of small molecules, Yamakoshi et al. used EdU with a terminal alkyne. The molecular structure of EdU is similar to dU (deoxyuridine), which is one of the compound molecules of RNA. EdU can be

efficiently incorporated into the nucleus of cells in the process of DNA replication.[12] They observed a gradual accumulation of EdU in the cell nucleus along with the incubation time. In addition to alkynes, nitrile,[13] diyne,[14] and carbon-deuterium[15] an also be used as Raman tags to observe specific small molecules in the cell.

Raman scattering microscopy can analyze and visualize molecular features from the Raman spectrum without any pre-processing of samples. Hence, label-free cell diagnosis and classification with Raman scattering spectroscopy and multivariate analysis is possible. Chan et al. investigated the effects of fixation type on normal/cancer cell type identifications by using Raman scattering and found that methanol fixation provides a significant impact on important biomarkers such as DNA and proteins, making it difficult to distinguish normal/cancer cells.[16] Brauchle et al. found the Raman spectral characteristics depending on the different types of cell death process.[17] Together with technological improvements, high-throughput analysis/screening by spontaneous Raman has recently been realized. Kumamoto et al. developed a high-throughput cell classification method based on 2D Raman imaging with narrow-band and low spectral resolution approach.[18] Kawagoe et al. recently demonstrated high-throughput Raman screening with a multi-well plate toward rapid and efficient drug screening.[19]

For further development and wider application of Raman scattering microscopy, improvements in the sensitivity and imaging speed would be required. These two issues are fundamentally limited by the low Raman scattering cross-section. It can be addressed from the technology and physics and chemistry sides. As for the sensitivity, since spontaneous Raman scattering is a weak process, it is important to reduce auto-fluorescence signals and background signals from out-of-focus and optical elements. One can also increase the Raman scattering cross-section by exploiting the electronic resonance Raman process and surface-enhanced Raman scattering (SERS) from metallic nanoparticles. For imaging speed, it is important to collect Raman scattering in a time-efficient manner. Therefore, optimizing the throughput of detection elements such as lenses and spectrometers can shorten the imaging time while maintaining the same SNR level. Parallel detection of Raman scattering, such as the multi-line scanning method, can accelerate the imaging time by a factor of 100 compared to single-line scanning Raman microscopy. The use of nonlinear coherent Raman scattering, such as coherent anti-Stokes Raman scattering (CARS) and stimulated Raman scattering (SRS), is also becoming a gold-standard technique for high-speed label-free chemical imaging. In the next sections, I mainly focus on SERS and SRS techniques for imaging molecules in living cells.

1.2 Surface-enhanced Raman scattering (SERS) microscopy

Electromagnetic enhancement of SERS

SERS is an optical phenomenon that can produce enhanced Raman scattering from molecules in the vicinity of a metallic nanoparticle. The enhancement factor is around several to ten of several magnitudes compared to spontaneous Raman scattering. Fleishmann et al. reported the first discovery of the

SERS effect in 1974 by observing the enhanced Raman scattering of pyridine on a silver electrode.[1] Since then, many studies investigating the mechanism of SERS have been coducted, concluding that the main enhancement factors are electromagnetic enhancement and chemical enhancement.[20, 21, 22] Electromagnetic enhancement is caused by localized surface plasmon resonance (LSPR) excited at the surface of the metallic nanoparticle, with enhancement factors ranging from 4 to 11 orders of magnitude. The other one, chemical enhancement, is around 10-100 orders of magnitude from the interaction of free electrons between the metallic surface and adsorbed molecules. Below, I focus on the origin of the LSPR effect and electromagnetic enhancement mechanism.

Plasmon is a collective oscillation of free electrons in a plasma. A metallic nanoparticle filled with free electrons is also the plasma. The collective oscillation of free electrons in the metallic nanoparticles is also plasmon. Localized surface plasmon (LSP) is the collective oscillation of free electrons excited at the surface of the metallic nanoparticle. LSP can be excited by directly illuminating the excitation light to metallic nanoparticles. The plasmon of the nanoparticle is a compressional longitudinal wave. It does not have the electric field component perpendicular to the wave propagation direction. The plasmon is not coupled with the energy of excitation light (transverse wave). However, when plasmon propagates at the metal-dielectric interface on the metallic surface, some of the electromagnetic fields oozes out in the dielectric. Since this electromagnetic field has a transverse wave component, the energy coupling with the excitation electric field occurs. Therefore, an enhanced electric field is formed only at the surface. This phenomenon is called LSPR. The magnitude of the enhanced electric field created by LSPR highly depends on the property of metal (gold, silver, copper, etc.), its shape (sphere, rod, star, etc.), and excitation wavelength (532 nm, 660 nm, etc.).

The equation of motion of the collective oscillation of free electrons can be explained by the Drude Sommerfeld model equation.[23]

$$m_e \frac{d^2\boldsymbol{x}}{dt^2} + m_e \Gamma \frac{d\boldsymbol{x}}{dt} = -e\boldsymbol{E} \tag{1.10}$$

where $\boldsymbol{x}$ is the displacement of the free electrons, e refers to the electron charge, m_e is the effective mass of free electrons, Γ is a damping term, which is inversely proportional to the relaxation time of scattering of free electrons, $\boldsymbol{E}$ is the applied electromagnetic field. Assuming $\boldsymbol{x} = \boldsymbol{x}_0 \exp(-i\omega t)$ and $\boldsymbol{E} = \boldsymbol{E}_0 \exp(-i\omega t)$, we can solve Eq. 1.10,

$$\boldsymbol{x} = \frac{e\boldsymbol{E}_0 \exp(-i\omega t)}{m_e(\omega^2 + i\Gamma\omega)} \tag{1.11}$$

The macroscopic polarization of a metallic nanoparticle is written as

$$\boldsymbol{P} = -Ne\boldsymbol{x} \tag{1.12}$$

From the Maxwell equation,

$$\boldsymbol{D} = \epsilon_2\epsilon_1\boldsymbol{E} = \epsilon_1\boldsymbol{E} + \boldsymbol{P} \tag{1.13}$$
$$\epsilon_2 = 1 + \frac{\boldsymbol{P}}{\epsilon_1\boldsymbol{E}}$$

where ϵ_1 is the permittivity of medium around the metal, and ϵ_2 is the permittivity of the metal. From Eq.1.11, 1.12 and 1.13, ϵ_2 can be written as a function of frequency of the electromagnetic field ω,

$$\epsilon_2(\omega) = 1 - \frac{\omega_p^2}{\omega^2 + i\Gamma\omega} \tag{1.14}$$

where ω_p is called the plasma frequency, which is given by

$$\omega_p = \sqrt{\frac{Ne^2}{\epsilon_1 m_e}} \tag{1.15}$$

When the applied electric field is in visible region, the real part of $\epsilon_2(\omega)$ is always negative, resulting in the strong scattering from metals (gold and silver) and less transmission into the material. In the case of metallic nanoparticles, the macroscopic induced dipole P can be written as

$$\boldsymbol{P} = 4\pi a^3 \frac{\epsilon_2(\omega) - \epsilon_1}{\epsilon_2(\omega) + 2\epsilon_1}\boldsymbol{E} \tag{1.16}$$

This equation shows that when $\mathrm{Re}[\epsilon(\omega)] \approx -2\epsilon_1$, the induced dipole become greatly large compared with the applied electric field. The dipole moment then emits strong enhanced electric field. From now I will discuss how much SERS is enhanced compared to spontaneous Raman scattering by the induced electric field. Simply, the enhanced electric field E_1 created by LSPR is given as follows

$$E_1(\lambda_{ex}) = G_1 E_0(\lambda_{ex}) \tag{1.17}$$

where λ_{ex} is excitation wavelength, G_1 is enhancement factor, $E_0(\lambda_{ex})$ is applied electric field. This equation means the excitation electric field to the molecules is enhanced by LSPR. Then, the Raman scattering E_2 from the molecule resulting from the applied field is again enhanced by the enhanced electric field around the nanoparticle.

$$E_2(\lambda_{em}) = G_2 E_0(\lambda_{em}) \tag{1.18}$$

where λ_{em} is emission wavelength, G_2 is enhancement factor, $E_0(\lambda_{em})$ is normal Raman scattering. The intensity of SERS signal is enhanced when both excitation of the incident light and emission of the scattering, which can be expressed as the product of electric field enhancement at incident light wavelength and scattered light wavelength.

$$G_{SERS} \propto |G_1|^2|G_2|^2 = \left|\frac{E_1(\lambda_{ex})}{E_0(\lambda_{ex})}\right|^2 \left|\frac{E_2(\lambda_{em})}{E_0(\lambda_{em})}\right|^2 \tag{1.19}$$

The created enhanced electric field around nanoparticles depends on the distance r from the particles as following equation.[24]

$$E(r) \propto \left(\frac{a}{a+r}\right)^3 \tag{1.20}$$

where a is the radius of the nanoparticle. From Eq.1.19, 1.20, the enhancement factor also greatly decreases away from the nanoparticle. Hence, due to this highly localized enhanced electric field, SERS is very sensitive to the molecules around the nanoparticles within several nm.

$$G(r) \propto \left(\frac{a}{a+r}\right)^{12} \tag{1.21}$$

SERS as an optical tool to detect biological molecules with high sensitivity

SERS greatly enhances Raman scattering with several to tens of several orders of magnitude. This makes it possible to detect Raman scattering with higher time resolution and sensitivity. This is a strong advantage for studying small-molecule dynamics with low concentration using Raman scattering. Single-molecule detection is also possible using SERS.[25, 26] SERS effect occurs only in the vicinity of metallic nanoparticles with around a few nanometers. By coupling this property with STORM concept,[27] Olson et al. demonstrated super-resolution SERS imaging of different types of bacteria.[28] SERS has also been widely applied to intracellular imaging and sensing of living cells. In order to acquire SERS signals of biological molecules in living cells, metallic nanoparticles need to be introduced into the cells. There are many candidates of nanoparticles (gold, silver, and copper) and shapes (a sphere, rod, and stars). The most common probe for SERS imaging in living cells is a gold nanoparticle with a sphere shape.[29, 30, 31, 32] For biological imaging, a red laser (such as 660 and 764 nm) is suitable because of its lower-energy photons. It can reduce the autofluorescence from the sample with less photodamage than a green laser (532 nm). When shined by the red laser, aggregations of gold nanoparticles show better SERS enhancements. Gold nanoparticles also have low toxicity for living cells than silver nanoparticles.

The very early study of intracellular SERS imaging was reported by Kneipp et al. in 2002.[29] They introduced 60 nm gold nanoparticles in living epithelial cells HT29 by endocytosis and acquired SERS spectra inside the cells. Endocytosis is one of the uptake processes of extracellular substances. When gold nanoparticles are adsorbed on the surface of the cellular membrane, the cellular membrane invades and surrounds the nanoparticles. Then, it forms a small vesicle called an endosome and is detached from the membrane. Endosome with gold nanoparticles reaches to lysosome at the end. Kneipp et al. successfully acquired SERS peaks from various molecules such as phenylalanine and DNA. In 2009, Fujita et al. performed time-lapse 2D SERS imaging of living macrophage cells for 90 min.[30] With line-scanning Raman microscopy,[8] they acquired SERS images of the cells every 2 min after the addition of gold nanoparticles into the sample. SERS signals around the cellular membrane were detected soon after the introduction. SERS peak intensity increased as many nanoparticles were

incorporated at the cellular membrane and inside the cell as time went by. Living cells have 3D complex structures with various types of organelles. However, 2D imaging captures the information only from the interest plane of the cells. In 2011, to see the movement of nanoparticles in 3D in living cells, Ando et al. developed SERS microscopy combined with the dark-field imaging system.[31] This system can track the movement of a gold nanoparticle in 3D and detect SERS signals from the interest particle with a temporal resolution of 50 ms. They observed that SERS spectral shape varied depending on the intracellular transportation, indicating the change in the local chemical environments during the uptake process.

Biological sensing: visualization of pH and small-molecules in living cells

SERS can be used as a pH sensing tool of the intracellular local environment of living cells. The pH measurement in time and space provides useful information about cell metabolism, cell division, and cellular apoptosis.[33] In 2010, Kneipp et al. developed SERS-based pH nano-sensors with gold nanoparticles functionalized with 4-mercapto benzoic acid (pMBA).[34] SERS spectral change of pMBA was found depending on the pH of the surrounding solution. Taking the signal ratios of the band at 1423 cm^{-1} or 1380 cm^{-1} to an aromatic ring vibration at 1076 cm^{-1}, they visualized the pH distributions of living cells. The pH values of each organelle are different. The local cellular dynamics also affect the pH values in time and space. Bando et al. in 2020 focused on the spatiotemporal dynamics of pH during the intracellular transportation mechanism of nanoparticles.[35] SERS spectroscopy with a dark-field imaging system was developed to monitor a single pMBA-modified nanoparticle in 3D while acquiring the SERS spectra from the nanoparticle. The decrease in pH was observed from the SERS spectrum, indicating the lysosome internalization. Zhang et al. demonstrated high-resolution 3D SERS imaging of the overall cells using 4MBA-coated gold nanostars and visualized how pH value changes during the nanostars' internalization.[36] One of the advantages of SERS-based pH sensors is no photobleaching during the measurement, allowing long-term observations of the cells. Also, a broad range of the SERS spectrum contains physiological and metabolic information from biological molecules, which can be correlated with pH values for a deeper understanding of biological processes.

Along with detecting biological molecules and corresponding chemical indicators such as pH, visualization of specific molecules (organelles) is also an essential application of SERS. One of the difficulties of such SERS-based detection is its molecular specificity. SERS spectra observed within living cells generally contain strong background signals and fingerprint SERS peaks from intrinsic molecules. Also, their temporal SERS intensity and peak position can fluctuate due to inherent SERS properties (molecular diffusion, nanoparticles movement, etc.). These issues make it challenging to detect target molecules selectively. In recent years, borrowing the idea of alkyne-tag spontaneous Raman imaging, SERS-nanotags functionalized with alkynes (or nitriles) have been proposed to visualize the molecules by SERS. In 2011, Kennedy demonstrated the use of silver nanoparticles functionalized by alkynes for the specific protein imaging of living cells.[37] They focused on occludin, an essential

protein for making the tight junction between cells, and investigated its spatial distribution by SERS. The nanoparticles were functionalized with phenylacetylene having anti-occludin antibodies. The terminal alkyne of the small molecule was connected with the surface of silver nanoparticles, resulting in a slight spectral shift of alkyne peak at around 1980 cm^{-1}. They successfully detected the SERS signals of alkyne from the cell surfaces, indicating that occludin proteins localize at the cell surfaces. In 2016, Chen et al. performed multiplex SERS imaging of cells using gold-coated silver nanoparticles functionalized with three 4-ethynylbenzene-thiol-derivatives.[38] The alkyne peak of each SERS-tag was modulated using different substituents to avoid spectral overlap of each probe. They realized three-color SERS imaging of alkyne-tagged SERS probes that reflect the distributions of different targeted proteins in living HeLa cells. In 2018, Ardini et al. achieved intracellular SERS imaging of alkyne-tagged dopamine molecules.[39] They modified dopamine with alkyne-tagged molecules and linked them with silver nanoparticles through an alkyne-silver connection. The silver nanoparticles with alkyne-tagged dopamine were incorporated into fibroblasts by endocytosis. Background-free SERS imaging of dopamine molecules was realized by detecting SERS signals of alkyne at 2000 cm^{-1}, where no Raman peaks of biological molecules exist. Li et al. developed multiplexed SERS-nanotags with alkyne- and nitrile-conjugated nanoparticles.[40] The SERS-nanotags were further conjugated with different antibodies against estrogen receptor (ER), progesterone receptor (PR), and epidermal growth factor receptor (EGFR) to perform background-free multiplex SERS profiling of each protein. Background-free SERS detection of molecules by exploiting the silent-region of the cells is not limited above examples. This idea can be expanded to imaging the drug uptake by living cells (Chapter 2).

1.3 Stimulated Raman scattering (SRS) microscopy

Coherent Raman scattering

Stimulated Raman scattering (SRS) is coherent Raman scattering that arises from nonlinear optical effects of the sample in the presence of the intense electric field. Under the electric field, material molecules have an induced electric dipole p. Assuming molecular density is N and applied electric field is $E(t)$, the macroscopic induced polarization of the material becomes

$$P = Np \tag{1.22}$$

Individual induced electric dipole is written as

$$p = \epsilon_0 \alpha E(t) \tag{1.23}$$

where ϵ_0 is vacuum permittivity and α is polarization of the molecule. From Eq.1.22 and 1.23, the induced polarization becomes

$$P = \epsilon_0 \alpha N E(t) \tag{1.24}$$

where αN is a macroscopic polarizability called electric susceptibility $\chi^{(1)}$. Now P is oscillating due to the presence of an applied electric field. Due to this oscillation, an electromagnetic field is released from the material. The phase and amplitude of the incoming electric field can be changed due to interaction with the applied field.

In the above example, the induced polarization linearly reacts with the applied electric field. When the intensity of the electric field becomes greatly large, the induced polarization shows a nonlinear response to the electric field. This effect is called the nonlinear optical effect. Nonlinear response of the induced polarization can be written as

$$\begin{aligned} P &= \epsilon_0(\chi^{(1)}E(t) + \chi^{(2)}E(t)^2 + \chi^{(3)}E(t)^3 + \cdot\ \cdot\ \cdot) \\ &= P^{(1)}(t) + P^{(2)}(t) + P^{(3)}(t) + \cdot\ \cdot\ \cdot \end{aligned} \tag{1.25}$$

where $\chi^{(2)}$ and $\chi^{(3)}$ are second-order and third-order susceptibility, respectively. $P^{(1)}(t)$ is linear polarization, and $P^{(2)}(t)$ and $P^{(3)}(t)$ are nonlinear polarizations.

Coherent Raman scattering arises from third-order susceptibility. In order to induce coherent Raman scattering, two ultrashort laser pulses are used. The differential frequency of the two lasers should be matched with the resonance frequency of the interest molecule. Unlike the incoherent spontaneous Raman scattering process, coherent Raman scattering is a coherent process because molecules with the same vibrational frequency with the differential frequency of lasers are forcibly excited to the vibrational mode. The electric fields induced from the excited molecules can be interfered with by the incoming electric fields.

When two laser pulses, pump beam with frequency ω_p and Stokes beam with frequency ω_S are applied to molecules with resonant frequency $\Omega = \omega_p - \omega_S$, the molecules are excited to the vibrational state at Ω. Under the condition, the interaction between the vibration mode Ω and pump beam ω_p gives two new electric fields with $\omega_p \pm \Omega$. The electric field with $\omega_p + \Omega = 2\omega_p - \omega_S$ is called coherent anti-Stokes Raman scattering (CARS), and the electric field with $\omega_p - \Omega = \omega_S$ is called stimulated Raman gain (SRG). In contrast, the interaction between the vibration mode Ω and Stokes beam ω_S gives the other two new electric fields with $\omega_S \pm \Omega$. The electric field with $\omega_p + \Omega = \omega_p$ is called stimulated Raman loss (SRL), and the electric field with $\omega_S - \Omega = 2\omega_S - \omega_p$ is called coherent Stokes Raman scattering (CSRS). SRG or SRL are referred to as SRS in general. These coherent Raman scatterings are third-order nonlinear Raman scattering since three electric fields are interacting with each other simultaneously: two electric fields E_p and E_S for exciting the molecules at the vibrational state, and one electric field E_p or E_S for detecting the signals.

CARS microscopy detects newly generated CARS signal $2\omega_p - \omega_S$ originated from $\chi^{(3)}$, as a chemical contrast. Because the wavelength of the CARS signal is different from the incident lasers, one can detect CARS signal easily by using a short pass filter or a spectrometer. In order to generate CARS signal, the phase-matching condition $\Delta\boldsymbol{k} = 2\boldsymbol{k_p} - \boldsymbol{k_S}$ should be satisfied, where $\boldsymbol{k_p}$ and $\boldsymbol{k_S}$ are wave vectors of pump and Stokes beams, respectively.[41] In most cases, the CARS signal propagates for-

ward in the same direction with incident lasers.[42] CARS microscopy is generally transmission type microscopy with two objective lenses for illumination and detection of CARS signal.[42] CARS signal is generated at the center focus spot where two beams spatially overlap. Therefore, CARS microscopy has a three-dimensional spatial resolution. The CARS signal intensity is givens as the following equation.

$$I_{CARS} \propto |\chi^{(3)}|^2 I_p^2 I_S \tag{1.26}$$

where

$$\begin{aligned} \chi^{(3)} &= \chi_{NR}^{(3)} + \chi_R^{(3)} \\ &= \chi_{NR}^{(3)} + \frac{A}{\Omega_R^2 - (\omega_p - \omega_S)^2 - 2i\Gamma(\omega_p - \omega_S)} \end{aligned} \tag{1.27}$$

where $\chi_{NR}^{(3)}$ and $\chi_R^{(3)}$ are non-resonant background signal and resonant signal from molecular vibration. Γ and A are dumping and real constants. Eq.1.26 indicates that non-resonant background signal from four-wave mixing can affect CARS signal, resulting in the distortions in CARS spectral shapes. This problem makes it difficult to interpret and analyze obtained CARS images. To remove this effect, mathematical post-processing of the spectrum is required. Vartiainen et al. developed a method to extract a spectrum that corresponds to spontaneous Raman spectrum from distorted CARS spectrum by calculating the imaginary part of CARS signal.[43]

SRS microscopy is also a coherent Raman scattering microscopy with high molecular sensitivity. SRS signal intensity can be expressed differently from the CARS signal, which is given by

$$I_{SRS} \propto \mathrm{Im}\chi^{(3)} I_p I_S \tag{1.28}$$

Unlike CARS, the SRS signal does not contain a non-resonant background signal. Therefore, the SRS spectrum is consistent with spontaneous Raman scattering, and the signal intensity can be used for the quantitative measurement of sample concentration. SRS microscopy also has the ability of three-dimensional spatial resolution since SRS effects only occur at the center of the focus spot. SRS signal automatically meets the phase-matching conditions $\boldsymbol{k_p}$ and $\boldsymbol{k_S}$.

SRS microscopy

Detailed condition of optical setup is described in Chapter 3. Here, I introduce the working principle of SRS microscopy and how to detect SRS signals. SRS is the same as the frequency of incident light and can not be distinguished from incident light. Conventional SRS microscopy relies on heterodyne detection by modulating the intensity of laser pulses.[44, 45, 46] Fig.4.7 shows a setup of SRS microscopy. Two picosecond laser pulses with around 2-6 ps are often used. A high repetition rate of laser pulses (20-80 MHz) is preferred for fast imaging with low noise. One of the lasers is tunable in the near-infrared region to change the wavenumber of interest. The intensity of either laser is modulated at

several to tens of several MHz by using acousto-optic modulator (AOM) or electro-optic modulator (EOM). The two beams are spatially and temporally coupled into a laser scanning microscope. When SRS occurs at a sample, a tiny part of pump intensity is transferred to Stokes intensity at the modulated frequency. The transferred intensity modulation is detected by a lock-in amplifier at the modulation frequency.

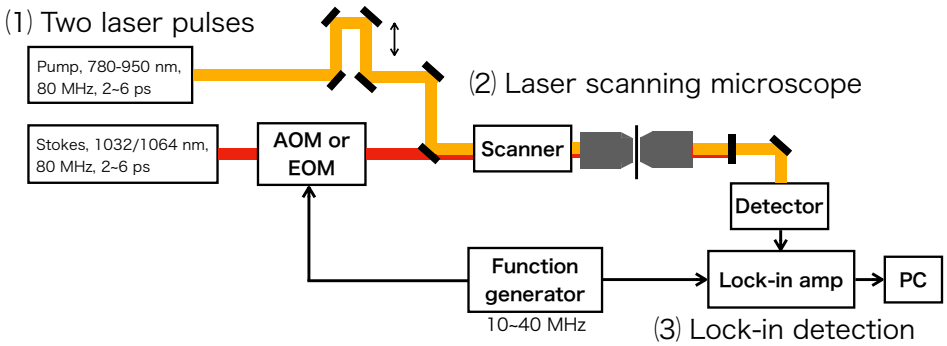

Figure 1.2. Schematic of SRS microscope setup.

SRS microscopy has many advantages over spontaneous Raman scattering microscopy, such as rapid signal acquisition, high contrast (=background-free detection), quantitative imaging (=SRS signal is proportional to molecular density N), and 3D imaging. Back in the 1960s, SRS was not exploited for biomedical applications. People were just trying to observe and study the SRS effect itself from samples such as organic liquids.[3] In 1980, Levine et al. developed SRS spectroscopy using laser amplitude modulation and lock-in detection.[47] They succeeded in observing the SRS spectrum of silicon on sapphire with several orders of magnitude of higher sensitivity than spontaneous Raman scattering. Although the principle of SRS detection was developed several decades ago, SRS imaging of biological samples was challenging mainly due to the low performance of laser and other optical instruments. With the advent of an optical parametric oscillator (OPO) with a high repetition rate and low noise, and a high-performance lock-in amplifier, three groups independently published papers about the label-free imaging of living cells by SRS microscopy in 2008-2009.[44, 45, 46] Among them, Sunny Xie group of Harvard University firstly reported SRS imaging of lipids in living cells and mouse tissues in 2D.[44] They also showed the use of SRS microscopy to monitor the penetration of two chemical compounds, DMSO and retinoic acid, into tissues. In 2010, the same group reported video-rate SRS microscopy.[48] Epi-detection SRS microscopy was developed to detect back-scattered photons from thick tissues. High-speed imaging of blood flows of mouse ear up to 25 frames/sec in 512x512 pixels was realized using a home-build lock-in amplifier and a resonant galvanometer mirror with 100 ns pixel dwell time.

Broadband SRS microscopy for spectral information acquisition with high-speed

SRS microscopy can detect a single vibrational frequency of molecules Ω_R by tuning the differential frequency of two lasers at $\Omega_R = \omega_p - \omega_S$. In other words, unlike spontaneous Raman scattering microscopy,[8, 9] SRS microscopy cannot detect several vibrational frequencies of molecules simultaneously. To acquire an SRS spectrum of the sample, the frequency of one of two laser pulses needs to be tuned. OPO laser, the most suitable light source for SRS microscopy, provides a wavelength-tunable output laser. However, optimizing the wavelength requires the temperature calibration of OPO crystal, which is time-consuming for acquiring the SRS spectrum. Various optical approaches have been reported to overcome this issue and realize rapid hyperspectral SRS imaging. Among them, Ozeki et al. developed two-color laser sources with fast wavelength scanner with a tunability of 300 cm^{-1} and a spectral resolution of around 3 cm^{-1}.[49] They acquired hyperspectral SRS images of biological samples with 30 fps with different wavenumber frame by frame. Spectral focusing of fs laser pulses is another major and currently the most popular technique. The method introduces linear chirp to both pump and Stokes beam to stretch the pulse width to several picoseconds.[50, 51, 52] Sweeping the time delay between pump and Stokes beam with motorized delay line allows rapid hyperspectral SRS imaging. Acousto-optic tunable filter (AOTF) is also useful for this type of application. AOTF is an electrically controllable spectral bandpass filter, which is capable of cutting out and emitting a single frequency (narrow spectral width) from a multi-color light source (such as fs laser pulses) depending on an applied RF frequency. Laptenok et al. utilized AOTF with spectral window of 8 cm^{-1} to the fs laser pulses to demonstrate SRS imaging covering fingerprint-to-CH region with high-speed.[53]

Background-free SRS microscopy

Although SRS is free from non-resonant background signals from four-wave mixing and thus provides a direct interpretation of spectrum and quantitative measurement, SRS is often accompanied by other nonlinear optical effects due to the heterodyne detection of the intensity-modulated pump beam. The nonlinear background signals include non-Raman-resonant cross-phase modulation (XPM), two-photon absorption (TPA), and thermal lensing (TL, or photothermal effect, PT). In XPM, the intense Stokes beam electric field modulates the refractive index in time due to intensity modulation, affecting the phase and divergence of the pump beam through the sample. This then causes the intensity change of the pump beam at a photodetector with the same frequency as the SRS signal, which will remain as a background signal on the final SRS image. XPM signals can be somehow reduced using a larger numerical aperture of the collection objective lens than the illumination objective. TPA gives an intensity loss in the pump beam from the absorption of one pump photon and one Stokes photon, which overlaps with the SRS signal. TL or PT is induced from the temperature-induced refractive index change in time by the local heating of the Stokes beam, which affects the propagation of the pump beam. In the case of weak SRS signals at nearly the detection limit, these nonlinear optical

effects become relatively strong and may overwhelm the signal. In order to remove these background artifacts and provide clean and genuine SRS images, non-intensity modulation schemes such as frequency modulation (or spectral modulation),[54, 55, 56] polarization modulation[57] techniques have been proposed and successfully demonstrated for solution samples and actual biological samples. Fig.1.3 summarizes simplified schemes for intensity and non-intensity modulation SRS.

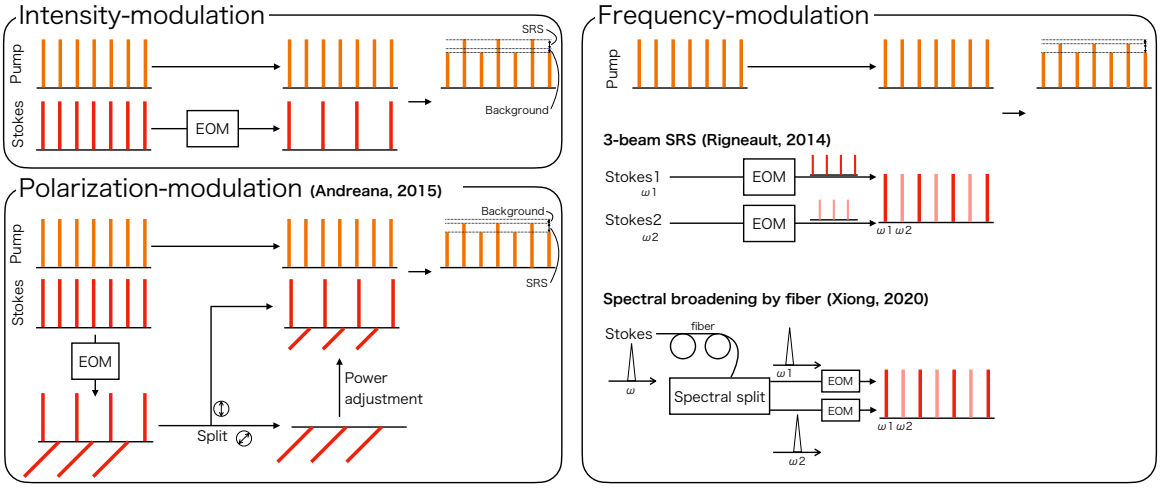

Figure 1.3. Various types of SRS signal detection schemes, intensity modulation, polarization modulation, and frequency modulation based SRS.

Non-intensity modulated SRS is based on the wavelength-independent properties of nonlinear optical effects such as XPM. In frequency modulation, two Stokes laser sources with intensity-modulated with a π phase difference are used. One is used to excite the molecules of interest by matching the vibration mode, and the other is spectrally shifted away from the Raman peak. In this scheme, only the SRS signal is modulated in time in the pump beam. So far, three-beam SRS,[54] and spectral broadening of the Stokes beam by fiber technology[56] have been proposed to realize frequency modulation scheme. Spectral modulation by using AOM and gratings[55] is also a simple and powerful technique for this purpose. The other scheme, polarization modulation SRS, utilizes the property of XPM.[57] XPM is insensitive to the polarization, and it will occur even when the pump and Stokes beam polarizations are parallel.[54] In this scheme, both parallel and perpendicular polarizations of Stokes beam are split by a beam splitter. The beam intensity ratio of each polarization is then adjusted to achieve the same XPM signal. The resulting pump beam will not contain the modulated signal from the XPM but only the SRS. Non-intensity modulated SRS microscopy is an attractive technique for background-free and highly sensitive SRS imaging. However, these techniques require relatively complex optical systems and in-depth optics and photonics knowledge. Therefore, the intensity modulation method is still the most common and most straightforward approach to perform SRS imaging. A simple method to improve the image contrast (signal-to-background ratio) in intensity modulation-based SRS is introduced in Chapter 3. From the chemistry side, Wei Min group of Columbia University and Ping Wang group

of Huazhong University of Science and Technology recently introduced ultrastrong Raman vibrational probes based on polymer engineering.[58, 59] Next, I describe the recent progress of Raman vibrational probes based on alkynes for highly sensitive super-multiplex SRS imaging.

Super-multiplex vibrational imaging with small-molecule Raman-tags

Three years later, after the first demonstration of click-free alkyne-tag imaging of small molecules by Yamakoshi et al. in 2011,[11] Wei Min et al. reported the first application of Raman-tags for SRS microscopy.[60] However, the number of organelles in a sample to be imaged was limited due to the fixed alkyne peak position at 2120 cm^{-1}. To realize multiplex imaging and observe a large number of targets with high sensitivity, they developed a frequency-tunable Raman-tag library, Carbow, by chemical engineering.[61, 62] The idea was based on the classical vibration model of molecules.[62]

$$\nu = \frac{1}{2\pi c}\sqrt{\frac{K}{u}}, u = \frac{m_1 m_2}{m_1 + m_2} \tag{1.29}$$

where ν is the vibrational frequency, K is the force constant, u is the reduced mass from the two molecules, m_1 and m_2. Hence, we can modulate the frequency (position of Raman peak) by changing the values of K or u. K represents the electron density and distribution. Thus, substituting groups attached to alkynes (or nitriles) can be significantly affected. u is obtained from the atoms. Changing the value u can be realized by substituting with isotopes such as C^{12} to C^{13}. Using these strategies, Hu et al. invented the Carbow library, engineered from polyynes.[61] The expansion of polyynes with alkynes and substituting with isotope allowed 20 different Raman peaks in the cell silent region. Furthermore, the increase of electronic density and polarizability induced enhanced Raman scattering. Moreover, supermultiplexed SRS and fluorescence imaging with 15-color in living cells was realized by substituting with organelle targeted molecules. In 2021, Shou et al. published high-speed hyperspectral SRS microscopy with the Carbow probes.[63] The acquisition speed was greatly improved, with 30 fps and 512x512 pixels, making it possible to observe temporal dynamics and interactions of multiple organelles labeled with the Carbow probes in living cells. In order to further boost the sensitivity from the chemistry side, Zhao et al. recently developed a new Raman-active nanoparticle (Rdots) by a simple swelling-diffusion method of polymer particles and Carbow probes.[58] Rdots generate an alkyne signal at nearly 10^5 RIE due to highly condensed Carbow probes in 20 nm polymer particles, which allows multiplexed SRS imaging in living cells with a single-particle sensitivity.

Electronic pre-resonance and photoswitchable SRS microscopy

Along with multiplexing, it is also important to improve the sensitivity of molecular detection in SRS to make it comparable to fluorescence microscopy. SRS signals from conventional Raman-tags such as alkynes and nitriles are relatively weak and easily buried in large nonlinear background signals. One of the ways is to increase the electron density and molecular polarization such as Carbow.[64, 58]

Another way is to increase the Raman scattering cross-section of molecules by exploring electronic pre-resonance with careful selection of excitation wavelength for SRS.[64, 65] When the absorption peak energy of molecules ω_e and excitation laser energy ω_{pump} are matched, electronic resonance occurs and molecules are excited to the excited state with higher probability. However, in the case of SRS, rigorous resonance ($\omega_e = \omega_{pump}$) should be avoided to suppress the concurrent nonlinear background signals such as electronic-resonance four-wave mixing, photothermal processes, and two-photon absorption.[64, 66] In 2017, Lu et al. demonstrated a first proof-of-concept pre-resonance SRS imaging using ATTO740 and MARS (Manhattan Raman scattering) dyes. By careful detuning of pump laser energy $\omega_e - \omega_{pump} \approx 3\Gamma$, where Γ is the homogeneous linewidth of absorption spectrum, typically around 700 cm^{-1}, the detection limit of pre-resonance SRS was determine to be 250 nM for C=C bond of ATTO740. They found that within the range $2\Gamma \leq \omega_e - \omega_{pump} \leq 6\Gamma$, good pre-resonance SRS enhancement can be achieved with sufficient suppressed background.[65] They also determined that the physics behind this limited region for electronic pre-resonance SRS follows Albrecht A-term pre-resonance approximation equation

$$\sigma_{Raman} = K \times \omega_{pump}(\omega_{pump} - \omega_{vib})^3 \Big[\frac{\omega_{pump}^2 + \omega_e^2}{(\omega_e^2 - \omega_{pump}^2)^2}\Big]^2 \tag{1.30}$$

where σ_{Raman} is a Raman scattering cross-section, K is a frequency-independent factors of the Raman dyes, ω_{pump} and ω_{vib} (= ω_{pump}-ω_{Stokes}) are the laser energy of pump and vibration transition energy, and ω_e is the molecular absorption peak energy. The pump beam energy (wavelength) should be carefully adjusted to excite a specific molecular vibration mode while maintaining enhanced Raman scattering cross-section by electronic pre-resonance.

The invention of electronic pre-resonance SRS has opened doors to the development of activatable Raman probes[67] and photoswitchable Raman probes[68, 69, 70] during 2020-2021. Fujioka et al. developed four types of activatable Raman probes based on a xanthene derivative bearing a nitrile group (9CN-JCP), which are targeted to different enzymes by isotope editing of the nitrile group.[67] The Raman probes showed the red-shift of absorption peak once reaction with targeted enzymes occurred, and pre-resonance SRS peak in the cell-silent region showed high sensitivity within living cells. Photoswitchable Raman probes are also next-generation Raman probes based on photochromism of molecules and electronic pre-resonance SRS. The idea is that the absorption peak red-shifts by photoisomerization with UV-light and enhanced pre-resonance SRS becomes on. The vibration energy of the molecules also varies due to molecular structural change. Shou et al. used CMTE molecules with two isomers, opened form and closed-form with an absorption peak at UV-region (270-430 nm) and visible region (357-512 nm), respectively.[68] Live-cell photoswitchable SRS imaging using HeLa cells was demonstrated with full reversibility. Another group in China focused on the photochromic diarylethene (DTE)-alkyne derivatives,[69] and demonstrated live-cell painting/erasing and imaged intracellular pulse-chase of mitochondria with SRS microscopy. Photoswitchable probes have been already

known and used in fluorescence microscopy for super-resolution imaging, but no application has been demonstrated in Raman microscopy so far. Photoswitchable Raman probes for super-resolution SRS imaging will be realized soon based on the principle of reversible switchable/saturable optical fluorescent transition (RESOLFT).[70]

Conclusion

This chapter provided a comprehensive overview of recent advances in spontaneous Raman scattering, SERS, and CARS/SRS microscopy for imaging molecules in biological samples. The recent developments of lasers, spectrographs, and optical elements have led to the emergence of Raman scattering microscopy. However, due to the small scattering cross-section, a long exposure time is required for Raman imaging with a good signal-to-noise ratio. This issue makes it difficult to use Raman scattering microscopy for the real-time observation of biological samples with high sensitivity, which limits the wide range of biological applications. To overcome this limitation, the use of other types of Raman scattering processes such as SERS and SRS has been proposed, paving the way for high-speed and highly sensitive imaging of biological molecules. Starting from Chapter 2, I will introduce my research towards highly sensitive Raman imaging of molecules in living cells using SERS and SRS.

Reference

1) M. Fleischmann, P.J. Hendra, and A.J. McQuillan. Raman spectra of pyridine adsorbed at a silver electrode. *Chemical Physics Letters*, 26(2):163 – 166, 1974.
2) P. D. Maker and R. W. Terhune. Study of Optical Effects Due to an Induced Polarization Third Order in the Electric Field Strength. *Phys. Rev.*, 137:A801–A818, Feb 1965.
3) Gisela Eckhardt, R. W. Hellwarth, F. J. McClung, S. E. Schwarz, D. Weiner, and E. J. Woodbury. Stimulated Raman Scattering From Organic Liquids. *Phys. Rev. Lett.*, 9:455–457, Dec 1962.
4) 浜口宏夫, 岩田耕一, 加納英明, 古川行夫, 山本達夫, and 吉川正信. **ラマン分光法**. 講談社, 2015.
5) G. J. Puppels, F. F. M. de Mul, C. Otto, J. Greve, M. Robert-Nicoud, D. J. Arndt-Jovin, and T. M. Jovin. Studying single living cells and chromosomes by confocal Raman microspectroscopy. *Nature*, 347(6290):301–303, 1990.
6) Henk-Jan van Manen, Yvonne M. Kraan, Dirk Roos, and Cees Otto. Intracellular Chemical Imaging of Heme-Containing Enzymes Involved in Innate Immunity Using Resonance Raman Microscopy. *The Journal of Physical Chemistry B*, 108(48):18762–18771, 2004.
7) Yu-San Huang, Takeshi Karashima, Masayuki Yamamoto, and Hiro-o Hamaguchi. Molecular-Level Investigation of the Structure, Transformation, and Bioactivity of Single Living Fission Yeast Cells by Time- and Space-Resolved Raman Spectroscopy. *Biochemistry*, 44(30):10009–10019, 2005. PMID: 16042377.
8) Keisaku Hamada, Katsumasa Fujita, Nicholas Smith, Isaac, Minoru Kobayashi, Yasushi Inouye, and Satoshi Kawata. Raman microscopy for dynamic molecular imaging of living cells. *Journal of Biomedical Optics*, 13(4):044027, 2008.
9) Masaya Okada, Nicholas Isaac Smith, Almar Flotildes Palonpon, Hiromi Endo, Satoshi Kawata, Mikiko Sodeoka, and Katsumasa Fujita. Label-free Raman observation of cytochrome c dynamics during apoptosis. *Proceedings of the National Academy of Sciences*, 109(1):28–32, 2012.
10) Aya Hashimoto, Yoshinori Yamaguchi, Liang-da Chiu, Chiaki Morimoto, Katsumasa Fujita, Masahide Takedachi, Satoshi Kawata, Shinya Murakami, and Eiichi Tamiya. Time-lapse Raman imaging of osteoblast differentiation. *Scientific Reports*, 5(1):12529, 2015.
11) Hiroyuki Yamakoshi, Kosuke Dodo, Masaya Okada, Jun Ando, Almar Palonpon, Katsumasa Fujita, Satoshi Kawata, and Mikiko Sodeoka. Imaging of EdU, an Alkyne-Tagged Cell Proliferation Probe, by Raman Microscopy. *Journal of the American Chemical Society*, 133(16):6102–6105, 2011. PMID: 21443184.
12) Adrian Salic and Timothy J. Mitchison. A chemical method for fast and sensitive detection of DNA synthesis in vivo. *Proceedings of the National Academy of Sciences*, 105(7):2415–2420, 2008.
13) Hiroyuki Yamakoshi, Almar F. Palonpon, Kosuke Dodo, Jun Ando, Satoshi Kawata, Katsumasa Fujita, and Mikiko Sodeoka. Simultaneous imaging of protonated and deprotonated carbonyl-cyanide p-trifluoromethoxyphenylhydrazone in live cells by Raman microscopy. *Chem. Commun.*, 50:1341–1343, 2014.
14) Hiroyuki Yamakoshi, Almar Palonpon, Kosuke Dodo, Jun Ando, Satoshi Kawata, Katsumasa Fujita, and Mikiko Sodeoka. A sensitive and specific Raman probe based on bisarylbutadiyne for live cell imaging of mitochondria. *Bioorganic and Medicinal Chemistry Letters*, 25(3):664–667, 2015.
15) Mitsuru Yasuda, Norio Takeshita, and Shinsuke Shigeto. Deuterium-labeled Raman tracking of glucose accumulation and protein metabolic dynamics in Aspergillus nidulans hyphal tips. *Scientific Reports*, 11(1):1279, 2021.
16) James W. Chan, Douglas S. Taylor, and Deanna L. Thompson. The effect of cell fixation on the discrimination of normal and leukemia cells with laser tweezers Raman spectroscopy. *Biopolymers*, 91(2):132–139, 2009.
17) Eva Brauchle, Sibylle Thude, Sara Y. Brucker, and Katja Schenke-Layland. Cell death stages in single apoptotic and necrotic cells monitored by Raman microspectroscopy. *Scientific Reports*, 4(1):4698, 2014.
18) Yasuaki Kumamoto, Kentaro Mochizuki, Kosuke Hashimoto, Yoshinori Harada, Hideo Tanaka, and Katsumasa Fujita. High-Throughput Cell Imaging and Classification by Narrowband and Low-Spectral-Resolution Raman Microscopy. *The Journal of Physical Chemistry B*,

123(12):2654–2661, 2019. PMID: 30830787.
19) Hiroyuki Kawagoe, Jun Ando, Miwako Asanuma, Kosuke Dodo, Tetsuya Miyano, Hiroshi Ueda, Mikiko Sodeoka, and Katsumasa Fujita. Multiwell Raman plate reader for high-throughput biochemical screening. *Scientific Reports*, 11(1):15742, 2021.
20) David L. Jeanmaire and Richard P. Van Duyne. Surface raman spectroelectrochemistry: Part I. Heterocyclic, aromatic, and aliphatic amines adsorbed on the anodized silver electrode. *Journal of Electroanalytical Chemistry and Interfacial Electrochemistry*, 84(1):1 – 20, 1977.
21) Janina Kneipp, Harald Kneipp, and Katrin Kneipp. SERS-a single-molecule and nanoscale tool for bioanalytics. *Chemical Society Reviews*, 37(5):1052–1060, 2008.
22) A. Otto. Theory of First Layer and Single Molecule Surface Enhanced Raman Scattering (SERS). *physica status solidi (a)*, 188(4):1455–1470, 2001.
23) Dustin W. Shipp, Faris Sinjab, and Ioan Notingher. Raman spectroscopy: techniques and applications in the life sciences. *Adv. Opt. Photon.*, 9(2):315–428, Jun 2017.
24) Cheng Zong, Mengxi Xu, Li-Jia Xu, Ting Wei, Xin Ma, Xiao-Shan Zheng, Ren Hu, and Bin Ren. Surface-Enhanced Raman Spectroscopy for Bioanalysis: Reliability and Challenges. *Chemical Reviews*, 118(10):4946–4980, 2018. PMID: 29638112.
25) Nicholas P. W. Pieczonka and Ricardo F. Aroca. Single molecule analysis by surfaced-enhanced Raman scattering. *Chem. Soc. Rev.*, 37(5):946–954, 2008.
26) William E. Doering and Shuming Nie. Single-Molecule and Single-Nanoparticle SERS:☒ Examining the Roles of Surface Active Sites and Chemical Enhancement. *The Journal of Physical Chemistry B*, 106(2):311–317, 2002.
27) Michael J Rust, Mark Bates, and Xiaowei Zhuang. Sub-diffraction-limit imaging by stochastic optical reconstruction microscopy (STORM). *Nature Methods*, 3:793 EP –, 08 2006.
28) Aeli P. Olson, Kelsey B. Spies, Anna C. Browning, Paula A. G. Soneral, and Nathan C. Lindquist. Chemically imaging bacteria with super-resolution SERS on ultra-thin silver substrates. *Scientific Reports*, 7(1):9135, 2017.
29) Katrin Kneipp, Abigail S. Haka, Harald Kneipp, Kamran Badizadegan, Noriko Yoshizawa, Charles Boone, Karen E. Shafer-Peltier, Jason T. Motz, Ramachandra R. Dasari, and Michael S. Feld. Surface-Enhanced Raman Spectroscopy in Single Living Cells Using Gold Nanoparticles. *Applied Spectroscopy*, 56(2):150–154, 2002.
30) Katsumasa Fujita, Sawako Ishitobi, Keisaku Hamada, Nicholas Smith, Isaac, Atsushi Taguchi, Yasushi Inouye, and Satoshi Kawata. Time-resolved observation of surface-enhanced Raman scattering from gold nanoparticles during transport through a living cell. *Journal of Biomedical Optics*, 14(2):024038, 4 2009.
31) Jun Ando, Katsumasa Fujita, Nicholas I. Smith, and Satoshi Kawata. Dynamic SERS Imaging of Cellular Transport Pathways with Endocytosed Gold Nanoparticles. *Nano Letters*, 11(12):5344–5348, 2011. PMID: 22059676.
32) Kazuki Bando, Nicholas I Smith, Jun Ando, Katsumasa Fujita, and Satoshi Kawata. Analysis of dynamic SERS spectra measured with a nanoparticle during intracellular transportation in 3D. *Journal of Optics*, 17(11):114023, 2015.
33) Zhiqiang Zhang, Kazuki Bando, Kentaro Mochizuki, Atsushi Taguchi, Katsumasa Fujita, and Satoshi Kawata. Quantitative Evaluation of Surface-Enhanced Raman Scattering Nanoparticles for Intracellular pH Sensing at a Single Particle Level. *Analytical Chemistry*, 91(5):3254–3262, 2019.
34) Janina Kneipp, Harald Kneipp, Burghardt Wittig, and Katrin Kneipp. Following the Dynamics of pH in Endosomes of Live Cells with SERS Nanosensors. *The Journal of Physical Chemistry C*, 114(16):7421–7426, 2010.
35) Kazuki Bando, Zhiqiang Zhang, Duncan Graham, Karen Faulds, Katumasa Fujita, and Satoshi Kawata. Dynamic pH measurements of intracellular pathways using nano-plasmonic assemblies. *Analyst*, 145:5768–5775, 2020.
36) Yizhi Zhang, Dorleta Jimenez de Aberasturi, Malou Henriksen-Lacey, Judith Langer, and Luis M. Liz-Marzán. Live-Cell Surface-Enhanced Raman Spectroscopy Imaging of Intracellular pH: From Two Dimensions to Three Dimensions. *ACS Sensors*, 5(10):3194–3206, 2020. PMID: 33092346.
37) David C. Kennedy, Craig S. McKay, Li-lin Tay, Yanouchka Rouleau, and John P. Pezacki. Carbon-bonded silver nanoparticles: alkyne-functionalized ligands for SERS imaging of mammalian cells. *Chem. Commun.*, 47(11):3156–3158, 2011.
38) Yong Chen, Jia-Qiang Ren, Xia-Guang Zhang, De-Yin Wu, Ai-Guo Shen, and Ji-Ming Hu.

Alkyne-Modulated Surface-Enhanced Raman Scattering-Palette for Optical Interference-Free and Multiplex Cellular Imaging. *Analytical Chemistry*, 88(12):6115–6119, 2016. PMID: 27223333.

39) Matteo Ardini, Jian-An Huang, Carlos S. Sánchez, Mansoureh Z. Mousavi, Valeria Caprettini, Nicolò Maccaferri, Giovanni Melle, Giulia Bruno, Lea Pasquale, Denis Garoli, and Francesco De Angelis. Live Intracellular Biorthogonal Imaging by Surface Enhanced Raman Spectroscopy using Alkyne-Silver Nanoparticles Clusters. *Scientific Reports*, 8(1):12652, 2018.
40) Mingmin Li, Jianzhen Wu, Mengtian Ma, Zhichao Feng, Ze Mi, Pengfei Rong, and Dingbin Liu. Alkyne- and Nitrile-Anchored Gold Nanoparticles for Multiplex SERS Imaging of Biomarkers in Cancer Cells and Tissues. *Nanotheranostics*, 3:113–119, 2019.
41) Ji-Xin Cheng, Andreas Volkmer, and X. Sunney Xie. Theoretical and experimental characterization of coherent anti-Stokes Raman scattering microscopy. *J. Opt. Soc. Am. B*, 19(6):1363–1375, Jun 2002.
42) Ji-Xin Cheng and X. Sunney Xie. Coherent Anti-Stokes Raman Scattering Microscopy:☒ Instrumentation, Theory, and Applications. *The Journal of Physical Chemistry B*, 108(3):827–840, 2004.
43) Erik M. Vartiainen, Hilde A. Rinia, Michiel Müller, and Mischa Bonn. Direct extraction of Raman line-shapes from congested CARS spectra. *Opt. Express*, 14(8):3622–3630, Apr 2006.
44) Christian W. Freudiger, Wei Min, Brian G. Saar, Sijia Lu, Gary R. Holtom, Chengwei He, Jason C. Tsai, Jing X. Kang, and X. Sunney Xie. Label-Free Biomedical Imaging with High Sensitivity by Stimulated Raman Scattering Microscopy. *Science*, 322(5909):1857–1861, 2008.
45) P Nandakumar, A Kovalev, and A Volkmer. Vibrational imaging based on stimulated Raman scattering microscopy. *New Journal of Physics*, 11(3):033026, 2009.
46) Yasuyuki Ozeki, Fumihiro Dake, Shin'ichiro Kajiyama, Kiichi Fukui, and Kazuyoshi Itoh. Analysis and experimental assessment of the sensitivity of stimulated Raman scattering microscopy. *Opt. Express*, 17(5):3651–3658, Mar 2009.
47) B. F. Levine, C. G. Bethea, A. R. Tretola, and M. Korngor. Stimulated Raman scattering from 20 - Å layers of silicon on sapphire. *Applied Physics Letters*, 37(7):595–597, 1980.
48) Brian G. Saar, Christian W. Freudiger, Jay Reichman, C. Michael Stanley, Gary R. Holtom, and X. Sunney Xie. Video-Rate Molecular Imaging in Vivo with Stimulated Raman Scattering. *Science*, 330(6009):1368–1370, 2010.
49) Yasuyuki Ozeki, Wataru Umemura, Yoichi Otsuka, Shuya Satoh, Hiroyuki Hashimoto, Kazuhiko Sumimura, Norihiko Nishizawa, Kiichi Fukui, and Kazuyoshi Itoh. High-speed molecular spectral imaging of tissue with stimulated Raman scattering. *Nature Photonics*, 6(12):845–851, 2012.
50) Esben Ravn Andresen, Pascal Berto, and Hervé Rigneault. Stimulated Raman scattering microscopy by spectral focusing and fiber-generated soliton as Stokes pulse. *Opt. Lett.*, 36(13):2387–2389, Jul 2011.
51) Dan Fu, Gary Holtom, Christian Freudiger, Xu Zhang, and Xiaoliang Sunney Xie. Hyperspectral Imaging with Stimulated Raman Scattering by Chirped Femtosecond Lasers. *The Journal of Physical Chemistry B*, 117(16):4634–4640, 2013. PMID: 23256635.
52) Mohammed S. Alshaykh, Chien-Sheng Liao, Oscar E. Sandoval, Gregory Gitzinger, Nicolas Forget, Daniel E. Leaird, Ji-Xin Cheng, and Andrew M. Weiner. High-speed stimulated hyperspectral Raman imaging using rapid acousto-optic delay lines. *Opt. Lett.*, 42(8):1548–1551, Apr 2017.
53) Sergey P. Laptenok, Vijayakumar P. Rajamanickam, Luca Genchi, Tual Monfort, Yeonwoo Lee, Imran I. Patel, Andrea Bertoncini, and Carlo Liberale. Fingerprint-to-CH stretch continuously tunable high spectral resolution stimulated Raman scattering microscope. *Journal of Biophotonics*, 12(9):e201900028, 2019.
54) Pascal Berto, Esben Ravn Andresen, and Hervé Rigneault. Background-Free Stimulated Raman Spectroscopy and Microscopy. *Phys. Rev. Lett.*, 112:053905, Feb 2014.
55) Delong Zhang, Mikhail N. Slipchenko, Daniel E. Leaird, Andrew M. Weiner, and Ji-Xin Cheng. Spectrally modulated stimulated Raman scattering imaging with an angle-to-wavelength pulse shaper. *Opt. Express*, 21(11):13864–13874, Jun 2013.
56) Hanqing Xiong, Naixin Qian, Zhilun Zhao, Lingyan Shi, Yupeng Miao, and Wei Min. Background-free imaging of chemical bonds by a simple and robust frequency-modulated stimulated Raman scattering microscopy. *Opt. Express*, 28(10):15663–15677, May 2020.
57) Marco Andreana, Marie-Andrée Houle, Douglas J. Moffatt, Andrew Ridsdale, Edlef Buettner, François Légaré, and Albert Stolow. Amplitude and polarization modulated hyperspectral Stimulated Raman Scattering Microscopy. *Opt. Express*, 23(22):28119–28131, Nov 2015.

58) Zhilun Zhao, Chen Chen, Shixuan Wei, Hanqing Xiong, Fanghao Hu, Yupeng Miao, Tianwei Jin, and Wei Min. Ultra-bright Raman dots for multiplexed optical imaging. *Nature Communications*, 12(1):1305, 2021.
59) Sidan Tian, Haozheng Li, Zhong Li, Huajun Tang, Mingming Yin, Yage Chen, Shun Wang, Yuting Gao, Xiangliang Yang, Fanling Meng, Joseph W. Lauher, Ping Wang, and Liang Luo. Polydiacetylene-based ultrastrong bioorthogonal Raman probes for targeted live-cell Raman imaging. *Nature Communications*, 11(1):81, 2020.
60) Lu Wei, Fanghao Hu, Yihui Shen, Zhixing Chen, Yong Yu, Chih-Chun Lin, Meng C Wang, and Wei Min. Live-cell imaging of alkyne-tagged small biomolecules by stimulated Raman scattering. *Nature Methods*, 11(4):410–412, Mar 2014.
61) Fanghao Hu, Chen Zeng, Rong Long, Yupeng Miao, Lu Wei, Qizhi Xu, and Wei Min. Supermultiplexed optical imaging and barcoding with engineered polyynes. *Nature Methods*, 15(3):194–200, 2018.
62) Yupeng Miao, Lixue Shi, Fanghao Hu, and Wei Min. Probe design for super-multiplexed vibrational imaging. *Physical Biology*, 16(4):041003, apr 2019.
63) Jingwen Shou, Robert Oda, Fanghao Hu, Keiko Karasawa, Mutsuo Nuriya, Masato Yasui, Bruce Shiramizu, Wei Min, and Yasuyuki Ozeki. Super-multiplex imaging of cellular dynamics and heterogeneity by integrated stimulated Raman and fluorescence microscopy. *iScience*, 24(8):102832, 2021.
64) Lu Wei, Zhixing Chen, Lixue Shi, Rong Long, Andrew V Anzalone, Luyuan Zhang, Fanghao Hu, Rafael Yuste, Virginia W Cornish, and Wei Min. Super-multiplex vibrational imaging. *Nature*, 544(7651):465–470, Apr 2017.
65) Lu Wei and Wei Min. Electronic Preresonance Stimulated Raman Scattering Microscopy. *The Journal of Physical Chemistry Letters*, 9(15):4294–4301, 2018. PMID: 30001137.
66) Peter Fimpel, Ashwin J. X. Choorakuttil, Andrea Pruccoli, Lukas Ebner, Shunji Tanaka, Yasuyuki Ozeki, Martin J. Winterhalder, and Andreas Zumbusch. Double modulation SRS and SREF microscopy: signal contributions under pre-resonance conditions. *Phys. Chem. Chem. Phys.*, 22:21421–21427, 2020.
67) Hiroyoshi Fujioka, Jingwen Shou, Ryosuke Kojima, Yasuteru Urano, Yasuyuki Ozeki, and Mako Kamiya. Multicolor Activatable Raman Probes for Simultaneous Detection of Plural Enzyme Activities. *Journal of the American Chemical Society*, 142(49):20701–20707, 2020. PMID: 33225696.
68) Jingwen Shou and Yasuyuki Ozeki. Photoswitchable stimulated Raman scattering spectroscopy and microscopy. *Opt. Lett.*, 46(9):2176–2179, May 2021.
69) Jianpeng Ao, Xiaofeng Fang, Xianchong Miao, Jiwei Ling, Hyunchul Kang, Sungnam Park, Changfeng Wu, and Minbiao Ji. Switchable stimulated Raman scattering microscopy with photochromic vibrational probes. *Nature Communications*, 12(1):3089, 2021.
70) Dongkwan Lee, Chenxi Qian, Haomin Wang, Lei Li, Kun Miao, Jiajun Du, Daria M. Shcherbakova, Vladislav V. Verkhusha, Lihong V. Wang, and Lu Wei. Toward photoswitchable electronic pre-resonance stimulated Raman probes. *The Journal of Chemical Physics*, 154(13):135102, 2021.

Chapter 2
Visualizing drug dynamics in living cells by alkyne-tag SERS microscopy

The contents of this chapter have been published in:
K. Koike, K. Bando, J. Ando, H. Yamakoshi, N. Terayama, K. Dodo, N. I. Smith, M. Sodeoka, K. Fujita, "Quantitative Drug Dynamics Visualized by Alkyne-Tagged Plasmonic-Enhanced Raman Microscopy", *ACS Nano*, 14 (11), 15032-15041 (2020). https://pubs.acs.org/doi/10.1021/acsnano.0c05010

Introduction

Visualizing drug uptake of living cells and understanding their behavior and interactions with intracellular molecules is important for drug development.[71, 72] In this process, detecting the drug molecules' locations selectively among the numerous endogenous intracellular molecules is required. These measurements give us useful information and deep insights for optimizing the design of drug molecules and improving their uptake efficiency and medical efficacies. Bioorthogonal fluorescence imaging with click chemistry has made a tremendous impact on this field.[73, 74] Click chemistry utilizes the bioorthogonality of cycloadditions between alkyne-containing small-molecule drugs and azide-containing fluorescence probes. However, relatively bulky fluorophores attached to the small molecule may modify their original functions. It also causes photobleaching, limiting the application of click chemistry-based imaging to study temporal drug dynamics in living cells. Spectroscopically, alkynes are also bioorthogonal to endogenous molecules. It possesses a unique Raman peak at around 2120 cm^{-1}, arising from symmetric vibration mode of carbon-carbon triple bond. The wavenumber region from around 1800 to 2700 cm^{-1} is called a silent region of biological cells, where endogenous molecules do not show any Raman peaks. Taking advantage of these properties of alkynes, Raman microscopy techniques have emerged as an alternative optical tool for direct visualization of alkyne-tagged small molecules.[75, 76, 77] Furthermore, stimulated Raman scattering (SRS) can be used for speeding up the acquisition rate of small molecules through coherent Raman process.[78, 79, 80, 81, 82] However, the detection limit of molecules by SRS and spontaneous Raman scattering is usually at the millimolar (mM) level. Therefore, it is still challenging to visualize the initial stages of drug uptake and dynamics in living cells because the local concentration of small molecule drugs is not typically greater than the detection limit.

In this chapter, I propose to use surface-enhanced Raman scattering (SERS) to boost the detection sensitivity by localized plasmon resonance of metallic nanoparticles and detect alkyne-tagged small-molecule drugs during the drug uptake of living cells in 3D. SERS spectroscopy has been used to analyze molecules and local environments in living cells with high sensitivity.[83, 84, 85, 86] Background-free SERS detection of alkynes has been successfully performed even in living cells using metallic nanoparticles modified with alkyne-tagged molecules.[87, 88, 89, 90] In the present study, to detect the entry of small-molecule drugs, I use gold nanoparticles as SERS probes and introduce them into lysosomes by endocytosis[84, 85, 86, 91] prior to drug administration. Therefore, when the entered small-molecule drugs come to nanoparticles, the Raman signal of alkynes can be enhanced and detected as a Raman peak of alkynes. I demonstrate alkyne-tagged SERS imaging of small molecules in living cells. I also introduce a digital SERS counting method for analyzing the relative increase of intracellular drug concentrations in living cells within a physiological environment.

2.1 Raman and SERS spectroscopy of small-molecule drug

Optical setup for spontaneous Raman and SERS measurements

Fig.2.1 shows a home-built slit-scanning SERS microscope for 2D and 3D SERS imaging of the sample. I thank Prof. K. Bando from Osaka University for his help developing the optical setup. The excitation laser for SERS measurement was a solid-state laser with a wavelength of 660 nm (opus660, Laser Quantum) to reduce photodamages on cells and strong fluorescence background from cells. The wavelength is also suitable for exciting plasmon resonance at gold nanoparticles with low scattering from the nanoparticles. For the spontaneous Raman measurement, a solid-state laser with a wavelength of 532 nm (Millennia eV, Spectra-Physics) was used. A half-wave plate and glan-laser polarizer were used to control an excitation intensity at the sample plane. The line-shaped laser was created by three cylindrical lenses and focused onto the sample by water immersion objective lens (Apo, 1.25 NA, 40x, Nikon or Plan Apo IR, 1.27 NA, 60x, Nikon). The sample was simultaneously illuminated in the y-direction by a line-focused laser. Thus, for 2D imaging, the sample was only scanned in the x-direction by galvanometer-mirror. The scattered light was corrected with the same objective lens. Rayleigh scattering was blocked by long-pass filters (LP02-664RU-25 for 660 nm excitation, LP03-532RU-25 for 532 nm excitation, Semrock). The transmitted Raman scattered light was focused onto the slit before the spectrometer (MK-300, Bunko Keiki). The spectrometer's center wavelength, grating setting, and blazed wavelength were 740 nm, 300 L/mm, and 760 nm, respectively. Raman spectrum of the sample was detected by EM-CCD camera (iXon Ultra888, Andor). The bright-field image was captured by an sCMOS camera (Zyla 4.2, Andor) attached to the side port of the microscope body. A piezoelectric translational stage attached with the objective lens changes the focal plane of interest rapidly, allowing three-dimensional SERS imaging. A function generator (WF1974, NF circuit) was used to control the galvanometer-mirror and piezo stage. The trigger signal from the EM-CCD camera was sent to the function generator once the spectrum acquisition by the EM-CCD camera started, and the temporal variant voltage from the function generator was sent to the galvanometer mirror and piezoelectric stage as shown in Fig.2.2. At first, the piezoelectric stage was rapidly scanned in the z-direction with 10 divisions (z1 to z10), while the galvanometer mirror was kept the same position at x1. Then, the galvanometer mirror moved to x2, and the piezoelectric stage was again rapidly scanned in the z-direction with 10 divisions(z1 to z10). Scanning of both instruments was stopped when the acquisition of spectra by EM-CCD was completed. This procedure was repeated to obtain a time-lapse 3D SERS hyperspectral dataset, which was post-processed using a home-built program on MATLAB (MathWorks) and the Volume Viewer plug-in on ImageJ to obtain 3D SERS images.

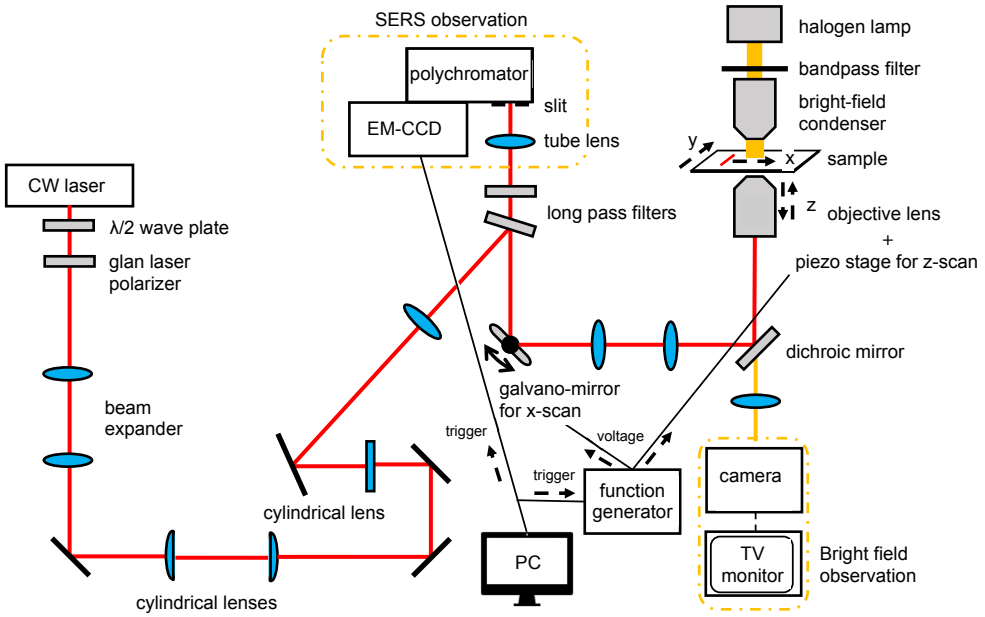

Figure 2.1. Optical setup of slit scanning SERS microscopy for 2D and 3D imaging. Reprinted with permission from ref.[92] Copyright 2020 American Chemical Society.

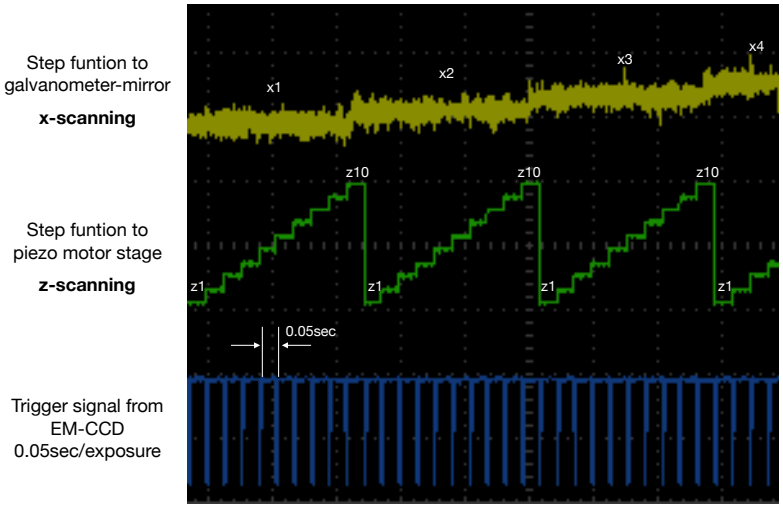

Figure 2.2. Step voltage sent from function generator to galvanometer-mirror and piezoelectric stage for the 3D imaging.

Raman and SERS spectroscopy of small-molecule drug

As a target small-molecule drug, I used an alkyne-tagged acyloxymethyl ketone type inhibitor (Alt-AOMK),[93] an alkyne-tagged cathepsin B inhibitor localized in lysosomes. The molecular structure of Alt-AOMK is shown in Fig.2.3A. Alt-AOMK was designed from Z-FG-AOMK and synthesized with the help of the Sodeoka group from RIKEN. Z-FG-AOMK was designed and developed as an inhibitor

of cysteine protease cathepsin B (CatB) in lysosome.[94] The design optimization and its efficacy of Alt-AOMK as a CatB inhibitor were confirmed by ATRaS and MS/MS analysis in a previous article.[93] However, visualizing the uptake process of Alt-AOMK into living cells by Raman microscopy has not yet been demonstrated.

At first, I measured Raman of Alt-AOMK to confirm alkyne peaks in the silent region. For spontaneous Raman measurement, a 532 nm excitation laser was used. A total of 2 μL of Alt-AOMK at a concentration of 40 mM dissolved in dimethyl sulfoxide (DMSO) was placed on a glass-bottom dish (Matsunami). The laser intensity at a sample plane was 2 mW/μm^2. The exposure time was 20 s. A total of 200 Raman spectra were simultaneously collected, and the averaged spectrum was used as a resultant Raman spectrum. Fig.2.3B shows spontaneous Raman spectrum of Alt-AOMK. The alkyne peak was observed at 2122 cm^{-1}. Strong peaks at 1040, 1320, and 1418 cm^{-1} are derived from DMSO. The other small peaks at 1176 and 1613 cm^{-1} can be assigned to vibrational modes of aromatic C-H bending and ring stretching of Alt-AOMK, respectively.[95] I also investigated the detection limit of alkyne peak in spontaneous Raman scattering (Fig.2.4). I measured the spontaneous Raman spectrum of Alt-AOMK five times at different concentrations (40 μM, 400 μM, 4 mM, 10 mM, and 20 mM), and calculated signal-to-noise ratio (SNR) of the alkyne peak with the following procedures. The signal was defined as a peak height of the Raman intensity at 2122 cm^{-1}, which is the difference of the peak intensity and the baseline estimated by averaging the intensity of the spectrum region (2000-2090 cm^{-1} and 2150-2200 cm^{-1}). The noise was defined as the standard deviation σ of the baseline region at 2000-2090 cm^{-1} and 2150-2200 cm^{-1}. In Fig.2.4, the average of SNR for five measurements at each concentration was plotted with red dots. I defined the detection limit as 3 SNR (= signal/3$\sigma \geqq 1$). From the calculation, the detection limit of spontaneous Raman scattering can be estimated to be around 2-4 mM for this drug molecule.

For SERS measurement, a 660 nm excitation laser was used. As a SERS substrate, I prepared a gold nanoparticle-modified MAS-coated glass substrate with a diameter of 50 nm of gold nanoparticles (EMGC50, BBI Solutions). The peak position of the extinction spectrum of the gold nanoparticle suspension, measured with UV-vis spectroscopy (Multiskan GO, Thermo Fisher Scientific), was at 535 nm. A total of 1 μL of Alt-AOMK at a concentration of 10 μM was dropped onto the substrate. The laser intensity at a sample plane was 0.79 mW/μm^2. The exposure time per line was 50 ms. In the SERS spectrum, the strong alkyne peak was confirmed at around 1980 cm^{-1}. Note that the intensity scale of spontaneous Raman is 20 times smaller than that of SERS. Even with a concentration of 10 μM, the alkyne peak with an SNR of 11.4 was detected. The other two SERS peaks at 1163 and 1594 cm^{-1} can be derived from the enhanced Raman signal of aromatic-ring vibrational modes of Alt-AOMK. As for the alkyne peak, there was a peak-shift of 140 cm^{-1} from spontaneous Raman to SERS. This effect has already been reported in previous reports.[87, 89, 93] This peak shift can be mainly caused by chemical absorption of alkynes onto the nanoparticle surface.[95, 96] Even so, the SERS peak of alkynes was still located in the silent region of living cells. The SERS peak can be used to identify

Alt-AOMK location inside living cells without overlapping the spectral information of endogenous intracellular molecules.

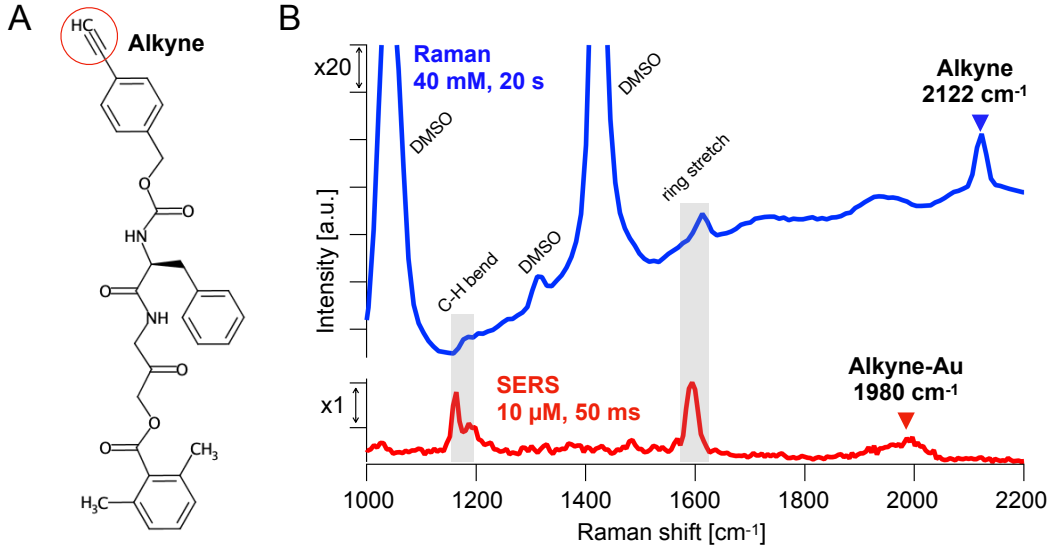

Figure 2.3. Raman spectroscopy of alkyne-tagged acyloxymethyl ketone type inhibitor (Alt-AOMK). (A) Molecular structure of Alt-AOMK. (B) Raman spectrum (blue color) and SERS spectrum (red color) of Alt-AOMK. Reprinted with permission from ref.[92] Copyright 2020 American Chemical Society.

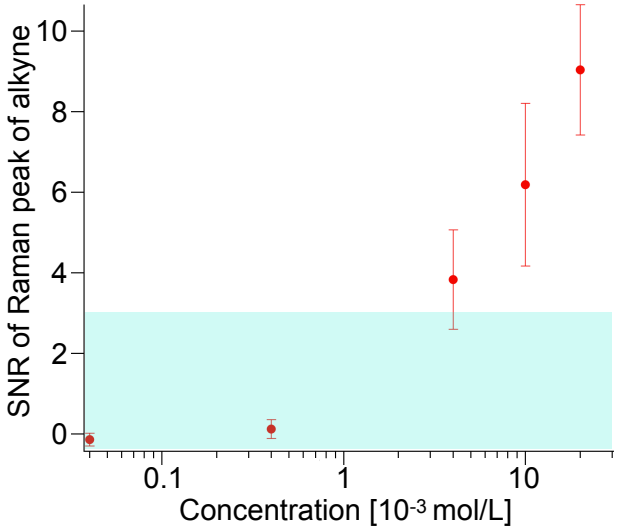

Figure 2.4. Detection limit of spontaneous Raman peak of alkynes in Alt-AOMK. The error bar is ± SD of the measurement at each concentration. Reprinted with permission from ref.[92] Copyright 2020 American Chemical Society.

SERS detection of small-molecule drug in living cells with high sensitivity

In order to prove that SERS can detect Alt-AOMK in living cells with high sensitivity, I performed Raman imaging of living cells with gold nanoparticles and Alt-AOMK. As a cell model, I used macrophages J774A.1. Previous studies demonstrated live-cell SERS imaging of the macrophage cells.[85, 86] Macrophages have CatB in lysosomes, and its over-expression has been studied for metabolic diseases.[97, 98]

At first, I performed SERS imaging of living cells using gold nanoparticles. The samples were prepared with the following procedures. Macrophages were cultured in glass-bottom dishes with a density of 2-3x10^5 cells/mL with DMEM (043-30058, FUJIFILM Wako Pure Chemical Corporation) supplemented with fetal bovine serum (SH30071.03, GE Healthcare HyClone) and penicillin-streptomycin (26252-94, Nacalai Tesque) as an antibiotic. The cells were maintained in an incubator (Sanyo) of 37 ℃ and 5% CO_2 environment for 6 h. The cells were then incubated with DMEM containing 100 μL of a gold nanoparticle suspension with a diameter of 50 nm with a density of 2.25x10^9 particles/mL for 16 h. During this procedure, gold nanoparticles can be delivered to lysosomes and form aggregates of several nanoparticles.[99] The diameter of 50 nm is an optimal size for living cells to uptake them through endocytosis.[100] After that, the cells were washed several times with PBS to remove the gold nanoparticles in the culturing medium. After introducing gold nanoparticles inside the cells, I incubated the cells with Alt-AOMK-containing DMEM at a concentration of 10 μM for 2 h. As a comparison, I prepared the cells with Alt-AOMK and without gold nanoparticles to confirm the detection sensitivity improvement by SERS. For the measurements, the laser intensity at the sample plane was 0.63 mW/μm^2. The exposure time per line was 50 ms. A Raman image was acquired from 100 scanning lines in the x-direction. Raman image of living cells with gold nanoparticles showed several SERS signals (Fig.2.5B). Many SERS peaks in the fingerprint regions were observed from red spots. In contrast, the alkyne peak was observed from the green spots (Fig.2.5A), which indicates the colocalization of Alt-AOMK and gold nanoparticles in living cells. Fig.2.5C shows a Raman image of the cells without gold nanoparticles. In this case, no Raman signal from both biological molecules and Alt-AOMK was observed under the same imaging conditions. From these results, I confirmed the improvement in the detection sensitivity of Alt-AOMK in living cells by SERS of gold nanoparticles.

Cell viability assay of gold nanoparticles and Alt-AOMK

I investigated the cytotoxicity of both gold nanoparticles and Alt-AOMK by Trypan Blue Assay. Macrophages with and without gold nanoparticles were prepared with the same procedure. For the macrophages with gold nanoparticles, Alt-AOMK was introduced at 0, 20, and 100 μM for each sample, and the cells were incubated at 37 ℃. After trypsinization, centrifugation was performed to collect the cells. Each cell sample was diluted by two times with 0.4% Trypan Blue solution (Thermo Fisher Scientific). A 10 μL amount of the diluted cell sample was then carefully introduced into a disposable

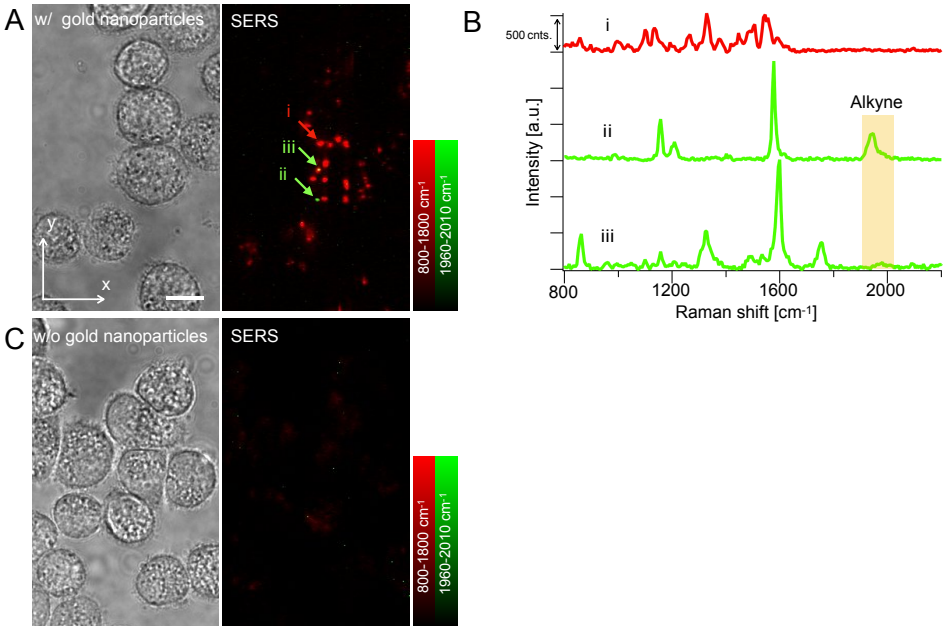

Figure 2.5. Raman imaging of living macrophages with and without gold nanoparticles. (A) Bright field and SERS images of the cells with gold nanoparticles. The SERS images were reconstructed from two Raman spectral windows; the red color is the average Raman intensity from 800 to 1800 cm^{-1} containing Raman peaks of endogenous molecules, and the green color is the average Raman intensity from 1960 to 2010 cm^{-1} assigned to the alkyne peak. Scale bar = 10 μm. (B) Raman spectra from the red and green spots in (A). (C) Bright field and SERS images of the cells without gold nanoparticles. Reprinted with permission from ref.[92] Copyright 2020 American Chemical Society.

hemocytometer (NanoEnTek). Dead and living cells were counted under the bright field microscope for four 1x1 mm squares (Fig.2.6). Table.2.1 summarizes the cell viability assay for nanoparticles and Alt-AOMK cytotoxicity for living cells. Five cells samples at different conditions were investigated. All samples showed more than 90% of cell viability. I found no significant correlation between cell viability and the existence of gold nanoparticles and drug concentrations. This result suggests the low cytotoxicity of gold nanoparticles and Alt-AOMK for the live-cell measurements.

Table2.1: Summary of cell viability assay of gold nanoparticles (GNP) and Alt-AOMK.

Sample	Incubation condition	Alt-AOMK	Viability (Live/(Live + Dead))
1 (Fig.2.6A)	16 h -GNP	No drug treatment	94.8% (259/273)
2	16 h +GNP	No drug treatment	95.9% (186/194)
3	16 h +GNP	20 μM, 30 min	94.2% (161/171)
4	16 h +GNP	100 μM, 30 min	93.0% (239/257)
5 (Fig.2.6B)	16 h +GNP	100 μM, 60 min	95.0% (236/248)

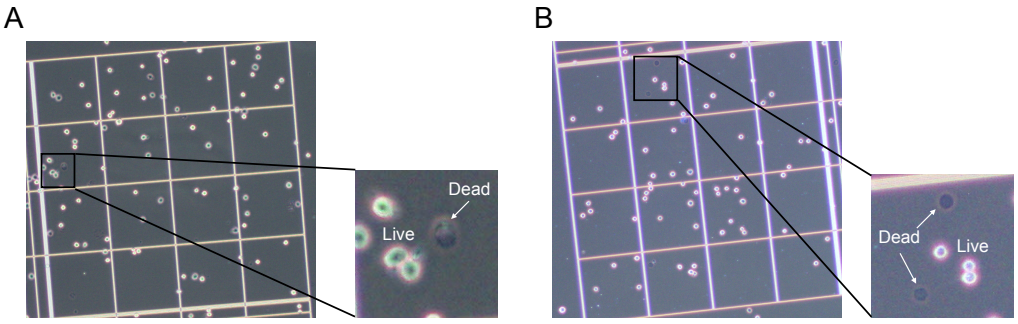

Figure 2.6. Bright field observation of macrophages with hemocytometers for cell viability assay using trypan blue solution. (A) Macrophages without gold nanoparticles and Alt-AOMK. (B) Macrophages with gold nanoparticles for 16 h and incubated with Alt-AOMK for 1 h at a concentration of 100 μM. Reprinted with permission from ref.[92] Copyright 2020 American Chemical Society.

2.2 Time-lapse SERS imaging of small-molecule drug in living cells

Time-lapse 2D SERS imaging of small-molecule drug in living cells

Monitoring drug uptake and dynamics requires high detection sensitivity and temporal resolution. SERS offers enhanced Raman signal of alkyne with only 50 ms exposure time, which can facilitate the imaging speed of Raman imaging and thus allows us to perform time-lapse imaging of the sample. To confirm the applicability of our technique for observing temporal dynamics of small-molecule drugs, I performed time-lapse 2D SERS imaging. At first, I introduced gold nanoparticles into the cells. Then, I cultured the cells with Alt-AOMK at a concentration of 10 μM for 4 h at 37 ℃ and 5% CO_2. The laser intensity of the sample plane was 1.3 mW/μm^2. The exposure time per line was 50 ms. One Raman image was acquired from 120 scanning steps in the x-direction with an acquisition time of 6.5 s. The imaging area was 80x173 μm^2 for x and y directions, respectively. A total of 400 Raman images were obtained in approximately 43 min. Selected SERS images were shown in Fig.2.7A along with the bright field image. The temporal changes of SERS signals from both fingerprint regions (red) and alkynes (green) were observed, indicating the movement of intrinsic intracellular molecules and Alt-AOMK and/or gold nanoparticles themselves. I selected six different SERS spots of alkynes at 32 min 23 s and obtained SERS spectra from the selected single pixels (Fig.2.7B). The SERS spectra of alkynes in Fig.2.7C showed a similar spectral shape of Alt-AOMK as I showed in Fig.2.3B. The peak position of alkynes slightly differed from each other. This may suggest the orientations of Alt-AOMK and the distances between the nanoparticle surface were different depending on the alkyne detection configuration. Such SERS peak shifts in the small spectral range have been well observed previously under low concentration conditions.[101, 102] Other than the alkyne peak, there are several SERS peaks not from Alt-AOMK between 1160 and 1580 cm^{-1}. These signals can be derived from endogenous molecules colocalized with Alt-AOMK.

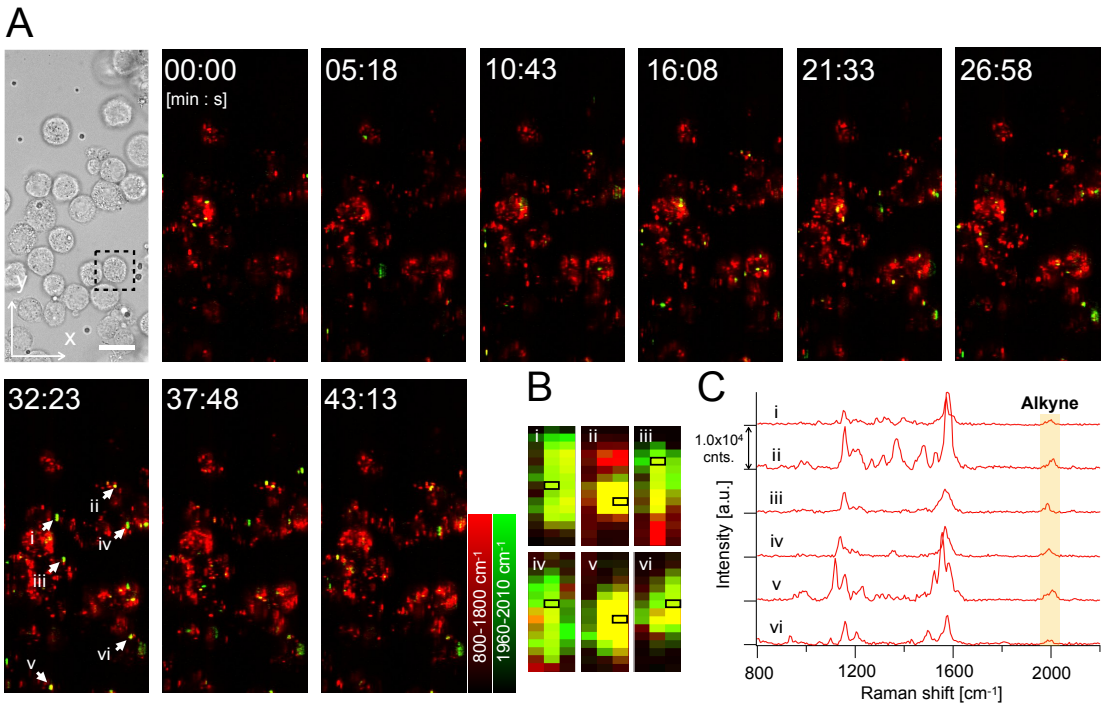

Figure 2.7. Time-lapse 2D SERS imaging of living cells at a concentration of 10 μM of Alt-AOMK. (A) Bright field and SERS images of the cells. Scale bar = 20 μm. (B) Magnified SERS signals of alkynes indicated as the white arrows in (A) at the time point 32 min 23 s. (C) SERS spectra from each single pixel indicated by the black squares in (B). Only background subtraction was applied for spectral processing. Reprinted with permission from ref.[92] Copyright 2020 American Chemical Society.

Fig.2.8A shows a time series of SERS images of the single-cell surrounded by the black dotted-square in Fig2.7A. The bright SERS spot indicated as the white arrow showed temporal fluctuations in spatial distributions and signal intensity. The SERS peak of alkynes at each time (Fig.2.8B) showed temporal variations of peak intensity and positions. This result indicates that the interaction between Alt-AOMK and the gold surface rapidly changed at the single nanoparticle level, such as adsorbed distance and orientation during the observation period. SERS signals from adsorbed molecules have shown such temporal variations.[103] Using other optical imaging techniques with a higher spatial and temporal resolution with a single-nanoparticle tracking system[104] should provide further insights into drug interactions with a single gold nanoparticle and local chemical environment.

To prove that the SERS signals of alkynes originate from inside the cells, I performed 3D SERS imaging of whole cells with Alt-AOMK. The cells with gold nanoparticles were cultured with Alt-AOMK at a 5 μM concentration for 30 min. The laser intensity of the sample plane was 0.78 mW/μm^2. The exposure time per line was 50 ms. A 3D SERS image was acquired with 40 and 10 scanning steps in the x- and z-directions, respectively, with an acquisition time of 21.8 s. Fig.2.9 shows a 3D SERS image of the cells at different z-positions and merged volumetric SERS image. The SERS signals of alkynes were observed at different z-positions, but all of them localized from 5.0 to 11.7 μm. By

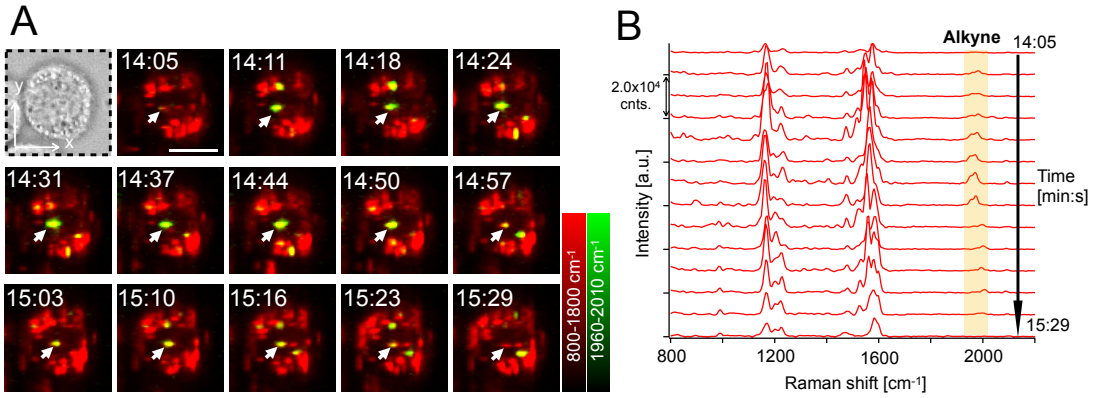

Figure 2.8. Time-lapse 2D SERS imaging of a single living cell at a concentration of 10 μM of Alt-AOMK. (A) Time-lapse SERS images of the single cell in Fig.2.7(A). (B) Time series of the SERS spectra obtained from the SERS signals indicated by white arrows in (A). Reprinted with permission from ref.[92] Copyright 2020 American Chemical Society.

performing 3D SERS imaging of living macrophages, I confirmed that Alt-AOMK-generating SERS signals were located inside the cells rather than originating from the glass-bottom substrate or out-of-cell locations.

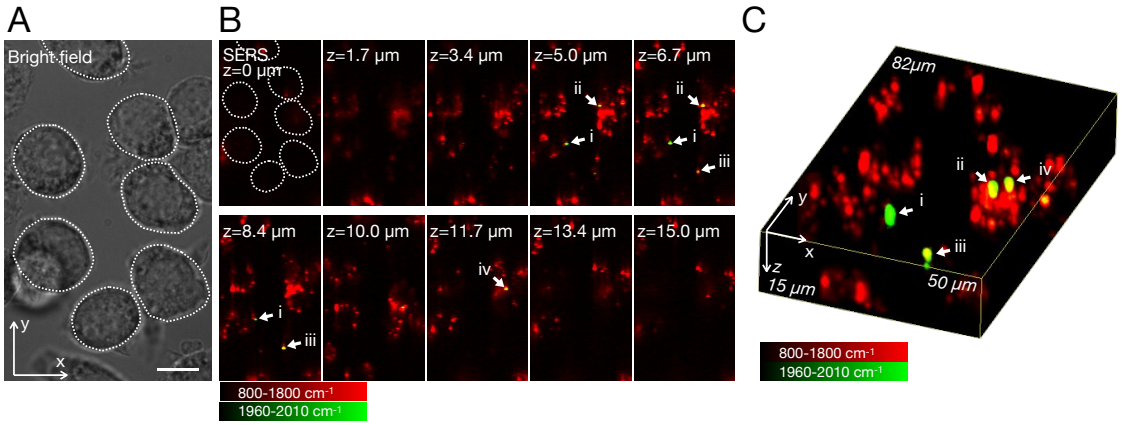

Figure 2.9. Three-dimensional SERS imaging of living cells with Alt-AOMK. (A) Bright field image of the cells. Scale bar = 10 μm. (B) Two-dimensional SERS images of the cells at different z positions from 0 to 15 μm with a step size of 1.67 μm. (C) Three-dimensional SERS image of the cells with an area of 50x82x15 μm^3. Reprinted with permission from ref.[92] Copyright 2020 American Chemical Society.

Time-lapse 3D SERS imaging of drug uptake into living cells

As I showed in Fig.2.9, SERS signals of alkynes in living cells can locate the different depths of the imaging plane even in a single living cell. Therefore, time-lapse 3D imaging of whole cellular volume is essential to visualize the uptake process of living cells. I performed time-lapse 3D SERS imaging with the following procedures. I prepared living macrophages with gold nanoparticles incubated on a glass-bottom dish. I did not add Alt-AOMK before the imaging to observe the uptake process of living

cells. The laser intensity of the sample plane was 0.78 mW/μm^2. The exposure time per line was 50 ms. A 3D Raman image was acquired from 40 scanning steps in the x-direction and 10 scanning steps in the z-direction. The acquisition time was 21.8 s. Although the image acquisition time for the 3D imaging was longer than that for the 2D imaging, it was still fast enough to observe the uptake of Alt-AOMK. A total of 150 Raman images were obtained in approximately 53 min. The imaging volume was 50x82x15 μm^3. During the measurement (at the 20th frame, 6 min after starting the imaging), I introduced Alt-AOMK gently into the cell culturing medium at final concentrations of 20 μM. Fig.2.10 shows a bright-field image of the measured cells and time-series of 3D SERS images. At the beginning of drug administration (00 min 00 s), only SERS signals from intracellular molecules (red color) were observed in 3D. Then, SERS signals of alkyne started to appear in some cells about 10 minutes after drug administration, and the number of signals gradually increased with time. From the beginning to the end of imaging, the SERS intensity from endogenous molecules (800-1800 cm^{-1}) and its temporal behavior were almost constant over time. This may suggest that there is no significant change in the amounts of the nanoparticles during the imaging, except for the random motion of the nanoparticles, molecular diffusion, and inherent SERS blinking. Therefore, the more the Alt-AOMK molecules were taken up into the cell, the higher the probability of co-localization of gold nanoparticles with alkynes. Therefore, the number of SERS spots of alkyne may correlate with relative changes in the intracellular Alt-AOMK concentration. But, absolute quantification of the concentration by SERS measurement is still challenging due to its unstable enhancement factor and temporal fluctuations of SERS intensity.

Photodamage by time-lapse observation

Time-lapse imaging of living cells by optical microscopy requires less photodamage to the sample by excitation laser. In this study, in order to reduce the damage to the cells, I used a 660 nm red laser for live-cell SERS imaging. In the following experiments, I investigated the photodamage by time-lapse 3D SERS imaging as well as the drug concentration dependence. I compared bright-field images before and after the time-lapse 3D SERS imaging for 53 min under the different administration concentrations of Alt-AOMK (Fig.2.11). Regardless of the drug concentration, there was basically no significant morphological change in the cells after 53 minutes of laser irradiation.

Next, I investigated the longest, total irradiation time for time-lapse measurements under the present conditions until the cells started to show photodamage. In this measurement, I performed measurements for 90 min with Alt-AOMK of 20 μM with and without laser irradiation. Fig.2.12 shows the results. With laser irradiation, some cells started to show damages after 70 min, but most of the cells did not show morphological degradations. In contrast, without laser irradiation, no cells showed cellular blebbing. Under the current conditions, the imaging time is limited to about 60-70 minutes. However, by imaging every few minutes instead of continuously irradiating the laser, we can effectively reduce photodamage and observe living cells in better physiological conditions for a longer period of time.

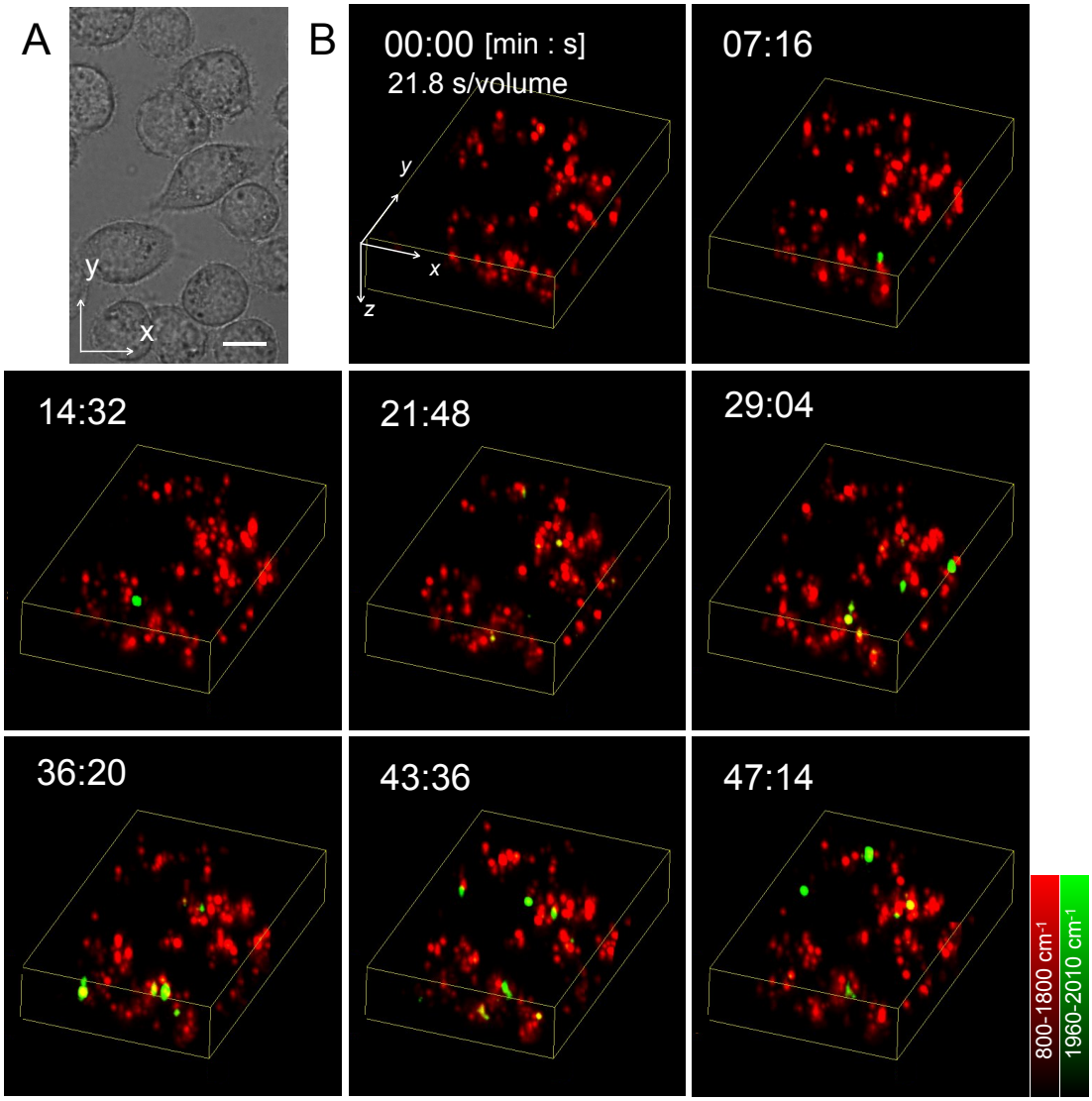

Figure 2.10. Time-lapse 3D SERS imaging to monitor the uptake of Alt-AOMK into living cells. (A) Bright field and SERS images of the cells. Scale bar = 10 μm. (B) Time-lapse 3D SERS images of the cells. Alt-AOMK was introduced into the cell culture dish at a concentration of 20 μM. Timeline indicates the time after the drug administration. Reprinted with permission from ref.[92] Copyright 2020 American Chemical Society.

2.3 Digital SERS counting for quantitative analysis of drug dynamics

Procedure of digital SERS counting

Toward quantitative detection of SERS signal of alkynes, the spectral shift of alkynes is not a significant problem for interpreting the molecular signature. There is basically no other Raman signal

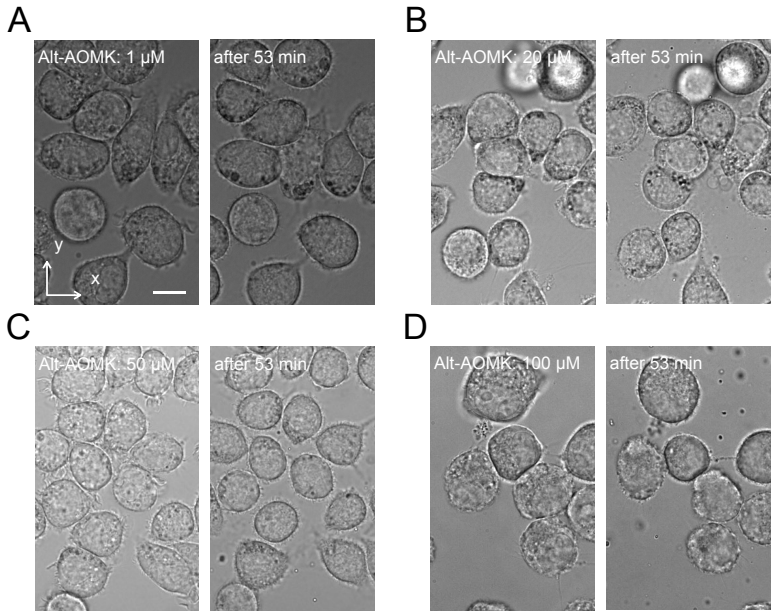

Figure 2.11. Bright field observation of living macrophages before and after the time- lapse 3D SERS measurement incubated with Alt-AOMK at concentrations of 1 μM (A), 20 μM (B), 50 μM (C), and 100 μM (D). The measurement was performed for 53 min. Scale bar = 10 μm. Reprinted with permission from ref.[92] Copyright 2020 American Chemical Society.

around 2000 cm^{-1} in living cells. Therefore, I can separately and selectively detect the SERS peak of Alt-AOMK. However, the intensity of the SERS peak cannot be controlled, and it is significantly affected by physical and chemical conditions such as nanoparticle configurations, enhancement factor of electric fields, adsorbed molecular orientation, and distances. Therefore, unlike spontaneous Raman scattering or stimulated Raman scattering (SRS), I cannot use the signal intensity as an indicator for the intracellular concentration of Alt-AOMK. Researchers in Canada have recently proposed the digital SERS counting technique for quantitative analysis of low concentration molecules[105] based on the concept of digital bioassays.[106] In this technique, they counted the number of SERS spots observed in the imaging area rather than measuring the intensity of each SERS spot. This method can provide a quantitative calibration curve between analyte concentration and the number of SERS spots. Following this article, I applied the concept of digital SERS counting to visualize the temporal behavior of the SERS signal of Alt-AOMK in living cells and quantify the uptake speed according to the administration concentration.

Fig.2.13 shows a schematic of digital SERS counting procedures for each cell in the imaging volume. At first, I performed quantitative detection of alkyne signals based on digital bioassay and created a cell-segmentation map. The procedure of alkyne detection is shown in Fig.2.14. Each voxel (3D pixel) in a 3D SERS image has a spectrum. The spectrum was smoothed with Savitzky-Golay filtering with an order of 3 and a window of 5 points to reduce sharp noise effectively. I defined the region from 1960 to 2020 cm^{-1} as "signal region" where alkyne peaks are typically found. The spectrum region

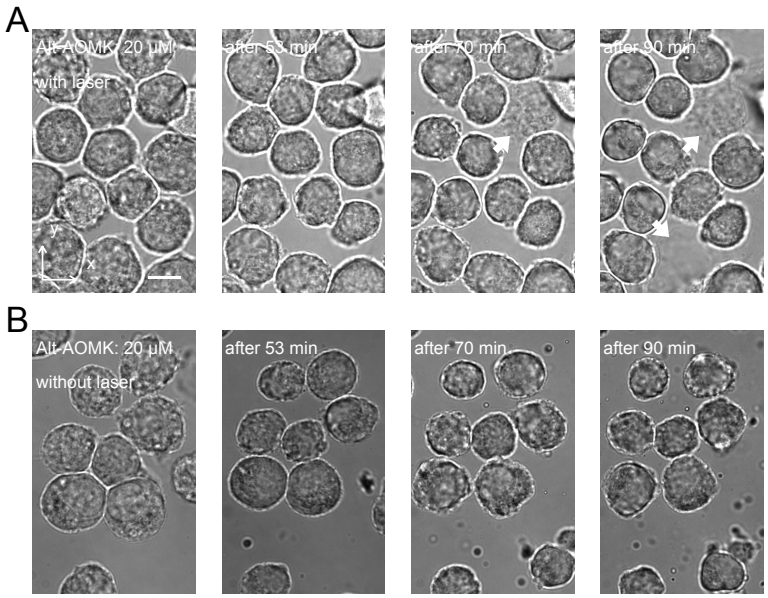

Figure 2.12. Bright field observation of living macrophages before and after the time-lapse 3D SERS measurement incubated with Alt-AOMK at concentrations of 20 μM with laser irradiation (A) and without laser irradiation (B). Scale bar = 10 μm. Reprinted with permission from ref.[92] Copyright 2020 American Chemical Society.

between 2140 to 2240 cm^{-1}, which is neighboring the alkyne peak, was defined as ”noise region”. The signal intensity of alkynes was estimated by calculating the difference between the peak intensity in the ”signal region” and the average value of the ”noise region”. The noise was calculated as the standard deviation of the signal at ”noise region” without Savitzky-Golay filtering. Then, the 3D SERS image was digitized with ”1” to voxels when the alkyne signal had a signal 7 times higher than the noise (standard deviation of noise region). The other voxels without alkyne signals were assigned ”0”. A cluster of voxels that contain the alkyne signal was defined as a single SERS spot of alkynes. For the cell segmentation, I used a bright-field image and a 3D SERS image as a reference (Fig.2.15). Finally, I counted the number of SERS spots in each cell based on the alkyne-signal distribution and cell-segmentation maps.

Quantitative analysis of temporal variation of Alt-AOMK concentration at single-cell level

With the digital SERS counting method, I counted the number of SERS spots for each cell for all frames (Fig.2.16). The number of alkyne-containing voxels differed from cell to cell (Fig.2.16A). This suggests that the uptake reaction and/or the number of gold nanoparticles may be different depending on the cells. At a concentration of 20 μM, as shown in Fig.2.10, the number of SERS spots increased at approximately 10-15 min after drug administration (Fig.2.16B). The drug uptake into the cells occurred during this period. Although the measurement of the absolute drug concentration was not available with this technique, the temporal change of the number of SERS spots reflects the speed of drug

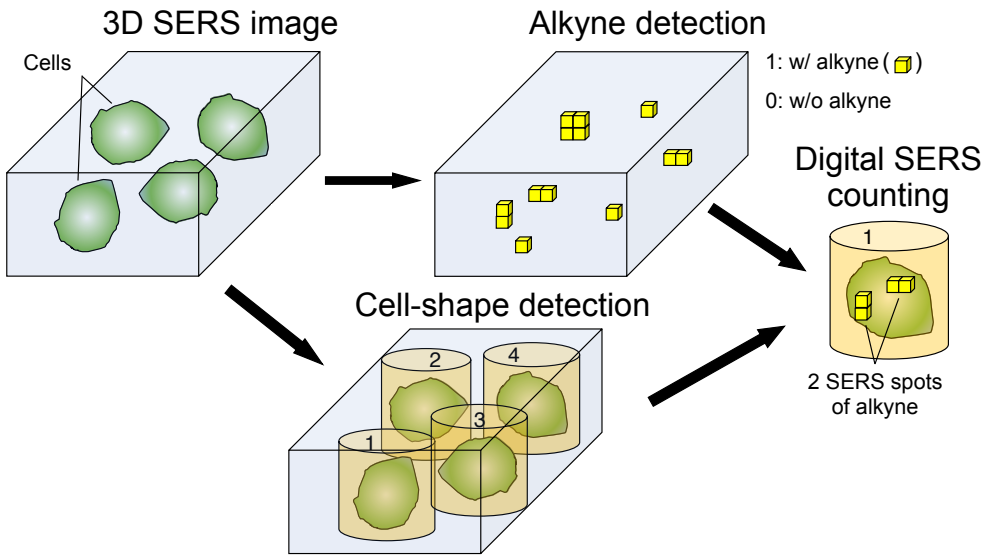

Figure 2.13. Scheme for digital SERS counting to obtain the number of SERS spots of alkynes in each cell. Each voxel of the SERS image was replaced with 1 if the spectrum had the alkyne signal. Reprinted with permission from ref.[92] Copyright 2020 American Chemical Society.

uptake.

I investigated how the temporal variation of SERS spots changes depending on the administration drug concentrations. First, I measured time-lapse 3D SERS imaging with different drug concentrations (0, 1, 20, 50, and 100 μM), following the same procedure of Fig.2.10. The imaging was performed two to three times at each concentration to confirm reproducibility and increase the number of cells to be analyzed. Afterward, the digital SERS counting was performed to visualize the temporal behavior of drug uptake. Fig.2.17A shows the results of the analysis. I found a strong correlation between the temporal behavior of the SERS spots and the concentration. The higher the administration concentration, the faster the increase in the number of SERS spots detected within the cells. At 100 μM, the SERS signals were detected few minutes after the drug administration. Since more molecules were taken up at higher concentrations, the detection probability could also be higher, assuming that the number of SERS hotspots and nanoparticles was nearly constant during imaging. In contrast, at a 0 μM concentration, the number of SERS spots showing the alkyne peak was almost zero because no drug was administered. Fig.2.17B shows a linear relationship between the concentration of Alt-AOMK in the culturing medium and the number of SERS spots at the relatively steady-state (47 min after the drug administration). Although our SERS technique is currently not capable of absolute concentration quantification in living cells, the linearity of the measurements indicates its usefulness in detecting relative changes in intracellular drug concentration over time. I have shown here that the quantitative combination of SERS imaging and digital counting is a promising tool to visualize the temporal behavior of drug uptake under different chemical concentrations, which has been challenging to do with

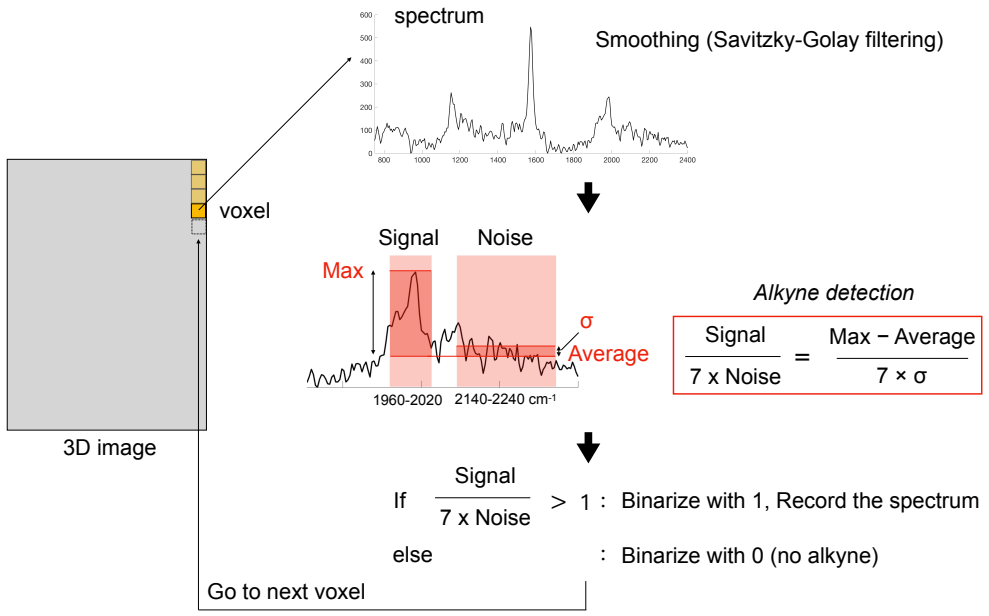

Figure 2.14. Processing flow for the alkyne peak detection. Reprinted with permission from ref.[92] Copyright 2020 American Chemical Society.

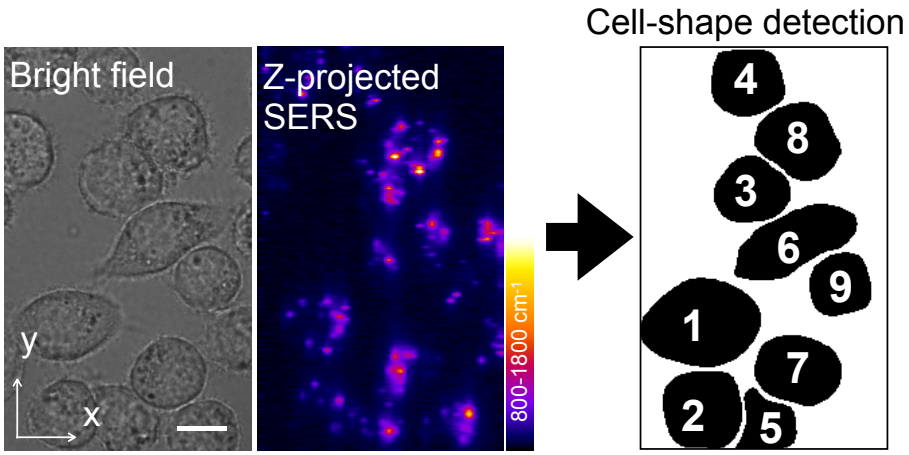

Figure 2.15. Cell-shape detection of the cells based on bright field image and 3D SERS image. Scale bar = 10 μm. Reprinted with permission from ref.[92] Copyright 2020 American Chemical Society.

conventional techniques.

Elucidation of the uptake pathway of Alt-AOMK into living cells

Although the strong correlation between drug concentration and temporal variation of the number of SERS signals was observed, it remains unclear how living cells take up Alt-AOMK. There are two possible pathways: one is permeabilization of the cell membrane. The other is via endocytosis. The cell membrane consists of two phospholipids, with their hydrophilic groups facing each other.

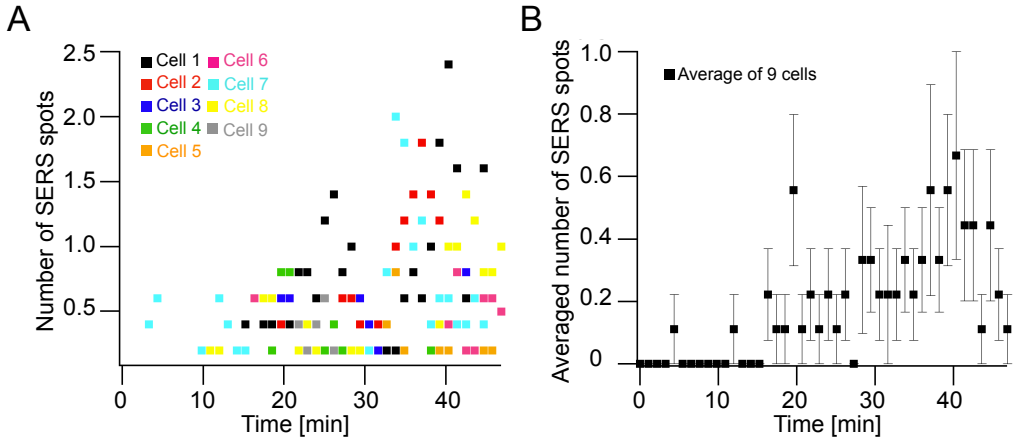

Figure 2.16. Temporal behaviors of the number of SERS spots in each cell. The administration concentration of Alt-AOMK was 20 μM. (A) Temporal behaviors of the number of SERS spots from each cell. (B) The average of the number of SERS spots from the nine cells (N = 9). Both plots show shows the value of temporal averaging over a window of 5 frames. The error bar is ± SE. Reprinted with permission from ref.[92] Copyright 2020 American Chemical Society.

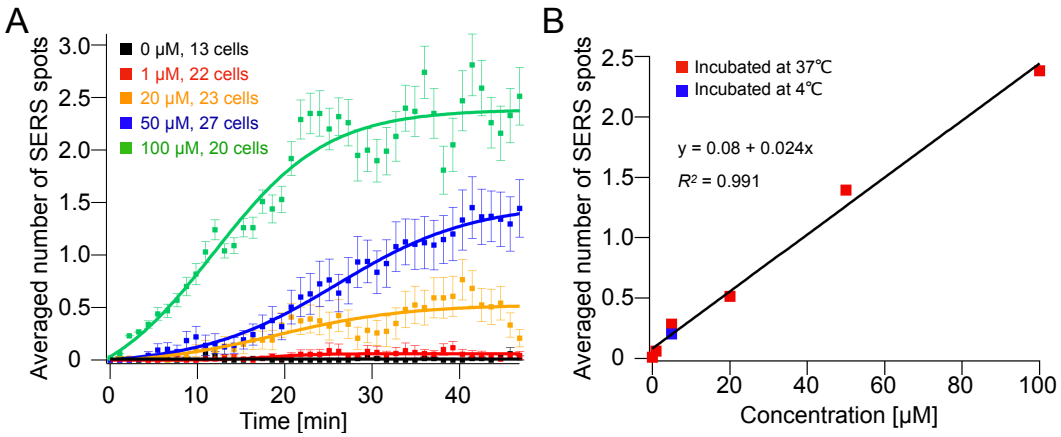

Figure 2.17. Digital SERS counting of alkynes at different administration concentrations. (A) Temporal behaviors of the number of SERS spots of alkynes at different concentrations. Squared dots at each color are the temporally averaged number of SERS spots with a window of 5 frames. Sigmoid fitting was applied to the dots for each concentration except 0 μM. Black line is the average of the dots at all times at 0 μM and indicates the background level. The error bar is ± SE (standard error). (B) Relationship between concentrations of Alt-AOMK and maximum values of sigmoid fitting on the temporal behaviors of the number of SERS spots. The values at 0, 1, 20, 50, and 100 μM were obtained from the result shown in (A). The other two values at 5 μM were obtained from the results shown in Fig.2.19. A linear fitting was performed using all plotted points. Reprinted with permission from ref.[92] Copyright 2020 American Chemical Society.

Therefore, the outside of the membrane is hydrophobic, and the inside is hydrophilic. Extracellular molecules can pass through the membrane due to the membrane's selectivity. For example, small non-polar molecules, CO_2 and N_2, can easily penetrate the membranes. Hydrophobic molecules with low molecular weight can also pass through the membrane and localize in the intracellular fluid. The membrane permeation is the passive transport of cells. Therefore, it does not consume the ATP energy

of the cell. The other pathway, endocytosis, is carried out by lysosomes. In endocytosis, ATP energy is consumed because it is active transport. By endocytosis, biological cells, such as macrophages, actively take up relatively large polar molecules, such as proteins or peptides, gold nanoparticles, and other nutrients. Alt-AOMK can be hydrophobic because it has one alkyne, three phenyl groups, and many double bonds. It has a molecular weight of 526 g/mol. This is a relatively low molecular weight for a drug molecule. Therefore, Alt-AOMK may be taken up into the cell by membrane permeation.

To determine which pathway is dominant for drug uptake, I blocked either pathway, administered the drug molecule to the cells, and performed 3D SERS imaging. The function of endocytosis can be easily blocked by using inhibitors.[107] Low-temperature incubation at 4 ℃ for 1-2 hours is also found to be an easier way to do that without the drug addition.[107, 108, 109, 110] All endocytotic pathways can be inactivated under the condition. In my experiments, I inhibited endocytosis by incubating living cells at 4 ℃ before the drug administration.

At first, I investigated the effect of the 4 ℃ incubation on endocytosis using 50 nm gold nanoparticles as markers for endocytosis inhibition. I prepared two types of cells incubated at 37 ℃ and 4 ℃ with gold nanoparticles for 2 h, respectively. The laser intensity on sample was 2.62 mW/μm^2. The exposure time per line was 50 ms. The size of imaged volume was 50x81x15 μm^3. Forty and 10 lines were exposed in the x- and z- directions. Acquisition time per volume was 21.8 sec. Fig.2.18A shows bright-field images and z-projected 3D SERS images of the cells incubated at 37 ℃. Many SERS hotspots of intracellular molecules were detected. All of the SERS spectra from the selected pixels have strong SERS peaks in the fingerprint regions of the cells (Fig.2.18B). This suggests that many gold nanoparticles were taken up into cells during 2 h incubation at 37 ℃. Fig.2.18C shows bright-field images and z-projected 3D SERS images of the cells incubated at 4 ℃. Compared with cells incubated at 37 ℃, No SERS signal was observed from the cells. These results suggest that gold nanoparticles could not enter the cells. As previously reported, I confirmed that low-temperature incubation with 4 ℃ can effectively inhibit the endocytosis of living cells.

Then, I performed time-lapse 3D SERS imaging of drug uptake of the cells incubated at 37 and 4 ℃. The gold nanoparticles were introduced via endocytosis as previously described at 37 ℃ before the SERS measurement. Then, I incubated the cells at 4 ℃ for 90 min before the SERS measurement. As a comparison, I also prepared a normal cell sample without endocytosis inhibition. The drug concentration in this measurement was 5 μM. Fig.2.19 shows the temporal behaviors of the SERS spots under the two different temperature conditions. Regardless of the endocytosis functions, the uptake trend based on the number of SERS spots of alkyne was almost identical, indicating that the speed of drug uptake did not show a strong dependence on the temperature. Also, the number of SERS spots at 4 ℃ were well fitted on the linear calibration curve (blue dot) as shown in Fig.2.17. Based on these results and because Alt-AOMK and lipid bilayer are both hydrophobic molecules, the cells may uptake Alt-AOMK through passive transport such as cellular membrane penetration, not by endocytosis transport.

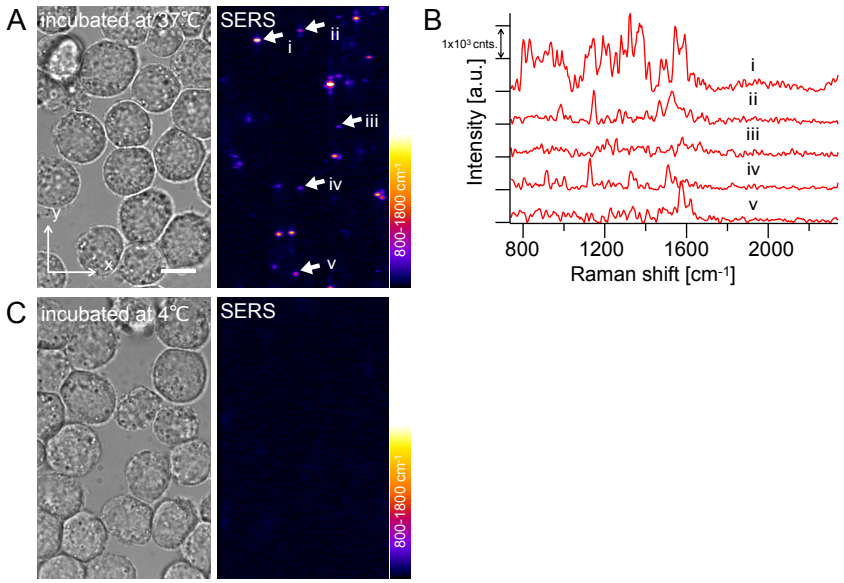

Figure 2.18. Three-dimensional SERS imaging of living macrophages with gold nanoparticles incubated at 37 ℃ and 4 ℃. (A) Bright field image and z-projected 2D SERS image of the cells incubated at 37 ℃ for 2 h with gold nanoparticles prior to the measurement. Scale bar = 10 μm. (B) SERS spectra from the signals indicated as white arrows in (A). Raman peaks from endogenous molecules were observed. (C) Bright field image and z-projected 2D SERS image of the cells incubated at 4 ℃ for 2 h with gold nanoparticles prior to the measurement. Reprinted with permission from ref.[92] Copyright 2020 American Chemical Society.

Discussion and Conclusion

In this chapter, I introduced a method for observing the drug uptake and dynamics in living cells with alkyne-tag SERS microscopy combined with the digital SERS counting method. A unique alkyne signal in the silent region allowed identifying the spatiotemporal signature of target molecules without overlapping with endogenous molecules. Several conditions should be satisfied to detect alkyne-tagged small molecules by SERS: (1) Small-molecule drugs show strong SERS signal of alkynes on SERS substrate. (2) The small molecule can be taken up by the cells. (3) After that, the molecule can colocalize with the nanoparticle aggregation. In the SERS spectrum, the alkyne peak showed a peak shift of 140 cm^{-1} due to its chemisorption on the gold surface. This can be one of the strongest pieces of evidence for the intracellular colocalization of Alt-AOMK and nanoparticles (see also Appendix). The surface modification of gold nanoparticles and the incubation time can change the localization and number of SERS hotspots. Since these parameters affect the probability of detection, they need to be carefully adjusted depending on the cell model and drug type. In the present measurements, living cells and gold nanoparticles were incubated together for about 16 h. In this time scale, gold nanoparticles can form aggregations inside lysosomes.[99] During the measurements, drastic change in the SERS intensity of endogenous molecules was not observed; thus, the number of gold nanoparticles

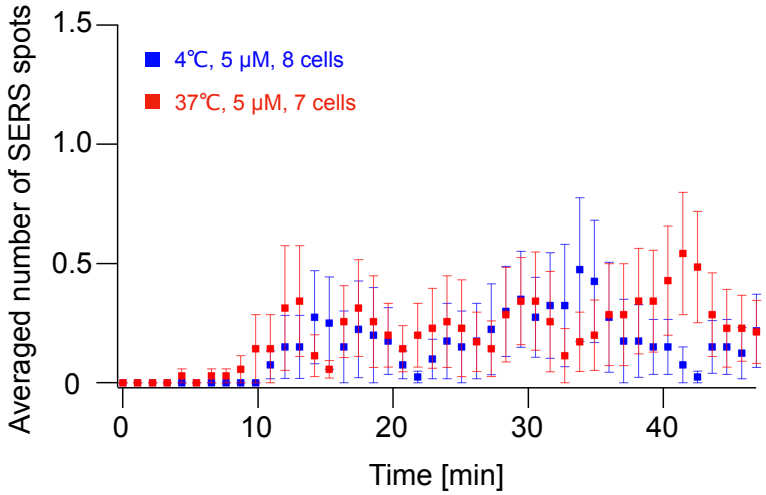

Figure 2.19. Temporal behaviors of the number of SERS spots of living macrophages incubated at 37 (red plot) and 4 ℃ (blue plot). The error bar is ± SE. This plot shows the value of temporal averaging over a window of 5 frames. Reprinted with permission from ref.[92] Copyright 2020 American Chemical Society.

was not expected to change significantly. Hence, the increase in SERS signals of alkynes observed through the time-lapse 3D SERS imaging was mainly due to the uptake of small-molecule drugs into the cells.

I also proposed the use of digital SERS counting to statistically visualize the rise of the number of SERS spots of alkyne over time. The method was proposed to quantify low concentration analytes at the single-molecule level.[105] However, in the present experiments, I could not confirm whether the SERS signals in the cells originated from single molecules or not. Therefore, the number of SERS spots obtained by digital SERS counting cannot be used for the absolute concentration quantification of drugs in living cells. However, as I showed in Fig.2.17, the number of SERS spots has a linear relationship with the administration concentrations. Thus, it can monitor the relative change of drug concentrations within the cells. The digital SERS counting combined with 3D visualization can be a strong tool to analyze and evaluate the drug uptake efficiency under different physical and chemical environments.

Besides the present study, there is an increasing number of studies on SERS detection of various alkyne-tagged molecules. Therefore, the proposed technique can be widely applicable for other cell lines and small-molecule drugs to study their dynamics. For example, Kennedy et al. used alkyne-functionalized silver nanoparticles to visualize receptor proteins on the surface of H9c2 cells.[87] Ardini et al. observed alkyne-tagged dopamines with silver nanoparticles in NIH-3T3 cells,[89] and Li et al. developed a series of alkyne-tag SERS probes for multiplex SERS imaging in MCF-7 cells.[90] All the related works focused on synthesizing multiplex SERS tags that can selectively bind to specific proteins and avoid spectral overlap with biomolecules. However, in this study, I used pre-incorporated bare gold nanoparticles in living cells as reporters that can tell the arrival of incoming alkyne-tagged

small molecules. In this sense, the present study has broadened the possibility of SERS toward quantitative drug dynamics.

The uptake efficiency of nanoparticles can vary depending on the cell types. In such case, however, there are well-established methods, such as surface modifications of nanoparticles[111] and electroporations[112] through cellular membrane, to improve both nanoparticle uptake rate and localization.

It would also be interesting to determine how much of the drug interacts with the protein and its effect on the SERS spectrum after the interaction. For this investigation, it might be better to start with SERS measurements with and without CatB inhibition by Alt-AOMK on SERS substrates,[93] rather than within complex cellular states. Also, using activatable Raman tags, in which the alkyne peak position shifts, disappears, or appears[113] as the drug interacts with the target molecule, may help to understand this problem and visualize the drug-molecule interaction process.

Appendix

Gold nanoparticles

Gold nanoparticles with 50 nm (EMGC50) used in this study were purchased from BBI Solutions, UK. Based on the specification sheet, the mean size of the nanoparticles was from 47 to 53 nm with a coefficient of variance of less than 8%. I measured the extinction spectrum of the nanoparticles by UV-vis spectroscopy (Multiskan GO, Thermo Fisher Scientific). Fig.2.20 shows the result. The extinction spectrum has a broad peak at around 535 nm. In all SERS measurements, I used a 660 nm laser. The wavelength is slightly away from the resonant wavelength of 535 nm. However, this allowed to generate SERS signal large enough from the aggregated gold nanoparticles in lysosomes due to the red-shift of the absorption peak of gold nanoparticles.

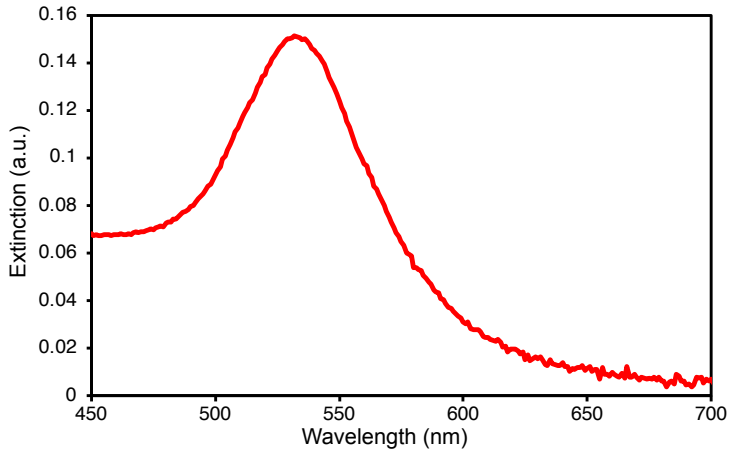

Figure 2.20. Extinction spectrum of gold nanoparticles with 50 nm diameter. Reprinted with permission from ref.[92] Copyright 2020 American Chemical Society.

SERS spectroscopy of Alt-AOMK on a gold nanoparticles-modified glass substrate

SERS spectrum of Alt-AOMK was determined with the following experiments. As described in Fig.2.21(a), I prepared a gold-nanoparticles-modified glass substrate with 50 nm diameter. The substrate was placed on a microscope stage. DMEM 5 μL without Alt-AOMK was dropped onto the substrate, and SERS imaging was performed with the exposure time of 50 ms and an excitation intensity of 0.53 mW/μm^2. After the imaging, DMEM 5 μL with Alt-AOMK 40 μM was added to the solution, so the final concentration of Alt-AOMK was 20 μM. SERS imaging was performed again with the same field of view and imaging parameters. SERS spectra before and after the Alt-AOMK addition from the same SERS hotspot were compared (Fig.2.21(b)). The black and red spectra are the SERS spectra before and after the Alt-AOMK addition, without post-processing. The red SERS spectrum shows three unique SERS peaks, which were not observed in the black spectrum without

Alt-AOMK. The two peaks around 1160 and 1590 cm^{-1} may be derived from the enhanced Raman signal of aromatic-ring vibrational modes of Alt-AOMK. It also shows a broad peak at 1960-2010 cm^{-1}, which can be assigned to the metal-alkyne conjugated mode. The downshift of the alkyne peak has been reported in a number of related papers.[87, 93, 89, 114, 115, 116]

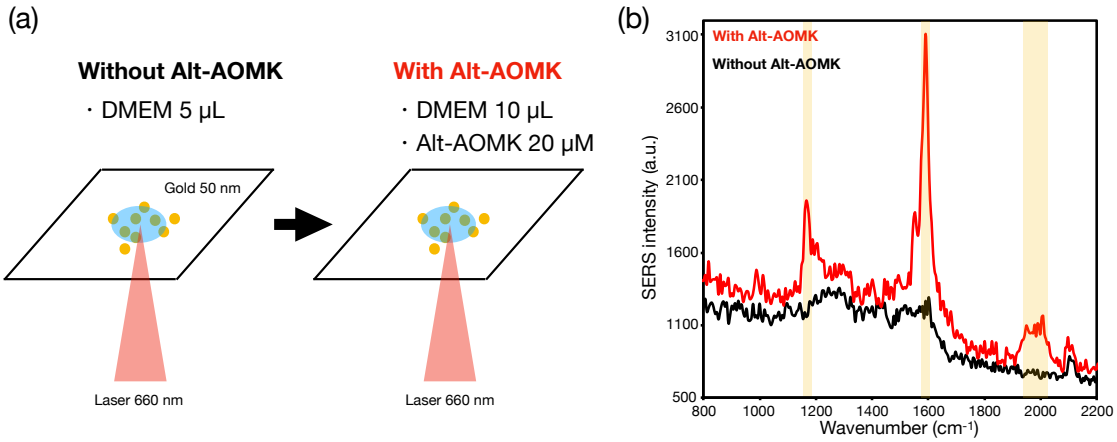

Figure 2.21. SERS spectroscopy of Alt-AOMK. (a) Sample preparation for SERS measurements with DMEM solutions with and without Alt-AOMK. (b) SERS spectra from the same SERS hotspot before and after Alt-AOMK addition onto the substrate.

In 2013, Maity et al. investigated the binding motifs between alkynes and gold surface.[115] There can be four different binding motifs of alkynes to a gold and silver surface as shown in Fig.2.22. They synthesized alkyne-protected gold nanoparticles using three types of ligands, 1-octyne, phenylacetylene, and 9-ethynyl-phenanthrene. FTIR spectra of the nanoparticles from 1000-4000 cm^{-1} were compared with those of their corresponding ligands (i.e., without gold nanoparticles). In the free ligands (without gold nanoparticles), a sharp Raman peak was observed at around 3300 cm^{-1}. In contrast, it was not observed in all the nanoparticles modified with the ligands, indicating the dissociation of the terminal C-H bond of the ligands. This result ruled out the possibility of intact types of bindings. Also, all the nanoparticles showed a down-shift of the alkyne stretching mode from 2100-2120 to -2000 cm^{-1}, which was consistent with our results (Fig.2.3, 2.21). In FTIR spectra,[115] the -C=C- stretching of the aromatic ring at 1500-1600 cm^{-1} appeared in both the free ligands and nanoparticles, which was also observed in our SERS measurements. From these results, the interaction between the aromatic ring close to the alkynes and gold surface is insignificant compared to the alkynes. Thus, the binding can be an upright configuration, not flat-lying, in the dehydrogenated model.[115] This binding efficiency can be affected by the pH value of the surrounding medium,[115, 87] indicating that the binding can occur via deprotonation of alkynes.

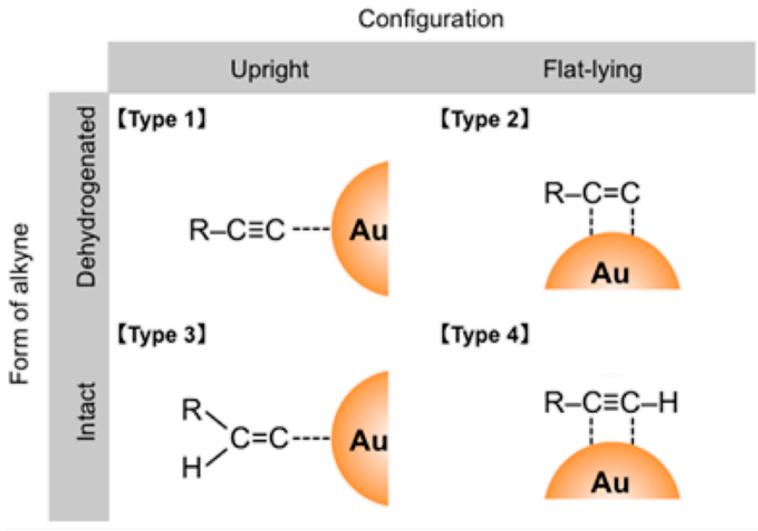

Figure 2.22. Possible binding motifs of alkyne-Au. Form of alkyne is (a) dehydrogenated or (b) intact. Each case has upright or flat-lying configurations. Reprinted with permission from ref.[115] Copyright 2013 American Chemical Society.

Time-lapse 2D SERS imaging without Alt-AOMK

This experiment is a control experiment of Fig.2.7. I performed time-lapse 2D SERS imaging with gold nanoparticles but without Alt-AOMK to confirm that the green SERS spots appear in the presence of Alt-AOMK conditions. Fig.2.23 shows a bright-field image of the cells and corresponding SERS images with different time points. The SERS images were reconstructed with two spectral regions; the red color is the average Raman intensity from 800 to 1800 cm^{-1} containing Raman peaks of endogenous molecules, and the green color is the average Raman intensity from 1960 to 2010 cm^{-1} assigned to the alkyne peak. As expected, no SERS signal of alkynes was observed, but only from the fingerprint regions. In the last frame, a single green spot was observed. The SERS spectrum from this spot contained a sharp peak around 1990 cm^{-1}, but the overall spectral shape was not similar to a typical Alt-AOMK spectrum with two strong peaks around 1160 and 1590 cm^{-1} (Fig.2.21). The cause of this is unknown, but it may be due to some molecular contamination.

Investigating the effects of excitation intensity on SERS signal blinking of alkynes

I have found that SERS signal intensities of alkynes (Alt-AOMK) frequently blinked in living cells in 2D and 3D imaging. There can be several reasons for this effect. One is the inherent SERS properties such as fluctuation of SERS hotspots, enhancement factor, and motion of molecules itself, etc. The other is the breaking of chemical interaction between alkynes and gold nanoparticles by the external force such as heat by laser irradiation. I investigated the origin of this effect with the following experiments and analysis.

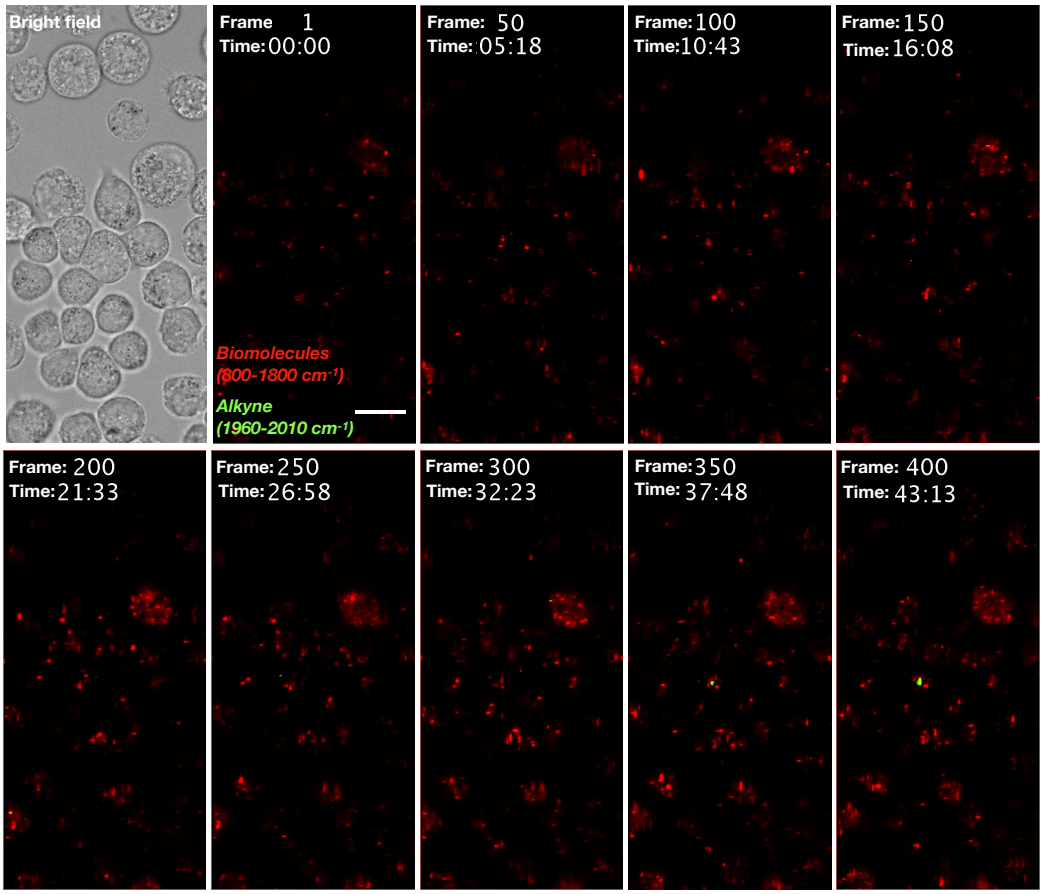

Figure 2.23. Time-lapse 2D SERS imaging of living cells without Alt-AOMK. Scale bar = 20 μm.

I investigated how the temporal behavior of SERS blinking vary depending on the laser excitation intensity. Fig.2.24 shows the procedure of the experiments. (1) I prepared 4 mas-coat glasses with a surface modification of 50 nm gold nanoparticles. Alt-AOMK 10 μM in water 2 μL was dropped onto the glasses. Waiting for 5 min, I performed 2D time-lapse SERS observation for about 6 min with an excitation intensity of 3.42 mW/μm^2. The imaging area was 50x82 μm, similar to the 2D and 3D SERS imaging of living cells. The acquisition time was 5.4 s/frame with 100 scanning lines in the x-direction and 50 ms of exposure time. I repeated the imaging with new samples with the excitation intensities of 2.10, 1.05, and 0.53 mW/μm^2. an excitation intensity used for 2D and 3D SERS imaging of alkynes in living cells was 1.3 and 0.78 mW/μm^2, respectively. (2) After the imaging, I obtained 4D SERS datasets with spatial information of xy, spectral information, and temporal information. I chose 5 different positions of xy for each dataset and (3) extracted the spectra to further analysis. (4) I calculated the alkyne peak intensity for each frame to know how the SERS signals of alkynes fluctuate with different time points and different excitation intensities. (5) I performed an autocorrelation analysis of the calculation results to investigate the effect of excitation intensity on the blinking frequency of the SERS signal. Autocorrelation is a powerful analysis technique for investigating periodic signals

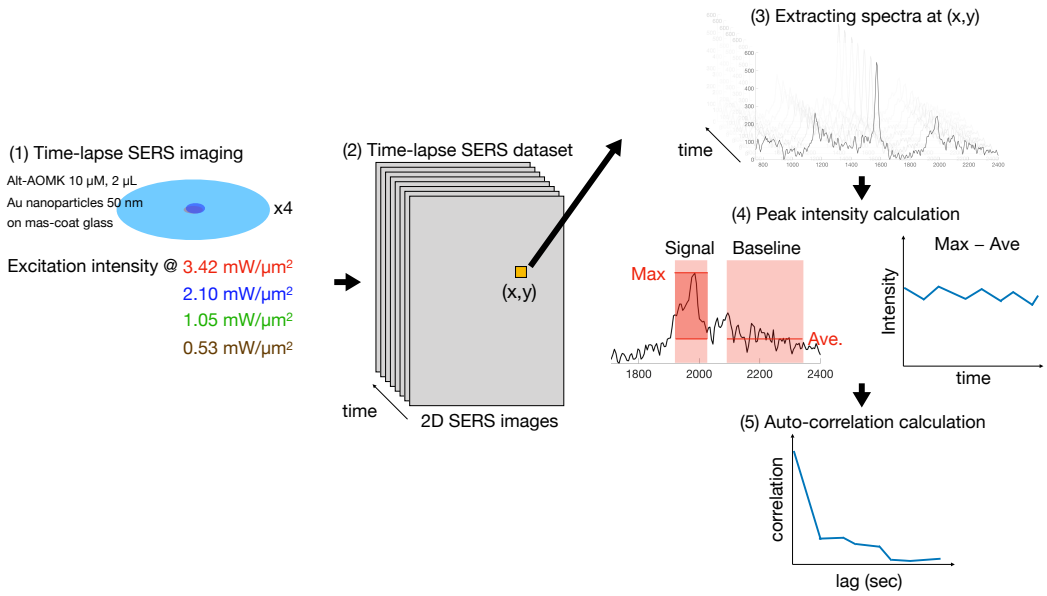

Figure 2.24. Analysis procedure of SERS signal blinking by autocorrelation.

buried in noise. Fig.2.25 shows the results of the autocorrelation analysis. SERS datasets of 5 different positions were analyzed by autocorrelation for each excitation intensity. Locations with high correlation values indicate a high correlation between the original waveform (temporal fluctuation of SERS signal intensity of alkynes) and the waveform displaced by a certain amount of time (lag). Overall, the highest correlation value was observed when the lag was zero, decreasing with time. The shape and peak of the autocorrelation function did not differ significantly depending on the intensity of the excitation light. This may suggest that the effect of laser excitation light intensity on the blinking of the SERS signal of alkynes is small under the current imaging conditions of 2D and 3D SERS imaging of living cells. This blinking may not be due to such external effects of laser excitation but high possibility due to inherent SERS effects such as diffusion of the molecule, variation in the position of the SERS hotspot, and distance between the molecule and the gold surface. However, these physical phenomena are difficult to analyze and determine with the current setup.

Are cells still alive after 4 ℃ incubation for 2 h?

To inhibit the endocytosis function of living cells, I used low temperature (4 ℃) incubation for about 2 h. I confirmed the method worked well based on the SERS measurements. But, under this condition, can macrophage cells survive? I investigated whether cells were still alive during 4 ℃ incubation with the following simple experiments. At first, the cells were incubated for 2 h at 4 ℃ (placed into a refrigerator) to inhibit the endocytosis pathways. Gold nanoparticles (GNPs) were also introduced. Fig.2.26(a) shows a dark-field image of the cells after 2 h incubation. The cells were washed by PBS to remove GNPs in the medium before the observation. I found no aggregation of GNPs as endocytosis

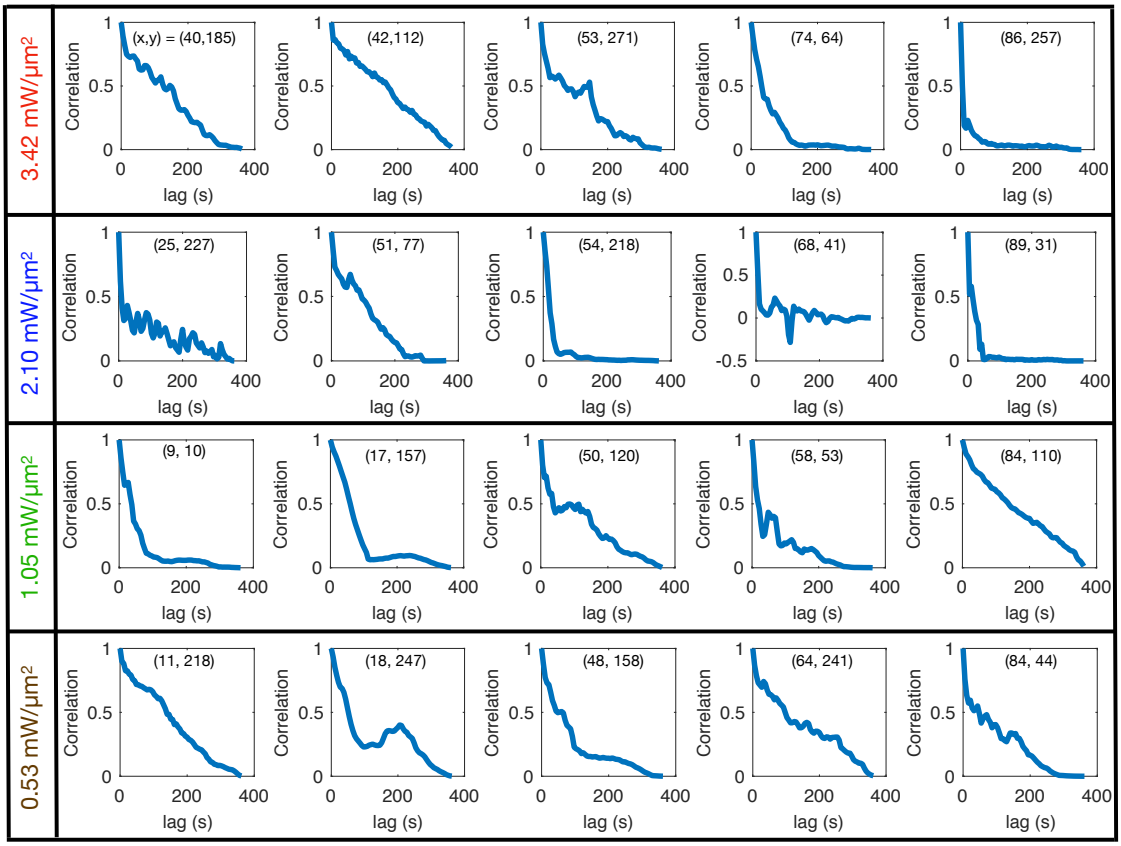

Figure 2.25. Autocorrelation analysis of SERS spectra of alkyne blinking with different excitation intensities.

was blocked. Then, the same cells (dish) were again incubated at 37 ℃, 5% CO_2 for 5 h with newly introduced GNPs. Fig.2.26(b) shows a dark-field image of the cells after 5 h incubation. A scattering of aggregated GNPS in the cells was observed. This indicates that the endocytosis of the cells was re-started by incubation at 37 ℃. Since this process is an active pathway that consumes energy, the cells were considered to be alive after 2 h of incubation at 4 ℃.

SERS spectroscopy of alkyne-tagged cell-penetrating peptides (CPP)

Cell-penetrating peptides (CPP) is recently getting attention from biomedical researchers due to their strong potential for drug-delivery system (DDS). CPP can bring the attached molecules into living cells through cellular permeation. Despite its importance, direct visualization of CPP during the uptake process has been challenging because of the limited imaging tool. In 2021, Ida et al. visualized morphological alteration of cellular membrane resulting from interaction with CPP by using scanning ion conductance microscopy and spinning disk confocal microscopy.[117] SERS nano-tags modified with CPP are also invented to monitor pH changes during cell cycle.[118] To demonstrate the applicability of our alkyne-tag SERS method to visualize the uptake of CPP itself, I designed alkyne-tagged CPP and performed SERS spectroscopy of the molecule. Among various kinds of CPP, I focused on

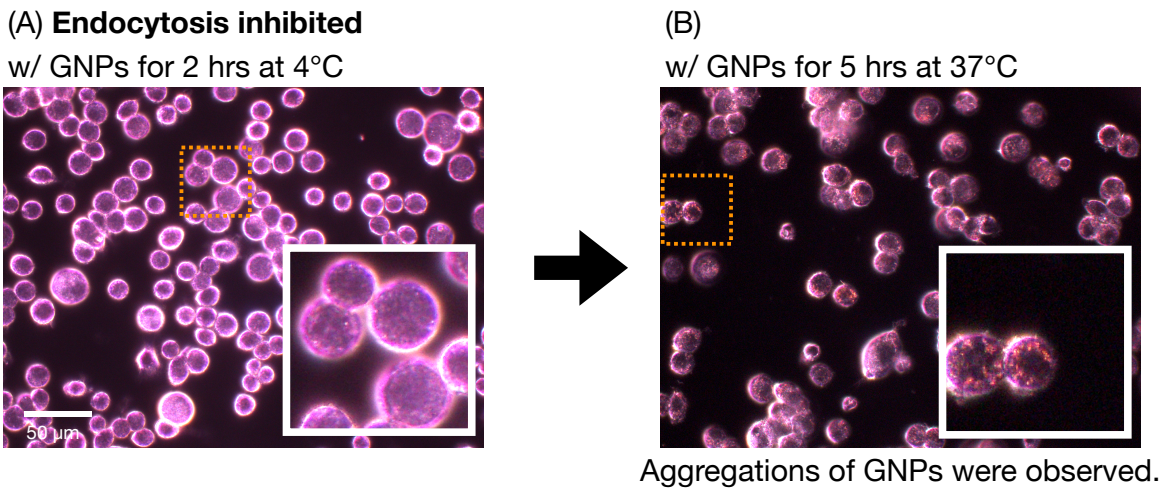

Figure 2.26. Dark-field observation of macrophage cells. (A) Dark-field image of the cells incubated for 2 h at 4 °C with gold nanoparticles (GNPs) 50 nm. Scale bar is 50 μm. (B) Dark-field image of the same cells as (A) incubated for 5 h at 37 °C with GNPs after endocytosis inhibition by 4 °C incubation.

HIV-1 Tat (positions 48-60) peptide (N-GRKKRRQRRRPPQ-C),[119, 120, 121] a first-discovered CPP in 1989. Tat-peptide can localize in the lysosome and nucleus after being taken up into cells. I designed an alkyne-tagged Tat-peptide (N-GRKKRRQRRRPPQ+Pra-C) (Fig.2.27(b)), and from now on called as Alt-Tat. Pra represents an amino acid L-Propargylglycine that has one terminal alkyne (Fig.2.27(a)). To confirm whether the alkyne signal can be detected with SERS, I performed SERS spectroscopy of Alt-Tat peptide with gold nanoparticles. SERS substrate was prepared by surface modification of glass substrate with gold nanoparticles 50 nm. Alt-Tat 2 mM in water 2 μL was dropped onto the substrate, and SERS measurements were employed with the exposure time of 50 ms and an excitation intensity of 0.53 mW/μm^2. Fig.2.27(c) shows representative SERS spectra obtained from different positions of a 2D SERS intensity map. I found no alkyne peak from the measurements at 1960-2010 cm^{-1}. A sharp peak at around 2115 cm^{-1} was not from alkynes but assumed to be contaminations such as CN. The same result was observed with a different set of samples. The main reason for not detecting the SERS signal of alkynes from this molecule is under investigation. Looking at the other types of molecules that were used for alkyne-tag SERS applications,[87, 90, 88] as well as Alt-AOMK,[93] benzene-ring attached to alkynes might play an important role to assist the SERS signal generation of alkynes. The molecular design of Alt-Tat should be further refined to gain the SERS signal of alkynes based on this knowledge.

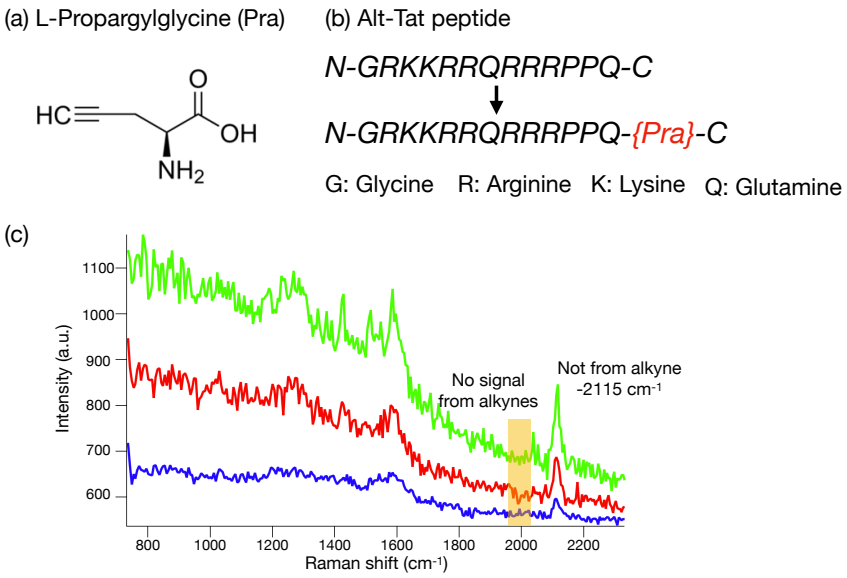

Figure 2.27. Molecular structures of (a) L-Propargylglycine and (b) alkyne-tagged Tat peptide. (c) Representative SERS spectra of Alt-Tat from gold nanoparticle SERS substrate.

Reference

71) Tarik F Massoud and Sanjiv S Gambhir. Molecular imaging in living subjects: seeing fundamental biological processes in a new light. *Genes Dev*, 17(5):545–580, Mar 2003.

72) Jürgen K. Willmann, Nicholas van Bruggen, Ludger M. Dinkelborg, and Sanjiv S. Gambhir. Molecular imaging in drug development. *Nature Reviews Drug Discovery*, 7(7):591–607, 2008.

73) Michael D. Best. Click Chemistry and Bioorthogonal Reactions: Unprecedented Selectivity in the Labeling of Biological Molecules. *Biochemistry*, 48(28):6571–6584, 2009. PMID: 19485420.

74) Tatiana Cañeque, Sebastian Müller, and Raphaël Rodriguez. Visualizing biologically active small molecules in cells using click chemistry. *Nature Reviews Chemistry*, 2(9):202–215, 2018.

75) Hiroyuki Yamakoshi, Kosuke Dodo, Masaya Okada, Jun Ando, Almar Palonpon, Katsumasa Fujita, Satoshi Kawata, and Mikiko Sodeoka. Imaging of EdU, an Alkyne-Tagged Cell Proliferation Probe, by Raman Microscopy. *Journal of the American Chemical Society*, 133(16):6102–6105, 2011. PMID: 21443184.

76) Hiroyuki Yamakoshi, Kosuke Dodo, Almar Palonpon, Jun Ando, Katsumasa Fujita, Satoshi Kawata, and Mikiko Sodeoka. Alkyne-Tag Raman Imaging for Visualization of Mobile Small Molecules in Live Cells. *Journal of the American Chemical Society*, 134(51):20681–20689, 2012. PMID: 23198907.

77) Samir F. El-Mashtoly, Dennis Petersen, Hesham K. Yosef, Axel Mosig, Anke Reinacher-Schick, Carsten Kötting, and Klaus Gerwert. Label-free imaging of drug distribution and metabolism in colon cancer cells by Raman microscopy. *Analyst*, 139:1155–1161, 2014.

78) Dan Fu, Jing Zhou, Wenjing Suzanne Zhu, Paul W. Manley, Y. Karen Wang, Tami Hood, Andrew Wylie, and X. Sunney Xie. Imaging the intracellular distribution of tyrosine kinase inhibitors in living cells with quantitative hyperspectral stimulated Raman scattering. *Nature Chemistry*, 6(7):614–622, 2014.

79) Lu Wei, Fanghao Hu, Yihui Shen, Zhixing Chen, Yong Yu, Chih-Chun Lin, Meng C Wang, and Wei Min. Live-cell imaging of alkyne-tagged small biomolecules by stimulated Raman scattering. *Nature Methods*, 11(4):410–412, 2014.

80) William J. Tipping, Martin Lee, Alan Serrels, Valerie G. Brunton, and Alison N. Hulme. Imaging drug uptake by bioorthogonal stimulated Raman scattering microscopy. *Chem. Sci.*, 8:5606–5615, 2017.

81) Fanghao Hu, Chen Zeng, Rong Long, Yupeng Miao, Lu Wei, Qizhi Xu, and Wei Min. Supermultiplexed optical imaging and barcoding with engineered polyynes. *Nature Methods*, 15(3):194–200, 2018.
82) Kristel Sepp, Martin Lee, Marie T. J. Bluntzer, G. Vignir Helgason, Alison N. Hulme, and Valerie G. Brunton. Utilizing Stimulated Raman Scattering Microscopy To Study Intracellular Distribution of Label-Free Ponatinib in Live Cells. *Journal of Medicinal Chemistry*, 63(5):2028–2034, 2020. PMID: 31829628.
83) Katrin Kneipp, Abigail S. Haka, Harald Kneipp, Kamran Badizadegan, Noriko Yoshizawa, Charles Boone, Karen E. Shafer-Peltier, Jason T. Motz, Ramachandra R. Dasari, and Michael S. Feld. Surface-Enhanced Raman Spectroscopy in Single Living Cells Using Gold Nanoparticles. *Applied Spectroscopy*, 56(2):150–154, 2002.
84) Janina Kneipp, Harald Kneipp, Margaret McLaughlin, Dennis Brown, and Katrin Kneipp. In Vivo Molecular Probing of Cellular Compartments with Gold Nanoparticles and Nanoaggregates. *Nano Letters*, 6(10):2225–2231, 2006. PMID: 17034088.
85) Katsumasa Fujita, Sawako Ishitobi, Keisaku Hamada, Nicholas Isaac Smith, Atsushi Taguchi, Yasushi Inouye, and Satoshi Kawata. Time-resolved observation of surface-enhanced Raman scattering from gold nanoparticles during transport through a living cell. *Journal of Biomedical Optics*, 14(2):1 – 7, 2009.
86) Jun Ando, Katsumasa Fujita, Nicholas I. Smith, and Satoshi Kawata. Dynamic SERS imaging of Cellular Transport Pathways with Endocytosed Gold Nanoparticles. *Nano Letters*, 11(12):5344–5348, 2011. PMID: 22059676.
87) David C. Kennedy, Kelly A. Hoop, Li-Lin Tay, and John Paul Pezacki. Development of nanoparticle probes for multiplex SERS imaging of cell surface proteins. *Nanoscale*, 2:1413–1416, 2010.
88) Yong Chen, Jia-Qiang Ren, Xia-Guang Zhang, De-Yin Wu, Ai-Guo Shen, and Ji-Ming Hu. Alkyne-Modulated Surface-Enhanced Raman Scattering-Palette for Optical Interference-Free and Multiplex Cellular Imagingcattering-Palette for Optical Interference-Free and Multiplex Cellular Imaging. *Analytical Chemistry*, 88(12):6115–6119, 2016. PMID: 27223333.
89) Matteo Ardini, Jian-An Huang, Carlos S. Sánchez, Mansoureh Z. Mousavi, Valeria Caprettini, Nicolò Maccaferri, Giovanni Melle, Giulia Bruno, Lea Pasquale, Denis Garoli, and Francesco De Angelis. Live Intracellular Biorthogonal Imaging by Surface Enhanced Raman Spectroscopy using Alkyne-Silver Nanoparticles Clusters. *Scientific Reports*, 8(1):12652, 2018.
90) Mingmin Li, Jianzhen Wu, Mengtian Ma, Zhichao Feng, Ze Mi, Pengfei Rong, and Dingbin Liu. Alkyne- and Nitrile-Anchored Gold Nanoparticles for Multiplex SERS Imaging of Biomarkers in Cancer Cells and Tissues. *Nanotheranostics*, 3:113–119, 2019.
91) Anna Huefner, Wei-Li Kuan, Karin H. Müller, Jeremy N. Skepper, Roger A. Barker, and Sumeet Mahajan. Characterization and Visualization of Vesicles in the Endo-Lysosomal Pathway with Surface-Enhanced Raman Spectroscopy and Chemometrics. *ACS Nano*, 10(1):307–316, 2016. PMID: 26649752.
92) Kota Koike, Kazuki Bando, Jun Ando, Hiroyuki Yamakoshi, Naoki Terayama, Kosuke Dodo, Nicholas Isaac Smith, Mikiko Sodeoka, and Katsumasa Fujita. Quantitative drug dynamics visualized by alkyne-tagged plasmonic-enhanced raman microscopy. *ACS Nano*, 14(11):15032–15041, 2020. PMID: 33079538.
93) Jun Ando, Miwako Asanuma, Kosuke Dodo, Hiroyuki Yamakoshi, Satoshi Kawata, Katsumasa Fujita, and Mikiko Sodeoka. Alkyne-Tag SERS Screening and Identification of Small-Molecule-Binding Sites in Protein. *Journal of the American Chemical Society*, 138(42):13901–13910, 2016.
94) Daisuke Kato, Kelly M Boatright, Alicia B Berger, Tamim Nazif, Galia Blum, Ciara Ryan, Kareem A H Chehade, Guy S Salvesen, and Matthew Bogyo. Activity-based probes that target diverse cysteine protease families. *Nature Chemical Biology*, 1(1):33–38, 2005.
95) Mary L. Patterson and Michael J. Weaver. Surface-enhanced Raman spectroscopy as a probe of adsorbate-surface bonding: simple alkenes and alkynes adsorbed at gold electrodes. *The Journal of Physical Chemistry*, 89(23):5046–5051, 1985.
96) K. Manzel, W. Schulze, and M. Moskvits. Surface-enhanced Raman spectra of C2H2 and C2H4 adsorbed on silver colloid. *Chemical Physics Letters*, 85(2):183–186, 1982.
97) Suzanne P. M. Lutgens, Kitty B. J. M. Cleutjens, Mat J. A. P. Daemen, and Sylvia Heeneman. Cathepsin cysteine proteases in cardiovascular disease. *The FASEB Journal*, 21(12):3029–3041, 2007.
98) Yuhei Mizunoe, Masaki Kobayashi, Shunsuke Hoshino, Ryoma Tagawa, Rei Itagawa, Ayana

Hoshino, Naoyuki Okita, Yuka Sudo, Yoshimi Nakagawa, Hitoshi Shimano, and Yoshikazu Higami. Cathepsin B overexpression induces degradation of perilipin 1 to cause lipid metabolism dysfunction in adipocytes. *Scientific Reports*, 10(1):634, 2020.

99) Mengmeng Liu, Qian Li, Le Liang, Jiang Li, Kun Wang, Jiajun Li, Min Lv, Nan Chen, Haiyun Song, Joon Lee, Jiye Shi, Lihua Wang, Ratnesh Lal, and Chunhai Fan. Real-time visualization of clustering and intracellular transport of gold nanoparticles by correlative imaging. *Nature Communications*, 8(1):15646, 2017.

100) B. Devika Chithrani, Arezou A. Ghazani, and Warren C. W. Chan. Determining the Size and Shape Dependence of Gold Nanoparticle Uptake into Mammalian Cells. *Nano Letters*, 6(4):662–668, 2006. PMID: 16608261.

101) Pablo G. Etchegoin and Eric C. Le Ru. Resolving Single Molecules in Surface-Enhanced Raman Scattering within the Inhomogeneous Broadening of Raman Peaks. *Analytical Chemistry*, 82(7):2888–2892, 2010. PMID: 20210327.

102) Addison R. L. Marshall, Jamie Stokes, Francesco N. Viscomi, John E. Proctor, Johannes Gierschner, Jean-Sebastien G. Bouillard, and Ali M. Adawi. Determining molecular orientation via single molecule SERS in a plasmonic nano-gap. *Nanoscale*, 9:17415–17421, 2017.

103) Nathan C. Lindquist, Carlos Diego L. de Albuquerque, Regivaldo G. Sobral-Filho, Irina Paci, and Alexandre G. Brolo. High-speed imaging of surface-enhanced Raman scattering fluctuations from individual nanoparticles. *Nature Nanotechnology*, 14(10):981–987, 2019.

104) Kazuki Bando, Zhiqiang Zhang, Duncan Graham, Karen Faulds, Katumasa Fujita, and Satoshi Kawata. Dynamic pH measurements of intracellular pathways using nano-plasmonic assemblies. *Analyst*, 145:5768–5775, 2020.

105) Carlos Diego L. de Albuquerque, Regivaldo G. Sobral-Filho, Ronei J. Poppi, and Alexandre G. Brolo. Digital Protocol for Chemical Analysis at Ultralow Concentrations by Surface-Enhanced Raman Scattering. *Analytical Chemistry*, 90(2):1248–1254, 2018. PMID: 29235850.

106) Yi Zhang and Hiroyuki Noji. Digital Bioassays: Theory, Applications, and Perspectives. *Analytical Chemistry*, 89(1):92–101, 2017. PMID: 28105823.

107) 中瀬生彦. エンドサイトーシス阻害試薬. *Drug Delivery System*, 31(1):83–84, 2016.

108) Christopher P Leamon and PHILIP S Low. Delivery of macromolecules into living cells: a method that exploits folate receptor endocytosis. *Proceedings of the National Academy of Sciences*, 88(13):5572–5576, 1991.

109) Eeva-Liisa Punnonen, Kirsi Ryhänen, and Varpu S. Marjomi. At reduced temperature, endocytic membrane traffic is blocked in multivesicular carrier endosomes in rat cardiac myocytes. *European Journal of Cell Biology*, 75(4):344 – 352, 1998.

110) Shiroh Futaki, Tomoki Suzuki, Wakana Ohashi, Takeshi Yagami, Seigo Tanaka, Kunihiro Ueda, and Yukio Sugiura. Arginine-rich peptides An abundant source of membrane-permeable peptides having potential as carriers for intracellular protein delivery. *Journal of Biological Chemistry*, 276(8):5836–5840, 2001.

111) Anna Huefner, Wei-Li Kuan, Roger A. Barker, and Sumeet Mahajan. Intracellular SERS Nanoprobes For Distinction Of Different Neuronal Cell Types. *Nano Letters*, 13(6):2463–2470, 2013. PMID: 23638825.

112) Juqiang Lin, Rong Chen, Shangyuan Feng, Yongzeng Li, Zufang Huang, Shusen Xie, Yun Yu, Min Cheng, and Haishan Zeng. Rapid delivery of silver nanoparticles into living cells by electroporation for surface-enhanced Raman spectroscopy. *Biosensors and Bioelectronics*, 25(2):388–394, 2009.

113) Hiroyoshi Fujioka, Jingwen Shou, Ryosuke Kojima, Yasuteru Urano, Yasuyuki Ozeki, and Mako Kamiya. Multicolor Activatable Raman Probes for Simultaneous Detection of Plural Enzyme Activities. *Journal of the American Chemical Society*, 142(49):20701–20707, 2020. PMID: 33225696.

114) Wei Chen, Nathaniel B. Zuckerman, Xiongwu Kang, Debraj Ghosh, Joseph P. Konopelski, and Shaowei Chen. Alkyne-Protected Ruthenium Nanoparticles. *The Journal of Physical Chemistry C*, 114(42):18146–18152, 2010.

115) Prasenjit Maity, Shinjiro Takano, Seiji Yamazoe, Tomonari Wakabayashi, and Tatsuya Tsukuda. Binding Motif of Terminal Alkynes on Gold Clusters. *Journal of the American Chemical Society*, 135(25):9450–9457, 2013.

116) Hannah Feilchenfeld and Michael J. Weaver. Binding of alkynes to silver, gold, and underpotential deposited silver electrodes as deduced by surface-enhanced Raman spectroscopy. *The Journal*

of Physical Chemistry, 93(10):4276–4282, 1989.

117) Hiroki Ida, Yasufumi Takahashi, Akichika Kumatani, Hitoshi Shiku, Tomo Murayama, Hisaaki Hirose, Shiroh Futaki, and Tomokazu Matsue. Nanoscale Visualization of Morphological Alteration of Live-Cell Membranes by the Interaction with Oligoarginine Cell-Penetrating Peptidesell Membranes by the Interaction with Oligoarginine Cell-Penetrating Peptides. *Analytical Chemistry*, 93(13):5383–5393, 2021. PMID: 33769789.

118) Xiao-Shan Zheng, Cheng Zong, Xin Wang, and Bin Ren. Cell-Penetrating Peptide Conjugated SERS Nanosensor for in Situ Intracellular pH Imaging of Single Living Cells during Cell Cycle. *Analytical Chemistry*, 91(13):8383–8389, 2019.

119) M Green and P M Loewenstein. Autonomous functional domains of chemically synthesized human immunodeficiency virus tat trans-activator protein. *Cell*, 55(6):1179–1188, Dec 1988.

120) A D Frankel and C O Pabo. Cellular uptake of the tat protein from human immunodeficiency virus. *Cell*, 55(6):1189–1193, Dec 1988.

121) Shiroh Futaki, Tomoki Suzuki, Wakana Ohashi, Takeshi Yagami, Seigo Tanaka, Kunihiro Ueda, and Yukio Sugiura. Arginine-rich Peptides: AN ABUNDANT SOURCE OF MEMBRANE-PERMEABLE PEPTIDES HAVING POTENTIAL AS CARRIERS FOR INTRACELLULAR PROTEIN DELIVERY. *Journal of Biological Chemistry*, 276(8):5836–5840, 2021/10/02 2001.

Chapter 3
Stimulated Raman scattering microscopy with spectral focusing of picosecond laser pulses

The contents of this chapter have been published in:
K. Koike, N. I. Smith, K. Fujita, "Spectral focusing in picosecond pulsed stimulated Raman scattering microscopy", *Biomedical Optics Express*, 13 (2), 995-1004 (2022). https://doi.org/10.1364/BOE.445640

Introduction

Stimulated Raman scattering (SRS) is based on an energy transfer mechanism in a sample between two laser pulses, called pump and Stokes beams. Compared to spontaneous Raman scattering, the strength of the SRS signal can be enhanced by more than 10^5. This enhancement has been exploited to nonlinear microscopy techniques to allow high-speed vibrational imaging of biological samples.[122, 123] Recent developments of small Raman probes have increased the degree of multiplexed detection of cellular organelles by modulating the Raman peaks in the silent region.[124, 125, 126] Multiplexing, however, increases the density of Raman peaks in the narrow spectral region, which can become separated by only around 10-15 cm^{-1}, thus requiring higher spectral resolution to resolve each peak. For this type of application, longer picosecond pulses have advantages due to narrow bandwidth, although the SRS generation process is itself nonlinear, and shorter pulses can produce higher signal intensities.[127] Longer pulse widths have also proven to have less nonlinear backgrounds such as cross-phase modulation (XPM) to the signals,[128] which can improve the signal-to-background ratio (SBR). It is also possible to reduce nonlinear photodamage due to lower excitation peak power.

However, this regime with more than 10 ps of pulse width has not been explored despite the above-mentioned advantages in terms of the signal-to-noise ratio (SNR), signal-to-background ratio (SBR), and the potential to reduce photodamage. These indicators are all crucial for live-cell biological imaging.

In this chapter, I report the application of spectral focusing to 2 ps laser pulses in intensity modulation-based SRS microscopy. The laser pulse width is stretched to 14 ps from 2 ps. As a result, SRS imaging is realized with a spectral resolution of 2 cm^{-1}, with improved SBR, and with reduced nonlinear photodamages in live-cell imaging. I design single-grating based chirpers[129] to realize the picosecond spectral focusing of pump and Stokes laser pulses without any complex optical system and alignment. I demonstrate SRS imaging of diamond crystals to confirm a higher spectral resolution in the longer pulse width regime. I also show that longer pulse width can improve the SBR due to decreased nonlinear background and higher spectral resolution in SRS measurements of PS beads, EdU in HeLa cells, and Rhodamine 800 probes. These findings can be easily applied to the widely used intensity modulation SRS setups with 2 ps laser pulses. It can also be widely exploited in live-cell imaging applications such as super-multiplex imaging and time-lapse 3D deep tissue imaging with high spectral resolution and reduced nonlinear photodamages.

3.1 Application of spectral focusing for SRS microscopy

SRS microscopy with spectral focusing of femtosecond laser pulses

In this section, I briefly review the applications of spectral focusing to SRS microscopy. SRS microscopy uses two synchronized picosecond lasers (2-6 ps) in order to match with the molecular vibration bandwidth (10-20 cm^{-1}) and ensure both sufficient spectral resolution and SRS signal.[122, 130] This narrow spectral bandwidth allows to observe specific Raman bands of molecules within complex intracellular environments. To obtain an SRS signal from different Raman bands, one of the two lasers' wavelengths has to be tuned to different values, which requires time to optimize cavity and nonlinear crystal temperature settings inside OPO (usually takes 3 s-1 min depending on the tuning wavelength). Therefore, SRS spectroscopy with a conventional picosecond laser system requires a longer time. In order to overcome this limitation and realize high-speed hyperspectral SRS imaging, spectral focusing of femtosecond (fs) laser pulses has been invented and applied to SRS microscopy.[131, 132, 133, 134] Spectral focusing is "focusing" of the "spectrum" of the broadband fs laser pulses in the spectral domain. Hence, the pulse width is stretched (= linear chirp) to 2-3 ps (= -10 cm^{-1} of instantaneous bandwidth) while maintaining the whole spectral bandwidth (= 100-300 cm^{-1}). Application of spectral focusing was demonstrated for the first time in CARS microscopy with fs laser pulses by Hellerer et al.[135] The linear chirp was introduced by controlling the group delay dispersion (GDD) of laser pulses, a dispersion of frequency components in the time domain, using a pair of grating-based pulse stretchers (= chirper). They performed hyperspectral CARS imaging of nitroprusside microcrystallites by scanning an optical delay line to change time delay between the two laser pulses. Afterward, SRS microscopy with spectral focusing was reported by Andresen et al.[131] Until today, various spectral focusing approaches have been successfully demonstrated with dispersion materials[132, 134] and grating stretchers.[131] Owing to the high peak intensity of the fs laser pulses, multimodal imaging such as two-photon fluorescence and second harmonic generation (SHG) can be performed simultaneously with the same laser source. In response to the growing demand for hyperspectral SRS applications, Newport, USA, recently launched an easy-to-use spectral focusing unit (SF-TRU)[136] for those unfamiliar with this technology.

Group delay dispersion (GDD) of grating-based chirper for spectral focusing

In this research, I used transmission gratings to control group delay dispersion (GDD) of laser pulses and eventually to chirp the pulse width. The laser source I used was picosecond pulse width (-2 ps), but the theoretical mechanism is the same as the fs laser pulses. In this section, I describe a theoretical model of grating-based chirper and what kind of physical parameters contribute to the spectral focusing. Finally, I propose the single-grating based chirper that can realize spectral focusing of picosecond laser pulses with minimal space, cost, and alignment.

Ultrashort laser pulses compose broadband frequency around the central frequency ω_0. Dispersion of the frequency ω in terms of phase ϕ can be described as below by using Taylor series expansion of the phase around the central frequency.[137, 138]

$$\phi(\omega) = \phi(\omega_0) + \Big(\frac{\partial\phi}{\partial\omega}\Big)_{\omega_0}(\omega-\omega_0) + \frac{1}{2}\Big(\frac{\partial^2\phi}{\partial\omega^2}\Big)_{\omega_0}(\omega-\omega_0)^2 + \frac{1}{6}\Big(\frac{\partial^3\phi}{\partial\omega^3}\Big)_{\omega_0}(\omega-\omega_0)^3 \tag{3.1}$$

The quadratic term is called group delay dispersion (GDD, $\partial^2\phi/\partial\omega^2$), and the cubic term is call third order dispersion (TOD, $\partial^3\phi/\partial\omega^3$), which are both responsible for the frequency distribution of the laser pulses in temporal domain. The derivative of time dependent phase of the laser pulses with respect to time gives instantaneous central frequency of $\omega(t)$[139]

$$\frac{\partial\phi}{\partial t} = \omega(t) = \omega_0 + 2\beta\cdot t \tag{3.2}$$

where the parameter β represents the linear slope of the frequency of the laser pulse. Fig.3.1 shows the time-frequency distribution of pulses before and after spectral focusing. The linear slope β can be related to the GDD as follows

$$\beta = \frac{2GDD}{\tau_0^4 + 4GDD^2} \tag{3.3}$$

where τ_0 and τ are the Fourier transform limited (FTL) pulse width, and the chirped pulse width. The presence of GDD stretches the pulse width from τ_0 to τ .

$$\tau = \tau_0\sqrt{1+\left[\frac{4\log 2\cdot GDD}{\tau_0^2}\right]^2} \tag{3.4}$$

In other words, with known parameters τ_0 and the expected chirped pulse width τ, the GDD value (fs^2) required for the spectral focusing can be determined as follows

$$|GDD| = \frac{1}{4\log 2}\sqrt{\tau_0^2(\tau^2-\tau_0^2)} \tag{3.5}$$

In the present study, a grating-based chirp system is used to introduce GDD in the laser pulses. Double-pass geometry with a dual-grating chirp system is often used to cancel the spatial chirp and realize temporal chirp in the output beam. In this system, GDD can be written as following equation.[138]

$$GDD = -\frac{m^2\lambda^3 L_g}{\pi c^2 d^2}\left[1-(-m\frac{\lambda}{d}-\sin\theta_i)^2\right]^{\frac{-3}{2}} \tag{3.6}$$

where m is diffraction order -1, λ is wavelength of laser pulses, L_g is grating-to-grating distance, c is the speed of light, d is groove distance, θ_i is the angle of incident light to the first grating. These parameters can be determined by the specification of gratings and experimental conditions. See Appendix

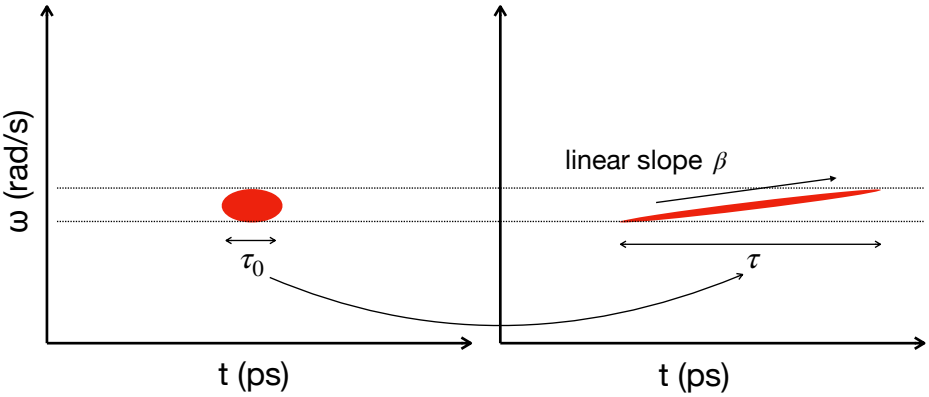

Figure 3.1. Time-Frequency profile of pulsed beam before and after chirp.

for the detail of this equation. With known GDD, the grating-pair distance L_g can be calculated, which is shown below.

$$Lg = -GDD\frac{\pi c^2 d^2}{m^2\lambda^3}\left[1-(-m\frac{\lambda}{d}-\sin\theta_i)^2\right]^{\frac{3}{2}} \tag{3.7}$$

In this study, I propose a single-grating-based chirp system (Fig.3.2(a)) to minimize the system size and simplify the alignment based on a previous paper.[129] In this system, the distance between the grating and retroreflector L is approximately half of the grating-pair distance L_g in the dual-grating geometry. The laser pulses are diffracted four times by the same grating with different heights and positions. The output chirped pulses are reflected by a pick-off mirror. With known parameters and Eq.3.8, one can calculate the distance L to obtain a specific pulse width.

$$\begin{aligned} L \approx \frac{1}{2}Lg &= -GDD\frac{\pi c^2 d^2}{2m^2\lambda^3}\left[1-(-m\frac{\lambda}{d}-\sin\theta_i)^2\right]^{\frac{3}{2}} \\ &= \frac{1}{8\log 2}\sqrt{\tau_0^2(\tau^2-\tau_0^2)}\frac{\pi c^2 d^2}{m^2\lambda^3}\left[1-(-m\frac{\lambda}{d}-\sin\theta_i)^2\right]^{\frac{3}{2}} \end{aligned} \tag{3.8}$$

The relationship between the diffraction angle and incident angle can be written as below,

$$\sin\theta_r = \sin\theta_i + m\frac{\lambda}{d} \tag{3.9}$$

Using Eq.3.8 and 3.9, the distance between grating to retroreflector can be obtained from the following equation,

$$\begin{aligned} L' &= \frac{L}{\cos\theta_r} \\ &= \frac{L}{\sqrt{1-\sin^2\theta_r}} = \frac{L}{\sqrt{1-(-m\frac{\lambda}{d}-\sin\theta_i)^2}} \\ &= \frac{1}{8\log 2}\sqrt{\tau_0^2(\tau^2-\tau_0^2)}\frac{\pi c^2 d^2}{m^2\lambda^3}\left[1-(-m\frac{\lambda}{d}-\sin\theta_i)^2\right] \end{aligned} \tag{3.10}$$

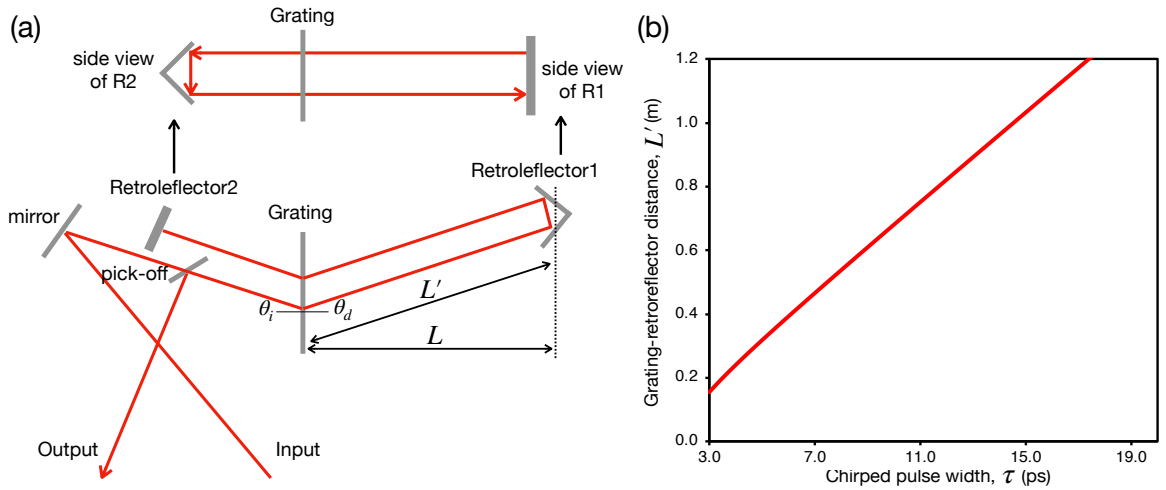

Figure 3.2. (a) Single-grating chirp setup. (b) The distance between grating and retroreflector required to stretch the laser pulses with specific pulse width.

I calculated the optimal distance at each chirped-pulse width using Eq.3.8. The following values were used for the calculation; non-chirped pulse width τ_0 was 2 ps, wavelength λ was 800 nm, speed of light c was 2.9979x10^8 m/s, groove distance d was 0.714 μm (groove density N of 1400 /mm), diffraction order m was -1, angle of incident θ_i was 34°. The parameters about gratings were based on the specification of the actual grating used for the pump beam (T1400-800, LightSmyth). Fig.3.2(b) shows the calculation result with linear relationship between the distance L and chirped pulse width τ. This graph shows that a distance of about 1 m is required to obtain a chirped pulse width of 15 ps with this system. If a conventional dual-pass system with two gratings is used, the distance becomes 2 m, and thus a large optical table would be required.

3.2 Development of SRS microscopy with single grating chirpers

Optical setup for SRS microscopy

Fig.3.3(a) shows a schematic of an SRS microscope with two pulse chirping systems that I have built for this study. A mode-locked Yb-fiber laser (Emerald Engine, APE) provided an output 2 ps laser pulse at 1031 nm with a repetition rate of 80 MHz. It was used as a Stokes beam for SRS imaging. A wavelength-tunable laser pulse emitted from OPO (Levante Emerald, APE) with a wavelength of 660 to 990 nm was used as a pump beam for SRS imaging. The intensity of the Stokes beam was modulated by EOM (APE) at 20 MHz with a modulation depth of more than 90%. A quarter-wave plate (QWP) was used to apply the polarization bias in laser pulses to reduce the applied voltage required for driving EOM. A motorized-optical delay stage (M-531.DD, PI) was placed to ensure the temporal overlap between the Stokes and pump pulse trains. The stage position was optimized every time the pulse width and wavelength used for the imaging were changed. The position was controlled by the LabView program. Half-wave plates (HWP) and polarizers (P) were used to control the laser power. HWP was mounted on a stepper motor rotation mount (K10CR1/M, Thorlabs) to control the rotation angle from a LabView program. Both laser beams were introduced into the chirp systems individually, which can easily switch the pulse widths between 2 (no-chirp), 7, and 14 ps. As for 2 ps mode, the laser was reflected by a retroreflector (RF, HRS1015-AG, Thorlabs) and picked off by a mirror (PM, BBD1-EO3, Thorlabs). As for the 7 and 14 ps modes, the combination of transmission gratings (Grating 1; T1400-800, Grating 2: T1000-1040, LightSmyth) and RFs enabled the picosecond pulse stretching (Fig.3.3(b)). The overall efficiency (throughput of average power) of each chirper was around 78% for the pump (847 nm) and 83% for the Stokes beam, respectively. The diffraction efficiency of each grating was around 94% for the pump and 95% for the Stokes beam, indicating no laser power loss in other optical components. After the chirper, the beams were spatially combined at a dichroic mirror (DM, DMS1000, Asashi Spectra). An autocorrelator (pulseCheck SM2000, APE) was used to measure the pulse width. Laser scanning was performed by a scan unit consisting of a galvanometer mirror (VM500+, General Scanning) and scan/tube lenses in front of an entrance port of the microscope body (ECLIPSE Ti, Nikon). I used water immersion objective lenses (Plan Apo IR 60x, 1.27 NA, Nikon) for focusing and collecting the beams. I used two identical optical bandpass filters (FF01-850/310-25, Semrock) to block the Stokes beam and only transmit the pump beam. A large-area silicon photodiode (PD, S3590-09, Hamamatsu Photonics) was used as a detector. The PD was reverse-biased with 90 V by DC power suppliers to increase the saturation threshold and response bandwidth. The bandwidth was around 40 MHz under this condition, enough to detect SRS signals modulated at 20 MHz. A low pass filter (BLP-1.9+, Mini-Circuits) was inserted between the DC power supplier and PD to reduce the fluctuation of the DC signal. The signal from PD was pre-filtered with a bandpass filter (BBP-21.4+, Mini-Circuits) to reject large DC signals and high-frequency signals at

80 MHz of the laser repetition rate. The signal was amplified by a pre-amplifier with a gain of 46 dB (SA-230F5, NF Corporation) to use the full dynamic range of the lock-in. Then the signal was sent to a fast lock-in amplifier (UHFLI, Zurich Instruments) for the SRS signal demodulation. Reference signal at 20 MHz was provided from the EOM. The demodulated signal was sent to the PC to reconstruct SRS images with a home-written LabView program.

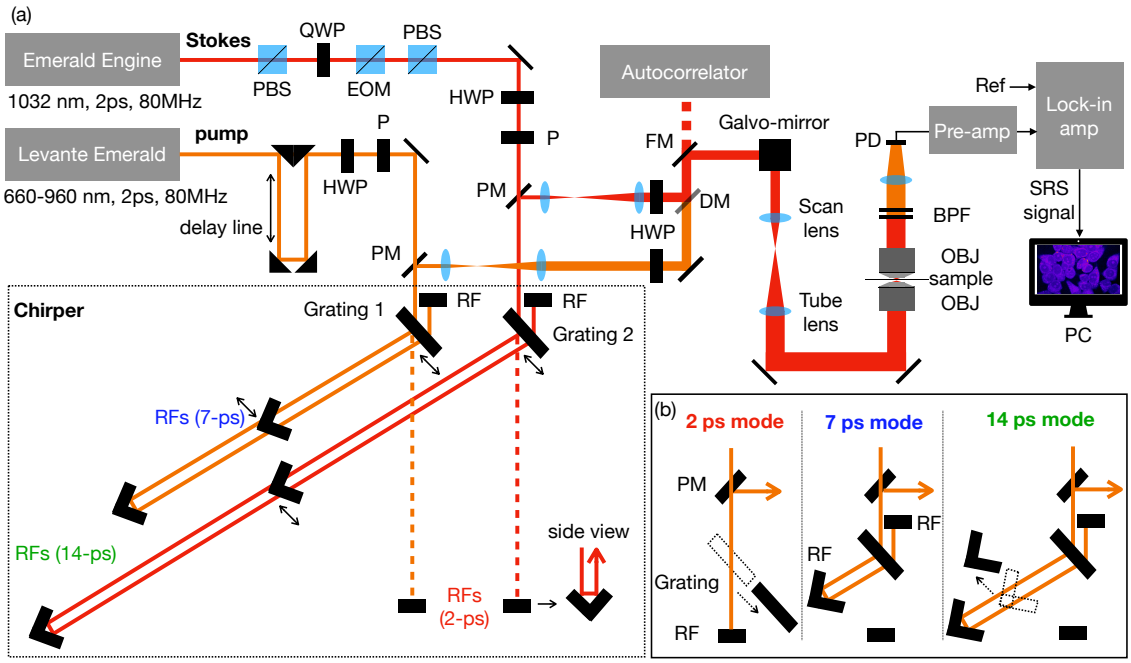

Figure 3.3. Optical setup for SRS microscopy with picosecond pulse chirpers (a) and schematic how to switch the pulse widths (b).

Characterization of chirped picosecond laser pulses

I measured the pulse width of chirped laser pulses by observing autocorrelation functions (Fig.3.4). The pulse widths without chirping were measured to be 1.79 and 1.96 ps for the pump (906.6 nm) and Stokes beam (1031.2 nm), respectively, based on full-width-at-half-maximum (FWMH) of sech^2 fitting functions. Theoretical chirped-pulse width τ was obtained from the measured unchirped pulse width τ_0 and grating-to-retroreflector distance L, as I have already shown in Eq.3.8. From these calculations, for the 7 ps mode, L was set to be 20 and 40 cm with GDD of -4.233x10^6 fs^2 for pump and Stokes beams with the expected chirped-pulse width of 6.8 and 6.3 ps, respectively. For the 14 ps mode, L was calculated to be 41 and 81 cm with GDD of -8.584x10^6 fs^2, providing chirped-pulse widths of 13.4 and 12.3 ps for pump and Stokes beam, respectively. The measured pulse widths of the pump and Stokes beams after chirping were 7.45 and 7.19 ps in the 7 ps mode, and 14.7 and 13.7 ps in the 14 ps mode, which was good agreement with the theoretical values.

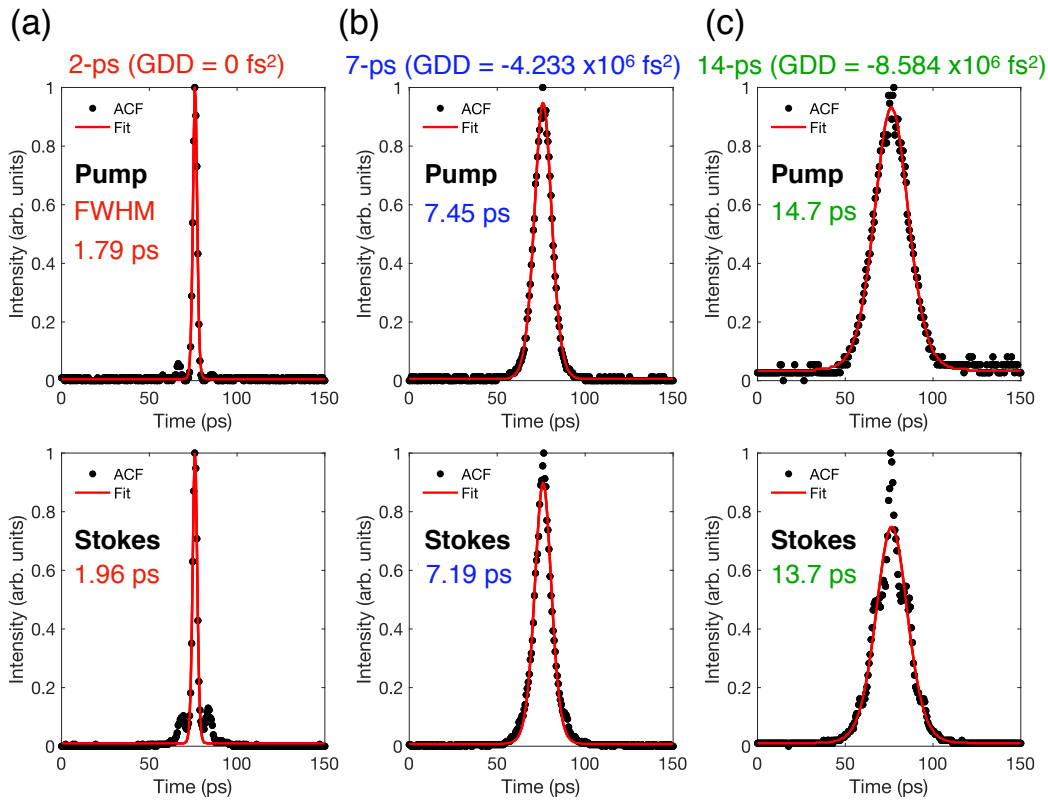

Figure 3.4. Autocorrelation measurement of pump and Stokes laser pulses with (a) 2 ps mode, (b) 7 ps mode, and (c) 14 ps mode. The black dots were the measured autocorrelation functions (ACF), and red lines were the sech^2 fitting functions, respectively. Reprinted and modified with permission from ref.[140] Copyright 2022 Optica Publishing Group.

Shot-noise limited sensitivity

It is crucial to achieving shot-noise limited sensitivity experimentally for highly sensitive SRS imaging. All SRS measurements should be performed under shot-noise limited sensitivity in order to fairly compare the sensitivity under different pulse width conditions and average power levels. I investigated the noise level of the detection system by measuring the temporal fluctuation (= standard deviation) of output voltage after the lock-in detection. I also here show how pre-amplifier works to achieve shot-noise limited sensitivity. Fig.3.5 shows the measurement setup of noise after the lock-in amplifier. I measured the noise with different pump power on a photodetector (PD). The wavelength of the pump beam was 790.8 nm. I used water sandwiched with two coverslips as a sample. Stokes beam was 0 mW on sample. The power on PD was changed from 0.3 to 60 mW on PD, measured with a power meter (Thorlabs). The output voltage from PD was then pre-filtered with a bandpass filter 20 MHz and demodulated at 20 MHz with a time constant of 30 μs at the lock-in amplifier. The demodulated signal was then digitally amplified by a factor of 1000 in the real-time arithmetic operation function of UHFLI. The amplified output signal was then sent to the Aux output. The output voltage was recorded

in the temporal domain using the plotter function of UHLIF to calculate the standard deviation. The sampling rate of the plotter was 1.7 MSa/s with a time scale of 2 s, which was enough samples to calculate the noise behavior. I also calculated a theoretical noise level with the following equations to compare them with the experimental results.

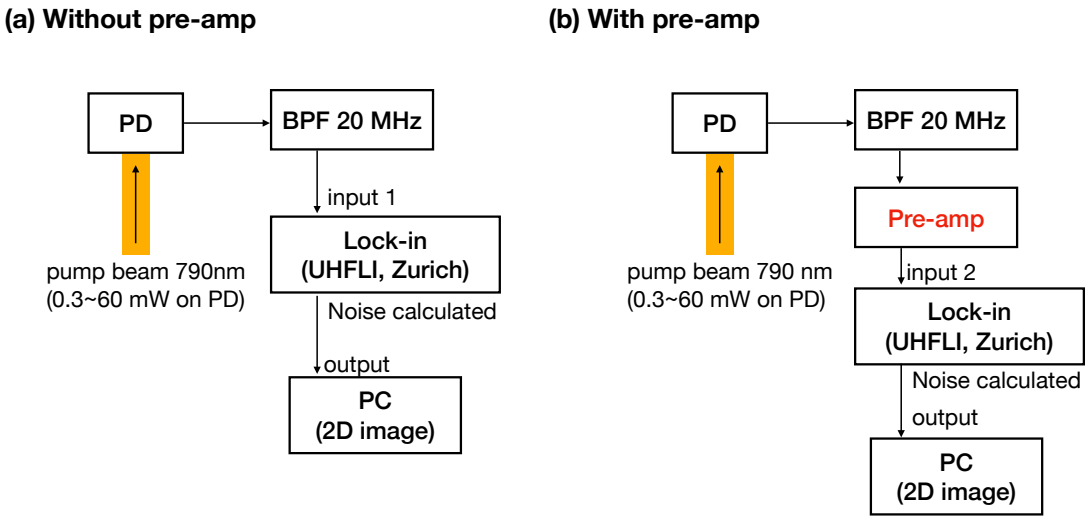

Figure 3.5. Block diagram of noise measurement (a) without pre-amplifier and (b) with pre-amplifier.

Total noise V_{all} after the lock-in amplifier is a sum of the following noise sources.

$$V_{all} = \sqrt{V_{shot}^2 + V_{dark}^2 + V_{johnson}^2 + V_{lock-in}^2 + V_{pre-amp}^2} \tag{3.11}$$

where V_{shot}, V_{dark}, $V_{johnson}$, $V_{lock-in}$, and $V_{pre-amp}$ are the shot-noise induced by incident pump beam, dark-current noise, thermal Johnson noise from a resistor of electronic circuit, the lock-in input noise, and the pre-amp input noise. Each noise value was estimated using the following equations,[141]

$$V_{shot} = RlG_{lock-in}G_{pre-amp}\sqrt{2eP_{pump}G_{res}\Delta f} \tag{3.12}$$

$$V_{dark} = RlG_{lock-in}G_{pre-amp}\sqrt{2eI_{dark}G_{res}\Delta f} \tag{3.13}$$

$$V_{johnson} = G_{lock-in}G_{pre-amp}\sqrt{4k_BTRl\Delta f} \tag{3.14}$$

$$V_{lock-in} = G_{lock-in}N_{lock-in}\sqrt{\Delta f} \tag{3.15}$$

$$V_{pre-amp} = G_{lock-in}G_{pre-amp}N_{pre-amp}\sqrt{\Delta f} \tag{3.16}$$

$$\Delta f = \frac{1}{4\Delta t} \tag{3.17}$$

Resistor Rl was 50 Ω. The lock-in output gain $G_{lock-in}$ was 1000. The pre-amplifier gain $G_{pre-amp}$ was 200 (=46 dB for the simulation with pre-amp, and 1 for the one without pre-amp). Electric charge e was 1.6x10^{-19} C. The pump power on PD P_{pump} was experimentally measured by the power meter. Detector responsivity G_{res} was about 0.6 A/W for 790 nm. The noise equivalent power bandwidth of the lock-in Δf was calculated from Eq. 3.17 with the filter order of lock-in of 1 (1st oder, 6 dB/oct). The signal-collection time constant Δt was 30 μs. Dark current I_{dark} of PD was 6 nA (S3590-09, Hamamatsu). Boltzmann constant k_B was 1.38x10^{-23} J/K. Temperature of measurement T was 300 K (room temperature). The lock-in input noise $N_{lock-in}$ was 7 nV/Hz$^{1/2}$, and 10 nV/Hz$^{1/2}$ (UHFLI, Zurich Instruments) when the input range was 10 mV with 1 MΩ impedance (used for the simulation without pre-amplifier), and 90 mV with 1 MΩ impedance (used for the simulation with pre-amplifier), respectively. The pre-amp input noise $N_{pre-amp}$ was 0.25 nV/Hz$^{1/2}$ (SA-230F5, NF circuits).

Fig.3.6 shows the relationship between measured noise (V) and pump power on PD (mW). The red and blue dots show experimental noise values without and with pre-amplifier, respectively. At first, to know the background noise level, I measured the noise with 0 mW on PD (indicated as "When no light irradiated" in the figure). The noise level without a pre-amplifier increased at around 30 mW on PD. This indicates that the shot-noise limited sensitivity can be obtained from more than 30 mW on sample, considering some power loss in the detection part. The red dot lines show simulated noise levels of shot-noise and other electronics noises without a pre-amplifier. The red solid line shows a total noise level. Experimental and simulated noise values well matched each other. The shot-noise was far below the electronics noise dominated by the lock-in input noise. In contrast, with pre-amplifier, the noise level increased from 1-2 mW on PD. This trend matched with the simulated noise behavior indicated as the blue lines. Using the pre-amplifier, shot-noise from the detector surpassed the significant lock-in input noise (electronics noise). The shot-noise limited sensitivity can be achieved in a low power region ($<$ 10 mW on sample).

I confirmed the SNR improvement in SRS imaging using pre-amplifier. I measured SRS image of PMMA beads with 1-10 μs diameter. The pixel dwell time was 100 μs with pixel number of 256x256, time-constant of 30 μs, and filter order of 1st on the lock-in. The power on sample of pump beam and Stokes beam was set to be 7 and 12 mW, respectively. Fig.3.7 shows the imaging results with and without using pre-amplifier. Obviously, the image contrast was improved with pre-amplifier. SNR of each image was calculated from the signal and noise value. Signal was calculated as subtraction between the mean SRS signal from the white square area indicated as "signal" and the mean background signal of the area "BG". Noise was calculated as a standard deviation of the area "BG". SNRs of the SRS images without and with pre-amplifier was 6 and 45. Hence, the improvement factor was calculated to be 7.5.

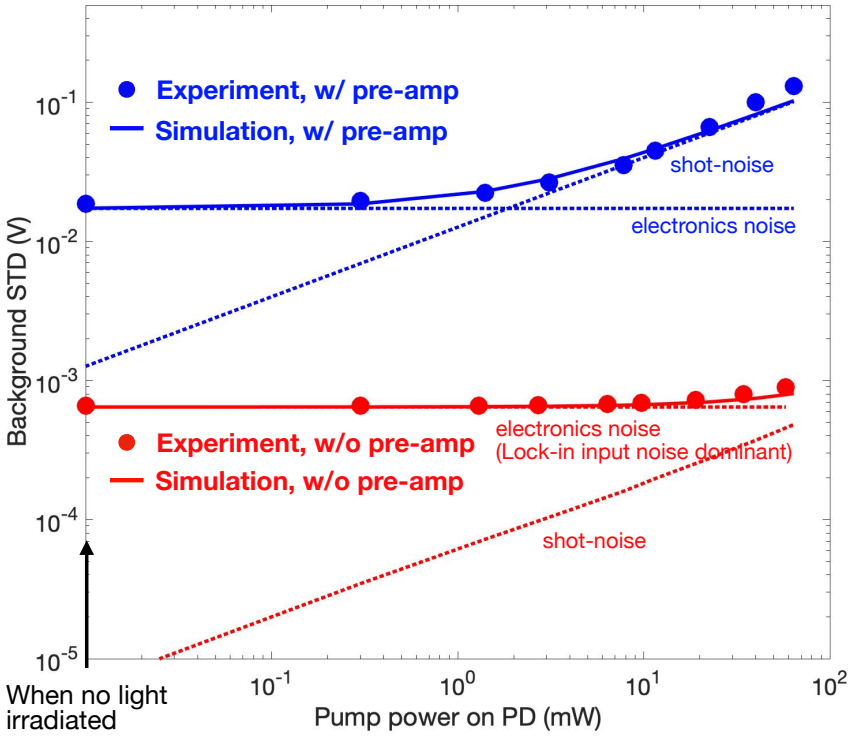

Figure 3.6. Relation between noise (standard deviation of output signal (V)) and pump power on PD (mW). Red and blue dots; experimental noise level without and with pre-amplifier. Red and blue solid lines; total simulated noise level without and with pre-amplifier. Red and blue dashed lines; simulated shot-noise and electronics noise level without and with pre-amplifier.

Spatial resolution

I have determined the system spatial resolution experimentally. I used PMMA beads with 300 nm diameter as samples. The pixel dwell time was 100 μs with a time-constant of 10 μs and 4th-order filtering. The imaging area was 3.71x3.71 μm^2 with pixel numbers of 128x128. The pump beam wavelength was 791.0 nm to match with a vibration mode at 2945 cm^{-1}. The average power of the pump beam and Stokes beams on sample was 10 and 22 mW, respectively. Fig.3.8(a) shows SRS image of a single PMMA bead. The beads aggregation was observed, however, each beads was not resolved due to large diffraction limit relative to the size of the beads. FWHMs of the SRS signal from the beads were shown in Fig.3.8(b). FWHMs in x- and y-directions were 410 and 400 nm. The experimental spatial resolution ν_{ex} was estimated from the deconvolution,

$$\nu_{ex} = \sqrt{\nu_{FWHM}^2 - \nu_{beads}^2} \tag{3.18}$$

where ν_{FWHM} and ν_{beads} are the measured FWHM value and beads size, respectively. Experimental spatial resolution obtained from Fig.3.8 was around 279.4 and 264.7 nm for x- and y-direction. The mean value of spatial resolution from four different beads was 309.95 $\pm$ 35.7 nm for x-direction,

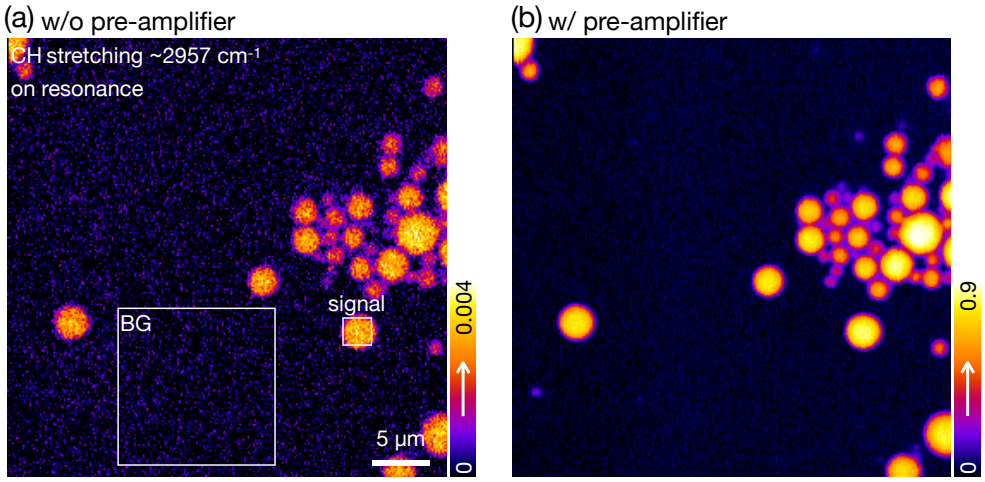

Figure 3.7. SRS imaging of PMMA beads without pre-amplifier (a) and with pre-amplifier (b).

and 282.8 $\pm$ 54.8 nm for y-direction. The experimental value was compared with theoretical spatial resolution based on Rayleigh criterion. In the nonlinear SRS case, it can be written from the following equation,

$$\nu_{th} = 0.61 \frac{\lambda_{pump}}{\sqrt{2}NA} \tag{3.19}$$

where λ_{pump} is the pump beam wavelength, NA is the numerical aperture of an illumination objective lens, and $\sqrt{2}$ is an additional gain for the nonlinear SRS. As I used the wavelength of 791 nm, a water immersion objective lens with NA of 1.27, theoretical value was determined to be 268.7 nm, which was close to the experimental result. The experimental resolution in the x-direction was larger than that in the y-direction. This suggests that the linear polarization can be in x-direction.

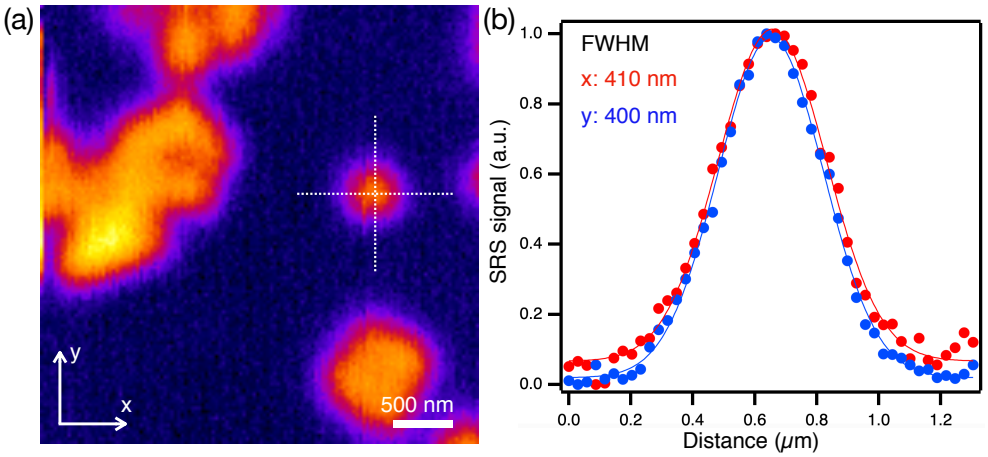

Figure 3.8. SRS imaging of PMMA beads with 300 nm diameter. (a) SRS image of PMMA beads. Scale bar is 500 nm. (b) Line profiles of a single PMMA beads in x- (red) and y-directions (blue). The dots and lines were the measured values and gaussian fitted functions, respectively.

Calibration curve between the delay line position and pump beam wavelength (wavenumber)

In the 2 ps mode, the SRS spectrum of a sample can be obtained by simply tuning the wavelength of the pump beam because the time delay between the pump and Stokes beams does not change within several nm ranges (tens of wavenumber). However, in 7 and 14 ps modes, I applied spectral focusing using single-grating based chirpers to the pump and Stokes beams. Hence, the optical path length of the chirper can vary slightly depending on the pump beam wavelength, which will cause a temporal overlap mismatch between the pump and Stokes beams. Therefore, I adjusted the delay line position depending on the pump beam wavelength to temporally overlap the pump and Stokes beam and fairly compare SRS signals with the 2 ps mode at each wavenumber.

Fig.3.9(a) shows the schematic of the delay line adjustment. First, using a known sample, the wavelength of the pump beam was tuned with the 2-ps excitation so that the beating frequency of the pump and Stokes beams matched with the wavenumber of Ω_1 (delay line at d_1). Then, I applied a linear chirp to the pump and Stokes beams to stretch to the 7 or 14 ps pulse width, which caused the temporal overlap mismatch. To achieve the overlap again, the delay line position was tuned until the strongest signal of the wavenumber at Ω_1 was observed (delay line at d_2). The selected wavenumber needs to be at the peak of an isolated Raman band or a flat off-resonant background.

In 7 or 14 ps modes, I created a calibration curve between the delay line position and the pump beam wavelength by applying the above procedure to obtain an SRS spectrum. For example, to make a calibration curve and perform SRS spectroscopy in a spectral region between 1565 to 1615 cm^{-1}, I used polystyrene (PS) beads as samples. I used two peaks (1583 and 1602 cm^{-1}) of PS beads and an off-resonance region (1569 cm^{-1}) to obtain the relationship between the optimal delay line position and the pump beam wavelength. Fig.3.9(b) shows the SRS images obtained at each wavenumber and optimal delay line positions with the 14 ps mode. The relationship was fitted well by a linear regression curve with R^2 of 0.999 (Fig.3.9(c)). Based on this curve, I obtained the SRS spectrum of the PS beads (Fig. 3.9(d)) by tuning the delay line position at each wavelength (wavenumber).

This procedure can also be performed in a spectral region with a single Raman peak (such as alkyne stretching of EdU). In such a case, one can choose a peak wavenumber and the other two from the off-resonant background region at either side of the peak.

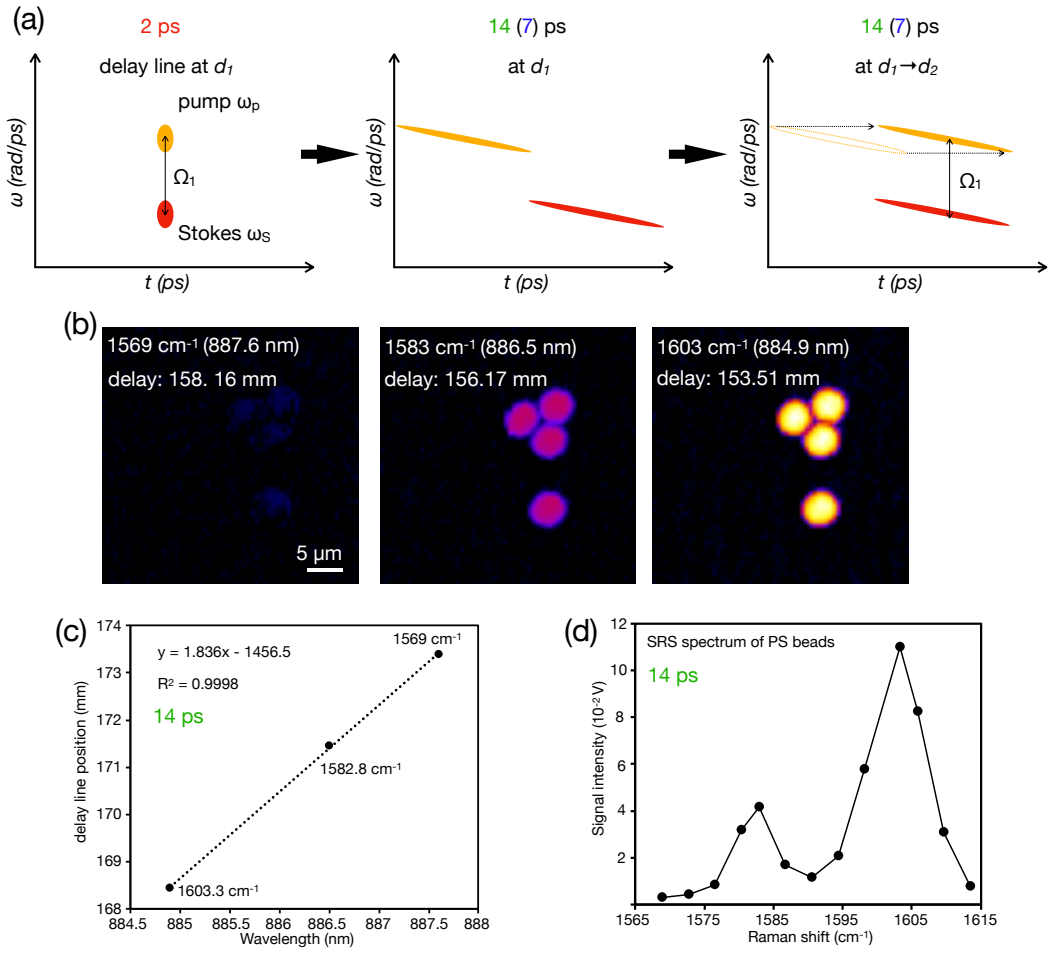

Figure 3.9. Calibration of delay line position and the pump wavelength. (a) Schematic of tuning the excitation Raman band by adjusting the delay line position and the wavelength of the pump beam. (b) SRS images of the PS beads obtained at different wavenumber with the 14 ps mode. (c) Calibration curve between the delay line position and the wavelength of pump beam in a spectral region of 1565 to 1615 cm^{-1} obtained by linear regression to the plots. (d) SRS spectrum of PS beads based on the calibration curve. Reprinted and modified with permission from ref.[140] Copyright 2022 Optica Publishing Group.

3.3 Spectral resolution improvement by spectral focusing

SRS imaging of diamond crystals

I experimentally confirmed the improvement of the spectral resolution by spectral focusing of 2 ps laser pulses by measuring diamond crystals. Diamond crystals have a sharp Raman peak at 1332.5 cm^{-1} with a spectral width of 1.7 cm^{-1}.[142, 143] I used the crystals (IRM2-4, Tomei Diamond) with a diameter of several micrometers for the measurement. The sample was immersed in water and sandwiched with two coverslips. The peak power on sample was the same for all pulse widths, with 31 W for the pump beam and 56 W for the Stokes beam. The pixel dwell time was 100 μs with a time constant of 10

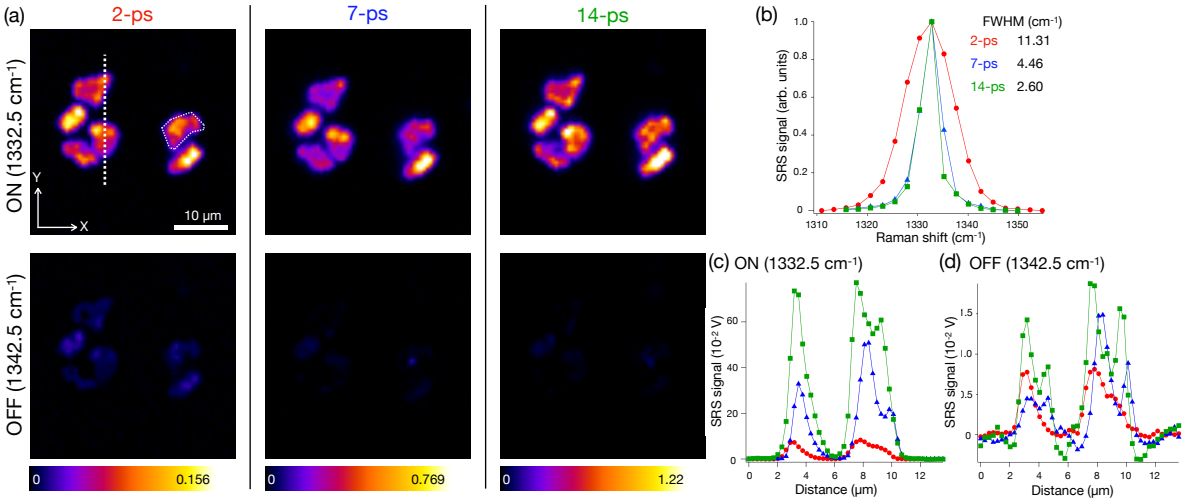

Figure 3.10. SRS imaging of diamond crystals with different pulse widths. (a) SRS images of diamond crystals obtained with 2 (red), 7 (blue), and 14 ps (green) at different wavenumber. (b) SRS spectra of the crystal measured from the white area in (a). (c) and (d) Line profiles of the crystals at on- and off-resonance images.

μs. The pump beam wavelength was tuned from 904.8 (1354.7 cm^{-1}) to 908 nm (1315.8 cm^{-1}). As shown in Fig.3.10(a), bright SRS signals were obtained at the SRS peak of 1332.5 cm^{-1} in the all pulse width modes, while small off-resonance signals remained at the peak shoulder (1342.5 cm^{-1}), mainly due to other nonlinear effects such as cross-phase modulation (XPM). As expected, the peak width in 7 and 14 ps excitation mode became narrower than that of 2 ps excitation due to spectral focusing (Fig.3.10(b)). The experimental and theoretical spectral resolutions were then calculated with the following equations.[139, 134] As for Eq.3.21, I assumed the sech^2 pulse shapes as I measured the pulse width by using sech^2 fitting function (Fig.3.4).

$$\Delta\nu_{ex} = \sqrt{\Delta\nu_m^2 - \Delta\nu_{sp}^2} \tag{3.20}$$

$$\Delta\nu_{th} = 14.9\sqrt{\tau_p^{-2} + \tau_S^{-2}} \tag{3.21}$$

where $\Delta\nu_m$ is the measured SRS peak width and $\Delta\nu_{sp}$ is the high-resolution spontaneous Raman line peak width, and τ_p and τ_S (ps) are the measured pump/Stokes pulse width, respectively. Table.6.1 summarizes the calculated results. The experimental and theoretical values of 2 ps pulses were almost identical. As for chirped pulses, experimental and theoretical values were 4.12 and 2.87 for the 7 ps mode, and 1.97 and 1.49 cm^{-1} for the 14 ps mode, respectively. A 30-40 % difference in the chirped pulses may be due to the existence of higher-order dispersion in the unchirped 2 ps laser pulses seen as side lobes in Fig.3.4(a). Finally, I achieved SRS imaging with a spectral resolution of 2 cm^{-1}.

Fig.6.2(c) shows the line-profiles of the diamond crystals indicated as a white line in the image. Under the same peak power excitation, I observed the SRS signal enhancement with about 3-4-fold in the

7-ps mode and 7-8-fold in the 14-ps mode. This is due to higher SRS excitation efficiency by improved spectral resolution, and higher optical average power used in longer pulse width.[141] Interestingly, the signal in the off-resonance image did not show a significant increase with only 2-3-fold as shown in Fig.6.2(d). This provides an improved image contrast by a factor of 2-3 between the SRS-ON/OFF images in Fig.6.2(a). These results suggest that longer pulse excitation may produce larger SRS signals while suppressing nonlinear background signals.

Table3.1: Spectral resolution.

	FWHM	Experimental resolution	Theoretical resolution	Pump pulse width	Stokes pulse width
2 ps	11.31 cm^{-1}	11.18 cm^{-1}	11.26 cm^{-1}	1.79 ps	1.96 ps
7 ps	4.46 cm^{-1}	4.12 cm^{-1}	2.87 cm^{-1}	7.45 ps	7.19 ps
14 ps	2.60 cm^{-1}	1.97 cm^{-1}	1.49 cm^{-1}	14.7 ps	13.7 ps

3.4 Quantitative analysis of imaging sensitivity with different pulse width

Quantitative comparison of signal-to-background ratio (SBR) and signal-to-noise ratio (SNR) with different pulse width

I further investigated how the spectral focusing of picosecond laser pulses affects the spectral shape with multiple peaks and the image contrasts such as SBR and SNR. This time, I used polystyrene (PS) beads 4.5 μm. The PS beads have two Raman peaks at 1583 and 1602 cm^{-1} assigned to C=C stretch and ring-skeletal stretch modes.[144, 145] The pixel dwell time was 100 μs with a time constant of 10 μs. The pixel number was 64x64 with an area of 38x38 μm^2. Fig.3.11(a) shows SRS images obtained with 2 and 14 ps modes with the same SRS signal level at 1603 cm^{-1}. The average power on sample of pump and Stokes beams was for 2, and 14 ps, respectively. At a Raman shift of 1590.5 cm^{-1}, which was approximately halfway between the two Raman peaks, the SRS signal decreased in the 14 ps mode due to the higher spectral resolution. In contrast, the 2 ps mode showed higher remained signal levels since the two Raman band' s shoulders were simultaneously excited due to low spectral resolution. Therefore, the two Raman peaks were not spectrally resolved in the 2 ps SRS spectrum (Fig.3.11(b)). The off-resonance signal intensities around 1570 and 1620 cm^{-1} were higher in the 2 ps mode than the 14 ps mode. This background signal can be derived from two factors; on-resonance excitation of the peak shoulder due to the broad excitation spectrum and an increase of nonlinear optical effects such as the cross-phase modulation (XPM) intensity due to short pulse width and higher peak power.[128] Therefore, the observed signal at 1603.3 cm^{-1} with a longer pulse width contains a more genuine SRS signal with fewer background artifacts, which leads to higher SBR.

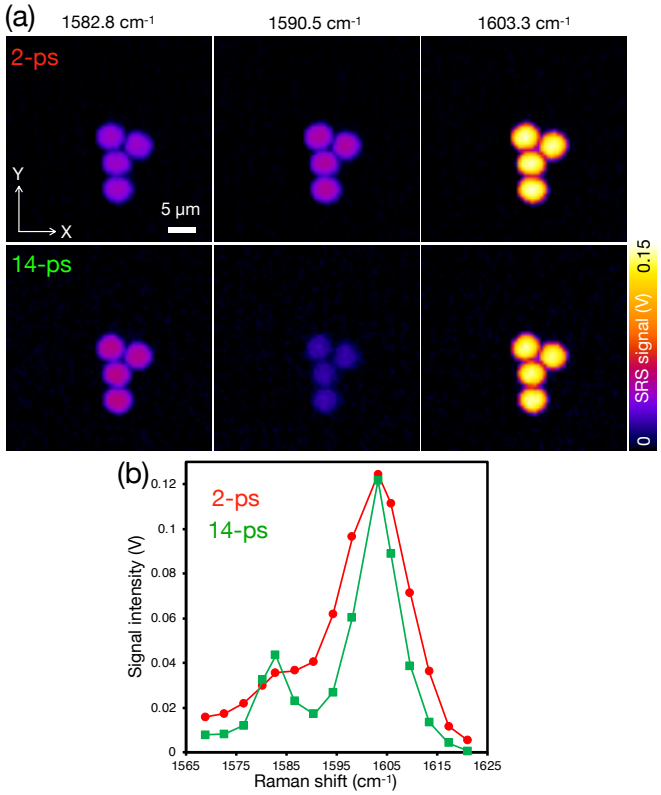

Figure 3.11. SRS imaging of PS beads 4.5 μm with different pulse widths. (a) SRS images obtained at 1582.8 cm^{-1} (C=C stretch), 1590.5 cm^{-1}, and 1603.3 cm^{-1} (ring-skeletal stretch) with 2 (red) and 14 ps (green). Scale bar, 5 μm. (b) SRS spectra of mean signal intensity obtained from 4 beads area with 2 (red) and 14 ps (green). Reprinted and modified with permission from ref.[140] Copyright 2022 Optica Publishing Group.

Next, I obtained the relationship between the on-resonance signal at the peak (SRS-on, 1603.3 cm^{-1}) and the off-resonance signal obtained at the peak shoulder (SRS-off, 1572.7 cm^{-1}) with different peak powers and pulse widths. In this experiment, I maintained the ratio of the pump to Stokes beam power at 1:2. Maximum peak powers were set to below the damage threshold (i.e., no damage or destruction of the sample observed after 30 consecutive images). The SRS-on signal increased linearly with the product of excitation peak powers (Fig. 3.12(a)). Under the same peak power, a larger SRS signal was observed with longer pulse width due to higher average power.[141] A saturation response in the 7 and 14 ps modes was observed at higher SRS signal levels. Hence the signals did not follow a linear relationship. The saturation was caused by the decrease in population difference between ground and vibrational states due to highly efficient excitation on top of the SRS peak. The SRS-off signal, mainly derived from XPM and small on-resonance excitation of the peak shoulder, also showed a linear response. Although refractive index changes experienced by the pump beam can be determined by the electric field of the Stokes beam,[146, 147] the final XPM signal amount was also affected by the pump beam intensity.[148] Based on the SRS-on/off images, SBR and SNR under different peak powers and pulse widths were calculated based on the following equations,[149, 150]

$$SBR = \frac{I_{ON}}{I_{OFF}} \tag{3.22}$$

$$SNR = \frac{I_{ON} - I_{OFF}}{\sigma_{ON}} \tag{3.23}$$

where I_{ON} and I_{OFF} were the PS beads signal intensity of the SRS-on and SRS-off images, respectively, and σ_{ON} was the standard deviation of the upper region of the SRS-on image without PS beads. In the SBR calculation, the background signal was assumed to be the off-resonant intensity. This can be considered as artifacts from other nonlinear optical effects overlapping with genuine SRS signals. In SNR, the prominent noise was assumed to be shot-noise, which was estimated from the pixel intensity fluctuation of the image. Even with longer pulse widths, SNR comparable to the 2 ps mode was observed using lower peak powers (Fig.3.12(b)). From Eq.3.22, SBR should not depend on peak powers (or SNR). However, in all pulse widths, a trade-off between SNR and SBR was observed. This might be due to the evolution of the SRS-off signal (nonlinear background signal) with increasing peak powers, and the saturation of the SRS signal at higher peak power (Fig.3.12(a)), resulting in a slight decrease in SBR (This saturation effect is further investigated in Rh800 measurement and chapter4). However, the SBR for the 14 ps remained the highest out of all pulse widths, at any given level of SNR, reaching a factor of around two compared to 2 ps. This could be because that the beat frequency of chirped laser pulses was highly concentrated at the peak and producing a strong SRS signal. Also, due to higher spectral resolution, the nonlinear background signal and on-resonance signal from the peak shoulder was lower compared to the genuine SRS signal at the peak.

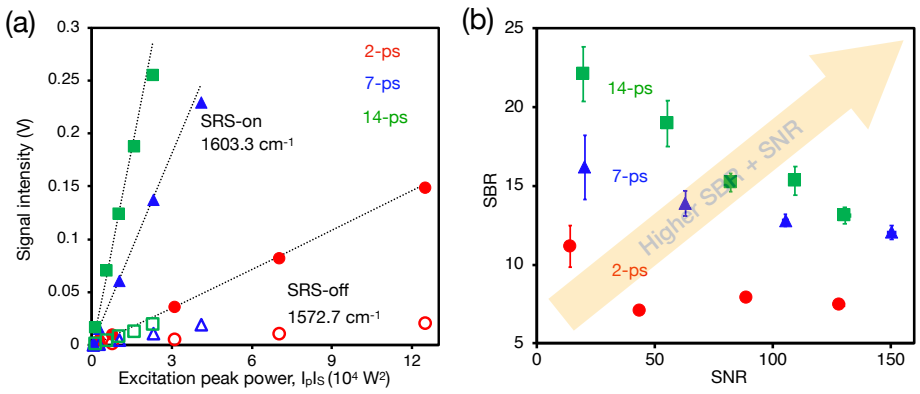

Figure 3.12. Pulse width dependence on the signal intensity, SBR, and SNR. (a) Relationship between the mean SRS signal intensity and the product of peak powers of pump and Stokes beams. N=4. (b) Relationship between SNR and SBR. N=4. Error bar, standard deviation. Reprinted and modified with permission from ref.[140] Copyright 2022 Optica Publishing Group.

Theoretical estimation of SBR with various pulse width and Raman bandwidth

To theoretically confirm the SBR improvement with the 14-ps excitation by spectral focusing, we mathematically simulated the relationship between signal-to-background ratio (SBR) and pulse width (= excitation spectral resolution). To obtain the SRS spectrum, we assumed a sample with a single spontaneous Raman peak (Fig.3.13(a)) and a laser excitation spectrum (Fig.3.13(b)). I set the Raman peak width (FWHM) at 9 cm^{-1} for the alkyne stretching and PS beads vibration modes based on a Lorentzian function (red). I also generated the flat nonlinear background signal without Raman resonance (black line). The SBR between the Raman peak intensity and background signal was set to be 20 based on our experimental results. The spectral resolutions of the excitation laser were set to 11.2, 4.1, and 2.0 cm^{-1} for 2, 7, and 14 ps modes, based on a Gaussian function. The SRS spectra (solid lines) in Fig.3.13(c) were calculated from the convolution of spontaneous Raman spectrum and excitation laser spectra. The non-resonant nonlinear background signal was also convolved (dashed lines). With the large excitation spectral width, a broad SRS spectrum with a higher peak shoulder and nonlinear background was observed, consistent with our experimental results.

The SBR of the simulated SRS spectra was determined to be the ratio of the SRS signal at the peak to the background values. The SBRs with Raman peak FWHMs of 3 and 15 cm^{-1} were also calculated. The relative SBRs were obtained by normalizing the values by the minimum SBR value at 2 ps with Raman peak FWHMs of 3 cm^{-1} (Fig.3.13(d)). Under these simulated conditions, the 14 ps mode exhibited the highest relative SBR in all Raman peak FWHM. At 3 cm^{-1} of Raman peak FWHM, the relative SBRs of 14 ps and 7 ps compared to 2 ps were 2.6 and 1.95, respectively, which is mostly consistent with the diamond particle measurement (Fig.3.10). At 9 cm^{-1}, they were 1.52 and 1.39. At 15 cm^{-1}, they were 1.25 and 1.21. For a typical Raman peak width of molecules from 3-15 cm^{-1}, the SBR can be improved by 1.2-2.6 times with chirped pulses. As increasing of the Raman peak FWHM ($>$ 30 cm^{-1}), the difference of SRS signal intensity among the three pulse widths becomes small, resulting in similar SBR values for the all pulse width. The improvement factor can vary slightly in the actual experiments depending on the wavenumber position for the background signal and how much the background signal contains the on-resonance SRS signals due to the peak shoulder excitation.

Saturation effect of pre-resonance SRS spectroscopy in Rhodamine 800 dye

Saturation of SRS signal has been well known and observed for long time in a gas,[151, 152] diamond particles,[143] and biological molecules.[153] It occurs due to competition with CARS process under high excitation intensity of laser pulses. Theoretical model of SRS signal under saturation effects can be described with below equations[154, 155, 151, 156, 151, 152] (see Chapter 4 for detail),

$$\Delta I_{SRS} = \mathrm{Im}(\chi_R^{(3)}) I_p I_S \tag{3.24}$$

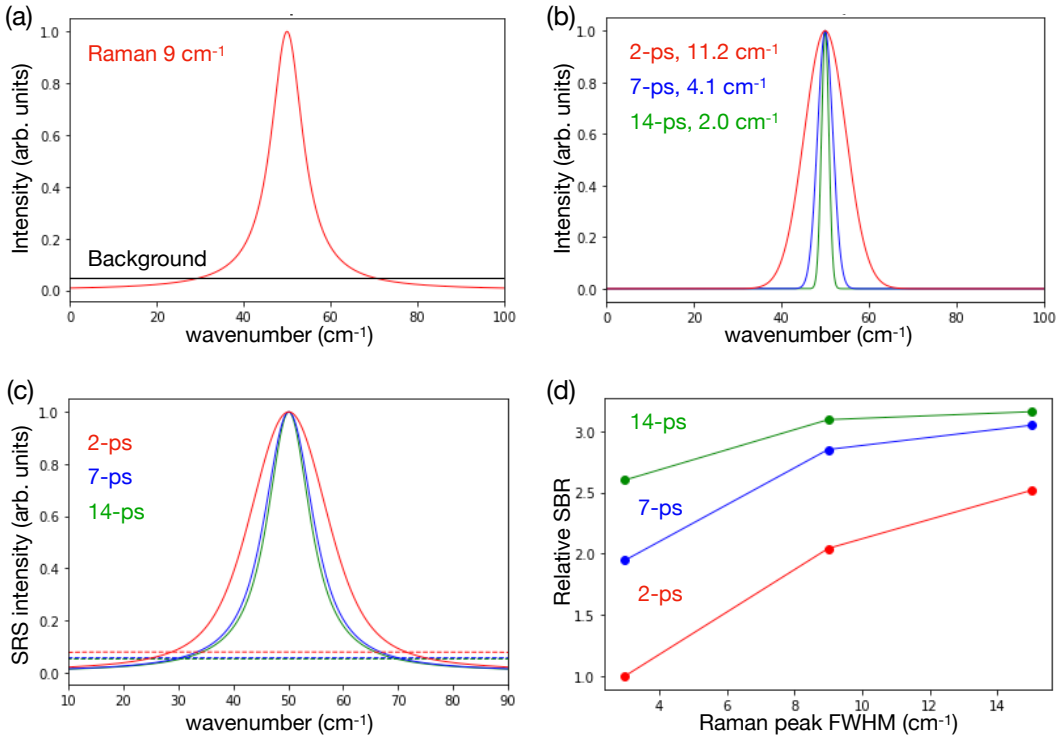

Figure 3.13. Mathematical SBR simulation based on SRS spectrum with different Raman peak widths and pulse widths. (a) Raman spectrum with Lorentzian function (red), nonlinear background with no dependence to Raman shift (black). (b) Excitation spectrum with each pulse width based on Gaussian function. (c) SRS spectra and background signals calculated by the convolution of Raman spectrum/background in (a) and excitation spectra in (b). (d) Relative SBRs as a function of Raman peak widths (FWHMs). Reprinted and modified with permission from ref.[140] Copyright 2022 Optica Publishing Group.

$$\chi_R^{(3)} = \frac{2Nc^4}{\hbar\omega_S^4}\left(\frac{\partial\sigma}{\partial\Pi}\right)\frac{\omega_v\Delta}{\omega_v^2 - \Omega^2 - i\Omega\Gamma} \tag{3.25}$$

$$\frac{1}{\Delta}\frac{\partial\Delta}{\partial t} = -2\left(\frac{4\pi c}{\hbar\omega_S^2}\right)^2\left(\frac{\partial\sigma}{\partial\Pi}\right)\frac{\Gamma}{4(\omega_v - \Omega)^2 + \Gamma^2}I_pI_S \tag{3.26}$$

where $\mathrm{Im}(\chi_R^{(3)})$ is the imaginary part of third-order susceptibility, I_p and I_S are the excitation peak intensity of pump and Stokes beams, $N\Delta$ is the population difference between the ground state and vibrational state, $\omega_S, \omega_v, \Omega$ are the frequency of Stokes beam, vibrational frequency of molecules, and differential frequency of Stokes (ω_S) and pump beams (ω_p), $\partial\sigma/\partial\Pi$ is Raman scattering cross section, Γ is spectral width of the Raman band, and t is the pulse width.

I simulated the SRS signal intensity of a famous pre-resonance Raman dye Rhodamine 800,[124, 157, 158] with pulse widths of 2 and 14 ps, as a function of excitation peak intensity using the above equations. The resonance frequency of Raman scattering ω_v is at 2229 cm^{-1}, spectral width Γ is 11 cm^{-1}, molecule density N is 6.022x10^{20} m^{-3} (= 1 mM), and Raman scattering cross-section is assumed to be $d\sigma/d\Pi$ is 1x10^{-26} cm^2 due to pre-resonance effect. The wavelength of pump and Stokes

beams was set to be 838.47 and 1031.2 nm to match with the CN vibration mode. The peak intensity of Stokes beam was fixed at $5x10^9$ W/cm^2, and the peak intensity of pump beam was gradually increased from $1x10^6$ to $1x10^{10}$ W/cm^2. Fig.3.14(a) shows the calculated SRS signal intensity from the Rh800 solution as a function of the product of excitation intensities. The green and red lines show the result of 14 and 2 ps modes. When compared under the same peak intensity, the SRS signal of 14 ps mode was higher than that of 2 ps due to the higher average power used in the 14 ps.[141] This was also consistent with the experimental result in Fig.3.12(a). Although the saturation in 14 ps was observed in lower excitation peak intensity (but higher average intensity) than 2 ps, the maximum SRS signal intensity was about 10 times higher. I then examined the degree of linearity of the SRS signal in each pulse width mode, defined as the ratio of the observed SRS signal (A) to the linear fitting function (B). Fig.3.14(b) shows the calculated result. The linearity of the 2 ps mode decreased rapidly as the SRS signal (excitation peak intensity) increased. Comparing under the same SRS signal A (x-axis), the SRS signal of 14 ps mode maintains higher linearity than that of 2 ps mode. This wide dynamic range of SRS signal intensity with higher linearity in the 14 ps mode may be useful for quantitative analysis of SRS imaging of molecules.

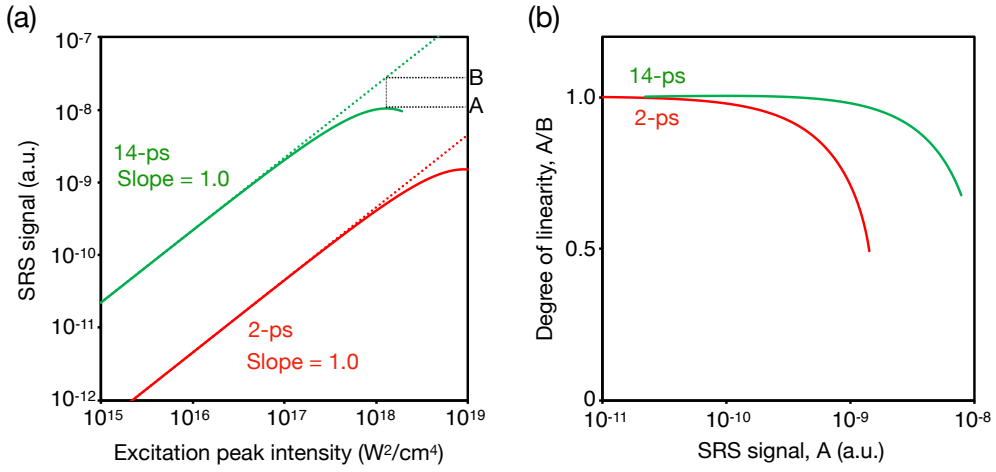

Figure 3.14. Simulation of saturation response of SRS with different pulse width. (a) SRS signal intensity as a function of product of excitation peak intensity. The solid and dashed lines are the SRS signal and linear fitting function with power of 1, respectively. (b) Degree of linearity as a function of SRS signal level.

To investigate whether the 14 ps mode is experimentally more linear in SRS signal intensity, I examined the effect of picosecond spectral focusing on pre-resonance SRS spectroscopy of Rhodamine 800 dye (Rh800, TCI, Japan) dissolved in DMSO. The chemical structure is shown in Fig.3.15(a). It has a terminal nitrile with a Raman band at around 2229 cm^{-1}. The absorption peak is around 682 nm.[157, 158] Hence, the wavelength of pump and Stokes beam of 838.5 and 1031.2 nm for the nitrile band can produce pre-resonance SRS signals of Rh800. Fig.3.15(b) shows the measurement configuration of Rh800 dye. The Rh800 dye solution was sandwiched between coverslips glued with a double-sided

tape imaging spacer. SRS imaging was performed at the boundary of Rh800 solution and air within the sample as it was easy to find the optimal focal plane to generate the SRS signal. Fig.3.15(c) shows SRS images obtained with 2 (red) and 14 ps modes (green). The pump and Stokes average powers on sample were 15 and 30 mW for 2 ps, and 50 and 100 mW for 14 ps. The pixel number was 128x128 with an area of 113x113 μm^2. The pixel dwell time was 100 μs with a time constant of 10 μs. The maximum SRS signal intensity was observed at 2229 cm^{-1}, showing the chemical contrast between the Rh800 solution and air. Away from the peak at 2210 cm^{-1}, the SRS signal disappeared, leaving only the nonlinear background signal contrast. The background signal level was higher in the 2 ps image, possibly due to the higher peak powers and lower spectral resolution. I obtained the 14 ps spectrum based on the calibration curve by tuning the pump beam wavelength and delay line position. Fig.3.15(d) shows SRS spectra of Rh800. Same as the PS beads sample, the 2 ps mode has a broader spectral width with higher background signal level around the peak shoulder. The FWHM of each spectrum was 17.1 and 12.8 for the 2 and 14 ps modes, calculated from the Lorentzian fitting function.

Next, I investigated how the pre-resonance SRS signal intensity changes along with the laser peak power and concentration of Rh800. I measured Rh800 samples at concentrations of 1 mM, 100 μM, and 20 μM. Fig.3.15(e) shows the relationship between the SRS signal intensity and the product of laser peak powers at each concentration. The ratio of the pump to the Stokes beam powers was set to 1:2 for all measurements. The SRS signal was obtained from the mean signal value of the subtraction image from the SRS on-resonance (2229 cm^{-1}) and off-resonance (2210 cm^{-1}) images. At the low peak power region, the SRS signals of both 2 ps and 14 ps showed a linear response to the peak powers with a power of around 1. At the higher peak power region, a gap between the linear slope and measured values was observed, indicating the saturation of the SRS signal of Rh800 occurred under these measurement conditions. The peak power required to saturate the SRS signal was larger for the shorter pulse width (the average power was higher in 14 ps than 2 ps), which was consistent with the simulation result (Fig.3.14) and previous studies.[151, 153] I obtained the degree of linearity at each concentration, and how much the saturation occurs at each SRS signal level was visualized. A. Fig.3.15(f) shows that the larger saturation occurs in the 2 ps than 14 ps when compared with the same SRS signal level and concentration (1 mM, 100 μM), which is in good agreement with what observed in Fig.3.14(b). This indicates that higher SRS signal levels can be obtained in the 14 ps mode than in the 2 ps mode by introducing higher power (until the sample is damaged). In addition, the SRS signal generated in the 14 ps mode can be more reliable in terms of quantitative analysis since the signal linearity is higher than that of the 2 ps mode.

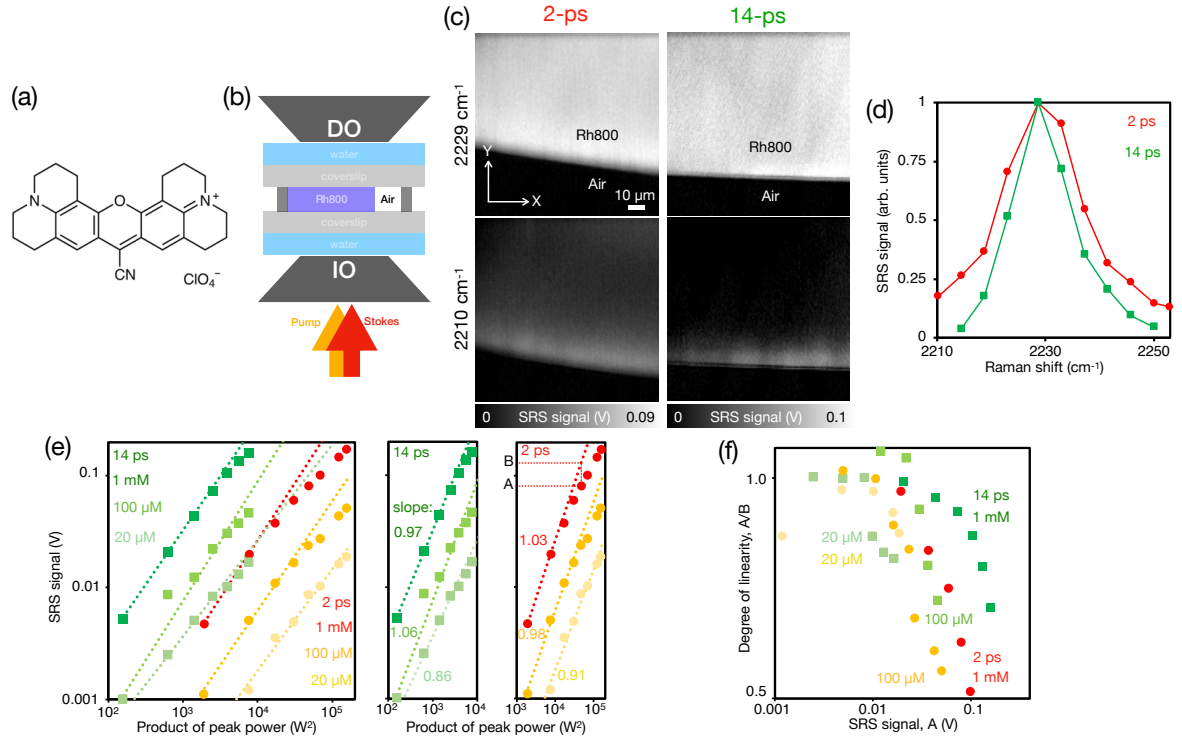

Figure 3.15. Pre-resonance SRS spectroscopy of Rhodamine 800. (a) Molecular structure of Rh800. (b) Experimental configuration of the sample. (c) SRS images of Rh800 with 2 (red) and 14 ps (green). Scale bar is 10 μm. (d) SRS spectra of Rh800 with 2 (red) and 14 ps (green). The concentration of Rh800 was 1 mM. (e) SRS signal intensity of Rh800 with the product of peak power of pump and Stokes beam on sample. Three sets of concentrations (20 μM, 100 μM, and 1 mM) were measured for each pulse width. The dots show the measured values, and dashed lines are obtained from linear fitting. Linear fitting was performed using the first three or four dots, depending on concentrations and pulse widths. (f) Degree of linearity defined as a ratio of the measured values (A) to the linear fitting function (B) at each concentration and pulse width.

3.5 SRS imaging of small molecule and biological molecules

EdU imaging with high sensitivity and high spectral resolution in HeLa cells

One of the possible applications of this technique is super-multiplex SRS imaging of Raman probes in cells based on the 2 ps laser system, where less nonlinear background and high spectral resolution are highly required. To show that the spectral focusing of 2 ps laser pulses has a potential for such an application, we performed SRS imaging/spectroscopy of EdU in HeLa cells with 2 and 14 ps modes. HeLa cells were cultured with serum-free DMEM for 24 h to synchronize the cell cycle.[159] Then, the cells were cultured with EdU 100 μM for another 24 h. Before imaging, the cells were chemically fixed with PBS with PFA 4%. With 2 ps mode, the pump and Stokes laser powers were 25 and 50 mW, respectively, while they were 60 and 120 mW for the 14 ps excitation. Hence, the peak powers were three times smaller in 14 ps mode. SRS image of CH_3 stretching mode in Fig.3.16(a)

was measured to locate the cells with 2 ps mode with the average power of 20 and 40 mW for the pump and Stokes beams. Fig.3.16(b) shows SRS images of the alkyne region obtained with 2 and 14 ps modes. SRS signal from EdU inside the cell nucleolus was observed at 2117 cm^{-1} with both 2 and 14 ps modes. Away from the peak top, the SRS signal from EdU decreased, leaving only nonlinear background signals with no Raman resonance. The SRS images of both 2 and 14 ps at 2117 cm^{-1} showed similar signal intensity around 2.5x10^{-3} V (Fig.3.16(c)). In the 2 ps mode, however, the signal intensity at 2101 cm^{-1} was around 1.5x10^{-3} V. This means that the 2 ps SRS-on signal largely contained the nonlinear background signals such as cross-phase modulation other than SRS. Fig.3.16(d) shows the reference SRS spectra of EdU powders. The 14 ps SRS spectrum showed narrower spectral width of 9 cm^{-1}. Therefore, the SRS signal of EdU in the cells decreased rapidly at 8 cm^{-1} away from the peak top with less nonlinear background signals (Fig.3.16(c)). This indicates that the 14 ps SRS-on image contained more genuine SRS signals. Finally, I performed the image subtraction between the off-resonance (at 2101 cm^{-1}) and on-resonance (at 2117 cm^{-1}) to eliminate the nonlinear background signals. This method is so-called intensity-modulated stimulated Raman loss imaging. The final subtraction image of 14 ps in Fig.3.16(e) showed a two times higher SRS signal than that of 2 ps mode. Since I used 2.5 times higher average power in the 14 ps mode than the 2 ps mode, the noise level also increased, resulting in the almost same SNRs of the subtraction EdU images. However, considering higher spectral resolution and background suppression capabilities, the 14 ps SRS can be a powerful tool for small molecule imaging in a complex biological sample.

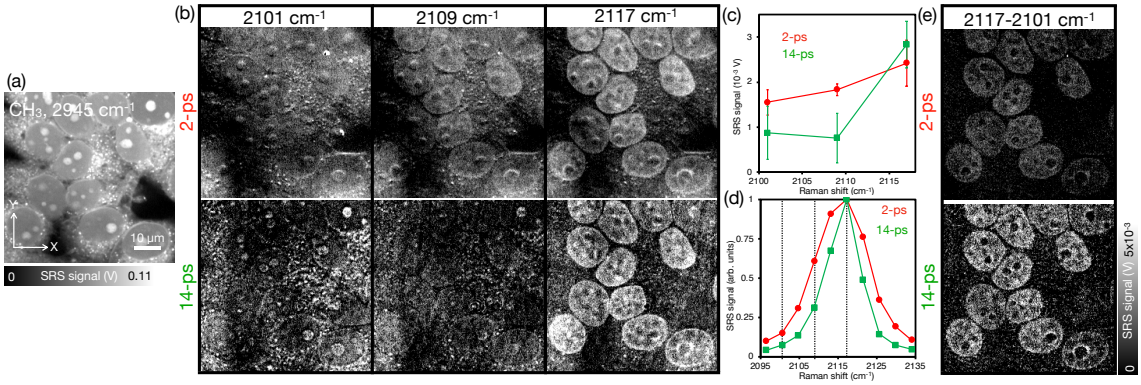

Figure 3.16. SRS imaging of EdU in HeLa cells with 2 ps and 14 ps laser pulses. (a) SRS image of CH_3 stretching mode to locate the cell positions by 2 ps laser pulses. Scale bar, 10 μm. (b) SRS images at different wavenumber around the alkyne peak with 2 (red) and 14 ps (green). Five images were continuously acquired, and the averaged images were shown. The brightness is the same. (c) Mean signal intensity of cellular nucleolus regions at 2101, 2109, and 2117 cm^{-1} with 2 (red) and 14 ps (green). Error bar, standard deviation. N = 12. (d) Reference SRS spectra of EdU powders with 2 (red) and 14 ps (green). The SRS signal was normalized by the SRS peak intensity. (e) Subtraction SRS image between 2101 and 2117 cm^{-1}. The signal shows only EdU contrast. The brightness is the same. Reprinted and modified with permission from ref.[140] Copyright 2022 Optica Publishing Group.

Photodamage characterization by time-lapse imaging of living HeLa cells

In live-cell SRS imaging, it is crucial to reduce nonlinear photodamages such as two-photon absorption, and coherent Raman-induced absorption[160, 161] induced by two laser pulses with intense peak power. I characterized the nonlinear photodamage in SRS imaging with and without spectral focusing of 2 ps laser pulses by performing time-lapse observation of living HeLa cells. I continuously acquired SRS images of CH_3 vibration mode with 100 frames. I measured the cells with lower and higher peak powers and observed how the SRS signal intensity and cellular morphology change according to the peak powers introduced. In order to have the same SNR level in three pulse width modes, I set the average powers of the pump and Stokes beams to 15 and 30 mW for 2 ps, 30 and 60 mW for 7 ps, and 45 and 80 mW for 14 ps, respectively. Therefore, the peak power used in 7 and 14 ps modes were about 1.75 and 2.6 times lower than that used in 2 ps mode, respectively. Fig.3.17(a) shows the results of time-lapse SRS imaging. No significant morphological change of the cells was observed for each condition. Then, SNR was calculated as the ratio of the SRS signal from the nucleus to the noise (standard deviation) in the blank region. Fig.3.17(b) shows the temporal variation of mean SNRs of the three pulse width modes. A 20% decrease in the 2 ps SNR was observed compared to the first frame. The decrease in SNRs of the 7 ps and 14 ps modes was only 5% compared to the first frame. There might be small photodamage within membranes and intracellular organelles in the 2 ps mode and have caused a small decrease in intracellular molecular concentration, which was invisible on the images. Although the peak power used in the 2 ps mode was higher, significant nonlinear photodamage was not observed. This indicates that the average power was lower than the threshold of nonlinear photodamage (see also Appendix for characterizing the nonlinear photodamage).

Next, I performed time-lapse imaging with 2 to 2.5 times higher average power conditions. In this measurement, the average powers of the pump and Stokes beams on sample were 30 and 60 mW for 2 ps, 75 and 150 mW for 7 ps, and 95 and 190 mW for 14 ps, respectively. Fig.3.18(a) shows the results of time-lapse SRS imaging. In 2 ps mode, the onset of cellular membrane breakdown appeared in the middle of the imaging. Accordingly, the SNR level rapidly decreased (Fig.3.18(b)). In 7 and 14 ps modes, however, such a significant change in the appearance of the cells was not observed. The SNR at frame 100 was only 25% and 17% lower than the first frame. The peak powers in the 7 and 14 ps modes were about 1.4 and 2.2 times lower than the 2 ps mode, respectively. Accordingly, nonlinear photodamages such as two-photon absorption and Raman-induced absorptions could be reduced due to longer pulse width and lower excitation peak powers,[161] and only the 2-ps excitation might exceed the damage threshold of living cells (see Appendix for detail). These results strongly suggest that spectral focusing of 14 ps (and 7 ps), compared to conventional 2 ps laser pulses, can reduce the nonlinear photodamage owing to the lower peak power. At the same time, it can also maintain sufficient SNR, making it suitable for long-term observation of living cells under physiological conditions.

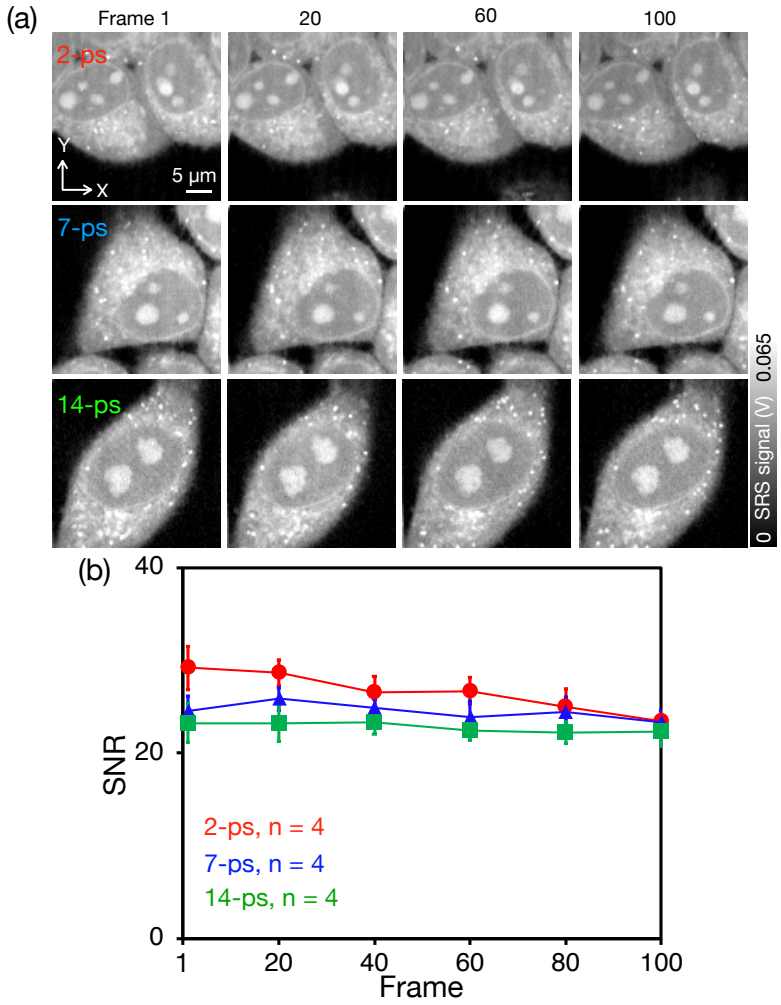

Figure 3.17. Time-lapse SRS imaging of living HeLa cells with 2, 7, and 14 ps laser pulses at low average powers. (a) SRS images of the cells at each frame with different pulse widths. Scale bar, 5 μm. (b) Time (frame)-dependence of SNRs obtained by 2 (red), 7 (blue), and 14 ps modes (green). Error bar, standard deviation. Reprinted and modified with permission from ref.[140] Copyright 2022 Optica Publishing Group.

Discussion and Conclusion

In this chapter, I have shown an application of spectral focusing of 2 ps laser pulses to obtain chirped 14 ps laser pulses. I found that SRS with higher spectral resolution can reduce both nonlinear background and photodamage in the intensity modulation SRS microscopy. Spectral resolution of 2 cm^{-1} was confirmed by measuring SRS spectrum of diamond crystals. Also, the low peak power and narrow instantaneous excitation bandwidth of the chirped 14 ps pulses reduced both the non-resonant nonlinear background and the on-resonance excitation of the Raman peak shoulder. This effect results in higher SBR by a factor of around two for SRS imaging of PS beads. I have also performed pre-resonance SRS spectroscopy/imaging of Rh800 dyes with 2 and 14 ps modes. I experimentally confirmed that 14 ps

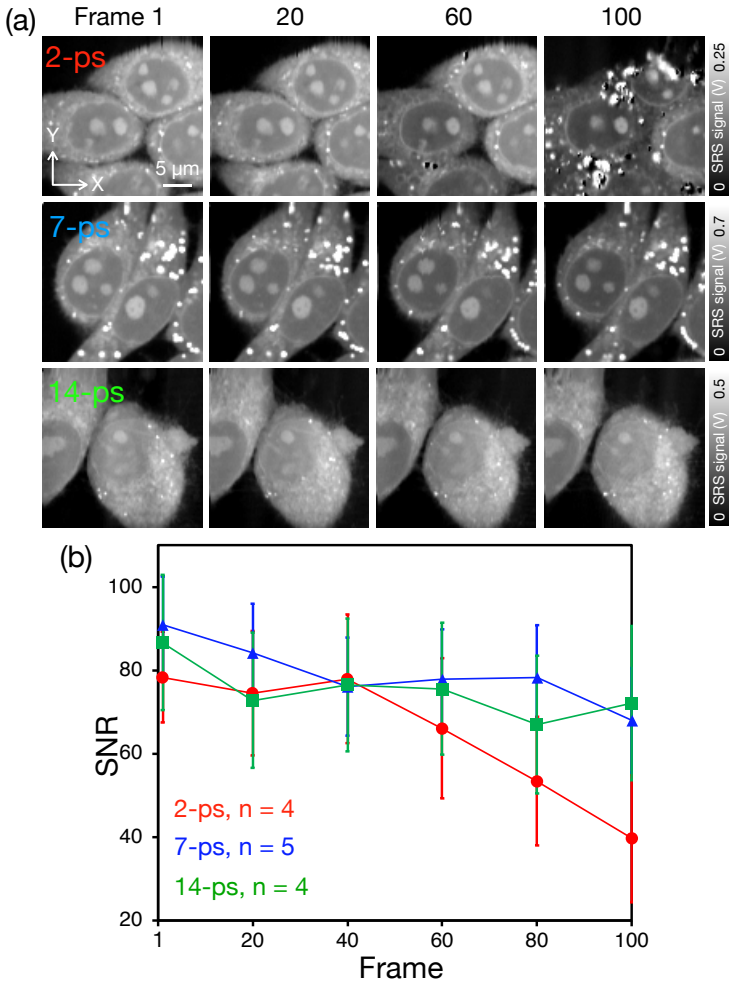

Figure 3.18. Time-lapse SRS imaging of living HeLa cells with 2, 7, and 14 ps laser pulses at high average powers. (a) SRS images of the cells at each frame with different pulse widths. Scale bar, 5 μm. (b) Time (frame)-dependence of SNRs obtained by 2 (red), 7 (blue), and 14 ps modes (green). Error bar, standard deviation. Reprinted and modified with permission from ref.[140] Copyright 2022 Optica Publishing Group.

excitation has less saturation response and maintains high linearity of the SRS signal with the product of peak power, which I believe is useful for quantitative analysis of samples. Taking these advantages, I visualized alkyne-tagged small molecules (EdU) in HeLa cells under higher spectral resolution and SBR. There are non-intensity modulation schemes such as frequency modulation[162, 146, 163] and polarization modulation[147] to eliminate the background artifacts. The proposed method can be easily applied to these schemes to improve the SBR. Owing to the reduced peak powers in chirped 14 ps (7 ps) pulses, I found that the SNR (SRS signal intensity) and cellular structures can be maintained without significant nonlinear photodamages during time-lapse SRS imaging. Note that in order to obtain the same SNR level, 2.3 and 3.7 times higher average powers can be required in the 7 and 14 ps mode, respectively (see Appendix for detail). However, this power level was still lower than the peak power of the 2 ps mode, allowing long-term SRS imaging with higher SNR and reduced photodamages.

In order to achieve higher SNR beyond the current limitation, it would be necessary to scan with much faster speed (1-5 μs/pixel) and higher average power (but not enough to damage the detector). Also, the use of boxcar averaging[164] and squeezed light as an excitation light source[165] can be used to gain higher sensitivity below the damage threshold. An appendix summarizes several demonstrations of boxcar averaging to compare SNR between lock-in and boxcar averaging with the current setup.

Due to the limited bandwidth of the 2 ps laser pulses ($<$1 nm of FWHM), hyperspectral imaging requires both adjustments of the pump beam wavelength and delay line position for each SRS image. To do this, a calibration curve between the delay line position and the pump beam wavelength was created before the measurement (as summarized in Fig.3.9). The wavenumber range in the present system was limited to 60-70 cm^{-1} for each hyperspectral imaging due to the size of retroreflector and grating. However, owing to the higher spectral resolution and lower background signal, it would be possible to observe several Raman tags and observe multiple cellular organelles in this narrow spectral region. The use of chirped femtosecond (fs) laser pulses is a promising solution for achieving high spectral resolution and fast wavenumber scanning over a wide spectral range. The developed pulse chirper is also applicable for fs laser pulses since the physical principles are the same as the conventional dual-grating geometry. In addition, the system can be made more compact for the fs pulses. For example, for a 200-fs laser pulse at 1031.2 nm, the distance between the grating and retroreflector can be only 10 cm to stretch the pulse width to 14 ps. One can scan a wider spectral range of around 150 cm^{-1} rapidly by tuning only the delay line position. For the fs laser-based systems, however, an additional system for compensation of higher-order dispersion may be required to ensure a spectral resolution less than 10 cm^{-1}.[139]

In conclusion, I have developed a single-grating chirp system that can be easily integrated into conventional SRS microscopy. Notably, I have shown here that sufficient SNR can be obtained from a variety of samples, such as PS beads, Rh800 dye, intracellular EdU, and living cells, with a reduced nonlinear background and nonlinear photodamage, by using a pulse width of 10 ps or more and lowering the peak power. I expect the proposed technique to be applied to super-multiplex SRS imaging of Raman tags and time-lapse 3D deep tissue imaging based on the 2 ps laser-based intensity modulation SRS microscopy.

Appendix

GDD of grating-based chirper

In this Appendix, group delay dispersion (GDD) of grating-based pulse chirper is described. A grating pair is prepared to calculate GDD as shown in Fig.3.19. At first, I calculate the distance $\overline{PACB}$.

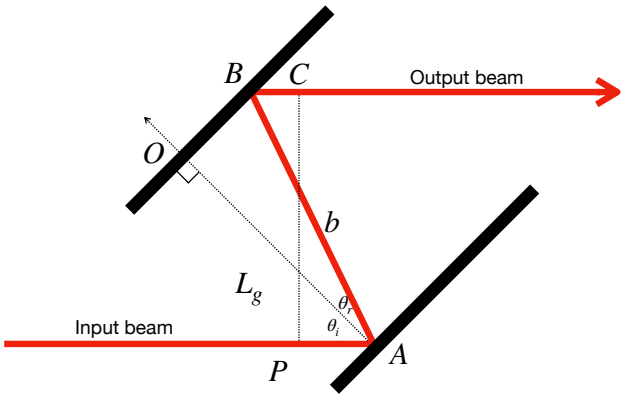

Figure 3.19. Grating-based chirper.

$$\overline{PACB} = p = b + b\cos(\theta_i + \theta_r) \tag{3.27}$$

$$b = \frac{L_g}{\cos\theta_r} \tag{3.28}$$

where b, θ_i, θ_r, and L_g are the distance $\overline{AB}$, the incident angle, the reflection angle, and the distance between the grating pair, respectively. The relationship between the incident angle and reflection angle can be written as follow.

$$\sin\theta_r - \sin\theta_i = m\lambda N = m\frac{\lambda}{d} = 2\pi m\frac{c}{\omega d} \tag{3.29}$$

where m, λ, N,and d are the diffraction order (usually -1), wavelength, groove density, and groove distance of the gratings, respectively. The phase relative to the position O during propagating p is a sum of geometrical path length p and grating phase $R(\omega)$.

$$\phi = \frac{\omega}{c}p + R(\omega) \tag{3.30}$$

$$R(\omega) = -\frac{2\pi m}{d} \times \overline{BO} = -\frac{2\pi m}{d} \times L_g \tan\theta_r \tag{3.31}$$

We can obtain phase shift depending on the frequency (wavelength) based on Eq.3.30 and 3.31.

$$\frac{d\phi}{d\omega} = \frac{d}{d\omega}\big[\frac{\omega}{c}p + R(\omega)\big] = \frac{p}{c} + \big[\frac{\omega}{c}\frac{dp}{d\omega} + \frac{d}{d\omega}R(\omega)\big] \tag{3.32}$$

We then calculate the term $dp/d\omega$ and $d/d\omega R(\omega)$, respectively, as follows.

$$\frac{d}{d\omega}R(\omega) = -\frac{2\pi m}{d} \times L_g \frac{d(\tan\theta_r)}{d\theta_r}\frac{d\theta_r}{d\omega} = -\frac{2\pi m L_g}{d}\frac{1}{\cos^2\theta_r}\frac{d\theta_r}{d\omega} \tag{3.33}$$

$$\begin{aligned}
\frac{dp}{d\omega} &= \frac{dp}{d\theta_r}\frac{d\theta_r}{d\omega} \\
&= \frac{d}{d\theta_r}\big[\frac{L_g}{\cos\theta_r}(1+\cos(\theta_i+\theta_r))\big]\frac{d\theta_r}{d\omega} \\
&= L_g\frac{d}{d\theta_r}\big[\frac{1}{\cos\theta_r}(1+\cos\theta_i\cos\theta_r - \sin\theta_i\sin\theta_r)\big]\frac{d\theta_r}{d\omega} \\
&= L_g\big[\frac{\sin\theta_r}{\cos^2\theta_r} - \frac{\sin\theta_i}{\cos^2\theta_r}\big]\frac{d\theta_r}{d\omega} \\
&= L_g \times \frac{m\lambda N}{\cos^2\theta_r}\frac{d\theta_r}{d\omega} \\
&= 2\pi m\frac{L_g c}{\omega d\cos^2\theta_r}\frac{d\theta_r}{d\omega}
\end{aligned} \tag{3.34}$$

From Eq.3.32,3.33, and 3.34, the phase shift can be written as

$$\begin{aligned}
\frac{d\phi}{d\omega} &= \frac{p}{c} + \big[\frac{\omega}{c}\frac{dp}{d\omega} + \frac{d}{d\omega}R(\omega)\big] \\
&= \frac{p}{c} + \big[\frac{\omega}{c}\big(2\pi m\frac{L_g c}{\omega d\cos^2\theta_r}\frac{d\theta_r}{d\omega}\big) - \frac{2\pi m L_g}{d}\frac{1}{\cos^2\theta_r}\frac{d\theta_r}{d\omega}\big] \\
&= \frac{p}{c}
\end{aligned} \tag{3.35}$$

GDD of this system is the differential of Eq.3.35 in terms of the frequency (wavelength). Therefore,

$$GDD = \frac{d^2\phi}{d\omega^2} = \frac{1}{c}\frac{dp}{d\omega} = \frac{1}{c}\frac{dp}{d\theta_r}\frac{d\theta_r}{d\omega} = \frac{2\pi m L_g}{\omega d\cos^2\theta_r}\frac{d\theta_r}{d\omega} \tag{3.36}$$

We can further obtain the term $d\theta_r/d\omega$ from Eq.3.29.

$$\begin{aligned}
\frac{d}{d\omega}(\sin\theta_r - \sin\theta_i) &= \frac{d}{d\omega}(2\pi m\frac{c}{\omega d}) \\
\frac{d}{d\theta_r}(\sin\theta_r - \sin\theta_i)\frac{d\theta_r}{d\omega} &= -2\pi m\frac{c}{\omega^2 d} \\
\frac{d\theta_r}{d\omega} &= -2\pi m\frac{c}{\omega^2 d\cos\theta_r}
\end{aligned} \tag{3.37}$$

From Eq.3.29, 3.36 ,3.37 GDD can be written as follows,

$$
\begin{aligned}
GDD &= \frac{2\pi m L_g}{\omega d \cos^2\theta_r}\frac{d\theta_r}{d\omega} = -\frac{2\pi m L_g}{\omega d \cos^2\theta_r} \times \frac{2\pi m c}{\omega^2 d \cos\theta_r} \\
&= -\frac{m^2 L_g (2\pi)^2 c}{\omega^3 d^2 \cos^3\theta_r} = -\frac{m^2 L_g (2\pi)^2 c}{(\frac{2\pi c}{\lambda})^3 d^2 \cos^3\theta_r} \\
&= -\frac{m^2 \lambda^3 L_g}{2\pi c^2 d^2}\left[1-\left(-m\frac{\lambda}{d}-\sin\theta_i\right)^2\right]^{-\frac{3}{2}}
\end{aligned}
\tag{3.38}
$$

In the conventional double-pass geometry of the dual-grating chirper, the total GDD is two times of Eq.3.38,[138] and hence it can be written as below,

$$
GDD = -\frac{m^2 \lambda^3 L_g}{\pi c^2 d^2}\left[1-\left(-m\frac{\lambda}{d}-\sin\theta_i\right)^2\right]^{-\frac{3}{2}} \tag{3.39}
$$

GDD of the grating-based chirper is negative. This means that at output, relative phase of higher frequency is faster than that of lower frequency, thus broadening the laser pulse.

Beam profile measurements before and after spectral focusing

I measured the beam profile of the pump and Stokes laser pulses before the galvanometer mirrors to check the beam quality after chirpers. A beam profiler from Thorlabs was used for the measurements. Fig.3.20 shows measurement results. As for the 2 ps mode, the ellipticity of each beam was more than 90%, and the beam diameter (defined as a position at the power decreased to 13.5% from the top) was around 3.1-3.3 mm, which can fulfill the back aperture of the objective after beam expansion. The beam profiles for the 7 and 14 ps modes were also measured (Fig.3.20(b), (c)). For both cases, the ellipticity was more than 80%, sufficient for the imaging. The beam diameter was slightly expanded by 10-20% in the chirped pulses compared to the 2 ps pulses mainly due to several meters longer optical path length in 7 and 14 ps modes.

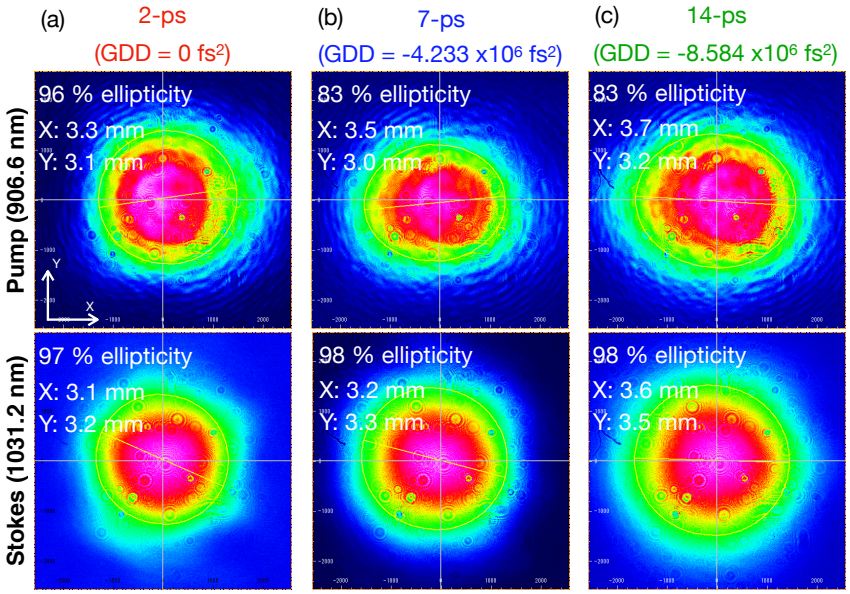

Figure 3.20. Beam profiles of pump and Stokes beams at 2 ps (a), 7 ps (b), and 14 ps modes (c).

Characterization of photodamage rate of living cells in 2-ps SRS microscopy

To confirm that the 2-ps SRS can induce nonlinear photodamage to living cells, I characterized a photodamage rate with the following procedures. The experimental and analysis protocols were based on an article, "Characterization of photodamage in coherent anti-Stokes Raman scattering microscopy" by Ji-Xin Cheng, et al.[160] I have performed time-lapse SRS imaging of living cells (CH_3) under various average powers (= excitation peak power) of the pump and Stokes beams. The ratio of average powers of the pump to Stokes beams was set to 1:2. The pump powers of 20, 30, 40, and 60 mW were used. The imaging area was 74x74 μm^2, so the number of cells was 15-20. The pixel dwell time was 100 μs with pixel numbers of 256x256 and a time constant of 10 μs. The imaging speed was thus 6.7 sec/frame. The imaging was performed continuously for 50 to 150 frames, depending on the average excitation powers. During the imaging, cells started to show cellular membrane blebbing[160] and produced strong signals caused by the modulation of pump beam divergence. The frame number that showed such damage and signals was recorded for each cell. Fig.3.21(a) shows the SRS images with pump and Stokes powers of 30 and 60 mW at 1st frame (w/o photodamage) and 50th frame (w/ photodamage). For the 20 different cells, I measured the average frame number that showed significant photodamage (cell blebbing, membrane breaking), which was 27.5. The inverse of this frame number (= imaging time) was then defined as photodamage rate. I also measured the photodamage rate by changing the average powers. Fig.3.21 shows relationship between photodamage rate and the product of excitation peak powers (log-log). The linear curve fitting was applied to obtain the nonlinear behavior of the photodamage. From the curve, the rate (slope) was determined to be around 1.9, indicating

that the photodamage rate was nonlinearly dependent on the peak power of the beams. Main reason for this nonlinearity should arise from second-order photodamages, such as two-photon absorption and coherent Raman-induced absorption (Raman resonance-enhanced photodamage).[160, 161] As previously shown,[160] if one observes different vibration channels, such as fingerprint, silent-region, or CH_2 mode), the photodamage rate can be changed because of the different number of molecules excited to the vibrational state.

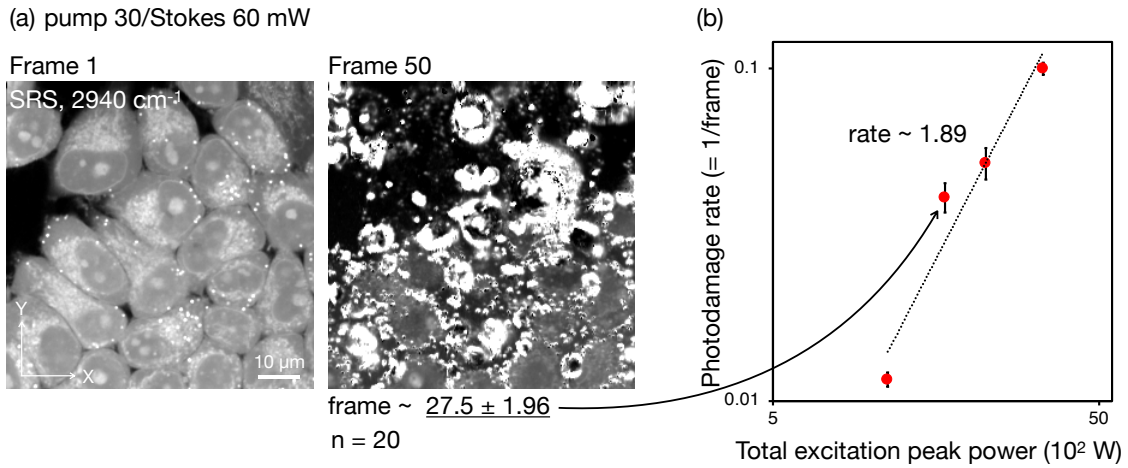

Figure 3.21. Characterization of photodamage rate in time-lapse live-cell imaging. (a) Time-lapse SRS imaging of living cells (2940 cm^{-1}) with pump and Stokes average powers of 30 and 60 mW. For each cell, the frame number that showed significant photodamage (cell membrane blebbing, etc) was obtained. The mean frame number was 27.5. n = 20. (b) Relationship between photodamage rate and product of excitation peak powers. The nonlinearity in photodamage rate was observed with order of nearly 2. n = 16 (pump 20/Stokes 40 mW), n = 20 (30/60 mW), n = 18 (40/60 mW), and n = 14 (60/120 mW). Error bar, standard error.

A theoretical estimation of the 14 ps average powers required to achieve the same SNR level as 2 ps mode

Longer pulses require higher average power to generate SRS signals from a sample. Indeed, in my experiments, I used 2.7-3.7 times higher average power in the 14 ps excitation to realize comparable SRS signal or SNR level to the 2 ps mode. This can also be theoretically explained using the following model.[141] SRS signal can be written as

$$I_{SRS} \approx \frac{1}{2} b_{SRS} Im(\chi^{(3)}) \frac{P_p P_S \tau_{SRS}}{A f_{rep} \tau_p \tau_S} \tag{3.40}$$

where b_{SRS} is constant value, $Im(\chi^{(3)})$ is imaginary part of third-order susceptibility, P_p and P_S are the average power of the pump and Stokes beams, A is the focusing area, f_{rep} is the repetition rate of laser pulses, τ_{SRS}, τ_p, and τ_S are the pulse width of SRS signal and each beam. Here, all pulse widths have the same value. Dominant noise in SRS measurements is assumed to be the shot-noise, which

can be written as

$$noise \approx \sqrt{\frac{P_p}{t}} \tag{3.41}$$

where t is the signal-collection time. Assuming that the Stokes power P_S is two times higher average power than the pump power P_p, SNR can be obtained as below

$$\begin{aligned} SNR = \frac{I_{SRS}}{noise} &= \frac{1}{2} b_{SRS} Im(\chi^{(3)}) \frac{\sqrt{P_p} P_S}{A f_{rep} \tau \sqrt{t}} \\ &\approx \frac{\sqrt{P_p} P_S}{\tau} = \frac{2\sqrt{P_p} P_p}{\tau} \end{aligned} \tag{3.42}$$

From Eq.3.42, I obtained the relationship between P_{14ps} and P_{2ps} under the same SNR level,

$$\begin{aligned} SNR_{14ps} &= SNR_{2ps} \\ \frac{2\sqrt{P_{14ps}} P_{14ps}}{14ps} &= \frac{2\sqrt{P_{2ps}} P_{2ps}}{2ps} \\ P_{14ps} &= 3.66 \times P_{2ps} \end{aligned} \tag{3.43}$$

In the case of 7 ps, the average power should be 2.3 times higher than that of 2 ps excitation.

SNR improvement by Boxcar Averaging in SRS imaging

We can improve the SNR in SRS imaging by employing boxcar averaging for SRS detection. Lock-in detection extracts the amplitude of the frequency of interest in the frequency domain by applying very narrow low-pass filtering.[166] It needs only the information of the signal frequency. Since it is easy to handle and one can get high SNR quickly, lock-in detection is traditionally the first choice for the SRS signal demodulation and imaging. Boxcar averaging consists of two main components, a gate width for signal integer and a window number for signal averager. It integrates the signal of interest in the temporal domain and averaging them with the window number.[167] The gate width requires a start point and an endpoint for the measurement. Only when the gate is opened, the input signal gets integrated. After that, the signals get averaged with the pre-determined window number. This averaging has an effect of a low-pass filter. It reduces the fluctuation of the signal of interest and improves SNR proportionally to the square root of the number of averaged samples (window number). Boxcar averaging is the best choice for analyzing periodic signals at low-duty cycles. In 2018, Fimpel et al. reported a first paper about the application of boxcar averaging to achieve higher sensitivity SRS imaging than lock-in detection.[164] They have confirmed that the use of boxcar averaging can improve SNR by around 20% compared to the lock-in detection even in the presence of a bandpass filter before the lock-in and boxcar averaging system. Hence, the pixel dwell time was shortened by a factor of two in boxcar averaging with the same SNR as lock-in detection because SNR is proportional to the square root of pixel dwell time. They used a UHFLI lock-in amplifier from Zurich Instruments in

which a high-speed digital boxcar averaging option is available on demand. Fortunately, I also use the same lock-in amplifier with the boxcar averaging function. Referring to the paper,[164] I compared the SNR of the SRS signals between lock-in detection and boxcar averaging, and with various imaging parameters.

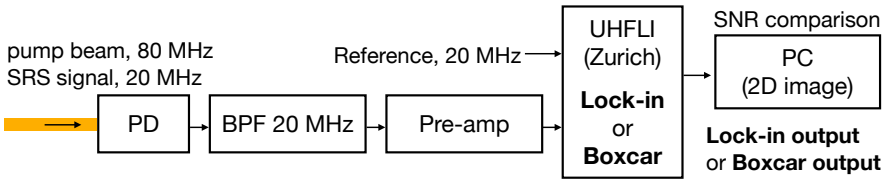

Figure 3.22. Block diagram of SRS measurements in lock-in detection and boxcar averaging with UHFLI.

Fig.3.22 shows an experimental setup to perform SRS imaging under lock-in detection and boxcar averaging. The pump beam after the sample was detected at a photodiode (PD). The voltage from the PD was pre-filtered by a bandpass filter (BPF), and a pre-amp then amplified the voltage. The amplified voltage was then input to the UHFLI lock-in amplifier, where I analyzed the signal simultaneously with lock-in detection and boxcar averaging functions. The lock-in or boxcar output signals were then sent to PC to reconstruct 2D SRS images and calculate SNR. I used PMMA beads as an imaging sample with 1-10 μm diameter.

I have tried two gate widths, 555 ps (minimum gate width available) and 18.9 ns (relatively large width to cover two pulses). Fig.3.23 shows the waveforms of the voltage coming from the PD analyzed and visualized by the built-in periodic waveform analyzer of the UHFLI boxcar averaging function. It shows four sine waves in 50 ns window length (20 MHz), coming from a laser repetition rate of 80 MHz. For 555 ps gate width, I have used the top of the sine wave. Accordingly, the boxcar baseline was chosen at 180 degrees shifted from the boxcar gate. The difference values of the integrated signals from the two gates were averaged over a specified number of windows. For 18.9 ns gate width, I have used two of the four sine wave peaks in the window. Due to the phase of the waveforms, I could not completely cover the two peaks. SRS imaging of PMMA beads was performed with the following parameters and compared SNR of lock-in and boxcar averaging.

Fig.3.24 shows the SRS imaging results with lock-in detection (a) and with boxcar averaging (b). The pixel dwell time was 210 μs with a pixel number of 256x256. The image acquisition was about 14 s. The lock-in time constant was 46 μs with 1st order of the filter. For the boxcar averaging, the gate width was 555 ps. Averaging window number was 4096, and thus the readout time is 205 μs for each pixel. The average power of the pump beam and Stokes beam on sample was 29 and 17 mW, respectively. The wavelength of the pump beam was 790.8 nm. SNR of the SRS signal with the lock-in detection was 141. SNR of the SRS signal with boxcar averaging was 113. Therefore, the relative signal-to-noise ratio (RSNR $= \mathrm{SNR_{Boxcar}}/\mathrm{SNR_{Lock\text{-}in}}$) is 0.8. Lock-in detection provided 25% higher SNR in this experimental condition. Compared to the lock-in, the background noise of the

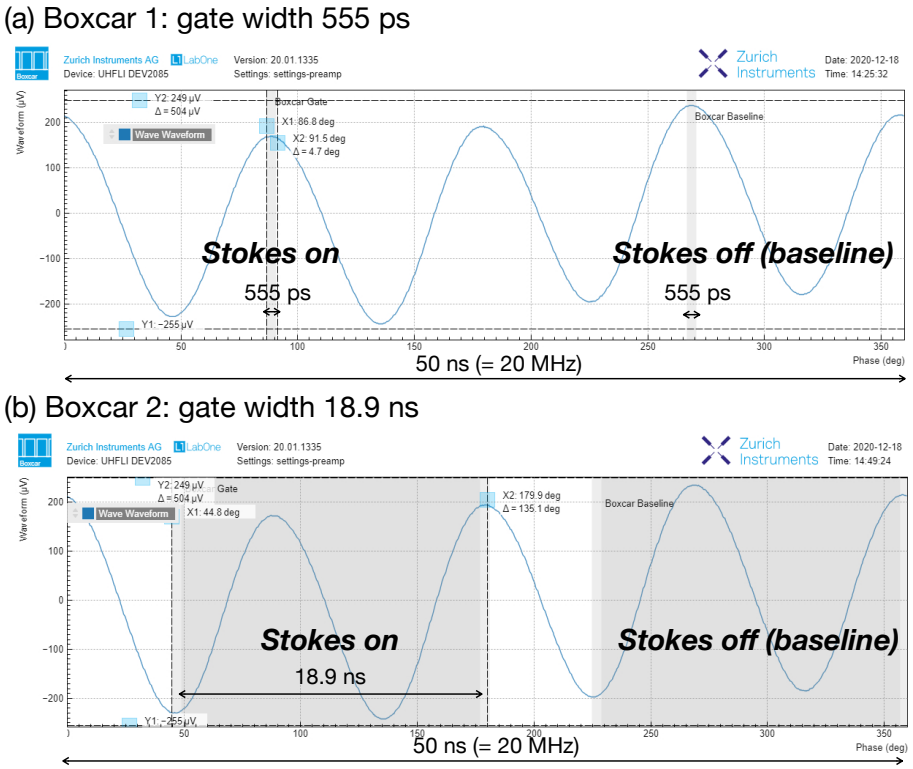

Figure 3.23. Waveform of the voltage signal from the detector. The shaded areas indicate the gate widths employed for boxcar averaging. The gate width was (a) 555 ps (minimum value available) and (b) 18.9 ns.

boxcar was slightly large despite the minimum gate width (555 ps). With this gate width, RSNR was always less than 1 at different pixel dwell times, window number, time constant (Table.3.2), which suggests lock-in detection worked better than boxcar averaging with this gate width. I then tried with a larger gate width of 18.9 ns. Fig.3.25 shows the SRS imaging results with lock-in detection (a) and with boxcar averaging (b). The imaging parameters for lock-in detection and boxcar averaging were the same as Fig.3.24 except the gate width. Because the z-position of the sample was slightly shifted, the signal value was different from Fig.3.24. The FOV was the same. SNR of the SRS signal with the lock-in detection was 157. SNR of the SRS signal with boxcar averaging was 211. Therefore, RSNR is 1.34. Boxcar averaging provided 34% higher SNR in this experimental condition. With this gate width, RNR was always larger than 1 at different pixel dwell times, window numbers, time constant (Table.3.3). Boxcar averaging showed better performance (10-35%) than boxcar averaging with this gate width. I have observed that the improvement factor was almost identical to the previous paper (24% with an electronic bandpass filter as a pre-filter).[164] They also used a relatively large gate width of 7.2 ns for 20 MHz of SRS signal with 40 MHz of laser repetition rate. The bandwidth of the PD, in this case, was about 40 MHz at 70 V bias voltage, and the bandpass filter was also about 20 MHz, so the 555 ps gate width was too narrow to cover the slow response of the signal. It may work better if the bandwidth of PD exceeds the laser repetition rate and can detect each laser pulse's evolution.

These results indicate that the boxcar averaging has great potential to improve my SRS system more. It can reduce the imaging dwell time by a factor of around two with comparable SNR to the current condition.

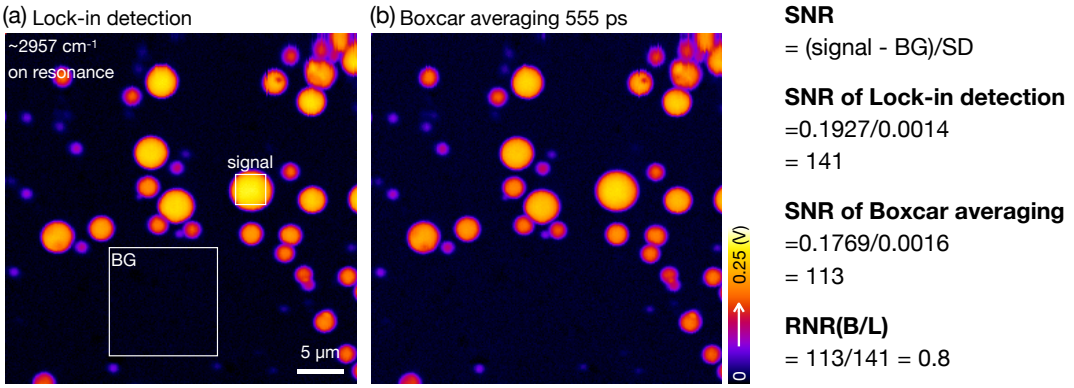

Figure 3.24. SRS imaging of PMMA beads with (a) lock-in detection and (b) boxcar averaging and calculation of SNR. The gate width was 555 ps for boxcar averaging.

Table3.2: Comparison of SNR between lock-in detection and boxcar averaging with 555 ps of gate width in SRS imaging.

	Boxcar averaging			Lock-in detection			
Dwell time	Gate	Windows	SNR_B	Time constant	Filter order	SNR_L	$RSNR_{B/L}$
110 μs	555 ps	2048	58	24 μs	1 st	63	0.92
110 μs	555 ps	2048	58	11 μs	4 th	86	0.67
210 μs (3.24)	555 ps	4096	113	46 μs	1 st	141	0.80
210 μs	555 ps	4096	112	21 μs	4 th	155	0.72

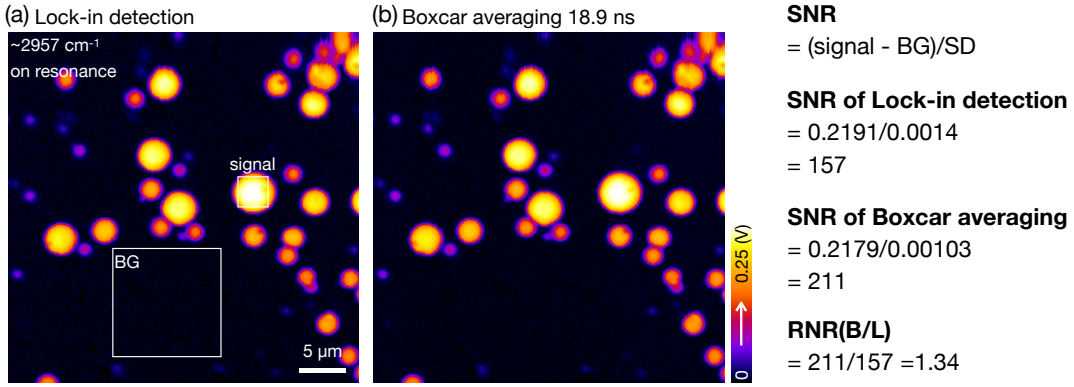

Figure 3.25. SRS imaging of PMMA beads with (a) lock-in detection and (b) boxcar averaging and calculation of SNR. The gate width was 18.9 ns for boxcar averaging.

Table3.3: Comparison of SNR between lock-in detection and boxcar averaging with 18.9 ns of gate width in SRS imaging.

	Boxcar averaging			Lock-in detection			
Dwell time	Gate	Windows	SNR_B	Time constant	Filter order	SNR_L	$RSNR_{B/L}$
110 μs	18.9 ns	2048	147	24 μs	1 st	119	1.24
110 μs	18.9 ns	2048	151	11 μs	4 th	136	1.11
210 μs (3.25)	18.9 ns	4096	211	46 μs	1 st	157	1.34
210 μs	18.9 ns	4096	208	21 μs	4 th	183	1.14

Choice of imaging parameters for both lock-in and boxcar averaging

- Boxcar averaging
  - averaging windows 2048 → 50 ns x 2048 = 103 μs readout → dwell time 110 μs
  - averaging windows 4096 → 50 ns x 4096 = 205 μs readout → dwell time 210 μs
- Lock-in detection
  - time constant 11 μs, filter order 4th → 11 x 10 =110 μs → dwell time 110 μs
  - time constant 24 μs, filter order 1st → 24 x 4.6 = 110 μs → dwell time 110 μs
  - time constant 21 μs, filter order 4th → 21 x 10 = 210 μs → dwell time 210 μs
  - time constant 46 μs, filter order 1st → 46 x 4.6 = 211 μs → dwell time 210 μs

Reference

122) Christian W. Freudiger, Wei Min, Brian G. Saar, Sijia Lu, Gary R. Holtom, Chengwei He, Jason C. Tsai, Jing X. Kang, and X. Sunney Xie. Label-Free Biomedical Imaging with High Sensitivity by Stimulated Raman Scattering Microscopy. *Science*, 322(5909):1857–1861, 2008.

123) Yasuyuki Ozeki, Wataru Umemura, Yoichi Otsuka, Shuya Satoh, Hiroyuki Hashimoto, Kazuhiko Sumimura, Norihiko Nishizawa, Kiichi Fukui, and Kazuyoshi Itoh. High-speed molecular spectral imaging of tissue with stimulated Raman scattering. *Nature Photonics*, 6:845–851, 11 2012.

124) Lu Wei, Zhixing Chen, Lixue Shi, Rong Long, Andrew V Anzalone, Luyuan Zhang, Fanghao Hu, Rafael Yuste, Virginia W Cornish, and Wei Min. Super-multiplex vibrational imaging. *Nature*, 544(7651):465–470, Apr 2017.

125) Fanghao Hu, Chen Zeng, Rong Long, Yupeng Miao, Lu Wei, Qizhi Xu, and Wei Min. Supermultiplexed optical imaging and barcoding with engineered polyynes. *Nature Methods*, 15:194–200, 01 2018.

126) Jingwen Shou, Robert Oda, Fanghao Hu, Keiko Karasawa, Mutsuo Nuriya, Masato Yasui, Bruce Shiramizu, Wei Min, and Yasuyuki Ozeki. Super-multiplex imaging of cellular dynamics and heterogeneity by integrated stimulated Raman and fluorescence microscopy. *iScience*, 24(8), 2021.

127) Delong Zhang, Mikhail N. Slipchenko, and Ji-Xin Cheng. Highly Sensitive Vibrational Imaging by Femtosecond Pulse Stimulated Raman Loss. *The Journal of Physical Chemistry Letters*, 2(11):1248–1253, 2011. PMID: 21731798.

128) Thomas Würthwein, Niklas M. Lüpken, Niels Irwin, and Carsten Fallnich. Mitigating cross-phase modulation artifacts in femtosecond stimulated Raman scattering. *Journal of Raman Spectroscopy*, 51(11):2265–2271, 2020.

129) Ming Lai, Shui T. Lai, and Casimir Swinger. Single-grating laser pulse stretcher and compressor. *Appl. Opt.*, 33(30):6985–6987, Oct 1994.

130) Lu Wei, Fanghao Hu, Yihui Shen, Zhixing Chen, Yong Yu, Chih-Chun Lin, Meng C Wang, and Wei Min. Live-cell imaging of alkyne-tagged small biomolecules by stimulated Raman scattering. *Nature Methods*, 11(4):410–412, 2014.

131) Esben Ravn Andresen, Pascal Berto, and Hervé Rigneault. Stimulated Raman scattering microscopy by spectral focusing and fiber-generated soliton as stokes pulse. *Opt. Lett.*, 36(13):2387–2389, Jul 2011.

132) Dan Fu, Gary Holtom, Christian Freudiger, Xu Zhang, and Xiaoliang Sunney Xie. Hyperspectral Imaging with Stimulated Raman Scattering by Chirped Femtosecond Lasers. *The Journal of Physical Chemistry B*, 117(16):4634–4640, 2013.

133) Chien-Sheng Liao, Kai-Chih Huang, Weili Hong, Andy J. Chen, Caroline Karanja, Pu Wang, Gregory Eakins, and Ji-Xin Cheng. Stimulated Raman spectroscopic imaging by microsecond delay-line tuning. *Optica*, 3(12):1377–1380, Dec 2016.

134) Mohammed S. Alshaykh, Chien-Sheng Liao, Oscar E. Sandoval, Gregory Gitzinger, Nicolas Forget, Daniel E. Leaird, Ji-Xin Cheng, and Andrew M. Weiner. High-speed stimulated hyperspectral Raman imaging using rapid acousto-optic delay lines. *Opt. Lett.*, 42(8):1548–1551, Apr 2017.

135) Thomas Hellerer, Annika M.K. Enejder, and Andreas Zumbusch. Spectral focusing: High spectral resolution spectroscopy with broad-bandwidth laser pulses. *Applied Physics Letters*, 85(1):25–27, 2004.

136) Aram Zeytunyan, Tommaso Baldacchini, and Ruben Zadoyan. Module for multiphoton high-resolution hyperspectral imaging and spectroscopy. In *Proc.SPIE*, volume 10498, 2 2018.

137) E. Treacy. Optical pulse compression with diffraction gratings. *IEEE Journal of Quantum Electronics*, 5(9):454–458, Sep. 1969.

138) R. L. Fork, C. H. Brito Cruz, P. C. Becker, and C. V. Shank. Compression of optical pulses to six femtoseconds by using cubic phase compensation. *Opt. Lett.*, 12(7):483–485, Jul 1987.

139) Mojtaba Mohseni, Christoph Polzer, and Thomas Hellerer. Resolution of spectral focusing in coherent Raman imaging. *Opt. Express*, 26(8):10230–10241, Apr 2018.

140) Kota Koike, Nicholas I. Smith, and Katsumasa Fujita. Spectral focusing in picosecond pulsed stimulated raman scattering microscopy. *Biomed. Opt. Express*, 13(2):995–1004, Feb 2022.

141) Chi Zhang, Delong Zhang, and Ji-Xin Cheng. Coherent Raman Scattering Microscopy in Biol-

ogy and Medicine. *Annual Review of Biomedical Engineering*, 17(1):415–445, 2015.
142) Diane S. Knight and William B. White. Characterization of diamond films by Raman spectroscopy. *Journal of Materials Research*, 4(2):385–393, 1989.
143) Yasuo Yonemaru, Almar F. Palonpon, Shogo Kawano, Nicholas I. Smith, Satoshi Kawata, and Katsumasa Fujita. Super-Spatial- and -Spectral-Resolution in Vibrational Imaging via Saturated Coherent Anti-Stokes Raman Scattering. *Phys. Rev. Applied*, 4:014010, Jul 2015.
144) Travis E. Bridges, Michael P. Houlne, and Joel M. Harris. Spatially Resolved Analysis of Small Particles by Confocal Raman Microscopy: Depth Profiling and Optical Trapping. *Analytical Chemistry*, 76(3):576–584, 2004. PMID: 14750849.
145) Michael Mazilu, Anna Chiara De Luca, Andrew Riches, C. Simon Herrington, and Kishan Dholakia. Optimal algorithm for fluorescence suppression of modulated Raman spectroscopy. *Opt. Express*, 18(11):11382–11395, May 2010.
146) Pascal Berto, Esben Ravn Andresen, and Hervé Rigneault. Background-Free Stimulated Raman Spectroscopy and Microscopy. *Phys. Rev. Lett.*, 112:053905, Feb 2014.
147) Marco Andreana, Marie-Andrée Houle, Douglas J. Moffatt, Andrew Ridsdale, Edlef Buettner, François Légaré, and Albert Stolow. Amplitude and polarization modulated hyperspectral Stimulated Raman Scattering Microscopy. *Opt. Express*, 23(22):28119–28131, Nov 2015.
148) Prathyush Samineni, Baolei Li, Jesse W. Wilson, Warren S. Warren, and Martin C. Fischer. Cross-phase modulation imaging. *Opt. Lett.*, 37(5):800–802, Mar 2012.
149) Alberto Lombardini, Pascal Berto, Julien Duboisset, Esben Ravn Andresen, Sandro Heuke, Edlef Büttner, Ingo Rimke, Sébastien Vergnole, Vasyl Shinkar, Philippe de Bettignies, and Hervé Rigneault. Background-suppressed SRS fingerprint imaging with a fully integrated system using a single optical parametric oscillator. *Opt. Express*, 28(10):14490–14502, May 2020.
150) Sandro Heuke, Alberto Lombardini, Edlef Büttner, and Hervé Rigneault. Simultaneous stimulated Raman gain and loss detection (SRGAL). *Opt. Express*, 28(20):29619–29630, Sep 2020.
151) F. Konig Robert L. Byer M.D. Duncan, P. Oesterun. OBSERVATION OF SATURATION BROADENING OF THE COHERENT ANTI-STOKES RAMAN SPECTRUM (CARS) OF ACETYLENE IN A PULSED MOLECULAR BEAM. *Chemical Physics Letters*, 80(2):253–256, 6 1981.
152) Gaetano Magnotti, Andrew D. Cutler, G. C. Herring, Sarah A. Tedder, and Paul M. Danehy. Saturation and Stark broadening effects in dual-pump CARS of N2, O2, and H2. *Journal of Raman Spectroscopy*, 43(5):611–620, May 2012.
153) Li Gong, Wei Zheng, Ying Ma, and Zhiwei Huang. Saturated Stimulated-Raman-Scattering Microscopy for Far-Field Superresolution Vibrational Imaging. *Phys. Rev. Applied*, 11:034041, Mar 2019.
154) Robert W Boyd. *Nonlinear optics*. Academic press, 2003.
155) Hervé Rigneault and Pascal Berto. Tutorial: Coherent Raman light matter interaction processes. *APL Photonics*, 3(9):091101, 2018.
156) W. M. Tolles, J. W. Nibler, J. R. McDonald, and A. B. Harvey. A Review of the Theory and Application of Coherent Anti-Stokes Raman Spectroscopy (CARS). *Appl. Spectrosc.*, 31(4):253–271, Jul 1977.
157) Hanqing Xiong, Lixue Shi, Lu Wei, Yihui Shen, Rong Long, Zhilun Zhao, and Wei Min. Stimulated Raman excited fluorescence spectroscopy and imaging. *Nature Photonics*, 13(6):412–417, 2019.
158) Peter Fimpel, Ashwin J. X. Choorakuttil, Andrea Pruccoli, Lukas Ebner, Shunji Tanaka, Yasuyuki Ozeki, Martin J. Winterhalder, and Andreas Zumbusch. Double modulation SRS and SREF microscopy: signal contributions under pre-resonance conditions. *Phys. Chem. Chem. Phys.*, 22:21421–21427, 2020.
159) Senlian Hong, Tao Chen, Yuntao Zhu, Ang Li, Yanyi Huang, and Xing Chen. Live-Cell Stimulated Raman Scattering Imaging of Alkyne-Tagged Biomolecules. *Angewandte Chemie International Edition*, 53(23):5827–5831, 2014.
160) Yan Fu, Haifeng Wang, Riyi Shi, and Ji-Xin Cheng. Characterization of photodamage in coherent anti-Stokes Raman scattering microscopy. *Opt. Express*, 14(9):3942–3951, May 2006.
161) Haifeng Wang, Yan Fu, and Ji-Xin Cheng. Experimental observation and theoretical analysis of Raman resonance-enhanced photodamage in coherent anti-Stokes Raman scattering microscopy. *J. Opt. Soc. Am. B*, 24(3):544–552, Mar 2007.
162) Delong Zhang, Mikhail N. Slipchenko, Daniel E. Leaird, Andrew M. Weiner, and Ji-Xin Cheng.

Spectrally modulated stimulated Raman scattering imaging with an angle-to-wavelength pulse shaper. *Opt. Express*, 21(11):13864–13874, Jun 2013.

163) Hanqing Xiong, Naixin Qian, Zhilun Zhao, Lingyan Shi, Yupeng Miao, and Wei Min. Background-free imaging of chemical bonds by a simple and robust frequency-modulated stimulated Raman scattering microscopy. *Opt. Express*, 28(10):15663–15677, May 2020.

164) P. Fimpel, C. Riek, L. Ebner, A. Leitenstorfer, D. Brida, and A. Zumbusch. Boxcar detection for high-frequency modulation in stimulated raman scattering microscopy. *Applied Physics Letters*, 112(16):161101, 2018.

165) Catxere A. Casacio, Lars S. Madsen, Alex Terrasson, Muhammad Waleed, Kai Barnscheidt, Boris Hage, Michael A. Taylor, and Warwick P. Bowen. Quantum-enhanced nonlinear microscopy. *Nature*, 594(7862):201–206, 2021.

166) Zurich Instruments. Principles of lock-in detection and the state of the art. *White Paper*, 2016.

167) 安藤 正典. ロックイン増幅器とボックスカー積分器の原理と実際. **応用物理**, 70(9):1104–1107, 2001.

168) M. Moester, F. Ariese, and J. de Boer. Optimized signal-to-noise ratio with shot noise limited detection in Stimulated Raman Scattering microscopy. *Journal of the European Optical Society*, 10(15022):1–6, 2015.

169) Xuesong Li, Meijuan Jiang, Jacky W. Y. Lam, Ben Zhong Tang, and Jianan Y. Qu. Mitochondrial Imaging with Combined Fluorescence and Stimulated Raman Scattering Microscopy Using a Probe of the Aggregation-Induced Emission Characteristic. *Journal of the American Chemical Society*, 139(47):17022–17030, 2017.

170) Cheng Ji-Xin and Xie X. Sunney. Vibrational spectroscopic imaging of living systems: An emerging platform for biology and medicine. *Science*, 350(6264):aaa8870, 2021/10/11 2015.

171) Faris Sinjab, Kazuki Hashimoto, Venkata Ramaiah Badarla, Junko Omachi, and Takuro Ideguchi. Multimodal laser-scanning nonlinear optical microscope with a rapid broadband fourier-transform coherent Raman modality. *Opt. Express*, 28(14):20794–20807, Jul 2020.

172) Jeffrey B. Guild, Chris Xu, and Watt W. Webb. Measurement of group delay dispersion of high numerical aperture objective lenses using two-photon excited fluorescence. *Appl. Opt.*, 36(1):397–401, Jan 1997.

173) Lu Wei and Wei Min. Electronic Preresonance Stimulated Raman Scattering Microscopy. *The Journal of Physical Chemistry Letters*, 9(15):4294–4301, 2018.

Chapter 4
SRS microscopy with saturated excitation for higher spatial resolution

Introduction

SRS microscopy is a label-free Raman imaging technique with many advantages over spontaneous Raman imaging, such as image acquisition time, detection sensitivity, and image contrast. The wavelength of the pump beam and Stokes beam are generally in the near-infrared region (790-1064 nm) for reducing photodamages to biological samples and increasing penetration depth for the 3D imaging. Therefore, the spatial resolution in SRS microscopy is relatively poor due to the longer wavelength. The improvement of spatial resolution in SRS microscopy is highly desirable to observe finer structures of a sample. In this chapter, to address this issue, I theoretically and experimentally demonstrate the improvement of spatial resolution by exploring saturated SRS signals. SRS signal from a sample is usually proportional to the excitation intensity. The saturation effect of SRS occurs due to competition with other coherent Raman processes, CARS, under the high excitation intensity of pump and Stokes laser.[174, 175, 176] By extracting the saturated signals only occurred at the center of focal spot with differential saturated excitation (dSAX) microscopy technique,[177, 178] higher spatial resolution beyond the diffraction limit can be realized. At first, the saturation effect of third-order susceptibility in the model of SRS signal is introduced to simulate the saturated SRS signal at higher excitation intensity. The point spread function (PSF) of SRS microscopy with smaller FWHM is confirmed after extracting the saturation signal based on dSAX technique. Finally, I experimentally demonstrate the spatial resolution improvements with diamond particles and PMMA beads. I also discuss recent approaches in super-resolution SRS techniques in the discussion section.

4.1 Theoretical description of saturation effects in SRS

Based on the classical model of harmonic oscillation, the SRS signal intensity can be described as below,

$$\Delta I_{SRS} \approx \mathrm{Im}(\chi_R^{(3)}) I_p I_S \tag{4.1}$$

where $\mathrm{Im}(\chi_R^{(3)})$ is the imaginary part of third-order susceptibility, I_p and I_S are the pump and Stokes beam intensity, respectively (please see Appendix for detail). This equation is only true under the assumption that the molecular population at the vibrational state N is constant. However, the population difference can actually change as the excitation intensity of both the pump and Stokes beams increases since SRS competes with another nonlinear coherent Raman process, CARS. The third order susceptibility $\chi_R^{(3)}$ can be rewritten as follow.[174, 179]

$$\chi_R^{(3)} = \frac{N}{m}\Big(\frac{\partial \alpha}{\partial q}\Big)_0^2 \frac{\Delta}{\omega_v^2 - \Omega^2 - i\Omega\Gamma} \tag{4.2}$$

where $N\Delta$ is the population difference between the ground state and vibrational state. $\Delta = 1$ is when all molecules are at the ground state. Raman scattering cross section is then defined as,

$$\frac{d\sigma}{d\Pi} = \Big(\tilde{\alpha}^{NL}\Big)^2 \Big(\frac{\omega_S}{c}\Big)^4 \tag{4.3}$$

where $\tilde{\alpha}^{NL}$ is non constant part of the polarization of the molecule,

$$\Big(\tilde{\alpha}^{NL}\Big)^2 = \Big(\frac{\partial \alpha}{\partial q}\Big)_0 < \tilde{q}(t)^2 > \tag{4.4}$$

From the quantum mechanical theory, $< \tilde{q}(t)^2 >$ for a harmonic oscillation can be expressed as[179]

$$< \tilde{q}(t)^2 > = \frac{\hbar}{2m\omega_v} \tag{4.5}$$

Inserting Eqs.4.4 and 4.5 into Eq.4.3, we can obtain Raman scattering cross section in the form of the following equation.

$$\frac{d\sigma}{d\Pi} = \frac{\hbar}{2m\omega_v}\Big(\frac{\partial \alpha}{\partial q}\Big)_0 \frac{\omega_S^4}{c^4} \tag{4.6}$$

We then insert this equation into Eq.4.2 and obtain

$$\chi_R^{(3)} = \frac{2Nc^4}{\hbar\omega_S^4}\Big(\frac{d\sigma}{d\Pi}\Big)\frac{\omega_v \Delta}{\omega_v^2 - \Omega^2 - i\Omega\Gamma} \tag{4.7}$$

As increasing excitation intensity of pump and Stokes beams, stimulated Raman pumping is also increasing, resulting in the decreasing in the population difference between the ground state and vibrational state Δ. Duncan and Magnotti expressed this rate change with the following differential equation.[174, 175]

$$\frac{1}{\Delta}\frac{\partial \Delta}{\partial t} = -2\Big(\frac{4\pi c}{\hbar\omega_S^2}\Big)^2\Big(\frac{\partial \sigma}{\partial \Pi}\Big)\frac{\Gamma}{4(\omega_v - \Omega)^2 + \Gamma^2} I_p I_S \tag{4.8}$$

From this equation, the population difference can be calculated by integration of time (pulse width), indicating that the shorter pulse width and higher excitation intensity can give decreased population difference. This will cause the decreased third-order susceptibility $\chi_R^{(3)}$. Inserting the solution for this equation into Eq.4.7, 4.1 will give us the SRS signal intensity with saturation effect at higher excitation intensity region. Let me summarize the equations as below for the calculation of SRS signal intensity with saturation effect.

$$\Delta I_{SRS} = \mathrm{Im}(\chi_R^{(3)}) I_p I_S \tag{4.9}$$

$$\chi_R^{(3)} = \frac{2Nc^4}{\hbar\omega_S^4}\Big(\frac{d\sigma}{d\Pi}\Big)\frac{\omega_v \Delta}{\omega_v^2 - \Omega^2 - i\Omega\Gamma} \tag{4.10}$$

$$\frac{1}{\Delta}\frac{\partial \Delta}{\partial t} = -2\Big(\frac{4\pi c}{\hbar\omega_S^2}\Big)^2\Big(\frac{\partial\sigma}{\partial\Pi}\Big)\frac{\Gamma}{4(\omega_v - \Omega)^2 + \Gamma^2} I_p I_S \tag{4.11}$$

The SRS excitation intensity depends on the imaginary part of third-order susceptibility and the excitation intensities of pump and Stokes beam. Third-order susceptibility has many parameters such as Raman scattering cross section, speed of light, frequency of pump and Stokes beams, and the population difference between ground state and vibrational state. The molecular population changes depending on the intensities of pump and Stokes beams.

For the simulation of SRS signal, I use diamond particle as a sample. All parameters such as resonance frequency, spectral width, and molecule density have been reported. The resonance frequency of Raman scattering ω_v is at 1332.5 cm^{-1}, spectral width Γ is 1.7 cm^{-1}, molecule density N is 1.762x10^{23} cm^{-3}, and Raman scattering cross section $d\sigma/d\Pi$ is 2.7x10^{-29} cm^2.[180, 181] The wavelength of pump and Stokes beams was set to be 931.8 and 1064 nm to match with the resonance frequency of diamond particles. The pulse width for both beams was 7 ps. The peak intensity of Stokes beam was fixed at 1x10^{10} W/cm^2 and the peak intensity of pump beam was gradually increased from 1x10^6 to 1x10^{11} W/cm^2. Fig.4.1 shows the relationship of SRS signal from a diamond particle and product of excitation intensities. Saturation of SRS signal is observed at around 1x10^{20} W^2/cm^4. This saturation response is used to realize super-resolution SRS microscopy with dSAX technique.

4.2 Spatial resolution of SRS microscopy

Before showing theoretical calculation results of PSF of SRS microscopy, I briefly explain how the spatial resolution can be determined and how to get the spatial resolution improvement in SRS microscopy by using saturation signal.

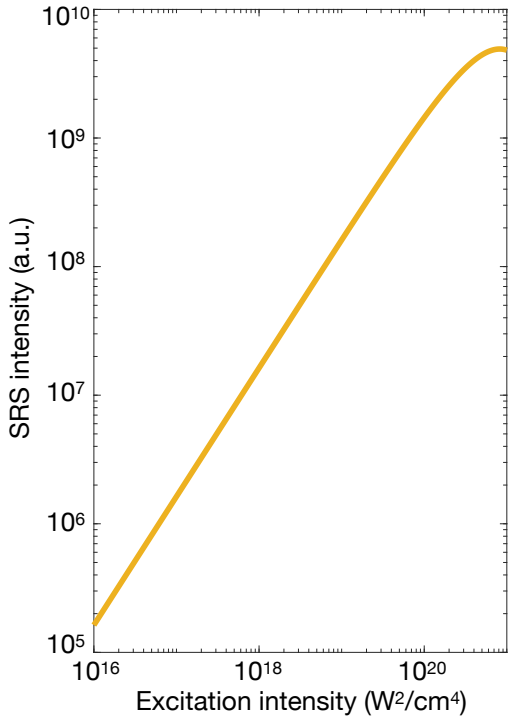

Figure 4.1. Calculated SRS signal intensity as a function with product excitation intensity of pump and Stokes beam.

Diffraction limit of lens

Optical microscopy observes light diffractions from samples using an objective lens. When the light hits some obstacle, the direction of light propagation changes. Some of the light goes around the back of the obstacle. This phenomenon is called the diffraction of light. Here, to describe the spatial resolution of optical microscopy, I assume a slit as an obstacle and a plane wave as light. When a plane wave passes through the slit, the wavefront becomes a spherical wave due to diffraction. The narrower the slit and the longer the wavelength, the larger the diffraction angle. The fine structure of a sample can be seen as a collection of narrow slits in different directions. How much we can see the detail of the sample by optical microscope can be rephrased as how much we can collect the diffraction lights from the sample. However, there is a limitation of collectible diffraction angle by a lens. Fig.4.2 shows a simple schematic of imaging property of lights by a lens, where λ is the wavelength of light, d' and d are slit width, n is the refractive index of imaging field, α' and α are diffraction angles, and NA is numerical aperture of the lens, defined as $n \sin \alpha$. In Fig.4.2(a), a diffraction light with angle α' is not collected by the lens; thus, this slit cannot be observed clearly with the lens. Using a shorter wavelength or larger lens to collect lights with a larger diffraction angle can image the narrow slit. In Fig.4.2(b), the slit d has a larger width than that of (a) so that the diffraction angle α match with the angle of numerical aperture. This slit width is the smallest width that the lens can image. Abbe defined

the spatial resolution of the lens as the smallest slit width $d = \lambda/NA$. Later, Rayleigh defined the spatial resolution as

$$d = \frac{0.61\lambda}{NA} \tag{4.12}$$

This distance corresponds to the minimum distance when two adjacent points can be resolved at the imaging plane.

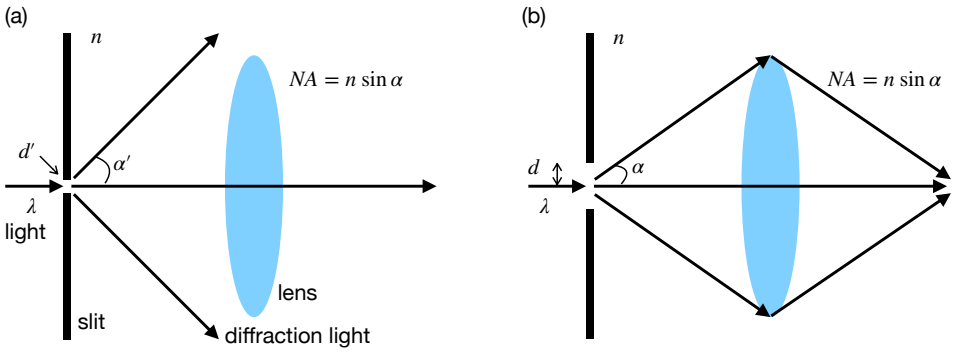

Figure 4.2. Imaging of light by a lens with (a) $\lambda/d' > NA$ and (b) $\lambda/d = NA$.

Optical microscopy with visible or NIR laser has been suffering from the spatial resolution limitation mentioned above. Assuming the wavelength of the laser is 532 nm, and NA is 1.27, the spatial resolution can be 255 nm. This means that we cannot observe a smaller structure than around 250 nm in detail under this condition. Recently, many techniques to overcome the limitation have been proposed, which are generally called super-resolution microscopy.[182, 183, 184, 185] In this study, one of the techniques called differential saturated excitation (dSAX) microscopy[177, 178] is used to improve the spatial resolution in SRS microscopy, as the method does not require a complex optical setup and can be applied to conventional SRS microscopy.

Differential saturated excitation (dSAX) microscopy for higher spatial resolution

SAX microscopy, including differential excitation SAX (dSAX), has been demonstrated in many kinds of saturation responses such as fluorescent light,[185, 178] scattering light from gold nanoparticles,[186] and CARS from diamond particles[176] for higher spatial resolution. The principle of dSAX microscopy is illustrated in Fig.4.3. Here, assume that we observe a finite small light scattering from the sample by SRS microscopy. The obtained SRS signal has a Gaussian shape with a linear response to the excitation intensity without a saturation signal. As the excitation intensity increases, the central part of the SRS signal no longer follows the linear SRS response in the absence of saturation (illustrated by the blue region). Thus, the extracted saturated signal, the so-called differential signal, has a smaller FWHM than the other SRS signals.

The saturated SRS signal can be expressed as the combination of linear term and nonlinear terms as

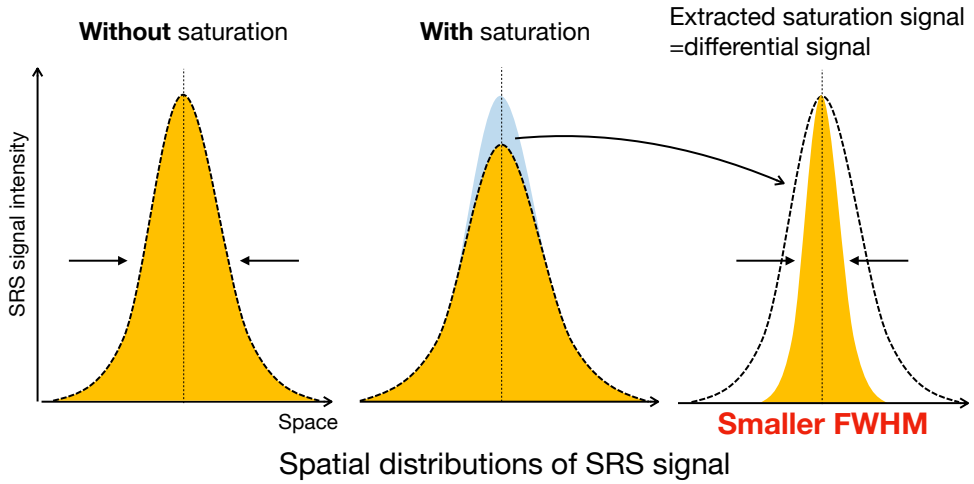

Figure 4.3. Idea of differential saturated-excitation microscopy. Left, and center figures show the PSFs of SRS microscopy with and without saturation signal. Right figure shows the extracted saturation signal of SRS calculated from the other two SRS signals.

shown in the following equation.

$$\begin{aligned} SRS(I_{ex}) &= a_1 I_{ex} + a_2 I_{ex}^2 + a_3 I_{ex}^3 + \cdot\cdot\cdot \\ &= SRS_L(I_{ex}) - SRS_{NL}(I_{ex}) \end{aligned} \tag{4.13}$$

where $SRS(I_{ex})$, a_n, and I_{ex} represent the SRS intensity, the imaginary part of the third-order susceptibility, and the excitation intensity produced by the intensities of pump and Stokes beams, respectively. SRS_L and SRS_NL represent the linear term and nonlinear terms in the equation.

Fig.4.4 explains how to calculate the differential signal (= extracted saturation signal) by using the relationship between excitation intensity and SRS signal intensity under the saturation response. Here assuming that only 2nd-order nonlinear response is observed with a lower degree of saturation. To obtain the differential signal, $SRS_{NL}^{(2)}$, two SRS signals at different excitation intensities are required: one, SRS_1 does not contain saturated signal illustrated in the left side of a red dot at excitation intensity of I_{ex1}, and the other one, SRS_2 contains saturation signal obtained at excitation intensity of I_{ex2}. If the SRS signal shows only linear response, the virtual SRS signal with the linear response is calculated as $(I_{ex2}/I_{ex1}) \times SRS_1$. At last, the 2nd-order nonlinear signal, $SRS_{NL}^{(2)}$, can be calculated as follows.

$$\begin{aligned} SRS_{NL}^{(2)}(I_{ex2}) &= SRS_L(I_{ex2}) - SRS(I_{ex2}) \\ &= \left(\frac{I_{ex2}}{I_{ex1}}\right) \times SRS_1 - SRS_2 \end{aligned} \tag{4.14}$$

where SRS_1 and SRS_2 are the SRS signals at the excitation intensity of I_{ex1} and I_{ex2}, respectively.

In the same manner, we can extract higher order saturated SRS signal for further spatial resolution improvement. To extract 3rd-order nonlinear SRS signal, SRS signals with 3 different excitation inten-

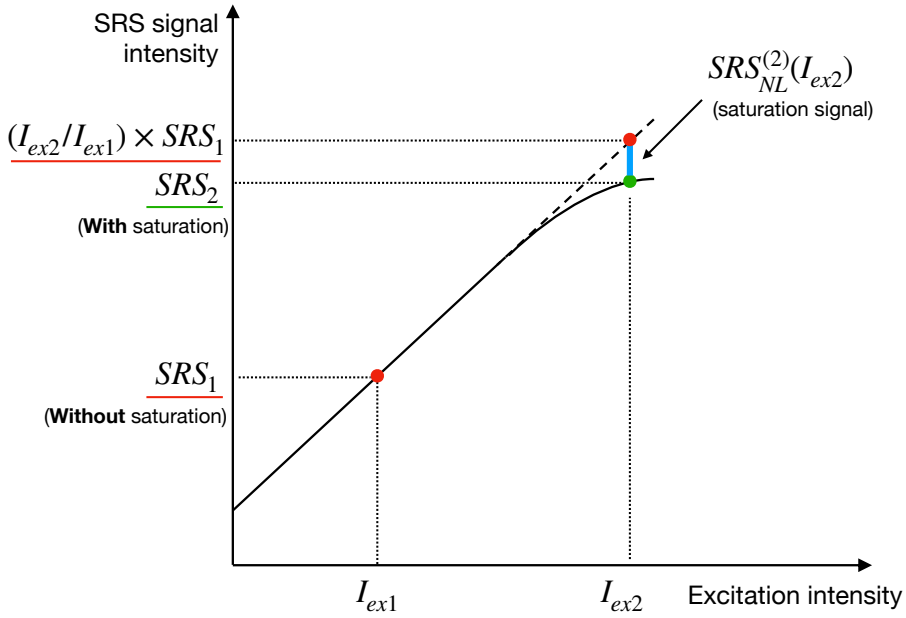

Figure 4.4. Relationship of excitation intensity and SRS signal intensity with saturation response, and how to extract the saturation signal.

sities at I_{ex1}, I_{ex2}, and I_{ex3} have to be obtained. The 3rd-order nonlinear SRS signal can be extracted by following equation.[178]

$$\begin{aligned} SRS_{NL}^{(3)}(I_{ex3}) &= SRS_{NL}^{(2)}(I_{ex3}) - SRS_L(I_{ex3}) + SRS(I_{ex3}) \\ &= \left(\frac{I_{ex2}^2}{I_{ex1}^2}\right)\left[\left(\frac{I_{ex2}}{I_{ex1}}\right) \times SRS_1 - SRS_2\right] - \left(\frac{I_{ex3}}{I_{ex1}}\right) \times SRS_1 + SRS_3 \end{aligned} \tag{4.15}$$

where SRS_1, SRS_2 and SRS_3 are the SRS signals at the excitation intensity of I_{ex1}, I_{ex2} and I_{ex3}, respectively.

Simulation of electric distribution of SRS signal

Theoretical estimation of spatial resolution improvement was performed using the dSAX technique on SRS microscopy. The calculation of 3D electric field distribution was based on the discussion "Electromagnetic diffraction in optical systems Ⅱ. Structure of the image field in an aplanatic system" by B. Richards and E. Wolf.[187] I also thank Dr. Oketani and Dr. Giulia for helping me with the simulation. A water immersion objective lens with 60x and NA1.2 was used for the calculation, the same as an actual setup. The intensity of Stokes beam was 1x10^{10} W/cm^2 and pump beam was 1x10^8 W/cm^2. The wavelength of pump and Stokes beams were 931.88 and 1064 nm, and the refractive index was 1.333. Then, to calculate the SRS signal, I inserted the electric distribution of pump and Stokes beams $I_p(x,y,z), I_S(x,y,z)$ into Eqs.4.9, 4.10 and 4.11. Fig.4.5(A) shows the electric field distributions of the pump and Stokes beams and the SRS signal generated by the two beams, respec-

tively. Fig.4.5(B) and (C) show the line profiles in x- and z-directions. The SRS signal shows a smaller spot than the other two beams since SRS occurs at the center part of the focal spots due to the nonlinear process.

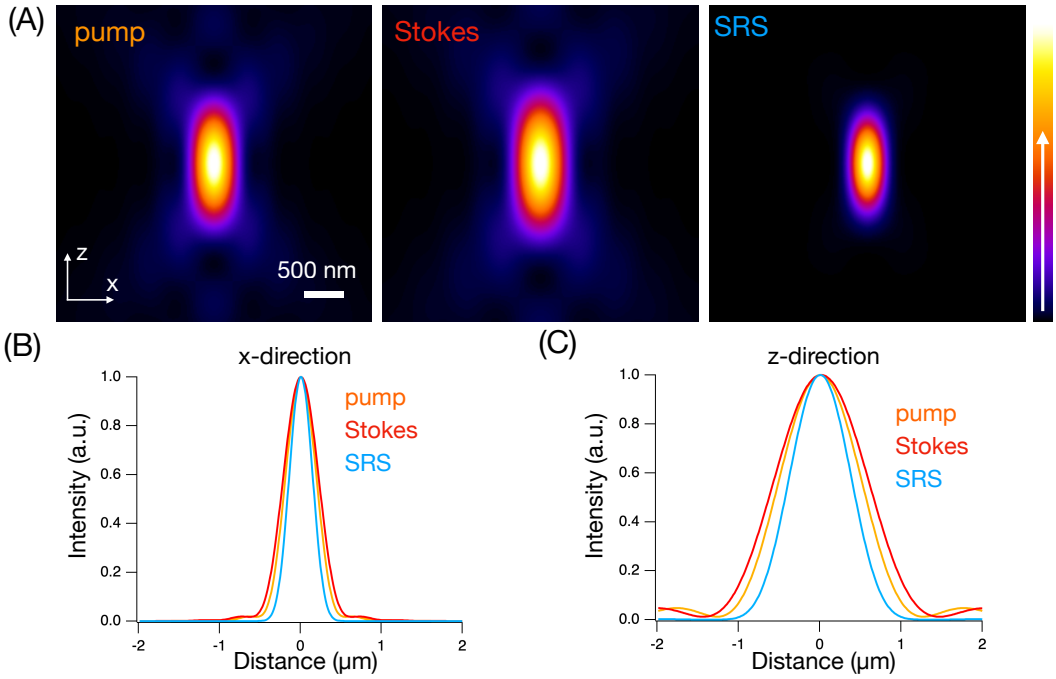

Figure 4.5. PSF calculations of pump, Stokes, and SRS signals. (A) Electric distribution of pump and Stokes beams, and the distribution of SRS signal. The scale bar is 500 nm. (B), (C) Line profiles in x- and z-direction of each intensity distribution. Orange, red and blue lines are pump, Stokes beam, and SRS signal, respectively.

Spatial resolution improvement in SRS microscopy with dSAX technique

In order to theoretically confirm the spatial resolution improvement in SRS microscopy by dSAX technique, I calculated 2nd- and 3rd-order nonlinear SRS signals. Fig.4.6(A) shows the calculated SRS signal when observed a diamond particle, which is same figure with Fig.4.1. To perform the dSAX calculation, two excitation intensities were chosen: $1x10^{18}$ W^2/cm^4 without saturation, $5x10^{20}$ W^2/cm^4 with saturation. Fig.4.6(B) shows the calculation results of the spatial distribution of SRS signal at the selected excitation intensities, and the spatial distribution of 2nd-order SRS signals. Obviously 2nd-order SRS signal has smaller spatial distributions than the normal SRS signal. Fig.4.6(C) and (D) shows the line profile in x- and z-directions. Red, green and black lines are SRS signal intensity at $1x10^{18}$ W^2/cm^4, $5x10^{20}$ W^2/cm^4 and 2nd-order nonlinear SRS signals, respectively. In x-direction, FWHM of SRS without saturation, with saturation, and calculated 2nd-order SRS signal were 328, 401, and 249 nm, respectively. In z-direction, they were 844, 1042, and 646 nm, respectively. The spatial resolution was improved by dSAX technique by 1.31 compared with SRS signal at $1x10^{18}$

W^2/cm^4.

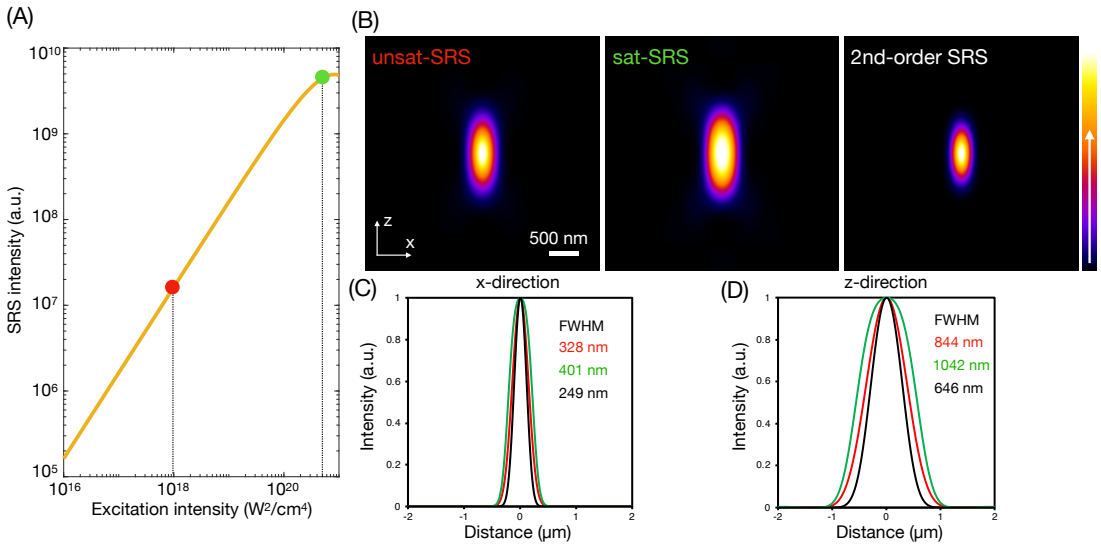

Figure 4.6. Calculation of PSFs of SRS signals with dSAX technique. (A) Calculated SRS signal intensity as a function with a product of excitation intensity of pump and Stokes beam. (B) Spatial distributions of SRS signal intensity at 1x10^{18} W^2/cm^4, 5x10^{20} W^2/cm^4, and 2nd-order nonlinear SRS signals when a diamond particle was observed as a sample. The scale bar is 500 nm. (C) and (D) are the line profiles in x- and z-directions. FWHMs were calculated from the gaussian fitting functions.

4.3 Experimental evaluation of spatial resolution improvement

Optical setup of SRS microscopy

Fig.4.7 shows intensity modulation SRS microscopy that I developed for this research. This setup used two laser pulses with 6-7 ps of pulse width and 76 MHz of repetition rate. As a Stokes beam, I used a 1064 nm laser pulse (picoTRAIN, High Q Laser, Austria) as a Stokes beam, and a wavelength-tunable laser pulse with 720-990 nm (Levante Emerald, Applied Physics & Electronics, Inc., Germany) as a pump beam. A function generator (WF 1974, NF) sent a 2 MHz sinusoidal signal to an acousto-optic modulator (AOM, 3080-197, Crystal Technology, Inc., USA) to modulate the intensity of 1064 nm Stokes beam at 2 MHz. The length of the optical path for the pump beam was changed with a delay line. Two laser pulses were temporally and spatially overlapped at the dichroic mirror (DM, LP1000, Asahi Bunko, Japan). The two beams were coupled into an inverted microscope (ECLIPSE Ti, Nikon, Japan) after 2D scanning galvano-mirrors. Two water immersion objective lenses (UPlanSApo 60X NA1.2, Olympus, Japan) were used to illuminate and detect beams. Two optical bandpass filters (Semrock 850/310, BrightLine) were used to block the transmitted Stokes beam after the collection objective lens. The 2 MHz modulated pump beam was detected by a large area fast photodetector (DET36A, Thorlabs). The output signal was electrically filtered by a lowpass filter (EF526, Thorlabs), a bandpass filter (KR electronics), and a highpass filter (EF517, Thorlabs) to reduce the noises, large

DC offset, and 76 MHz signals. Then, the filtered signals were detected by a fast lock-in amplifier (SR844, Stanford Research Systems, USA) with the 2 MHz reference signal from the function generator to demodulate the SRL signal. A two-dimensional SRS image was reconstructed with a home-built LabView software on PC synchronized with the galvanometer-mirror scanning.

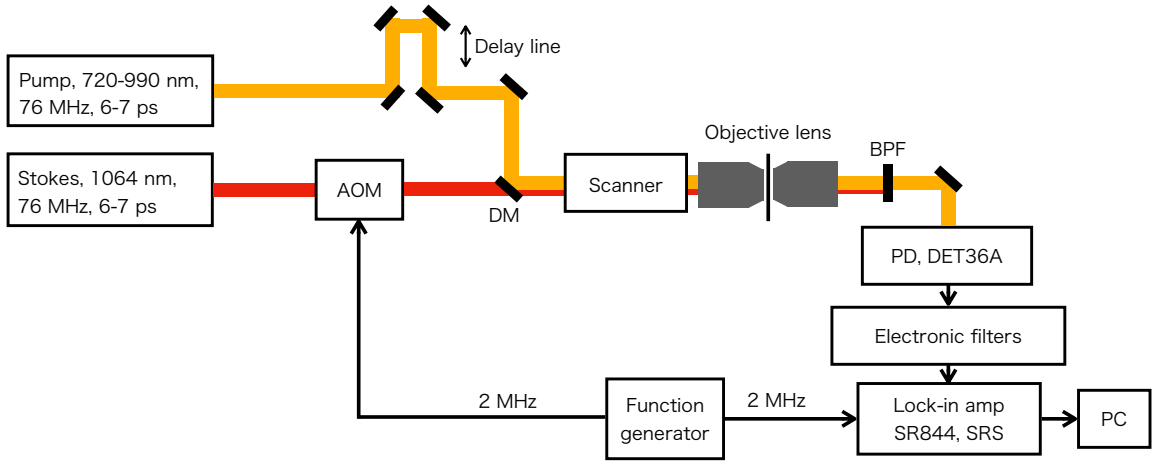

Figure 4.7. Optical setup of SRS microscopy.

SRS imaging of diamond particles

To demonstrate the applicability of the technique, I performed SRS imaging of diamond particles with a diameter of 3-5 μm (Tomei Diamond). I put diamond particles on MAS-coat cover glass with water and dried them. Then, the cover glass with diamond particles was sandwiched with another cover glass. Since the resonant frequency of diamond particles is 1332.5 cm^{-1}, the wavelength of the pump beam was tuned at around 932 nm. Thus the difference between the frequencies of Stokes and pump was the same as the resonant frequency of diamond particles. During the measurement, I fixed the peak intensity of Stokes beam at 2.80x10^9 W/cm^2 and gradually increased only the intensity of pump beam from 9.80x10^8 to 1.57x10^{10} W/cm^2 at every image acquisition. The pixel number was 128x128 with a pixel dwell time of 200 μs. The acquisition time was 3.3 s/frame. Fig.4.8 shows SRS images obtained at 10 different excitation intensities. The SRS signals from two diamond particles were used to obtain a relation between excitation intensity and SRS signal intensity of the diamond particles.

Fig.4.9(A) shows relationship between the average intensity of SRS signal from the two diamond particles shown in Fig.4.8 and the product of excitation intensities. In low intensity region, the measured signals behave linearly with the excitation intensity. The saturation effect started from around 2x10^{19} W/cm^2 of the excitation intensity, which was similar to the theoretical estimation. In order to calculate the differential SRS signal, I selected two SRS images: red one (B) is for SRS image with almost linear response at 1.37x10^{19} W^2/cm^4, and green one (C) is for SRS image with saturated signals

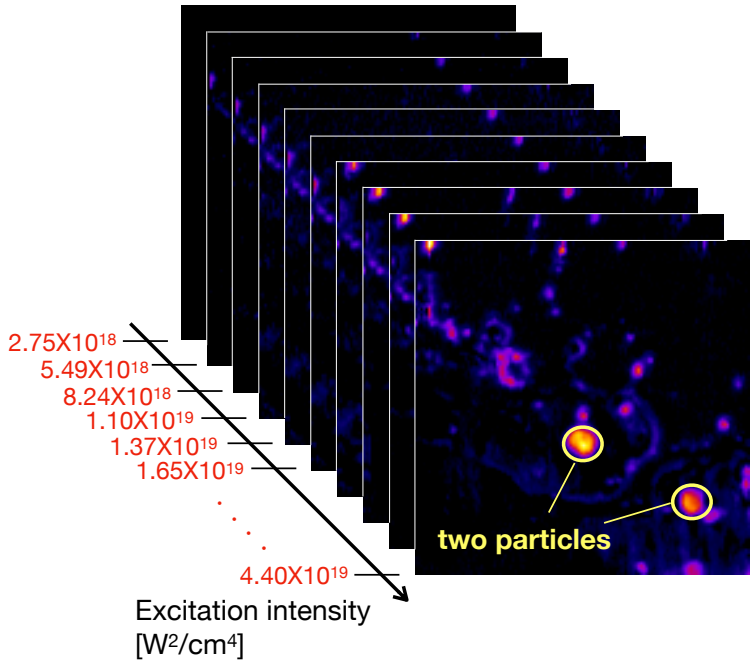

Figure 4.8. Schematic of SRS imaging procedure. Two diamond particles were selected for calculating the relation between the excitation intensity and SRS signal.

at 4.40x10^{19} W^2/cm^4. I calculated the 2nd-order differential SRS image as shown in Fig.4.9(D). The difference is clearly seen from the line profile obtained between the yellow arrows. The gap between the two crystals is clearly separated and the size of each crystal is smaller, although the signal level is reduced due to differential calculations and less saturated signals compared to unsaturated signals.

Next, I performed the differential calculation at four different saturated points to understand the relationship between SNR and spatial resolution of differential SRS images. Fig.4.10(A) shows the relationship between the SRS signals from diamond particles and excitation intensity. I chose an open-red dot (B) in Fig.4.10(A) for unsaturated SRS signals, and open-green dots (C)-(F) in Fig.4.10(A) were chosen for saturated SRS signals. The result of the differential calculation is shown in Fig.4.10(C)-(F). SRS image of (B) is the original SRS image, and SRS image of (C)-(F) is the 2nd-order SRS images calculated from SRS images at the excitation intensity at (B) and (C)-(F) illustrated in Fig.4.10(A). The contrast of all SRS images was unified. The amount of extracted SRS signals was small at lower excitation intensity, such as (C) and (D). In contrast, since the degree of saturation becomes large at higher excitation intensity, such as (E) and (F), the differential SRS images contain more saturated SRS signals than those in (C) and (D). To evaluate the resolution improvement in each SRS image, I measured the intensity profile of the diamond particle illustrated as a yellow arrow in Fig.4.10(A). Fig.4.11 shows the intensity profiles of each SRS image. Red dots are raw intensity at the pixels, and red lines are Gaussian functions fitted to the raw data. Although FWHM of the intensity profile in (C) became smaller than in (F) by a factor of 1.36, the SNR was larger in (F) than in (C). Therefore,

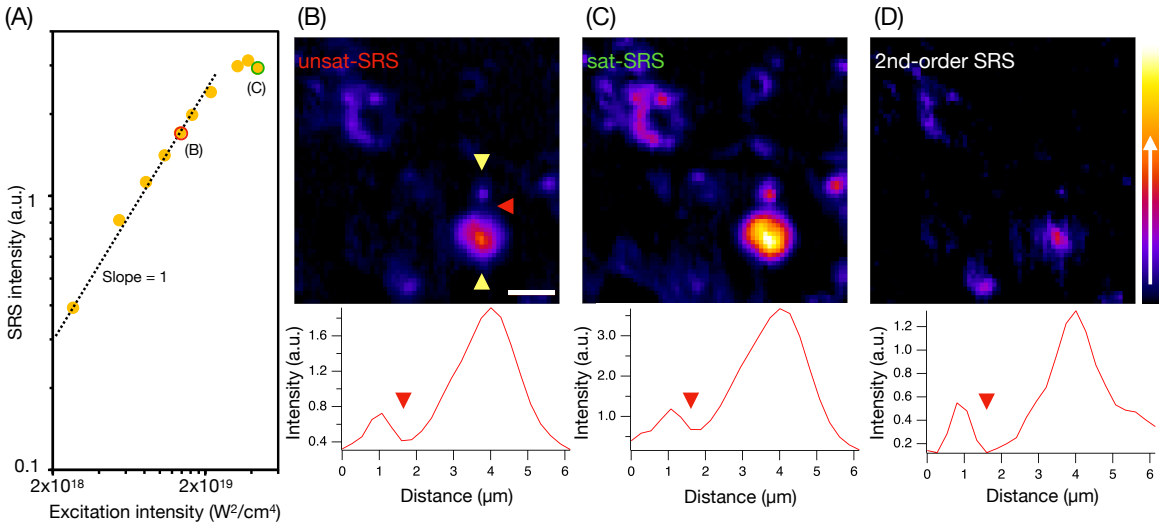

Figure 4.9. SRS imaging of diamond crystals with different excitation intensities. (A) Relation between the average intensity of SRS signals from two diamond particles and incident excitation intensity. SRS image of diamond particles (B) at 1.37x10^{19} W^2/cm^4, (C) at 4.40x10^{19} W^2/cm^4, and (D) 2nd-order saturated SRS image calculated from the two images. Bottom graphs are line profiles of yellow arrowed area in each image. Scale bar is 3 μm. Pixel dwell time was 200 μs. Pixel number is 63x63 cropped from the original images with 128x128.

in the dSAX method, there is a trade-off between the spatial resolution improvement and the image contrast (SNR). It is important to select appropriate images for dSAX calculation to obtain a higher spatial resolution with sufficient SNR.

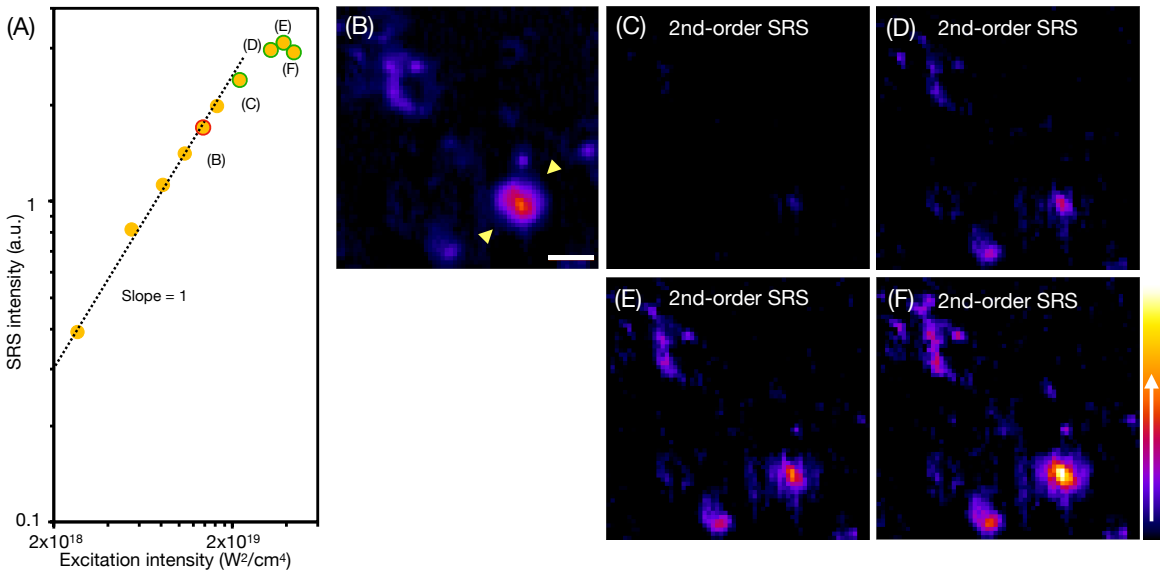

Figure 4.10. Applying dSAX for saturated SRS images obtained with different excitation intensities. (A) Relation between the average intensity of SRS signals from two diamond particles and incident excitation intensity. (B) SRS images of diamond particles at 1.37x10^{19} W^2/cm^4, (C)-(F) differential SRS images of diamond particles calculated from SRS image at the excitation intensity at (B) and (C)-(F) in (A). Scale bar is 3 μm. Pixel dwell time was 200 μs. Pixel number is 63x63 cropped from the original images with 128x128.

SRS imaging of PMMA beads

As well as diamond particles, I demonstrated SRS imaging with 1-10 μm PMMA beads. I tuned the wavelength of the pump beam to 810 nm to match with the resonance frequency of PMMA beads at around 2947 cm^{-1}. Same with the SRS imaging of diamond particles, PMMA beads were placed on a MAS coated cover glass and imaged by the SRS microscope. I obtained 20 SRS images at the same field of view with 20 different excitation intensities. Fig.4.12(A) shows the relation between the average intensity of SRS signals from seven PMMA beads and incident excitation intensity. The saturation response of SRS from PMMA beads was successfully observed at the higher excitation intensity. In order to calculate the differential SRS image, I chose two SRS images at different excitation intensities from Fig.4.12: red one (B) is for the SRS image with linear response at 3.04x10^{21} W^2/cm^4, and green one (C) is for the SRS image containing saturated signal at 4.08x10^{21} W^2/cm^4. Fig.4.12(D) is the 2nd-order differential SRS image calculated from the two SRS images. All images were unified to the same image contrast. The two beads were separated in (D) by the differential calculation. This is because the signal between the two beads had nothing to do with the SRS saturation response of PMMA beads. Thus, differential calculation from the two SRS images effectively removed these background signals, resulting in a higher spatial resolution.

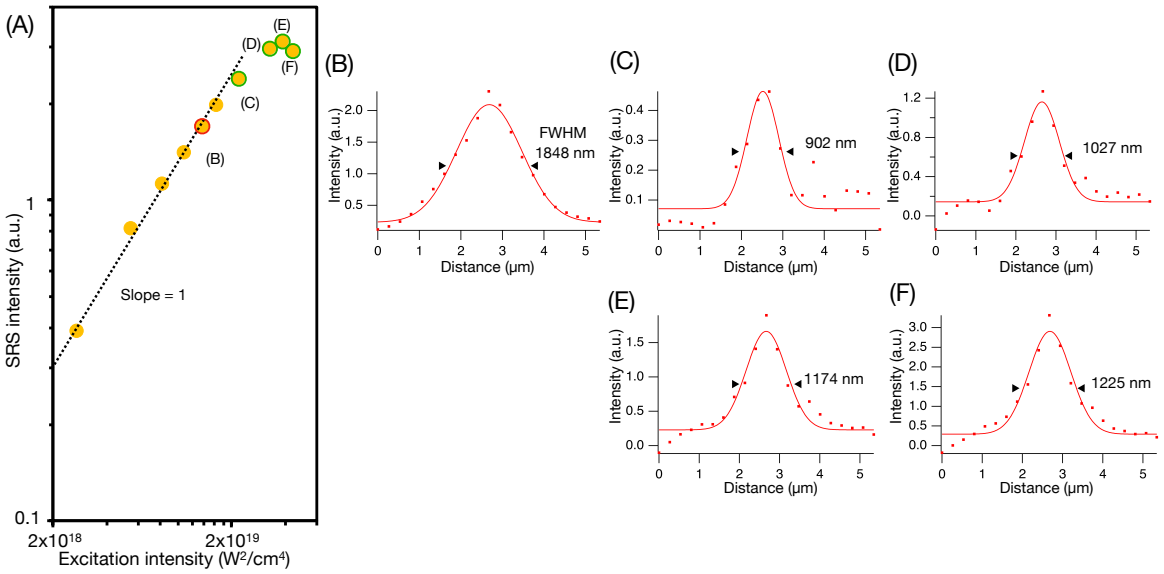

Figure 4.11. Line profiles of the 2nd-order SRS signals. (A) Relation between the average intensity of SRS signals from two diamond particles and incident excitation intensity. (B)-(F) Line profiles of the SRS signal intensity between yellow arrows illustrated in Fig.4.10. Red dots are raw data and red lines are gaussian fitting function to the raw data. Each FWHM was calculated from a gaussian fitting function.

Discussion and Conclusion

I theoretically and experimentally confirmed the spatial resolution improvement in SRS microscopy by extracting saturated SRS signals. The proposed technique does not need additional optics to achieve a resolution improvement. Thus, it can be easily applied to conventional SRS microscopy. In addition, unlike other super-resolution fluorescence microscopy, the proposed approach is label-free. Photobleaching does not occur during the measurement. However, photodamage should be carefully characterized and minimized for living-cell super-resolution SRS imaging.[188] For this purpose, the pixel dwell time and excitation intensity are critical factors to be considered. In addition, since this technique requires multiple SRS images with different excitation intensities, image artifacts may appear in the computed super-resolution SRS image if the sample can move during the measurement. Some methods should be applied for live-cell imaging using saturated SRS microscopy. Since no modifications to the optical setup are required, this easy-to-use method could lead to a super-resolution Raman imaging platform for label-free and vibrational tags imaging of living cells and tissues. A group in Singapore published a paper on super-resolution SRS microscopy with a similar idea in 2019.[188] Their work is well described from theoretical assessment to experimental results of super-resolution saturated SRS imaging of living HeLa cells. Besides the attempts to achieve super-resolution SRS microscopy with NIR laser source, two groups from China and USA recently demonstrated visible-wavelength SRS microscopy beyond the diffraction limit by NIR laser.[189, 190] They achieved a spatial resolution of around

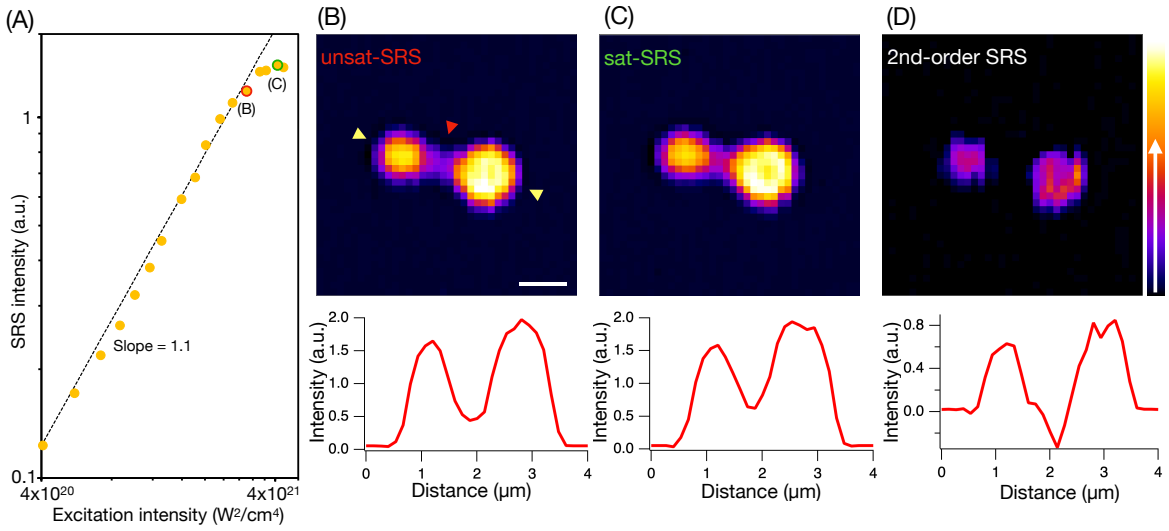

Figure 4.12. SRS imaging of PMMA beads with different excitation intensities. (A) Relation between the average intensity of SRS signals from two PMMA beads and the excitation intensity. Yellow dots show the measured value of SRS signal intensity, behaving linearly in lower excitation intensity. SRS images of PMMA beads at (B) 3.04x10^{21} W^2/cm^4, at (C) 4.08x10^{21} W^2/cm^4, and (D) 2nd-order saturated SRS image calculated from the two images. Bottom graphs are line profiles of yellow arrowed area in each image. Scale bar is 1 μm. Pixel dwell time was 500 μs. Pixel number is 38x38.

130 nm with visible-wavelength excitation with a high numerical aperture (NA) of 1.49. Also, near-resonance (or pre-resonance) of electronic transition by visible excitation can help the improvement of the detection sensitivity of molecules. Currently (as of Jan. 2022), no further papers have broken the diffraction barrier at visible wavelengths since the publication of these two papers. Therefore, further improvements of spatial resolution at visible wavelengths may expand the applications of SRS microscopy. The next chapter presents my first experimental (but failed) attempts of super-resolution visible wavelength SRS microscopy based on the dSAX technique.

Appendix

Classical theory of SRS

Calculations and discussions are mainly based on "Nonlinear optics" by Boyd[191] and "Tutorial: Coherent Raman light matter interaction processes" by Rigneault.[192] Now assuming that molecular vibration is interacting with the applied electric field by laser, the vibrational mode is written as a simple harmonic oscillator with a resonance frequency of ω_v and damping constant Γ. The equation of molecular vibration is thus written as

$$\frac{d^2\tilde{q}}{dt^2} + 2\Gamma\frac{d\tilde{q}}{dt} + \omega_v^2\tilde{q} = \frac{\tilde{F}(t)}{m} \tag{4.16}$$

where $\tilde{q}$ is the deviation of the internuclear distance from the equilibrium position q_0, $\tilde{F}(t)$ indicates any forces induced by such as irradiated electromagnetic fields, and m is a nuclear mass of the molecule. As I mentioned in Chapter 1, the Raman scattering process is described by time-changing optical polarizability, and the concept is the same in SRS. We now assume the optical polarizability $\tilde{\alpha}(t)$ of the molecule depends on $\tilde{q}$.

$$\tilde{\alpha} = \alpha_0 + \Big(\frac{\partial\alpha}{\partial q}\Big)_0\tilde{q}(t) \tag{4.17}$$

where α_0 is the polarizability at the equilibrium position q_0. This equation shows that when the molecule starts to oscillate at a specific frequency, its polarization will also be modulated in time. Next, I assume the situation when the optical field $\tilde{E}(z,t)$ is applied to the molecular vibration. Each molecule will be polarized with the optical field, and then the dipole moment will be induced, as shown in the following equation.

$$\tilde{\mathbf{p}}(\mathbf{z},\mathbf{t}) = \epsilon_\mathbf{0}\alpha\tilde{\mathbf{E}}(\mathbf{z},\mathbf{t}) \tag{4.18}$$

This dipole moment has the potential energy which is given by

$$W = -\frac{1}{2}\left\langle\tilde{\mathbf{p}}(\mathbf{z},\mathbf{t})\bullet\tilde{\mathbf{E}}(\mathbf{z},\mathbf{t})\right\rangle = -\frac{1}{2}\epsilon_0\alpha\left\langle\tilde{E}^2(z,t)\right\rangle \tag{4.19}$$

where the brackets indicate that the energy is time-averaged value. Since the energy is calculated by multiplying force by distance, the optical field generates force which is given by

$$\tilde{F} = -\Big(\frac{dW}{dq}\Big) = +\frac{\epsilon_0}{2}\Big(\frac{\partial\alpha}{\partial q}\Big)_0\left\langle\tilde{E}^2(z,t)\right\rangle \tag{4.20}$$

Eq.4.20 shows if the applied optical field contains two frequency components, that is, in the case of stimulated Raman scattering process, and the vibration molecule will be exposed to a time-varying force at the beat frequency of two components. This optical field generates a strong stimulated Raman scattering process.

Assuming two frequency components are applied to the molecule. Total optical fields can be illustrated as

$$\tilde{E}(z,t) = E_p \exp(i(k_p z - \omega_p t)) + E_S \exp(i(k_S z - \omega_S t)) + c.c. \tag{4.21}$$

where $c.c.$ is the complex conjugate. From Eq.4.20 and Eq.4.21, the time-variant optical force onto the molecule is given by

$$\tilde{F} = \frac{\epsilon_0}{2}\Big(\frac{\partial \alpha}{\partial q}\Big)_0 \langle \tilde{E}^2(z,t)\rangle = \epsilon_0 \Big(\frac{\partial \alpha}{\partial q}\Big)_0 \big[E_p E_S^* \exp(i(Kz - \Omega t)) + c.c.\big] \tag{4.22}$$

where

$$K = k_p - k_S \text{ and } \Omega = \omega_p - \omega_S \tag{4.23}$$

Now we are going to find the solution for Eq.4.16 with a force term of Eq.4.22. Beforehand, assume that a solution will be the following form.

$$\tilde{q} = q(\Omega) \exp(i(Kz - \Omega t)) + c.c. \tag{4.24}$$

Then we insert Eq.4.22 and Eq.4.24 into Eq.4.16, and we can get

$$-\Omega^2 q(\Omega) - 2i\Omega\Gamma q(\Omega) + \omega_v^2 q(\Omega) = \frac{\epsilon_0}{m}\Big(\frac{\partial \alpha}{\partial q}\Big)_0 E_p E_S^* \tag{4.25}$$

We then find that the deviation of the molecular vibration can be expressed as

$$q(\Omega) = \frac{(\epsilon_0/m)(\partial\alpha/\partial q)_0 E_p E_S^*}{\omega_v^2 - \Omega^2 - 2i\Omega\Gamma} \tag{4.26}$$

At near resonance where $\omega_v \approx \Omega$, Eq.4.26 is simply written as follows

$$\begin{aligned} q(\Omega) &= \frac{(\epsilon_0/m)(\partial\alpha/\partial q)_0 E_p E_S^*}{\omega_v^2 - \Omega^2 - 2i\Omega\Gamma} = \frac{(\epsilon_0/m)(\partial\alpha/\partial q)_0 E_p E_S^*}{(\omega_v - \Omega)(\omega_v + \Omega) - 2i\Omega\Gamma} \\ &\simeq \frac{(\epsilon_0/m)(\partial\alpha/\partial q)_0 E_p E_S^*}{2\omega_v(\omega_v - \Omega) - 2i\omega_v\Gamma} = \frac{-(\epsilon_0/2m\omega_v)(\partial\alpha/\partial q)_0 E_p E_S^*}{(\Omega - \omega_v) + i\Gamma} \end{aligned} \tag{4.27}$$

When we assume that other molecules are also collectively oscillating at the same time and polarized in the same manners, the polarization of the molecules is given from Eq.4.17 and Eq.4.18 and written as

$$\begin{aligned} \tilde{P}(z,t) &= N\tilde{p}(z,t) = \epsilon_0 N \tilde{\alpha}(z,t)\tilde{E}(z,t) \\ &= \epsilon_0 N\big[\alpha_0 + \Big(\frac{\partial \alpha}{\partial q}\Big)_0 \tilde{q}(t)\big]\tilde{E}(z,t) \end{aligned} \tag{4.28}$$

Since SRS is the third-order nonlinear process, we have to consider the nonlinear part of the polarization Eq.4.28. Thus, with Eq. 4.21, Eq.4.24 and Eq.4.28, nonlinear part of the polarization, that is, the

polarization which depends on $q(\Omega)$ is given by

$$\tilde{P}^{NL}(z,t) = \epsilon_0 N\Big(\frac{\partial\alpha}{\partial q}\Big)_0 \big[q(\Omega)\exp(i(Kz-\Omega t)) + c.c.\big] \\ \times \big[E_p\exp(i(k_p z-\omega_p t)) + E_S\exp(i(k_S z-\omega_S t)) + c.c.\big] \tag{4.29}$$

As you see, the nonlinear polarization has several frequency components. In particular the part of the components that oscillates at frequency ω_S is called as the Stokes polarization, which is given by

$$\tilde{P_S}^{NL}(z,t) = P(\omega_S)\exp(-i(\omega_S t)) + c.c. \tag{4.30}$$

where $P(\omega_S)$ is given by

$$P(\omega_S) = \epsilon_0 N\Big(\frac{\partial\alpha}{\partial q}\Big)_0 q^*(\Omega)E_p\exp(ik_S z) \tag{4.31}$$

Inserting Eq.4.24 into Eq.4.31 brings us the complex amplitude of the Stokes polarization given by

$$P(\omega_S) = \frac{(-\epsilon_0^2 N/2m\omega_v)(\partial\alpha/\partial q)_0^2|E_p|^2E_S}{(\Omega-\omega_v)-i\Gamma}\exp(ik_S z) \tag{4.32}$$

In general, the polarization of the medium in optical field caused by intense laser can be represented as follows.

$$\boldsymbol{P}(\omega) = \epsilon_0\chi^{(1)}(\omega)\boldsymbol{E}(\omega) + \epsilon_0\chi^{(2)}(\omega)\boldsymbol{E}^{(2)}(\omega) + \epsilon_0\chi^{(3)}(\omega)\boldsymbol{E}^{(3)}\cdot\cdot\cdot \tag{4.33}$$

where $\boldsymbol{P}$ is the macroscopic polarization electric field, $\chi^{(i)}$ is the i-th order of dielectric nonlinear susceptibility of the medium, and $\boldsymbol{E}$ is irradiated electric field which comes from pump and Stokes beam. Thus, Eq.4.32 represents the Stokes polarization containing the third-order susceptibility, which is given by

$$\chi_R^{(3)}(\omega_S) = \chi^{(3)}(\omega_S = \omega_S + \omega_p - \omega_p) = \frac{(-\epsilon_0 N/12m\omega_v)(\partial\alpha/\partial q)_0^2}{(\Omega-\omega_v)-i\Gamma} \tag{4.34}$$

In the same manner, we can calculate the third order susceptibility of the pump polarization.

$$\chi_R^{(3)}(\omega_p) = \chi^{(3)}(\omega_p = \omega_S + \omega_p - \omega_S) = \frac{(-\epsilon_0 N/12m\omega_v)(\partial\alpha/\partial q)_0^2}{(\Omega-\omega_v)+i\Gamma} \tag{4.35}$$

With Eq.4.34, the Stokes polarization is represented as follows

$$P(\omega_S) = 6\epsilon_0\chi^{(3)}(\omega_S)|E_p|^2E_S\exp(ik_S z) \tag{4.36}$$

The third order susceptibility has two components, the real part $\chi_R'(\omega_S)$ and the imaginary part $\chi_R''(\omega_S)$. At the Raman resonance $\omega_S = \omega_p - \omega_v$, where stimulated Raman scattering occurs, the real part becomes zero and only the imaginary part has negative value.

In order to obtain the evolution of the amplitude amplification of the Stokes polarization, I consider the field propagation of the Stokes field[192] generated in a nonlinear medium with length L.

$$\frac{dE_S}{dz} = \frac{i\omega_s}{2n_p\epsilon_0 c}P(\omega_S)\exp(-ik_S z) \tag{4.37}$$

Then we can get a following differential equation for the evolution of the amplitude of the Stokes polarization by inserting Eq.4.36

$$\frac{dE_S}{dz} = \frac{3i\omega_S}{n_S c}\chi_R^{(3)}(\omega_S)|E_p|^2 E_S \exp(i\delta k z) \tag{4.38}$$

The phase components $\delta\boldsymbol{k}$ is always zero, thus in SRS process, the Stokes fields is in phase and coherent in the nonlinear material. We can obtain the Stokes field amplitude by integrating Eq.4.38 from 0 to L

$$E_S(L) = E_S(0)\exp\Big[\frac{3i\omega_S}{n_S c}\chi_R^{(3)}(\omega_S)|E_p|^2 L\Big] \tag{4.39}$$

From, Eq.4.34 and Eq.4.35, we can write $\chi_R^{(3)} = \chi_R^{(3)}(\omega_p) = \chi_R^{(3)}(\omega_S)^*$. In addition, we divide $\chi_R^{(3)}$ into real and imaginary parts. Note that the imaginary part of $\chi_R^{(3)}(\omega_S)$ is always negative.

$$\begin{aligned}
E_S(L) &= E_S(0)\exp\Big[\frac{3i\omega_S}{n_S c}\chi_R^{(3)*}|E_p|^2 L\Big] \\
&= E_S(0)\exp\Big[\frac{3i\omega_S}{n_S c}(\mathrm{Re}(\chi_R^{(3)}) - i\mathrm{Im}(\chi_R^{(3)}))|E_p|^2 L\Big] \\
&= E_S(0)\exp\Big[\frac{3\omega_S}{n_S c}(\mathrm{Im}(\chi_R^{(3)}))|E_p|^2 L\Big]\exp\Big[i\frac{3\omega_S}{n_S c}\mathrm{Re}(\chi_R^{(3)})|E_p|^2 L\Big]
\end{aligned} \tag{4.40}$$

At the resonance, the real part of $\chi_R^{(3)}$ becomes mostly zero. the pump intensity is written as $I_p(z) = 2n_p\epsilon_0 c|E_p|^2$. From Eq.4.40, the Stokes intensity with nonlinear interaction becomes

$$I_S(L) = I_S(0)\exp\Big[\frac{3\omega_S}{2n_p n_S\epsilon_0 c^2}(\mathrm{Im}(\chi_R^{(3)}))I_p(0)L\Big] \tag{4.41}$$

Assuming that the value within the exponential is several tens of magnitude smaller than 1, we can expand Eq.4.41 as follows.

$$I_S(L) = I_S(0) + \frac{3\omega_S L}{2n_p n_S\epsilon_0 c^2}(\mathrm{Im}(\chi_R^{(3)}))I_S(0)I_p(0) \tag{4.42}$$

This means that the Stokes field experiences the intensity growing after the nonlinear material with length L. This mechanism is called "stimulated Raman gain (SRG)," and its intensity is given by

$$\Delta I_{SRG} = b_{SRG}\mathrm{Im}(\chi_R^{(3)})I_p I_S \tag{4.43}$$

where $b_{SRG} \approx 2\text{x}10^2$ at a certain experimental parameters of refractive index $n_p = n_S = 1.3$, wavelength of Stokes beam $\lambda_S = 1064$ nm, focusing area $L = 1\ \mu$m. As we discussed, the intensity change

in the amplitude of the Stokes wave is a positive value (SRG). This transferred energy is originally coming from the energy of the pump wave. This energy loss in the pump wave is called "stimulated Raman loss(SRL)." Contrast to SRG, the intensity change of SRL ΔI_{SRL} becomes negative value and the relationship between SRG and SRL is $\omega_p \Delta I_{SRG} = \omega_S \Delta I_{SRL}$.[192] To detect stimulated Raman scattering, we generally measure the signal intensity of either SRG or SRL.

Reference

174) F. Konig Robert L. Byer M.D. Duncan, P. Oesterun. OBSERVATION OF SATURATION BROADENING OF THE COHERENT ANTI-STOKES RAMAN SPECTRUM (CARS) OF ACETYLENE IN A PULSED MOLECULAR BEAM. *Chemical Physics Letters*, 80(2):253–256, 6 1981.

175) Gaetano Magnotti, Andrew D. Cutler, G. C. Herring, Sarah A. Tedder, and Paul M. Danehy. Saturation and Stark broadening effects in dual-pump CARS of N2, O2, and H2. *Journal of Raman Spectroscopy*, 43(5):611–620, May 2012.

176) Yasuo Yonemaru, Almar F. Palonpon, Shogo Kawano, Nicholas I. Smith, Satoshi Kawata, and Katsumasa Fujita. Super-Spatial- and -Spectral-Resolution in Vibrational Imaging via Saturated Coherent Anti-Stokes Raman Scattering. *Phys. Rev. Applied*, 4:014010, Jul 2015.

177) Ryosuke Oketani, Atsushi Doi, Nicholas I. Smith, Yasunori Nawa, Satoshi Kawata, and Katsumasa Fujita. Saturated two-photon excitation fluorescence microscopy with core-ring illumination. *Opt. Lett.*, 42(3):571–574, Feb 2017.

178) Yasunori Nawa, Yasuo Yonemaru, Atsushi Kasai, Ryosuke Oketani, Hitoshi Hashimoto, Nicholas I. Smith, and Katsumasa Fujita. Saturated excitation microscopy using differential excitation for efficient detection of nonlinear fluorescence signals. *APL Photonics*, 3(8):080805, Aug 2018.

179) W. M. Tolles, J. W. Nibler, J. R. McDonald, and A. B. Harvey. A Review of the Theory and Application of Coherent Anti-Stokes Raman Spectroscopy (CARS). *Appl. Spectrosc.*, 31(4):253–271, Jul 1977.

180) Diane S. Knight and William B. White. Characterization of diamond films by Raman spectroscopy. *Journal of Materials Research*, 4(2):385–393, 1989.

181) R.L. Aggarwal, L.W. Farrar, S.K. Saikin, X. Andrade, A. Aspuru-Guzik, and D.L. Polla. Measurement of the absolute Raman cross section of the optical phonons in type ia natural diamond. *Solid State Communications*, 152(3):204–209, 2012.

182) M. G. L. Gustafsson. Surpassing the lateral resolution limit by a factor of two using structured illumination microscopy. *Journal of Microscopy*, 198(2):82–87, 2019/01/27 2000.

183) Samuel T. Hess, Thanu P.K. Girirajan, and Michael D. Mason. Ultra-High Resolution Imaging by Fluorescence Photoactivation Localization Microscopy. *Biophysical Journal*, 91(11):4258 – 4272, 2006.

184) Michael J Rust, Mark Bates, and Xiaowei Zhuang. Sub-diffraction-limit imaging by stochastic optical reconstruction microscopy (STORM). *Nature Methods*, 3:793 EP –, 08 2006.

185) Katsumasa Fujita, Minoru Kobayashi, Shogo Kawano, Masahito Yamanaka, and Satoshi Kawata. High-Resolution Confocal Microscopy by Saturated Excitation of Fluorescence. *Phys. Rev. Lett.*, 99:228105, Nov 2007.

186) Gitanjal Deka, Kentaro Nishida, Kentaro Mochizuki, Hou-Xian (丁厚獻) Ding, Katsumasa Fujita, and Shi-Wei (朱士維) Chu. Resolution enhancement in deep-tissue nanoparticle imaging based on plasmonic saturated excitation microscopy. *APL Photonics*, 3(3):031301, 2018.

187) E. Wolf B. Richards. Electromagnetic diffraction in optical systems, II. Structure of the image field in an aplanatic system. *Proceedings of the Royal Society of London A: Mathematical, Physical and Engineering Sciences*, 253(1274):358–379, 1959.

188) Li Gong, Wei Zheng, Ying Ma, and Zhiwei Huang. Saturated Stimulated-Raman-Scattering Microscopy for Far-Field Superresolution Vibrational Imaging. *Phys. Rev. Applied*, 11:034041, Mar 2019.

189) Yali Bi, Chi Yang, Yage Chen, Shuai Yan, Guang Yang, Yaozu Wu, Guoping Zhang, and Ping

Wang. Near-resonance enhanced label-free stimulated Raman scattering microscopy with spatial resolution near 130 nm. *Light: Science & Applications*, 7(1):81, 2018.

190) Minghua Zhuge, Kai-Chih Huang, Hyeon Jeong Lee, Ying Jiang, Yuying Tan, Haonan Lin, Pu-Ting Dong, Guangyuan Zhao, Daniela Matei, Qing Yang, and Ji-Xin Cheng. Ultrasensitive Vibrational Imaging of Retinoids by Visible Preresonance Stimulated Raman Scattering Microscopy. *Advanced Science*, 8(9):2003136, 2021.

191) Robert W Boyd. *Nonlinear optics*. Academic press, 2003.

192) Hervé Rigneault and Pascal Berto. Tutorial: Coherent Raman light matter interaction processes. *APL Photonics*, 3(9):091101, 2018.

Chapter 5
Visible-wavelength SRS microscopy toward super-resolution and high-sensitivity vibrational imaging

The contents of this chapter is currently under preparation as:
K. Koike, N. I. Smith, K. Fujita, ”Super-resolution visible-wavelength stimulated Raman scattering microscopy with saturated excitation”, in preparation.

Introduction

This chapter describes the first attempts to break the diffraction limit of visible-wavelength stimulated Raman scattering (VW-SRS) microscopy by exploring the saturation effect of SRS. The spatial resolution of conventional SRS microscopy has been limited to around 300 nm due to NIR laser pulses. Recently, the use of visible-wavelength for SRS microscopy has been proposed and successfully achieved a spatial resolution of about 130 nm.[193, 194] Although the spatial resolution can be improved by a 2-fold compared to the NIR excitation, the spatial resolution of VW-SRS microscopy is still restricted by the diffraction limit of the wavelength used for the imaging. To go beyond this limitation, I try to apply the dSAX technique[195] on the saturation response of VW-SRS signals. I anticipate the spatial resolution of around 110 nm in VW-SRS with dSAX. The VW-SRS optical setup is realized based on the conventional 2-ps SRS microscope developed in Chapter 3. The VW wavelength conversion is performed by using SHG nonlinear crystals. The experimental spatial resolution of VW-SRS microscopy is evaluated with PS beads with 147 nm diameter and fixed HeLa cells. To break the limitation, I try to perform VW-SRS imaging of HeLa cells labeled with the Carbow2086 Lyso probe to demonstrate dSAX for the saturation signal. However, only a significant background signal coming from absorption of cytochrome c and significant photodamage is observed during the measurement. As well as spatial resolution improvement, VW-SRS has strong potential to increase the detection sensitivity via visible pre-resonance SRS process.[194] Hence, the combination of VW-SRS with dSAX and visible pre-resonance will allow super-resolution VW-SRS imaging of molecules with ultra sensitivity.

5.1 Super-resolution visible-wavelength SRS microscopy

Theoretical spatial resolution improvement in VW-SRS microscopy by applying dSAX technique

I performed a theoretical calculation of the VW-SRS signal distribution and compared it with the NIR-SRS. The simulation method and calculation model are the same as I described in Chapter 4. At first, I calculated the 3D electric field distribution for the pump and Stokes beams. Then, with Eqs.4.9, 4.10 and 4.11, the SRS signal distribution (PSF) was simulated. A water immersion objective lens with 60x and NA 1.27 was used for the pump and Stokes beam distribution. The refractive index n was therefore 1.33. The pixel number was 256x256 with 4 μm area. The wavelength of the pump and Stokes beams was 482.45 and 515.6 nm for VW-SRS, and 906.62 and 1031.2 nm for NIR-SRS, to be matched with the vibration mode of diamond crystals at 1332.5 cm^{-1}. The other parameters of diamond crystals were assumed to be the same for the VW-SRS and NIR-SRS calculations (see Chapter 4 for detail). Fig.5.1(a) and (b) show the intensity distributions of the pump and Stokes beams and the resultant SRS signal distribution for NIR-SRS and VW-SRS, respectively. The resultant SRS signal

only occurs at the center of the focal spot due to the nonlinear SRS process by the two beams. The size of the signal spot was smaller in VW-SRS than NIR-SRS due to the shorter wavelength. From the line profiles in x- and z-directions (Fig.5.1(c) and (d)), the full-width at half maximum (FWMH) was calculated based on a gaussian fitting function. FWHM in x-direction was 159 and 307 nm for VW-SRS and NIR-SRS, respectively. The improvement factor is around 1.93. In z-direction, FWHM was 349 and 676 nm for VW-SRS and NIR-SRS, respectively, which indicates the 1.94 times improvement. Although VW-SRS can reach spatial resolution nearly two times compared to NIR-SRS, it is still the diffraction limit of an objective lens.

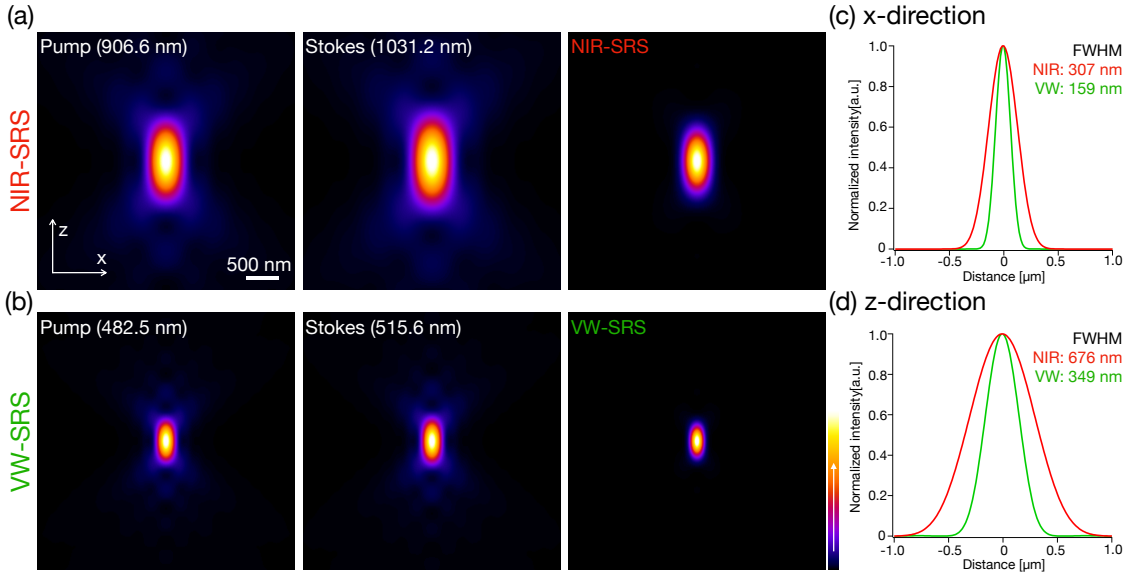

Figure 5.1. Electric distribution of pump and Stokes beams and the distribution of SRS signal under (a) NIR-SRS and (b) VW-SRS excitations. The scale bar is 500 nm. (c) and (d) are the line profiles in x- and z-direction of each intensity distribution.

In order to theoretically confirm the further spatial resolution improvement in VW-SRS microscopy by dSAX technique, I calculated 2nd-order nonlinear SRS signals by considering saturation response of SRS (see Chapter 4 for the detail calculation process). To perform the dSAX calculation, three different excitation intensities were chosen: $5\text{x}10^{19}$ W^2/cm^4 without saturation, $2.5\text{x}10^{22}$ W^2/cm^4 with saturation, with the fixed excitation intensity of Stokes beam at $5\text{x}10^{11}$ W/cm^2. Fig.5.2(a) shows the calculation result. The 2nd-order SRS signal showed the smallest spatial distribution, which indicates the further spatial resolution improvement by dSAX. Fig.5.2(c) and (d) shows the line profiles in x- and z-directions. Red, green, and blue lines are the 2nd-order SRS signal, unsaturated and saturated SRS signal intensity at $5\text{x}10^{19}$ and $2.5\text{x}10^{22}$ W^2/cm^4, respectively. In x-direction, FWHMs of the unsaturated SRS and 2nd-order SRS signal were 159, and 119 nm, respectively. In z-direction, they were 349, and 264 nm, respectively. The spatial resolutions in both directions were improved by a factor of around 1.3. The total improvement compared to the conventional NIR excitation can be 2.6 times (=

307 nm/119 nm) in x- and 2.56 (= 676 nm/264 nm) in z-direction by exploring the saturation response of VW-SRS. The use of oil immersion lens with NA of 1.4 can further enhance the resolution up to 108 nm with saturated SRS.

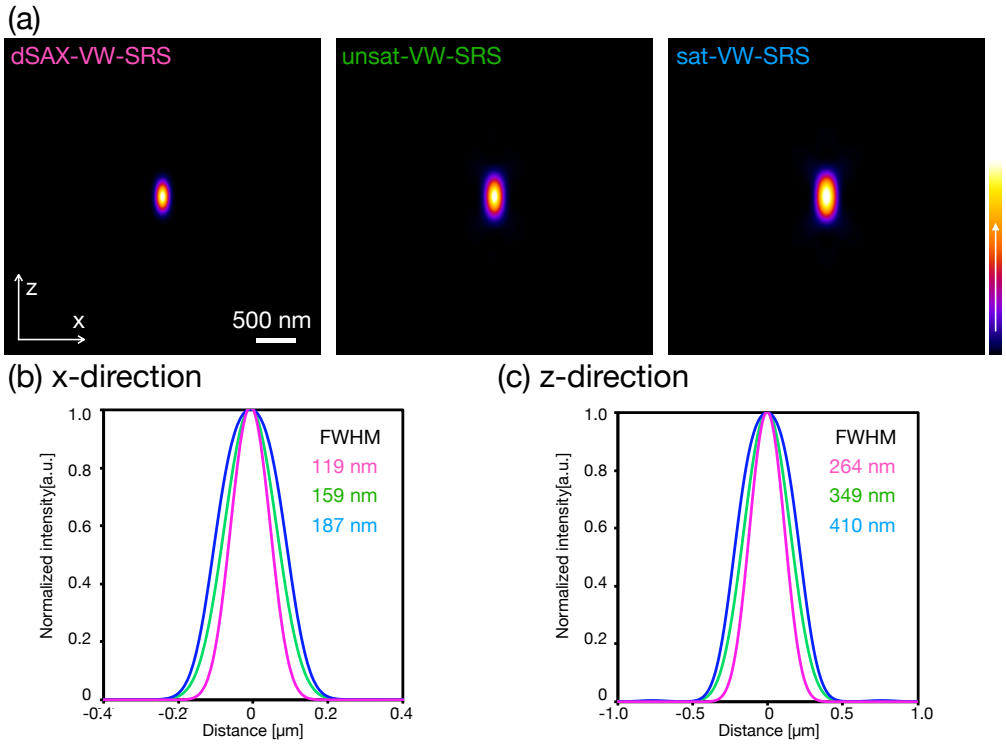

Figure 5.2. (a) Spatial distributions of VW-SRS signal with dSAX technique. The scale bar is 500 nm. (b) and (c) are the line profiles in x- and z-direction of each intensity distribution.

5.2 Development of visible-wavelength SRS microscopy

Optical setup of visible-wavelength SRS microscopy

Fig.5.3 shows the visible-wavelength SRS (VW-SRS) microscopy I have developed. The optical setup was based on the SRS microscope I have developed in Chapter 3. The only difference was that I used nonlinear crystals for frequency conversion of both pump and Stokes laser pulses. LBO crystal (5x5x8 mm, Castech) optimized for 2 ps laser pulses with 895-950 nm was used for pump beam. For Stokes beam, BBO crystal (5x5x9 mm, Castech) optimized for 1031.2 nm was used. The crystals were placed on kinematic mounts (KPY1/M, Thorlabs) to change the pitch and yaw angles. After the crystals, optical bandpass filters (BPF1: BrightLine Fluorescence Filter 447/60, Semrock for the pump, BPF2: BrightLine Fluorescence Filter 520/15, Semrock for THE Stokes) were placed to block NIR laser pulses. Lenses and mirrors after the crystals were optimized for the visible-wavelength range. The visible laser pulses were spatially combined at a short-wavelength pass dichroic mirror (DM, FF505-SDi01, Semrock). The inset is an actual picture of the laser passing through the nonlinear crystals, and both laser pulses were converted to visible light. After the sample, the pump beam was detected by a large area photo-diode (PD, Hamamatsu) through an optical bandpass filter (BPF3: FF02-460/80-25, Semrock). The voltage from PD was then amplified by a pre-amplifier and sent to the fast lock-in amplifier (UHF, Zurich Instruments). The demodulated SRS signal from the lock-in was visualized by PC.

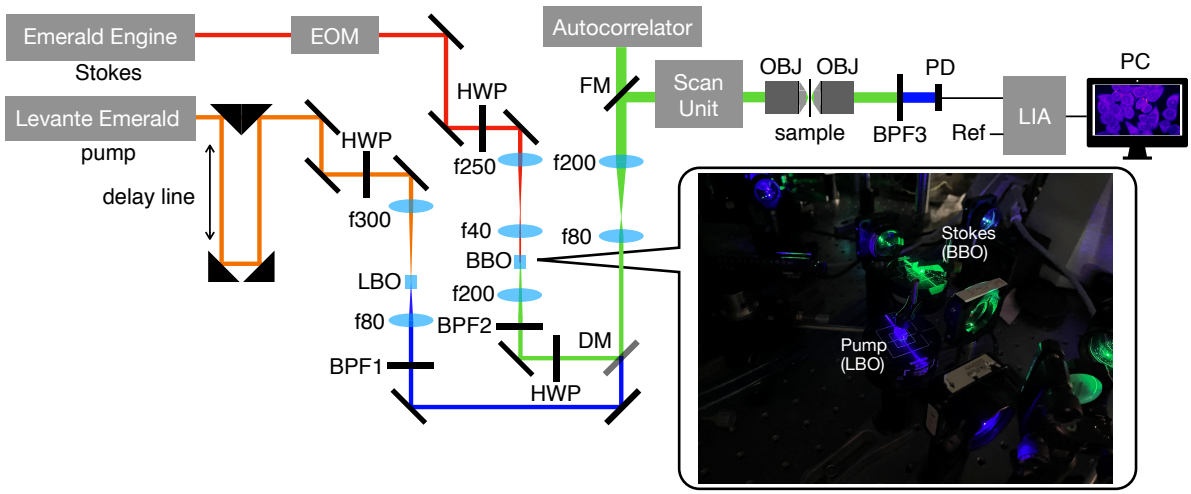

Figure 5.3. Optical setup for visible-wavelength SRS microscopy.

Characterization of conversion efficiency of SHG crystals

・Theoretical model of SHG signal intensity

A theoretical model of conversion efficiency (SHG signal intensity) due to nonlinear interaction be-

tween laser and nonlinear crystal is obtained from solving Maxwell equations with nonlinear polarization term. Suppose the fundamental frequency of ω_1, SHG frequency of ω_2, we have the SHG signal intensity as follows,[196, 197]

$$I_{(2\omega)} = \frac{2I_{(\omega)}^2 \omega_1^2 L^2 d_{eff}^2}{A\epsilon_0 c^3 n_\omega^2 n_{2\omega}^2} \mathrm{sinc}^2(L\Delta k/2) \tag{5.1}$$

where crystal length of L, effective nonlinear optical coefficient of $d_{eff} = \chi^{(2)}/2$, focusing spot size of A, vacuum permittivity of ϵ_0, speed of light of c, refractive index of n. Also, Δk inside of the sinc function is related to the phase-matching of SHG effect,

$$\Delta k = 2k_{(\omega)} - k_{(2\omega)} \tag{5.2}$$

where k_1 and k_2 are the wavenumber of fundamental and SHG waves, respectively. The sinc function $\mathrm{sinc}^2(L\Delta k/2) = (\sin(L\Delta k/2)/(L\Delta k/2))^2$ has maximum value of 1 under $\Delta k = 0$. This condition is called phase-matching. Under this condition, to have higher conversion efficiency, one can have a longer crystal length of L, higher beam intensity of $I_{(\omega_1)}$, smaller focusing area of A, higher nonlinear optical coefficient of d_{eff}. Phase matching can be achieved for nonlinear crystals with refractive index anisotropy (birefringence) when the fundamental laser pulse is introduced at an appropriate angle of incidence. Fig.5.4 shows refractive indices of the z-axis (optic axis) and xy-plane corresponding to the incident angle of light to the crystal (type- I). The refractive index value is expressed as the distance from the origin to the curved surface. There are two refractive indices for the wavelengths of the fundamental and SHG waves. The first is the ordinary refractive index n_o, whose value does not change with direction (corresponding to a circle). The other is called the extraordinary index n_e, which has a different refractive index depending on the direction (corresponding to an ellipse). n_o is the ordinary refractive index under a negative uniaxial crystal. Phase matching condition of Eq.5.2 can be rewrote as below using a relationship $k = n\omega/c$ and $\omega = 2\pi/\lambda$,

$$\Delta k = 2k_{(\omega)} - k_{(2\omega)} = \frac{4\pi}{\lambda_{(\omega)}}(n_\omega - n_{2\omega}) = 0 \tag{5.3}$$

Therefore, there is an optimal incident angle and direction of the fundamental wave, where the ordinary refractive index n_o and extraordinary index n_e become the same value, as shown in Fig.5.4. This is when the conversion efficiency and SHG signal intensity become strong. However, in general, the light propagates in the direction normal to the refractive index plane, so there is a gap between the propagation direction of the fundamental wave and the SHG wave (walk-off angle). This angle acts as an attenuation factor for the SHG intensity. Also, the fundamental wave intensity attenuates as SHG generates along with the crystal length L. The focusing spot size of A also varies with the crystal length L. In an actual experiment, the SHG signal intensity does not always follow with the factors of L^2, $I_{(\omega)}^2$, and A.

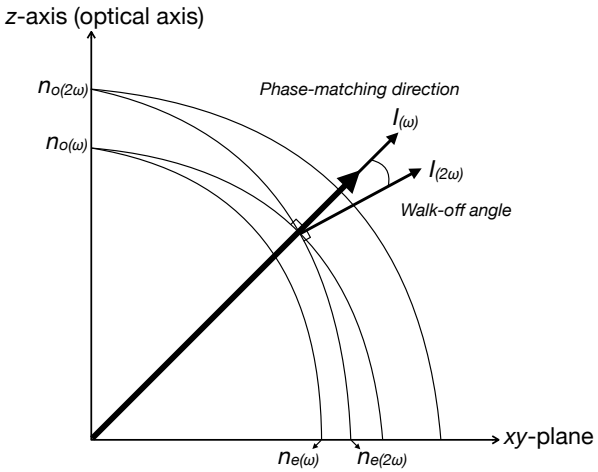

Figure 5.4. Phase matching of type-I SHG in a uniaxial crystal. Directions of $I_{(\omega)}$ and $I_{(2\omega)}$ show the propagation directions for fundamental and SHG waves.

・Experimental results

Considering the above models of SHG generation, I measured the SHG generation conversion efficiency of both pump and Stokes beams. The setup was the same as depicted in Fig.5.3. I used BBO crystal purchased from Castech, China for the Stokes beam. The crystal length was 5x5x9 mm to increase the efficiency. BBO has a narrow acceptable angle for phase-matching but higher conversion efficiency than other materials such as LBO. Since Stokes beam wavelength is fixed at 1031.2 nm, BBO crystal was a better choice. I used LBO crystal for the pump beam also purchased from Castech, China. The crystal length was 5x5x8 mm to increase the efficiency. I chose LBO since it has a wider acceptable angle for the phase-matching for a particular wavelength range. LBO was a better choice than BBO because the pump beam with 895-950 nm can be used to cover the wavenumber range from 1650 to 2950 cm^{-1}. Half-wave plates (HWP) were placed to optimize polarization direction. To have a higher conversion efficiency of SHG as much as possible, I used several sets of lenses with longer focal lengths to make the smaller diameter of beams at the crystal and maintain good beam profiles of the SHG beams. Also, the z-position was carefully adjusted to focus the lasers at the center of the crystals. After optimizing lenses and crystal angles, I measured the average powers before and after the crystals for the pump beam (895 nm) and Stokes beam (1031.2 nm). Table.5.1 shows the measurement results. As for the pump beam, I obtained the average power of 30 mW with 4% conversion efficiency. As for the Stokes beam, I obtained 10 mW with 1% conversion efficiency. The powers of 10 and 6.5 mW for the pump and Stokes beams after objective are enough to demonstrate VW-SRS imaging with 2 ps pulse width.[193, 194]

Table5.1: Conversion efficiency measurement of SHG crystals.

	Pump (LBO 5x5x8 mm)	Stokes (BBO 5x5x9 mm)
Before crystal	780 mW (895 nm)	1 W (1031.2 nm)
After crystal	31 mW (447.5 nm), 4 %	12 mW (515.6 nm), 1 %
After objective	10 mW (447.5 nm)	6.5 mW (515.6 nm)

Characterization of laser pulses after SHG crystals

I characterized the beam profiles after the frequency conversion using a beam profiler. Fig.5.5(a) shows the beam profiles of pump and Stokes beams with Gaussian distribution even after the SHG crystals. This was made possible by careful selection of the collimation lenses before and after the crystals. The ellipticity of both beams was about 90%, which was sufficient to perform SRS imaging. Next, I indirectly measured the pulse width of the pump and Stokes beams. At first, I tried to measure both laser pulses with an autocorrelator (pulseCheck SM2000, APE). However, I could not find the optimal settings in visible-mode to get the signal. Hence, I measured the temporal profile of SRS signal intensity by changing the time delay between pump and Stokes laser pulses and estimated the pulse width. PMMA beads with 1-10 μm were used as samples. The position of the delay line was moved back and forth, and the relative distance from the peak position was converted to the time domain (in picoseconds). Fig.5.5(b) shows the measurement results. As expected, the SRS signal intensity decreased when the temporal overlap of the pump and Stokes beam was destroyed. The FWHM of the profile was calculated to be 2.24 ps from the gaussian fitting. Assuming that the pump and Stokes beams were the same pulse width, the pulse width was estimated to be 1.58 ps.

VW-SRS imaging of PS beads and HeLa cells

To confirm the spatial resolution improvement by visible-wavelength excitation compared to NIR, I imaged polystyrene (PS) beads with 147 nm with the developed VW-SRS system. The wavelength of the pump and Stokes beam was 476.3 and 515.6 nm, respectively, to match 1603 cm^{-1} vibration mode. The average power on sample was 2.6 and 5 mW for pump and Stokes beams. The number of pixels was 256x256 with a pixel dwell time of 50 μs and an area of 7.4x7.4 μm^2. Fig.5.6(a) shows the VW-SRS image of the beads and (b) is line profiles of the selected bead in x- and y-directions. Compared to NIR excitation (refer to the spatial resolution evaluation in Chapter 3), each bead was clearly distinguished due to its shorter wavelength. The FWHMs of the bead profile were calculated to be 253 and 191 nm in x- and y-directions from Gaussian fitting (solid lines). The linear polarization direction could be in x-direction rather than y-direction due to the larger width of the profile. The mean FWHM was thus 222 nm. From the size of the beads of 147 nm and the FWHM of 222 nm, the experimental spatial resolution was estimated to be around 166 nm, which is very close to the

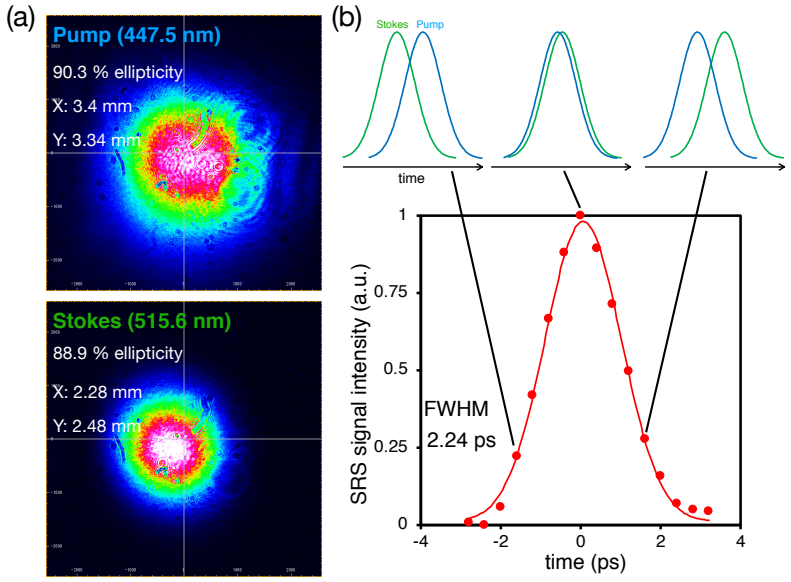

Figure 5.5. Characterization of laser pulses after SHG crystals. (a) Beam profiles of pump (447.5 nm) and Stokes beams (515.6 nm). (b) Indirect measurement of laser pulse width by SRS imaging of PMMA beads.

theoretical estimation of 162 nm ($= 0.61\lambda_{pump}/\sqrt{2}NA$). The experimental spatial resolution of the VW-SRS in this study is slightly inferior to that of previously published papers (-130 nm)[193, 194] due to the smaller NA of illumination objective lens and slightly longer wavelength of the pump beam. Our system uses a water immersion lens with 1.27 NA, while they used an oil immersion lens with 1.49 NA.

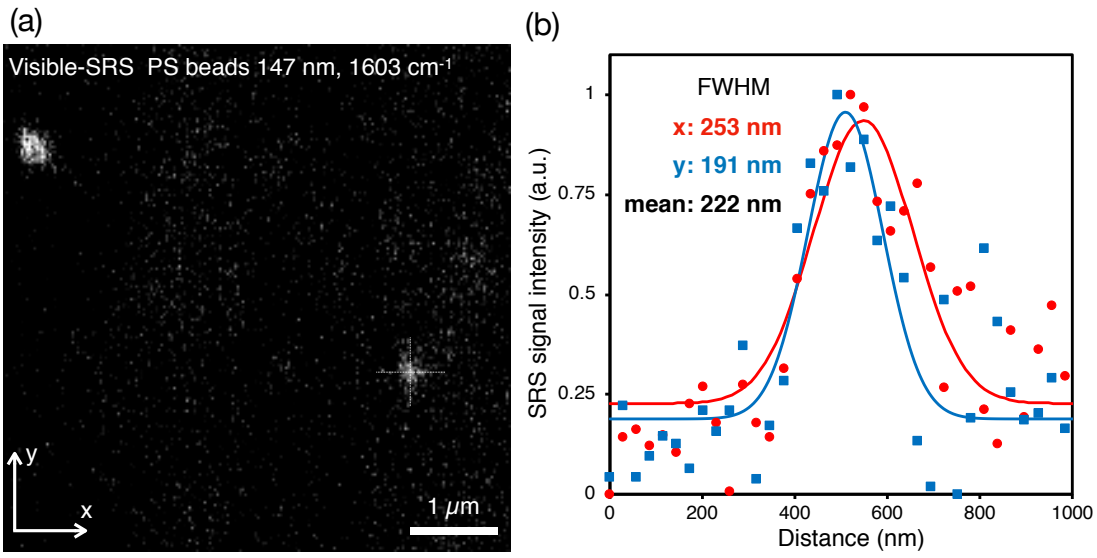

Figure 5.6. VW-SRS imaging of PS beads 147 nm. (a) VW-SRS image of the beads at 1603 cm^{-1}. (b) Line profiles of the bead in x (red dots) and y (blue dots) directions and gaussian fitting functions (red and blue lines). The FWHM was calculated to be 253 and 191 nm for x- and y- directions.

Next, to show the capability for imaging biological samples with the system, I demonstrated imaging of HeLa cells. The cells were chemically fixed before measurement to avoid structural movement during imaging. The target vibration mode was set to CH_3 with 2950 cm^{-1}. The wavelength of the pump beam on sample was set to 447.5 nm. The average power on sample was 4 and 3.4 mW for pump and Stokes beams. The number of pixel was 1000x1000 with a pixel dwell time of 50 μs and an area of 108.5x108.5 μm^2. Thus, the total acquisition time per image was around 50 sec. Fig.5.7(a) shows the VW-SRS image of the fixed HeLa cells. The distributions of lipid droplets and proteins were visualized. The thin nuclear membranes (20-40 nm) of each cell were also clearly distinguished due to the higher spatial resolution of visible-wavelength excitation. Fig.5.7(b) is the enlarged image of the cellular structure indicated as a white square area in (a), and Fig.5.7(c) is line profiles of the selected lipid droplet in the x-direction. The FWHM was 216 nm by a gaussian fitting. After the deconvolution with experimental spatial resolution, the true size of these droplets can be estimated to be around 130 nm in diameter.

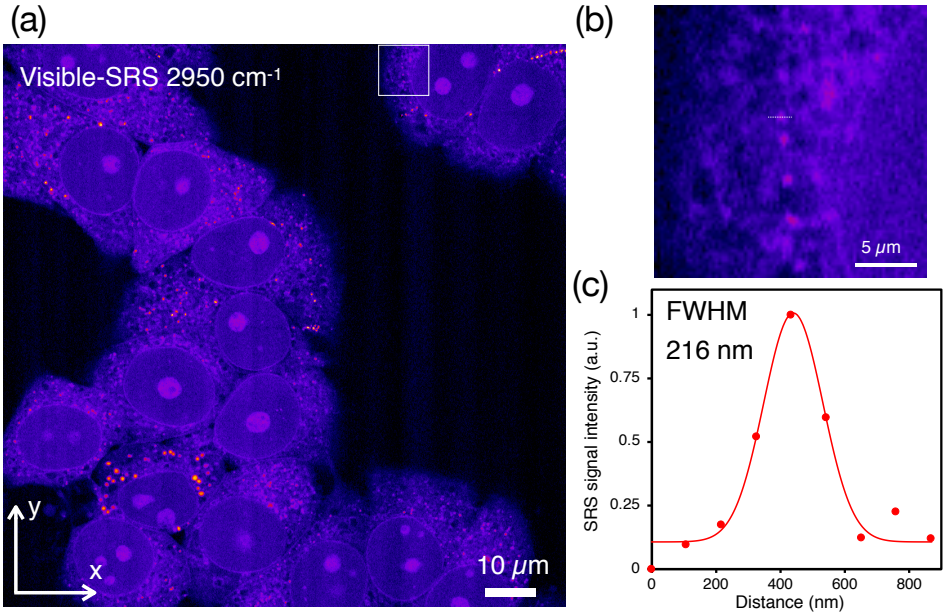

Figure 5.7. VW-SRS imaging of fixed HeLa cells. (a) VW-SRS image of the cells at 2950 cm^{-1}. (b) Lipid droplets of the cells at the selected white squared area in (a). The white dashed line was used for measuring the line profile. (c) Line profile of the lipid droplet (red dots) and gaussian fitting function (red line). The FWHM was calculated to be 216 nm.

5.3 Toward super-resolution VW-SRS with dSAX technique

Observation of saturation response of Carbow2086 Lyso probe by VW-SRS

To go beyond the diffraction limit of VW-SRS microscopy, I utilize the saturation response of SRS, which is observed under higher laser intensity conditions. Initially, I tried to observe the saturation response of the SRS signal from PS beads, PMMA beads, EdU crystals, and biomolecules (protein, lipids) in HeLa cells. However, all of these attempts were unsuccessful due to the low peak power on sample and the low damage threshold of the sample. In a paper demonstrating saturated super-resolution SRS microscopy, the authors utilized a diyne-based Raman probe for labeling mitochondria.[198] So, I focused on molecules with large Raman scattering cross-sections. As a sample, I used Carbow 4-yne probe (Carbow2086 Lyso)[199] as a first attempt to do super-resolution SRS imaging. The molecule has phenyl-capped four carbon-carbon triple-bonds and a lysosomal targeting moiety. At first, I measured the VW-SRS signal with different optical peak powers to observe saturation response. The molecule with 1 mM was sandwiched by two coverslips and measured with a VW-SRS system. The pump beam wavelength was set to 465.8 and 465.3 nm for imaging the on- and off-resonance SRS images. Fig.5.8(a) shows the imaging results with pump and Stokes laser powers of 8 and 4 mW. The pixel number was 128x128 with an imaging area of 74x74 μm^2. The pixel dwell time was 100 μs with a time constant of 10 μs. When the beams were matched with the SRS peak at 2089 cm^{-1}, a relatively higher SRS signal was observed from the solution area of the image. The signal was decreased away from the peak, leaving only nonlinear background signals. These background signals may be from cross-phase modulation and nonlinear absorptions. Therefore, the genuine SRS signal was retrieved by subtracting the average signal intensity of the two images. Fig.5.8(b) shows the relationship between the SRS signal (red dots) and the product of the laser peak intensity of pump and Stokes beams. The ratio of the average power of the pump to the Stokes beams was fixed at 2:1. I changed the average power of the pump beam from 3 to 12 mW. The signal increased linearly with a power of 1.05 (black curve) in the low intensity, while the saturation response was confirmed at the higher peak intensity region. Therefore, using two points with and without saturation, the dSAX technique can be applied to the VW-SRS images to obtain a super-resolution image.

VW-SRS imaging of lysosome labeled with Carbow2086 Lyso in HeLa cells

Next, I tried to observe the VW-SRS signal of HeLa cells labeled with Carbow2086 Lyso toward super-resolution imaging. Living HeLa cells were cultured with a glass-bottom dish for 24 h. The cells were incubated with 4 μM Carbow2086 Lyso for 30 min. Then, the cells were washed with PBS three times and chemically fixed with PFA 4% before the experiment. As a control, the cells without any labeling were also prepared. The SRS imaging was performed with an area of 37x37 μm^2, pixel numbers of 200x200, a pixel dwell time of 50 μs, and a time constant of 5 μs. The average powers of

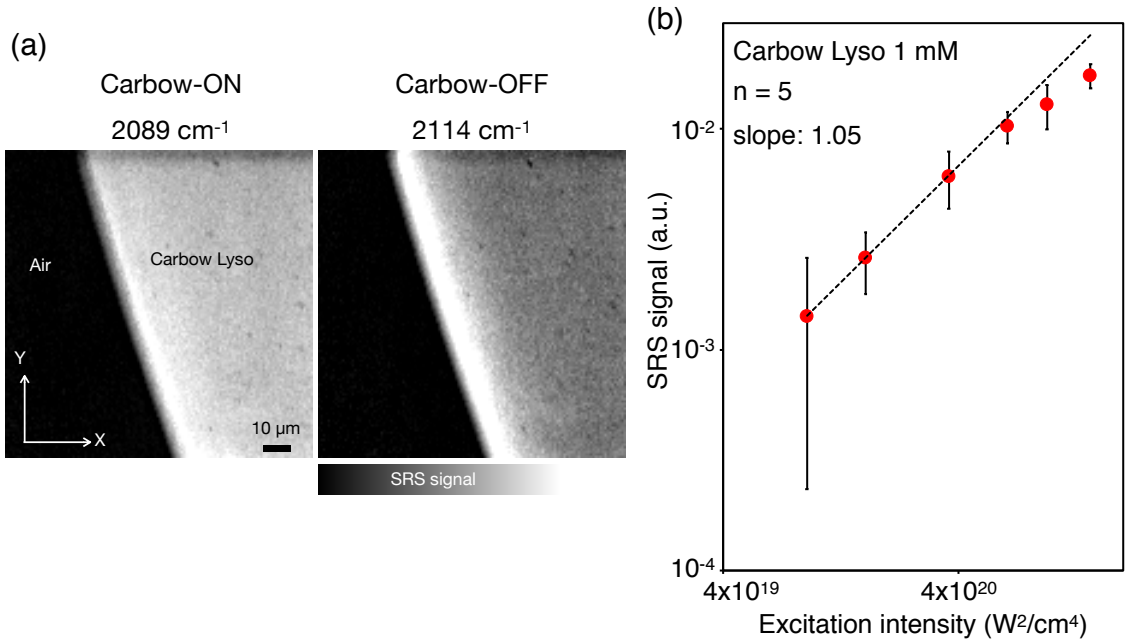

Figure 5.8. VW-SRS measurement of Carbow2086 Lyso. (a) VW-SRS images of Carbow2086 Lyso at SRS-on (2089 cm^{-1}) and SRS-off (2114 cm^{-1}). (b) Relationship between SRS signal and product of laser peak power of pump and Stokes beams. The red dots are the measured values with error bar (standard deviation, n = 5). The black line is a fitting curve with power of 1.05.

pump and Stokes beams on sample were 2 and 3 mW, respectively. Fig.5.9 shows time-lapse images of the cells (a) without and (b) with Carbow2086 Lyso. A large signal was observed in the first frame and gradually decreased in both conditions. This may not be from the Carbow signal as it was found to be stable over 100 frames.[199] The signal may be due to the nonlinear photothermal effect caused by absorption of cytochrome c, which was also observed in a previous paper.[194] Since there is no significant difference in absorption spectra between oxidized and reduced cytochrome c, this bleaching might be due to molecular destruction rather than oxidation. After bleaching of background signals, SRS signal from lysosomes was not observed (Fig.5.9(b)), unlike previous observations.[199, 200] The same trend was observed with other cells and live-cell conditions. In the future, it will be important to improve the detection sensitivity, accumulate Raman probes in the cells, and search for other Raman probe candidates for super-resolution VW-SRS imaging of biological samples.

Discussion and Conclusion

This chapter proposed applying the dSAX technique to visible-wavelength SRS (VW-SRS) microscopy to achieve super-resolution VW-SRS imaging. Conventional VW-SRS microscopy can resolve molecular distributions by a factor of two (130-150 nm) compared to NIR-based SRS microscopy. However, the resolution has been limited by Rayleigh's criteria. By applying the dSAX

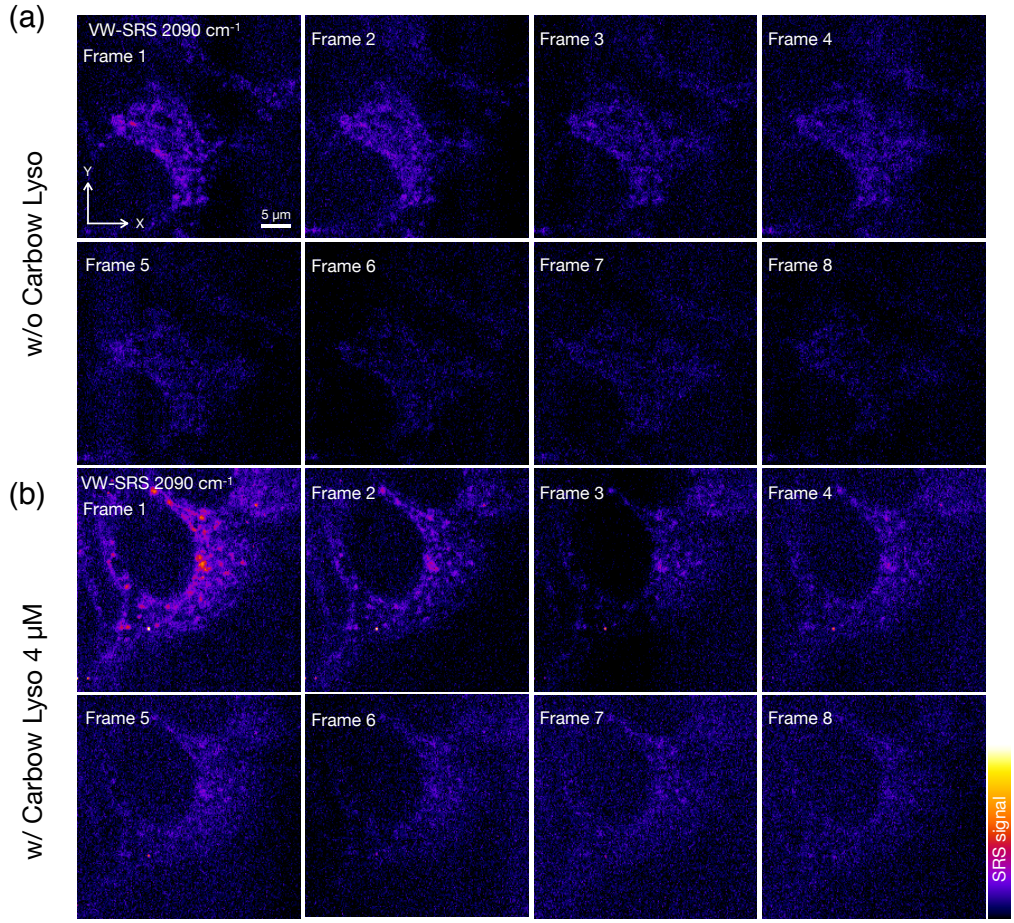

Figure 5.9. VW-SRS imaging of living HeLa cells (a) without Carbow2086 Lyso and (b) labeled with Carbow2086 Lyso at 2089 cm^{-1}.

technique to the saturation response of SRS, I theoretically confirmed the spatial resolution improvement compared to the conventional VW-SRS. In VW-SRS with dSAX and NA of 1.27, the spatial resolution can be improved up to around 120 nm. To prove this simulation experimentally, I developed a VW-SRS setup based on the conventional NIR-SRS microscope with nonlinear SHG crystals for the wavelength conversion. When the phase-matching was satisfied, the visible light was successfully observed with enough laser powers on sample for imaging.

By measuring PS beads with 147 nm diameter, the experimental spatial resolution of the system was determined to be around 166 nm, which was close to the theoretical calculation. I applied the proposed technique for imaging biological cells. I performed an initial evaluation of VW-SRS microscopy for imaging Raman probes in HeLa cells. Saturation response was successfully observed from the solution sample of the Carbow2086 Lyso probe under the available laser powers of pump and Stokes beams. Then, I tried to observe the SRS signals from lysosomes labeled with the Carbow2086 Lyso probe in HeLa cells. A significant background signal was observed, possibly from the photothermal effect due

to the absorption of cytochrome c. The Carbow signal was not observed possibly because the probes might not accumulate well in the lysosome during incubation, despite following the preparation protocol.[199] It may be worth changing the preparation conditions or trying different organelle-targeting Carbow probes. Also, conventional NIR-SRS should be performed to confirm the distribution of lysosomes labeled with the Carbow as it does not provide strong nonlinear background from cytochromes. The detection sensitivity of VW-SRS might still be lower than the molecular concentration within the cells. The SNR can be improved by increasing the laser power. However, it is limited by the conversion efficiency of SHG crystals and nonlinear visible wavelength light damage to cells. Currently, the average power on sample is limited to 3-5 mW due to the strong photodamage to the cells. In order to simultaneously reduce photodamage and increase sensitivity, faster-scanning speed (1-5 μs dwell time) and higher average power (30-50 mW) should be required.[194] In VW-SRS, the nonlinear background signal was significant due to the absorption of biological molecules. The frequency-modulation scheme may help to efficiently remove such a background contrast from the pure SRS signal.[201, 202]

Using the VW pre-resonance effect can be a good way to perform VW-SRS imaging with reasonable laser power below the damage threshold of biological samples. The SNR enhancement can be 10^2-10^4 depending on the absorption peak and Raman vibrational mode of molecules (see Appendix). The development of new VW pre-resonance Raman probes can further accelerate the successful application of VW-SRS microscopy toward super-resolution and high-sensitivity vibrational imaging of molecules.

Appendix

SNR enhancement by VW pre-resonance effect toward ultra-sensitivity super-resolution VW-SRS imaging

With known wavenumber for Raman vibration mode and center wavelength of absorption spectrum of target molecules, one can estimate the SNR enhancement factor of VW-SRS compared to NIR-SRS excitations due to pre-resonance effect. The calculations below are based on the previous papers.[193, 203, 194] The laser power P used for VW-SRS and NIR-SRS is assumed to be the same.

When stimulated Raman loss (SRL) is detected, the SRS signal intensity can be written as below,

$$\begin{aligned} \Delta I_{SRL} &= \mathrm{Im}(\chi_R^{(3)}) I_p I_S \\ &\approx N \sigma_{Raman} I_p I_S \end{aligned} \tag{5.4}$$

where ΔI_{SRL} is the relative loss in the pump beam, N is the number of vibrational chemical bonds in the focusing volume, σ_{Raman} is the Raman scattering cross-section, and I_p, I_S are the laser intensities of the pump and Stokes beam. The signal enhancement of VW-SRS compared to NIR-SRS is the ratio of each SRS signal intensity, ΔI_{VW-SRL} and $\Delta I_{NIR-SRL}$,which can be written as

$$\frac{\Delta I_{VW-SRL}}{\Delta I_{NIR-SRL}} = \frac{N_{VW-SRL}}{N_{NIR-SRL}} \times \frac{\sigma_{VW-Raman}}{\sigma_{NIR-Raman}} \times \frac{I_{VW-p}}{I_{NIR-p}} \times \frac{I_{VW-S}}{I_{NIR-S}} \tag{5.5}$$

To estimate the signal enhancement factor, one need to know a target Raman peak, the wavelength of pump and Stokes beam used for both NIR-excitation, $\lambda_{NIR-p}, \lambda_{NIR-S}$ (nm), and VW-excitation, $\lambda_{VW-p}, \lambda_{VW-S}$ (nm), and the molecule's absorption peak λ_e (nm). With these parameters, the enhancement factors of each component of Eq.5.5 is calculated as below.
(1) N, the number of vibrational chemical bonds in the focusing volume.

$$\frac{N_{VW-SRL}}{N_{NIR-SRL}} = \frac{r_{VW}^3}{r_{NIR}^3} = \frac{\lambda_{VW-p}^3}{\lambda_{NIR-p}^3} \tag{5.6}$$

(2) σ_{Raman}, the Raman scattering cross section

$$\sigma_{Raman} = K \times \omega_{pump} \times \omega_{Stokes}^3 \times \left[\frac{\omega_{pump}^2 + \omega_e^2}{(\omega_e^2 - \omega_{pump}^2)^2}\right]^2 \tag{5.7}$$

$$\begin{aligned} \frac{\sigma_{VW-Raman}}{\sigma_{NIR-Raman}} &= \frac{\omega_{VW-p} \times \omega_{VW-S}^3 \times \left[\frac{\omega_{VW-p}^2+\omega_e^2}{(\omega_e^2-\omega_{VW-p}^2)^2}\right]^2}{\omega_{NIR-p} \times \omega_{NIR-S}^3 \times \left[\frac{\omega_{NIR-p}^2+\omega_e^2}{(\omega_e^2-\omega_{NIR-p}^2)^2}\right]^2} \\ &= \frac{\frac{1}{\lambda_{VW-p}} \times \frac{1}{\lambda_{VW-S}}^3 \times \left[\frac{\frac{1}{\lambda_{VW-p}}^2+\frac{1}{\lambda_e}^2}{(\frac{1}{\lambda_e}^2-\frac{1}{\lambda_{VW-p}}^2)^2}\right]^2}{\frac{1}{\lambda_{NIR-p}} \times \frac{1}{\lambda_{NIR-S}}^3 \times \left[\frac{\frac{1}{\lambda_{NIR-p}}^2+\frac{1}{\lambda_e}^2}{(\frac{1}{\lambda_e}^2-\frac{1}{\lambda_{NIR-p}}^2)^2}\right]^2} \end{aligned} \tag{5.8}$$

(3) I_p, I_S, the laser intensities of the pump and Stokes beam.

$$\frac{I_{VW-p}}{I_{NIR-p}} = \frac{\frac{P}{r_{VW}^2}}{\frac{P}{r_{NIR}^2}} = \frac{r_{NIR}^2}{r_{VW}^2} = \frac{\lambda_{NIR-p}^2}{\lambda_{VW-p}^2} \tag{5.9}$$

$$\frac{I_{VW-S}}{I_{NIR-S}} = \frac{\lambda_{NIR-S}^2}{\lambda_{VW-S}^2} \tag{5.10}$$

Multiplying from (1) to (3) gives the total enhancement factor.

The image contrast is determined by SNR, not just by the signal amount. Under the shot-noise limited condition, noise is proportional to the square root of photon count of the pump beam, which can be written as

$$i_{shot} \approx \sqrt{\frac{P}{h\nu}} = \sqrt{\frac{P\lambda}{hc}} \tag{5.11}$$

Therefore, the shot noise ratio of VW-SRS and NIR-SRS is

$$\frac{i_{VW-shot}}{i_{NIR-shot}} = \frac{\sqrt{\frac{P\lambda_{VW-p}}{hc}}}{\sqrt{\frac{P\lambda_{NIR-p}}{hc}}} = \sqrt{\frac{\lambda_{VW-p}}{\lambda_{NIR-p}}} \tag{5.12}$$

Finally, the relative SNR (RSNR) is calculated by the ratio of total signal enhancement (Eq.5.5) and the noise ratio (Eq.5.12)

$$RSNR = \frac{\frac{\Delta I_{VW-SRL}}{\Delta I_{NIR-SRL}}}{\frac{i_{VW-shot}}{i_{NIR-shot}}} \tag{5.13}$$

With the use of VW-SRS, the SNR enhancement can be 10^2-10^4 under the same average power on sample. However, experimental results may vary depending on the extent of competing background signals due to nonlinear optical processes such as cross-phase modulation (XPM), and photothermal effects (thermal lensing).[194]

Reference

193) Yali Bi, Chi Yang, Yage Chen, Shuai Yan, Guang Yang, Yaozu Wu, Guoping Zhang, and Ping Wang. Near-resonance enhanced label-free stimulated Raman scattering microscopy with spatial resolution near 130 nm. *Light: Science & Applications*, 7(1):81, 2018.

194) Minghua Zhuge, Kai-Chih Huang, Hyeon Jeong Lee, Ying Jiang, Yuying Tan, Haonan Lin, Pu-Ting Dong, Guangyuan Zhao, Daniela Matei, Qing Yang, and Ji-Xin Cheng. Ultrasensitive Vibrational Imaging of Retinoids by Visible Preresonance Stimulated Raman Scattering Microscopy. *Advanced Science*, 8(9):2003136, 2021.

195) Yasunori Nawa, Yasuo Yonemaru, Atsushi Kasai, Ryosuke Oketani, Hitoshi Hashimoto, Nicholas I. Smith, and Katsumasa Fujita. Saturated excitation microscopy using differential excitation for efficient detection of nonlinear fluorescence signals. *APL Photonics*, 3(8):080805, Aug 2018.

196) 立野 公男. フレッシュマンのための現代光学-Ⅶ SHG 光学 (1). **光学**, 23(1):58–64, Jan. 1994.

197) 吉村 政志 and 森 勇介. 非線形光学結晶による高調波変換の基礎. *J. Plasma Fusion Res.*, 85(5):239–242, May 2009.

198) Li Gong, Wei Zheng, Ying Ma, and Zhiwei Huang. Saturated Stimulated-Raman-Scattering Microscopy for Far-Field Superresolution Vibrational Imaging. *Phys. Rev. Applied*, 11:034041, Mar 2019.

199) Fanghao Hu, Chen Zeng, Rong Long, Yupeng Miao, Lu Wei, Qizhi Xu, and Wei Min. Supermultiplexed optical imaging and barcoding with engineered polyynes. *Nature Methods*, 15:194–200, 01 2018.

200) Jingwen Shou, Robert Oda, Fanghao Hu, Keiko Karasawa, Mutsuo Nuriya, Masato Yasui, Bruce Shiramizu, Wei Min, and Yasuyuki Ozeki. Super-multiplex imaging of cellular dynamics and heterogeneity by integrated stimulated Raman and fluorescence microscopy. *iScience*, 24(8):102832, 2021.

201) Hanqing Xiong, Naixin Qian, Zhilun Zhao, Lingyan Shi, Yupeng Miao, and Wei Min. Background-free imaging of chemical bonds by a simple and robust frequency-modulated stimulated Raman scattering microscopy. *Opt. Express*, 28(10):15663–15677, May 2020.

202) Pascal Berto, Esben Ravn Andresen, and Hervé Rigneault. Background-Free Stimulated Raman Spectroscopy and Microscopy. *Phys. Rev. Lett.*, 112:053905, Feb 2014.

203) Lu Wei, Zhixing Chen, Lixue Shi, Rong Long, Andrew V Anzalone, Luyuan Zhang, Fanghao Hu, Rafael Yuste, Virginia W Cornish, and Wei Min. Super-multiplex vibrational imaging. *Nature*, 544(7651):465–470, Apr 2017.

204) Rehab M. Amin, Carmen Hauser, Ingrid Kinzler, Angelika Rueck, and Claudia Scalfi-Happ. Evaluation of photodynamic treatment using aluminum phthalocyanine tetrasulfonate chloride as a photosensitizer: new approach. *Photochem. Photobiol. Sci.*, 11:1156–1163, 2012.

205) Yasuo Yonemaru, Almar F. Palonpon, Shogo Kawano, Nicholas I. Smith, Satoshi Kawata, and Katsumasa Fujita. Super-Spatial- and -Spectral-Resolution in Vibrational Imaging via Saturated Coherent Anti-Stokes Raman Scattering. *Phys. Rev. Applied*, 4:014010, Jul 2015.

Chapter 6
Hyperspectral multiplex SRS spectroscopy of preresonance Raman probes

Introduction

Recently, the development of small Raman probe libraries such as Carbows,[206] and MARS probes[207] has enabled super-multiplex vibrational imaging of organelles in living cells. These probes have enabled highly sensitive Raman spectroscopy by exploiting the large molecular polarizability of Carbows and the electronic pre-resonance effect of MARS probes. These probes also have a sharp Raman line width in the silent region of the cell. Conventional SRS microscopy using picosecond laser pulses is suitable for resolving and detecting each peak. However, it is not ideal for rapid hyperspectral imaging of multiple organelles because of the time-consuming wavelength adjustment of the pump beam, which is challenging to the spatiotemporal dynamics of the molecules. Here, I demonstrate high-speed multiplex SRS spectroscopy of Raman probes using a hyperspectral SRS microscope. Spectral focusing allows high-speed spectral scanning in the femtosecond laser pulse-based SRS microscopy. The femtosecond laser pulses area stretched into the picosecond range by the grating pair while maintaining a broadband spectral width. Therefore, by moving the delay line position for each frame, fast spectral scans of 150 to 300 cm^{-1} can be achieved. The spectral resolution of the system is determined to be about 9 cm^{-1} by SRS spectroscopy of monochromatic Carbow probe solution. Hyperspectral SRS imaging of PS beads and HeLa cells labeled with the Carbow probe is then performed. I also successfully demonstrate four-color multiplex pre-resonance SRS spectroscopy of MARS and Rhodamine 800 probes, showing a great potential of hyperspectral SRS microscopy for multiplex Raman probe imaging applications. These results illustrate the advantages of fast hyperspectral SRS imaging for visualizing the dynamics of multiple organelles in living cells using Raman probes.

6.1 Hyperspectral SRS microscopy

Optical setup

Fig.6.1 shows a schematic of a hyperspectral SRS microscope used in this study. A femtosecond laser (InSight X3 Dual, Spectra Physics) has two output beams; Stokes beam at 1045 nm with 80 MHz repetition rate and 200 fs pulse width, and a tunable pump beam at 680-1300 nm with 120 fs pulse width. The beams were guided to the spectral focusing timing and recombination unit (SF-TRU, Newport), which allowed us to do femtosecond spectral focusing by diffraction grating pairs, and temporal/spatial overlap simultaneously inside the box.[208] Two variable attenuators (VA, Newport) were used for controlling beam powers. The intensity of the Stokes beam was modulated by EOM (Thorlabs) at 10 MHz with a modulation depth of more than 95%. A motorized-optical delay stage (Newport) was placed to ensure the temporal overlap between the Stokes and pump pulse trains. Both laser beams were introduced into the transmission diffraction grating pairs individually. The distance between the gratings can be adjusted depending on the wavelength and the degree of applied GDD (= resultant output pulse width). The reflection mirror in the pulse stretcher was slightly tilted so that pick-off mirrors reflected the output laser pulses. The beams were spatially combined at a dichroic mirror (DM). The output beam was directly guided to the Olympus laser scanning microscope to perform 2D scanning of lasers at a sample plane. A water immersion objective lens (XLPLN25XWMP2 25x, 1.05 NA, Olympus) was used for illumination, and an oil immersion condenser lens (1.4 NA, Olympus) was used for collecting the beams. An optical short-wavelength pass filter (SPF, Semrock) was used to block the Stokes beam. A large-area silicon photodiode (PD, S3590-09, Hamamatsu Photonics) was used as a detector. The PD was reverse-biased with 64 V by DC power suppliers to increase saturation threshold and response bandwidth. A low pass filter (BLP-1.9+, Mini-Circuits) was inserted between the DC power supplier and PD to reduce the fluctuation of the DC signal. The signal from PD was pre-filtered with a bandpass filter (BBP-21.4+, Mini-Circuits) to reject large DC signals. The signal was sent to a fast lock-in amplifier (SR844, SRS, and HF2LI, Zurich Instruments) for the SRS signal demodulation. The image reconstruction was done by Olympus software FLUOVIEW.

Spectral resolution

A higher spectral resolution is required for super-multiplex SRS imaging of vibrational probes. To determine the spectral resolution of the system, I measured the SRS spectrum of a single Raman probe. I used Carbow 2-yne (peak at 2226 cm^{-1}) and 3-yne (peak at 2183 cm^{-1})[206] as sample. Fig.6.2(a) shows a schematic of measurement setup. The Carbow solution was sandwiched by a coverslip for the objective side and slide glass 1 mm thickness for the condenser side. An imaging spacer 100 μm thickness was used to store the solution. Hyperspectral SRS measurement was done by changing the time delay between pump and Stokes laser pulses by moving the position of the delay line. I have

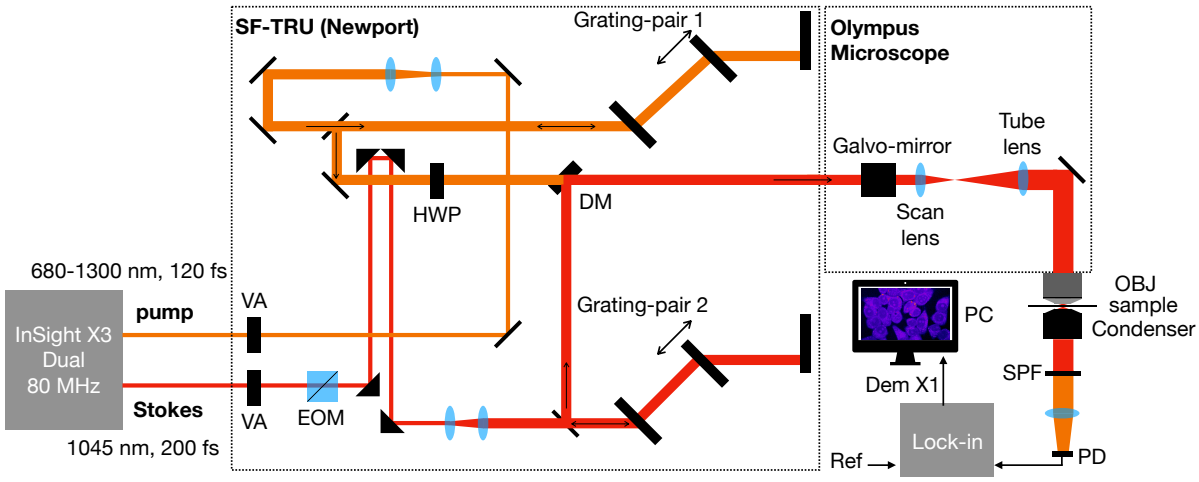

Figure 6.1. Optical setup of a hyperspectral SRS microscope with femtosecond laser pulses.

made a calibration curve showing the relationship between the delay line position and wavenumber by measuring the peak position of two sets of solutions (Fig.6.2(b)). The pump and Stokes beam wavelengths were 849 and 1045 nm, respectively. Hence, the central wavenumber was 2210 cm^{-1}. The curve shows that a displacement of delay line with 10 μm corresponds to the shift in spectral-domain with 1.3 cm^{-1}. Next, the Carbow 2-yne solution with 10 mM was measured from 2190 to 2265 cm^{-1}. The pump and Stokes beam powers on sample were 60 and 115 mW. The number of pixels per image was 256x256 with a pixel dwell time of 10 μs. In total, 61 images were acquired at delay line position from 106.360 to 106.960 mm (10 μm step). I calculated the mean value of each image to obtain the SRS spectrum. Fig.6.2(c) shows the SRS spectrum after the wavenumber calibration. A single and sharp peak was observed at 2226 cm^{-1}. Based on the Lorentzian fitting function, FWHM of the peak was obtained to be 15.1 cm^{-1}. The experimental spectral resolution was then calculated with the following equation[209, 210]

$$\Delta\nu_{ex} = \sqrt{\Delta\nu_m^2 - \Delta\nu_{sp}^2} \tag{6.1}$$

where $\Delta\nu_m$ is the measured SRS peak width and $\Delta\nu_{sp}$ is the high-resolution spontaneous Raman line peak width (-12 cm^{-1}). The experimental spectral resolution was thus determined to be around 9.2 cm^{-1}. If the pulse widths of the pump beam and Stokes beam were the same, the pulse width after spectral focusing can be estimated to around 3.2 ps.

I have also compared sensitivity (signal-to-noise ratio) between the conventional APE-based picosecond SRS system and this newly developed InSight-based hyperspectral SRS system. The APE system was based on picosecond laser pulses with 6-7 ps pulse width and 76 MHz repetition rate. The Stokes beam was modulated at 8 MHz, while the InSight system was at 10 MHz. As a sample, I used Carbow 2-yne solution with 10 mM. The imaging conditions were set to be the same between the two

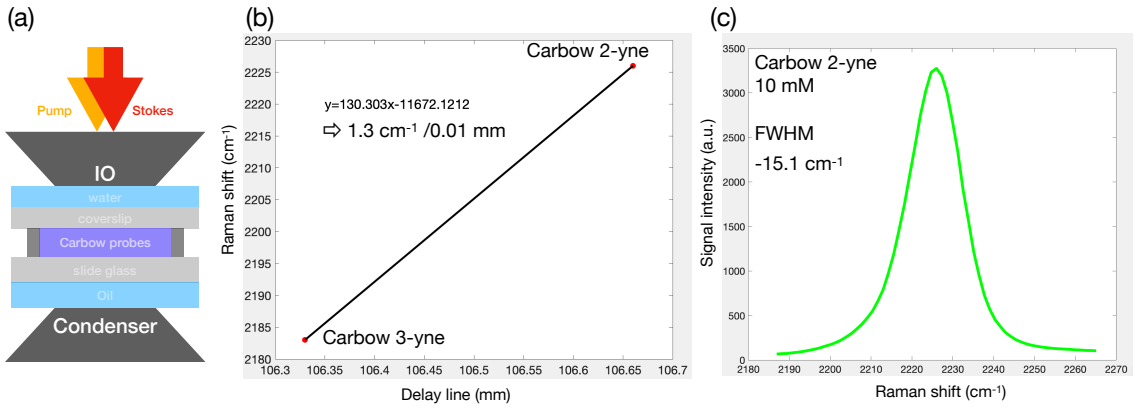

Figure 6.2. SRS spectroscopy of Carbow probes 10 mM. (a) Measurement setup of Carbow solution 10 mM dissolved in DMSO. The solution was stored within imaging spacer between coverslip and slide glass. (b) Calibration curve between delay line position and wavenumber by measuring multiple Carbow solutions 2-yne and 3-yne. (c) SRS spectrum of Carbow 2-yne 10 mM after calibrating the wavenumber.

systems except for the laser properties. The average powers of pump and Stokes beams were 20 and 60 mW, respectively. The number of pixels was 512x512 with pixel dwell time and time constant of 4 μs. The lock-in amp HF2LI from Zurich Instruments was used. As for the InSight system, the pump beam wavelength was set to be 851 nm (2181.5 cm^{-1} with Stokes beam at 1045 nm) for hyperspectral imaging around 2050-2350 cm^{-1}. To calculate SNR, I obtained three images; on-resonance (2226 cm^{-1}), off-resonance (2074 cm^{-1}), and image without Stokes beam on sample. SNR was then calculated from the following equation,

$$SNR = \frac{I_{ON} - I_{OFF}}{\sigma} \tag{6.2}$$

where I_{ON} and I_{OFF} were the mean signal intensity of the on-resonance and off-resonance (2074 cm^{-1}) images, respectively, and σ was the standard deviation of the image with only pump beam on sample (without Stokes beam on sample). The prominent noise was assumed to be shot-noise, which was estimated from the pixel intensity fluctuation of the image. The following table shows the measurement results and calculated SNRs of each system. The sensitivity of conventional APE SRS system was 1.45 times higher than that of InSight-based hyperspectral SRS system. This small difference may affect the image contrast in the case of a small SRS signal in a large nonlinear background signal, but may be negligible for molecules with large Raman scattering cross sections and high concentrations. This slight difference might come from the laser specs such as wavelength, repetition rate, modulation frequency, and peak intensity on sample. The difference in excitation method (APE: narrowband picosecond excitation, InSight: femtosecond spectral focusing) may also have affected the resulting signal intensity.

Table6.1: SNR comparison between InSight and APE SRS systems based on Carbow 2-yne measurement.

SNR	APE SRS	InSight SRS
FOV1	$\frac{2486(\text{on})-51(\text{off})}{108(\text{noise})} = 22.5$	$\frac{1853-95}{106} = 16.6$
FOV2	$\frac{2482-64}{107} = 22.6$	$\frac{1944-122}{119} = 15.3$
FOV3	$\frac{2426-52}{106} = 22.4$	$\frac{1972-151}{126} = 14.5$
average	22.5	15.5

Hyperspectral SRS imaging of polystyrene beads labeled with three-color Carbows

Multi-color hyperspectral SRS imaging of Carbow probes was demonstrated by using PS beads as samples. At first, the PS beads were labeled with three different Carbow probes, 2-yne (2226 cm^{-1}), 2-yne isotope (2203 cm^{-1}), and 3-yne (2183 cm^{-1}).[211] The pump beam wavelength was 848 nm with an average power of 20 mW on sample. The Stokes beam was around 30 mW on sample. In total, I continuously acquired 101 images with a delay line position of 104.34 to 105.34 mm. The number of pixels was 256x256 with a pixel dwell time of 12.5 μs. Hence, the total imaging time for hyperspectral scanning was around 83 s. During scanning, the SRS signal became stronger three times at different locations of the delay lines, which corresponded to the SRS signal of each Carbow probe. Fig.6.3(a) shows SRS image of the PS beads obtained at 104.84 mm (2202 cm^{-1}). A bright SRS signal was observed from the beads. With known wavenumber and delay line positions, I created a calibration curve that can convert the delay line position to the wavenumber as shown in Fig.6.3(b). To obtain the SRS spectrum of the beads, mean SRS signal intensity was measured from the white square area in (a) at each frame. After the wavenumber calibration, the SRS spectrum with multiple Carbow peaks was obtained (Fig.6.3(c)). Due to high spectral resolution of the system with 9 cm^{-1}, the three SRS peaks were clearly resolved by an interval of 20 cm^{-1}.

SRS imaging of HeLa cells with Carbow 2-yne

Next, I demonstrated SRS imaging of HeLa cells labeled with Raman probes. Tubulin of living HeLa cells was labeled by Rdots2220, which is small polystyrene beads containing Carbow 2-yne probes.[211] The cells were then fixed and sandwiched by a coverslip and slide glass. At first, I adjusted the pump beam wavelength and delay line position to measure the signal at 2226 cm^{-1}. The pump and Stokes beam powers on sample were 60 and 115 mW. The number of pixels per image was 512x512 with a pixel dwell time of 400 μs and a time constant of 100 μs. The sensitivity of lock-in (SR844, SRS) was 300 μV. Fig.6.4(a) shows an SRS image of Carbow 2-yne localized in tubulin of fixed HeLa cells. The pump beam wavelength was then tuned to 800 nm to observe biological molecules (proteins) at around 2940 cm^{-1}. The system can be used for imaging Raman probes in biological samples.

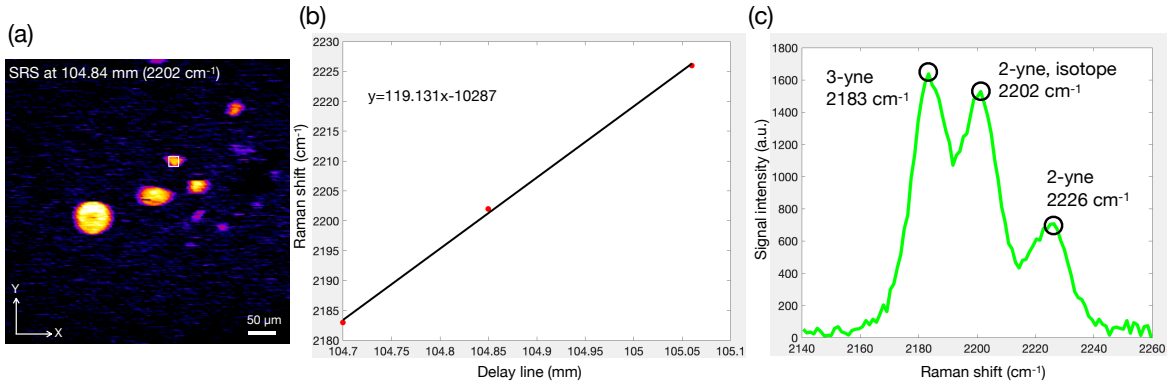

Figure 6.3. Hyperspectral SRS imaging of polystyrene (PS) beads labeled with three Carbow probes. (a) SRS image of PS beads at a delay line position of 104.84 mm, corresponding to the Raman shift at 2202 cm^{-1}. Scale bar is 50 μm. (b) Calibration curve between delay line position and wavenumber. (c) SRS spectrum of PS beads indicated as a while square in (a) after calibrating the wavenumber.

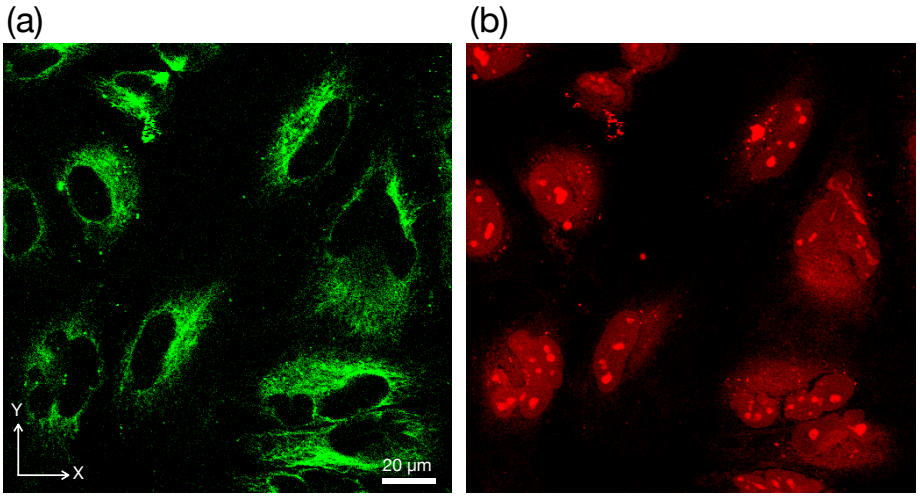

Figure 6.4. SRS imaging of (a) tubulin of fixed HeLa cells labeled with Carbow 2-yne and (b) CH-region. Scale bar is 20 μm.

6.2 Multiplex pre-resonance SRS spectroscopy

SRS spectroscopy of pre-resonance Raman probes

High-speed hyperspectral SRS imaging of the Carbow probes in living cells has been published this year, visualizing temporal dynamics of multiple organelles.[212] Recently developed Raman probes, such as MARS, are 10-10^2 times more sensitive than Carbow probes due to the electronic pre-resonance effect.[213, 207, 214] The modulation of the Raman peaks of CN-bond in MARS can be realized by isotope editing, allowing super-multiplex vibrational imaging of organelles with high sensitivity.[213, 207, 214] Besides MARS probes, Rhodamine 800 (Rh800) molecule is also well used for

the pre-resonance SRS measurement.[215, 216] Here, I show that the developed system can be used for high-speed hyperspectral imaging of pre-resonance probes by measuring single- and multiple-color Rh800 and MARS probes.

Four different derivatives of Rh800 and MARS probes with and without isotope substitution[216, 207] were used for the measurement. The pump beam wavelength was set to 851 nm with 20 mM on sample. The Stokes beam was 60 mW on sample. I used the lock-in amplifier SR844. Hence, the shortest time constant 30 μs (no-filter mode) was used with a pixel dwell time of 4 μs. The delay line position was scanned from 105.215 to 106.215 mm (10 μm step), covering around 2120 to 2260 cm^{-1}. The number of pixels for each wavenumber was 128x128, so the total imaging time for 101 frames was around 7 sec. As for Rh800, the concentrations for all probes were set to 1 mM. For MARS probes, MARS2228 (C12N14) was 600 μM, and others were 1 mM. Fig.6.5(a) and (b) show pre-resonance SRS spectra of Rh800 and MARS probes. Each Raman peak was observed with sufficient SNR. The FWHMs of the peaks were around 14-18 cm^{-1}, depending on the probe types and peak positions. The spectral resolution was estimated to 9-11 cm^{-1}. The background signal intensity in the central wavenumber region (2160-2220 cm^{-1}) was relatively large, which may be due to the cross-phase modulation caused by the overlap of the pump and Stokes beams in the time domain. Fig.6.5(c) shows the calibration curve created from the eight different Raman peak positions and corresponding delay line positions. Next, I examined how well the system could spectrally resolve the Raman peaks close to each other. I used MARS2228 (C12N14) with 100 μM and O4CN2241 (C12N14) with 500 μM[213] as samples. Fig.6.5(d) shows single-color SRS spectra of each probe. The FWHMs were around 14 cm^{-1}. Fig.6.5(d) is a SRS spectrum of mixed solution of MARS2228 with 50 μM and O4CN2241 with 250 μM. I adjusted the concentrations to achieve the same SRS signal level. By doing so, two peaks corresponding to each Raman probe appeared in the SRS spectrum. The position where the signal intensity decreased was at 2233 cm^{-1}, which is approximately in the middle of the two peaks. From this two-color solution measurement, I found the system to be able to resolve peaks at a separation of at least 13 cm^{-1}.

4- and 8-color SRS spectroscopy of pre-resonance Raman probes

As a next step, 4- and 8-color SRS spectroscopy of mixed solution was demonstrated toward high-speed multiplexed SRS imaging of pre-resonance Raman probes. As for 4-color SRS spectroscopy, I prepared two sets of samples (MARS and Rh800). To have a similar level of SRS signal intensity, the concentration of each probe was carefully adjusted. In 4-color MARS solution, MARS2228 (C12N14) was 300 μM, MARS2200 (C12N15) was 100 μM, MARS2176 (C13N14) was 250 μM, and MARS22147 (C13N15) was 500 μM. In 4-color Rh800 solution, Rh800 2155 (C13N15) was 1 mM, and others were set to be 500 μM. The pump beam wavelength was set to 851 nm with 20 mM on sample, while the Stokes beam (1045 nm) was 60 mW on sample. I used the lock-in amplifier SR844. Hence, the shortest time constant 30 μs (no-filter mode) was used with a pixel dwell time of 4 μs. The delay line position was scanned from 105.237 to 107.237 mm (10 μm step), covering around

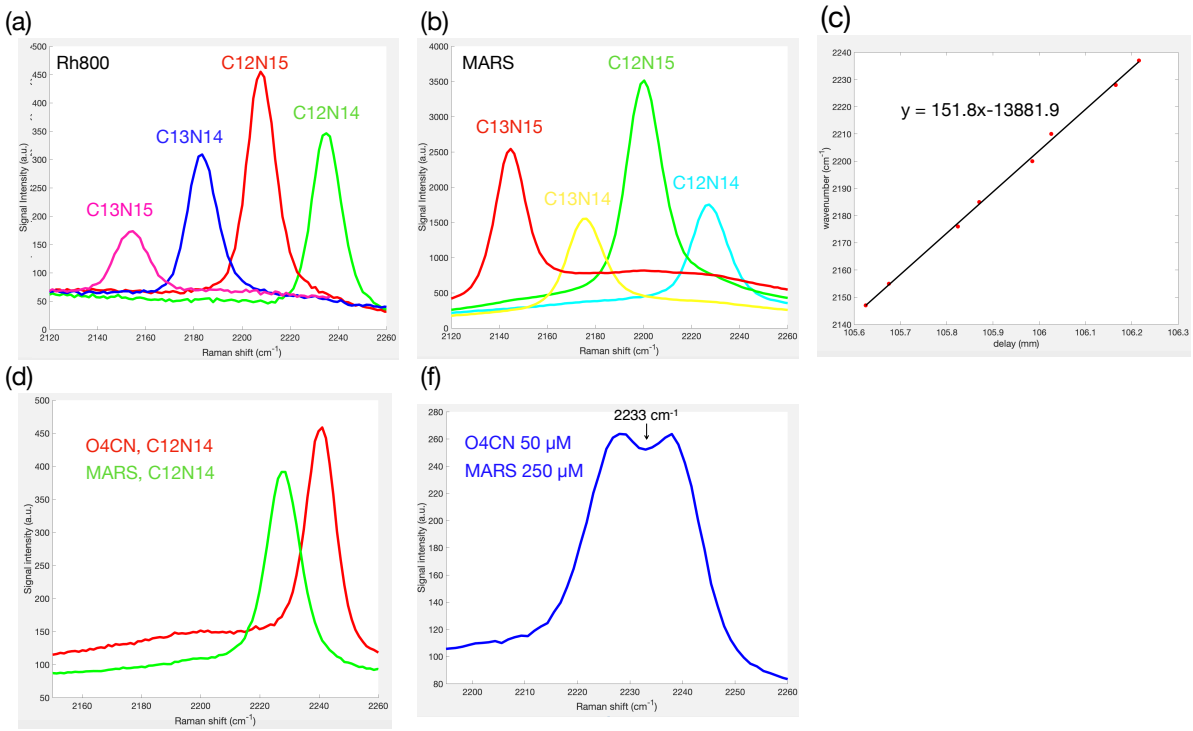

Figure 6.5. SRS spectroscopy of Rh800 and MARS probes. (a) Single-color SRS spectra of Rh800 dyes. (b) Single-color SRS spectra of MARS probes. (c) Calibration curve created from the single-color SRS measurement of Rh800 and MARS probes. Red dots are the measured values and a black line is linear fitting function. (d) Single-color SRS spectra of MARS and O4CN probes. (f) Two-color SRS spectra of MARS and O4CN probes.

2100 to 2300 cm^{-1}. The number of pixels for each wavenumber was 128x128, so the total imaging time for 201 frames was around 13 sec. Fig.6.6(a) shows 4-color SRS spectra of MARS (green line) and Rh800 (red line). Each Raman peak was resolved and distinguished from the neighboring peaks with 25-30 cm^{-1} separation. Compared to Rh800 probes, the MARS probe solution had a larger background signal. This was also seen in single-color MARS spectroscopy (Fig.6.5(b)). This can be due to the absorption peak difference of Rh800 and MARS probes, hence the degree of resonance and other nonlinear absorption effects such as two-photon absorption or photothermal process. While Rh800 has a maximum absorption peak at 700 nm, MARS probes used in this study were 760 nm.[207] Therefore, nonlinear absorption effects may have caused higher background signal of the MARS measurement than Rh800.

Next, I mixed the Rh800 and MARS probes to perform an 8-color SRS spectroscopy. I carefully adjusted the concentration of each probe so as not to overwhelm the other Raman signals. As for MARS probes, MARS2228 (C12N14) was 50 μM, MARS2200 (C12N15) was 25 μM, MARS2176 (C13N14) was 50 μM, and MARS22147 (C13N15) was 94 μM. As for the Rh800 solution, Rh800 2155 (C13N15) was 750 μM, and the others were set to be 375 μM. The measurement conditions were the same as the 4-color spectroscopy. Fig.6.6(b) shows the result. Even with eight different

Raman probes, only four peaks were observed. The position of each peak was almost in the middle of the Rh800 and MARS probe pairs. For example, the peak at 2233 cm^{-1} was located in the middle of the two peaks of Rh800 2237 and MARS 2228. This indicates that Raman peaks of Rh800 and MARS pairs were completely merged in a spectral domain. Lower spectral resolution of the system with around 10 cm^{-1} can be one of the reasons. The other reason might be the overlapping of large background signals of each probe.

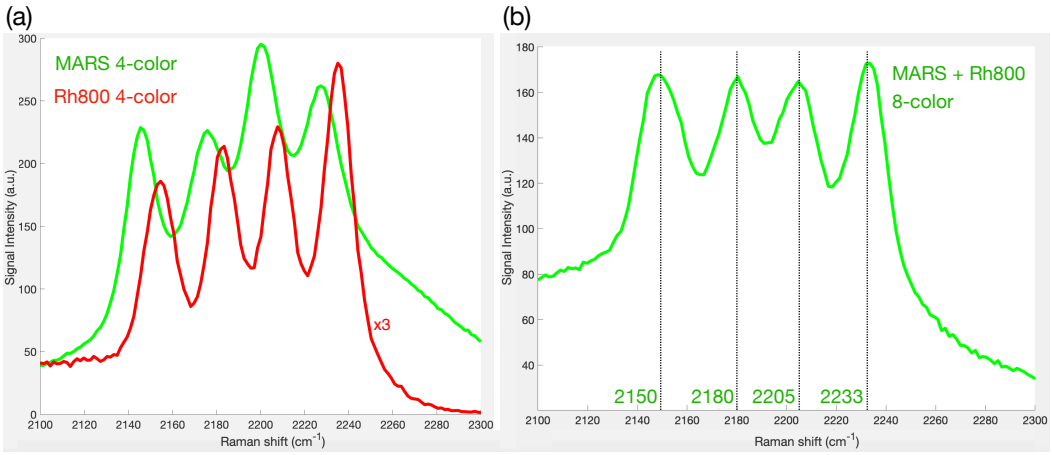

Figure 6.6. (a) 4-color and (b) 8-color SRS spectroscopy of Rh800 and MARS probes.

Discussion and Conclusion

In this chapter, I presented high-speed multiplex SRS spectroscopy of various samples such as PS beads, HeLa cells, and pre-resonance Raman probes. The spectral resolution of the hyperspectral SRS system was evaluated to be around 9-10 cm^{-1}. The sensitivity was compared with a conventional picosecond laser (APE)-based SRS microscope and found to be almost the same (1.45 times higher than that of the APE system). This slight difference might be due to differences in the laser repetition rate, the modulation frequency, and the peak intensity on sample. Also, the differences in the laser wavelength and the excitation schemes (w/ and w/o spectral focusing) might also affect the sensitivity difference. The developed hyperspectral SRS system can be particularly useful in multiplex imaging, where many Raman peaks exist in a small spectral range. Toward multiplex pre-resonance SRS imaging, I demonstrated SRS spectroscopy of MARS and Rh800 probes. In 2- and 4-color SRS spectroscopy, each Raman peak was well separated with 20-30 cm^{-1} away from neighboring peaks. However, in the 8-color SRS measurement (4-color MARS + 4-color Rh800), only four peaks were observed, possibly due to the spectral merge of the probes and high background signal. Several improvements can be made for 8-color or more multiplexed SRS spectroscopy/imaging of the preresonance probe. First, we should make the most of the 200-300 cm^{-1} spectral region that can be observed at once, and the

peak separation should be increased from the current 10 cm^{-1} to about 20-30 cm^{-1}. In this way, 10 Raman probes can be observed in one hyperspectral scan. The second approach is to stretch the pulse width to 14 ps while correcting for higher-order dispersion. This method mitigates the nonlinear background signal (see Chapter 3) and at the same time improves the spectral resolution and provides good spectral resolution of nearby peaks. This work was carried out in Wei Min's lab of the Department of Chemistry, Columbia University.

Reference

206) Fanghao Hu, Chen Zeng, Rong Long, Yupeng Miao, Lu Wei, Qizhi Xu, and Wei Min. Supermultiplexed optical imaging and barcoding with engineered polyynes. *Nature Methods*, 15(3):194–200, 2018.

207) Lu Wei, Zhixing Chen, Lixue Shi, Rong Long, Andrew V Anzalone, Luyuan Zhang, Fanghao Hu, Rafael Yuste, Virginia W Cornish, and Wei Min. Super-multiplex vibrational imaging. *Nature*, 544(7651):465–470, Apr 2017.

208) Aram Zeytunyan, Tommaso Baldacchini, and Ruben Zadoyan. Module for multiphoton high-resolution hyperspectral imaging and spectroscopy. In *Proc.SPIE*, volume 10498, 2 2018.

209) Mojtaba Mohseni, Christoph Polzer, and Thomas Hellerer. Resolution of spectral focusing in coherent Raman imaging. *Opt. Express*, 26(8):10230–10241, Apr 2018.

210) Mohammed S. Alshaykh, Chien-Sheng Liao, Oscar E. Sandoval, Gregory Gitzinger, Nicolas Forget, Daniel E. Leaird, Ji-Xin Cheng, and Andrew M. Weiner. High-speed stimulated hyperspectral Raman imaging using rapid acousto-optic delay lines. *Opt. Lett.*, 42(8):1548–1551, Apr 2017.

211) Zhilun Zhao, Chen Chen, Shixuan Wei, Hanqing Xiong, Fanghao Hu, Yupeng Miao, Tianwei Jin, and Wei Min. Ultra-bright Raman dots for multiplexed optical imaging. *Nature Communications*, 12(1):1305, 2021.

212) Jingwen Shou, Robert Oda, Fanghao Hu, Keiko Karasawa, Mutsuo Nuriya, Masato Yasui, Bruce Shiramizu, Wei Min, and Yasuyuki Ozeki. Super-multiplex imaging of cellular dynamics and heterogeneity by integrated stimulated Raman and fluorescence microscopy. *iScience*, 24(8):102832, 2021.

213) Yupeng Miao, Naixin Qian, Lixue Shi, Fanghao Hu, and Wei Min. 9-cyanopyronin probe palette for super-multiplexed vibrational imaging. *Nature Communications*, 12(1):4518, 2021.

214) Lu Wei and Wei Min. Electronic Preresonance Stimulated Raman Scattering Microscopy. *The Journal of Physical Chemistry Letters*, 9(15):4294–4301, 2018.

215) Peter Fimpel, Ashwin J. X. Choorakuttil, Andrea Pruccoli, Lukas Ebner, Shunji Tanaka, Yasuyuki Ozeki, Martin J. Winterhalder, and Andreas Zumbusch. Double modulation SRS and SREF microscopy: signal contributions under pre-resonance conditions. *Phys. Chem. Chem. Phys.*, 22:21421–21427, 2020.

216) Hanqing Xiong, Lixue Shi, Lu Wei, Yihui Shen, Rong Long, Zhilun Zhao, and Wei Min. Stimulated Raman excited fluorescence spectroscopy and imaging. *Nature Photonics*, 13(6):412–417, 2019.